On Enhancing Microgrid Control and the Optimal Design of a Modular Solid-State Transformer with Grid-Forming Inverter

by

Robert Scott Mongrain

A Dissertation Presented in Partial Fulfillment
of the Requirements for the Degree
Doctor of Philosophy

Approved November 2019 by the
Graduate Supervisory Committee:

Raja Ayyanar, Chair
Qin Lei
George Pan
Jiangchao Qin

ARIZONA STATE UNIVERSITY

December 2019

ABSTRACT

This dissertation covers three primary topics and relates them in context. High frequency transformer design, microgrid modeling and control, and converter design as it pertains to the other topics are each investigated, establishing a summary of the state-of-the-art at the intersection of the three as a baseline. The culminating work produced by the confluence of these topics is a novel modular solid-state transformer (SST) design, featuring an array of dual active bridge (DAB) converters, each of which contains an optimized high-frequency transformer, and an array of grid-forming inverters (GFI) suitable for centralized control in a microgrid environment. While no hardware was produced for this design, detailed modeling and simulation has been completed, and results are contextualized by rigorous analysis and comparison with results from published literature. The main contributions to each topic are best presented by topic area. For transformers, contributions include collation and presentation of the best-known methods of minimum loss high-frequency transformer design and analysis, descriptions of the implementation of these methods into a unified design script as well as access to an example of such a script, and the derivation and presentation of novel tools for analysis of multi-winding and multi-frequency transformers. For microgrid modeling and control, contributions include the modeling and simulation validation of the GFI and SST designs via state space modeling in a multi-scale simulation framework, as well as demonstration of stable and effective participation of these models in a centralized control scheme under phase imbalance. For converters, the SST design, analysis, and simulation are the primary contributions, though several novel derivations and analysis tools are also presented for the asymmetric half bridge and DAB.

DEDICATION

For my loving wife, whose willingness to help with errands and meals saved countless hours, whose steadfast and unwavering faith in me made every challenge seem surmountable, and whose affection and good nature I will cherish for the rest of my days.

For my family and dear friends, whose love, patience, guidance, and support formed the foundation on which this work was built, and whose company has been sorely missed during the last portion of this degree program.

For my fellow graduate students in the power electronics lab, whose insights, teaching, questions, and discussions have engaged and stimulated my mind; I hope the feeling is mutual.

For the professors of courses in my plan of study, who so graciously imparted their knowledge, wisdom, and experience to me over the years.

For Dr. Karady, whose mentorship led me to pursue postgraduate studies, and who is now at eternal peace; a peace well-earned for a life well-lived.

Last, but certainly not least, for Dr. Ayyanar, who has been tireless in guiding me toward success and away from failure, and whose patience, advice, and kindness made all of this seem almost easy. Almost.

ACKNOWLEDGMENTS

This work was funded in part by the US Department of Energy's Power America project. It was also partially funded by the Consejo Nacional de Ciencia y Tecnología in Mexico through the Bi-National Laboratory on Smart Sustainable Energy Management and Technology Training program.

Thomas Kirk and the OPAL-RT support team were incredibly helpful during the real-time simulation portion of this work, ensuring that the simulator's licensing was both consistent and appropriate for the task at hand, and guiding me through advanced (and sometimes quite lengthy) troubleshooting via email and web calls.

TABLE OF CONTENTS

Page

CHAPTER Page

CHAPTER Page

LIST OF TABLES

Table Page

LIST OF FIGURES

Figure Page

Figure Page

Figure Page

Figure Page

Figure Page

1 INTRODUCTION

The microgrid is a natural product of the continued proliferation of distributed energy resources (DER) and the advancement of power system technology. Improvements in power system and power electronics devices, and measurement and communication technologies have enabled the possibility of small portions of the grid to operate as distinct units, and even to assist the bulk electrical network in regaining stable operation after interruptions. With proper controls, microgrids are potentially capable of both islanded and grid-connected operation, and participation in scheduling and economic dispatch. While they are not yet able to realize their full potential, microgrids are sure to be a cornerstone of the future energy landscape.

One of the key, enabling technologies for microgrids is the inverter, which simply and efficiently converts power from DC to AC, either for a specific application or for injection into the grid. Multi-stage inverters, with a DC-DC stage followed by a DC-AC stage allow tight control of input and output quantities, and often contain high-frequency transformers to ease the burden of voltage amplification and galvanically isolate converter components for protection. Single-stage inverters trade a bit of flexibility for improved efficiency and power density, in some cases due to the removal of the transformer, which is almost guaranteed to be their largest, least efficient component.

Another cornerstone of the microgrid is its control architecture, which has evolved steadily in the intervening years since the inception of the idea. Inverters connecting loads and DER to the network are overseen by various control schemes to provide stability and high performance across the microgrid, whether by distributed or decentralized control of individual inverters, or by a centralized control method, such as

the popular hierarchical control scheme proposed within about the first decade of the new millennium. Communication – wired or wireless – enables information sharing between controllers, allowing distributed network elements to work together to achieve a variety of objectives. Information about generation and load, performance and stability, and control signals can be rapidly propagated across the network, driving fast responses to critical events.

Perhaps one of the most important advancements, the solid-state transformer (SST) is a natural outgrowth of the continued drive for high efficiency and has been discussed as an alternative to traditional line frequency transformers, combining power electronics with high-frequency transformers to perform the necessary voltage and frequency adjustments between segments of the network. These intelligent devices build on decades of experience with converters, electrical networks, and magnetic component design to leverage their strengths in such a way that conventional transformers, while well understood and spectacularly reliable, may be phased out during future replacement at ever-increasing power levels as technology continues to advance. Modular in nature, the SST can be constructed to fit practically any operating condition, power level, or voltage, and can be used to correct frequency and power factor issues, regulate voltage and current, and even manage harmonic distortion, with proper controls.

This report will provide details on the design and optimization of high-frequency transformers, the modeling and control of microgrids, including a detailed description of a real-time simulation testbed, and will finally explain the operation of several converters, culminating with the complete design and simulation results of a novel SST topology. The main body of the report is arranged with the literature review at the beginning to

introduce published literature for each topic, followed by a section on analysis and design, where design equations and analytical methods are presented and explained, and ending with the results of all tests performed to validate analysis. Each of those sections is arranged in the same way, with transformers first, microgrids second, and converters third.

2 LITERATURE REVIEW

Here we will investigate both the history and the state-of-the-art in transformers, microgrids, and the converters that tie them together. The focus will be on high-efficiency design of magnetic components, robust and stable control of microgrids, and analysis and controller design for converters enabling high-efficiency delivery of power.

2.1 Transformers

To ensure optimal transformer design, a thorough literature review was conducted to survey the landscape of magnetic component design and analysis. Transformer design will be the primary focus of this review, despite similarities and overlap with inductor design. Briefly, the topics discussed include core properties, winding properties, optimization, complex impedance, and losses.

Several reference books, [1], [2], [3], [4], and [5], were used to build a foundation of fundamentals for the topics of magnetic component design and analysis. Within these references reside the standard tools used by engineers to design transformers for power electronics applications. However, while easy to employ, the simplified treatment of some topics leaves something to be desired in terms of accuracy. In the current climate of energy efficiency concerns, efficiency differences of 1–2% can be the deciding factor between a good and a bad design. Furthermore, it is often the case that the formulas are derived using sine waves as input, or are only valid near line frequency, neither of which is suitable for modern power converters, which predominantly feature piecewise-linear (PWL) switching waveforms. It is here that deeper investigation is required, and thus we turn to the in-depth treatments presented in recent literature.

A handful of excellent papers provide an overview of the transformer design process or suggest design modifications that do not exclusively address any one specific subtopic. In [6], a step-by-step algorithm for transformer design in high-frequency power electronics circuits is presented. The paper addresses loss minimization, and provides a complete set of design equations, along with a push-pull converter transformer design example for illustration. The "high-frequency" used in this paper, however, is 50 kHz, which is now on the low end of converter switching frequency, with switching occurring in the MHz range in newer converters utilizing wide-bandgap semiconductors. Similarly, [7] presents a collection of design equations and some novel work related to loss modeling. This holistic approach references some of the work presented later in this review, including a measurement method for analysis of the effect of DC premagnetization on core losses. Regarding winding design, replacement of copper windings with aluminum windings or copper-clad aluminum windings is explored as a design alteration in [8], and suggestions are given for reducing the loss thereof by leveraging the lower material cost of aluminum relative to copper. Similar work was performed in an investigation on the use of stranded wire, rather than litz wire, in [9]. The same author provides a roadmap for continued improvements in magnetic component design in power electronics in [10], demonstrating a truly admirable dedication to advancement in the field. The roadmap summarizes the state-of-the-art at the time of writing and provides the author's suggestions for research in transformer windings and core materials.

While [6] provides some optimal design strategies as part of the overall design process, other works have focused more heavily on optimization of the transformer. An

early example, [11], is based on older equations and ideas, but it is very thorough, covering core loss, copper loss, thermal modeling, and providing optimal design equations and a design procedure. In [12], the transformer design is optimized by genetic algorithms (GA), using simplified expressions for losses, and considering thermal performance. The work is continued and extended to the overall design of isolated converters in [13]. A different approach is taken using particle swarm optimization (PSO) in [14], with more detailed loss modeling, and with consideration for leakage inductance as well as physical dimensions. High frequency transformer design is a daunting task for the inexperienced designer, and even with experience there are still many parameters to consider and numerous tradeoffs between design choices. Making the best selection among a set of choices with similar performance can be a challenging task but following an optimal design strategy or directly optimizing the design can help to narrow the focus for selection and make tradeoff evaluation simpler.

2.1.1 Winding Loss

Considering high-frequency transformer winding losses, germane in a climate of increasing switching speeds, two primary mechanisms are responsible. First, as the electrical frequency increases, the depth to which current density penetrates a conductor is reduced by current crowding. This effectively reduces the cross-sectional area of the conductor, restricting current primarily to an annulus-shaped “skin”, from which the skin effect gets its name. The resistance of the conductor increases inversely with the area of this annulus, and so does the resistive power dissipation. Second, the proximity effect occurs due to the changing motion of charge carriers in proximity to one another, as there are in the AC currents traveling through the closely wound coils of a transformer.

Faraday's law states that changes in current induce changing magnetic fields, and vice-versa. These induced fields are what couple the input and output sides of a transformer through the core, but they also induce circulating currents in the conductors that oppose the flow of current in portions of their cross-sectional area. In the case of both effects, eddy currents are generated within the conductors, increasing their effective resistance, and thus their losses. Furthermore, these losses increase with frequency as the skin depth decreases and the fields change direction more rapidly. These effects also occur in stranded wire or litz wire at the bundle level, though this is generally dealt with in the wire construction, as will be discussed later. A summary illustration is presented in Fig. 1, inspired by similar figures in literature.

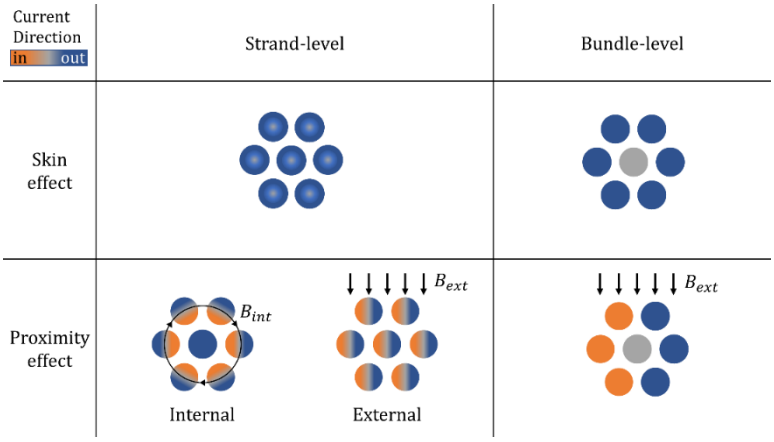

Fig. 1. Eddy effects at strand and bundle level.

Whereas line frequency transformers are almost always operated with sinusoidal waveforms, switching converters apply trapezoidal waveforms or other piecewise linear waveforms to the coils. The difference in energy between these waveforms is non-negligible, especially considering the resulting power dissipation at higher frequency, and most simplified models do not account for it. It follows that the approximations valid for line frequency sinusoids must be replaced by more accurate models.

No small amount of literature addresses the design of loss-optimized transformer windings. Wire construction, winding geometry, and a host of converter-dependent factors, including excitation frequency and waveform shape, affect the loss in the windings. The use of Litz wire in the windings of magnetic components at high frequency is a common practice, because the thin, individually insulated conductors are typically smaller in diameter than the skin depth, and the twisted construction allows for each conductor to occupy every radial position in the wire along its route, reducing loss due to the proximity effect. These effects are modeled in detail in [15], with the primary focus being the effect of twisting pitch (turns per unit length). In even greater detail, the complete decomposition and analysis from first principles of eddy effects in round wires in [16] gives a complete picture of the minutia, and provides an increase in accuracy, while making a minimum number of simplifying approximations. The result is a relatively simple finite element analysis (FEA) method, meant to replace both Dowell's equation, and the full Bessel function formulation. In [17], it is demonstrated that there exists an optimal number of strands to minimize overall winding loss in the litz-wire windings of a transformer. This work proceeds in [18], [19], [20], and [21], culminating in a MATLAB-based litz-wire optimization script, which was later ported to a web application at Dartmouth's website. This tool is an excellent starting point for winding design, and is easily accessible to the naïve designer, but it has several deficiencies that preclude its use generally. First, it does not consider current density per conductor, a simple, but important safety consideration. Second, its calculations are valid for a wide range of transformer winding designs, but it is constrained to discrete, rectangular winding cross-sections. For large step-up or step-down ratios, the number of turns of the

primary or secondary winding will be much smaller than that of the other windings, which means that to achieve maximum coupling, the lower number of turns will occupy a "slot" in such a rectangle, destroying the discrete structure assumed. Further, bifilar winding of primary or secondary winding pairs cannot be modeled by this simple structure, as the rectangular cross sections would be enmeshed within one another. A similar approach, performed specifically for gapped components (but still viable using an air gap of length zero), was taken in [22], where huge improvements in time-to-calculate, but moderate error increases were observed. In the work presented in this document, Dowell's well-known equation, given later in (19) for the ratio of AC to DC resistance in a conductor is implemented directly, as it is a good approximation under the condition that the diameter of the coil is much greater than the thickness of the conductors. Doing so also allows for arbitrary winding geometries to be evaluated.

In winding a transformer with numerous turns, layered windings, concentric sets of turns encircling the core, are employed to reduce core size. It is possible to determine an optimal thickness for turn layers within a given transformer winding, as demonstrated in [23]. This work also introduces a simplified means by which to calculate the effective frequency of an arbitrary periodic waveform using only the RMS current and the RMS value of the current derivative. It is well-known that arbitrary periodic signals can be decomposed into their harmonics via Fourier analysis, and each harmonic component can be investigated individually. The method presented in [23] avoids the necessity of truncating an infinite Fourier series, which is the general result of Fourier analysis for arbitrary waveforms. This allows for faster calculation with no appreciable trade-off in accuracy. Another article worth mentioning regarding winding construction is [24],

which specifically deals with LLC resonant converters, but contains discussion on balancing winding currents in center-tapped transformers by using bifilar windings. Bifilar windings decrease the difference in position with respect to the primary winding, since the conductors of the two windings now lay side-by-side, nearly equidistant turn-for-turn from each turn of the primary. This has the effect of reducing imbalanced magnetic field impingement on the conductors' surfaces, which is a non-negligible cause of current imbalance in an otherwise balanced, isolated circuit design. Further, it increases the coupling between these windings, which is equivalent to reducing leakage inductance, a generally undesirable parasitic nonideality.

The use of finite element method simulation (FEM) in magnetic component design is nigh compulsory, as the field solutions necessary for accurate calculation of parameters are intractable for hand calculation. Care must be taken to account for nonidealities in the model used, and one pertinent point of interest arises in the modeling of litz wire. Since litz wire consists of many individually insulated strands, it presents a problem for modeling, as the designer cannot simply place a solid copper cylinder (circle in 2D) in the winding area and consider the task complete. The immediate alternative of modeling every strand is also unappealing. A compromise is suggested in [25], where an effective conductivity is proposed such that the total conductor area is assigned a conductivity based on its construction, accounting for copper, air, and insulation with a single winding bundle.

2.1.2 Core Loss

Moving on to the core, losses are generally attributable to two mechanisms: eddy currents, and hysteresis. Eddy currents are generated in the core material due to the

changing magnetic flux linking the windings. This is unavoidable as it is the primary operating principle of a transformer; however, in iron cores it was minimized by using laminations, thin sheets of iron that lay side by side, reducing the cross-sectional area in which eddy currents could develop, thereby reducing the current density and thus, the loss. In ferrites, ceramics formed by alloying iron oxides with nickel, zinc, and/or manganese, the material itself all but eliminates the effect due to a reduction in electrical conductivity. Soft ferrites, used in high-frequency transformers, also have high permeability, and low coercivity, allowing them to easily demagnetize under a relatively low magnetic field intensity. This reduces the effect of hysteresis loss, as the alternating currents in the windings require the field to change directions as rapidly as the frequency dictates. Each of these effects changes as material properties change due to temperature, magnetic field intensity, frequency, and even waveform shape.

Core loss estimations have a long, rich history dating back to 1892, when Steinmetz first published his eponymous equation in [26]. This equation was not frequency dependent, as its later correction was, but it introduced the idea that the energy consumed by hysteresis is dependent on the magnetic flux density to the power 1.6, and what Steinmetz called a ‘magnetic resistance’ coefficient. Initial corrections to the equation included the addition of both temperature and frequency dependence, and replacement of the 1.6th power by a material-specific constant, as it was determined that different magnetic materials respond differently under the same operating conditions. The Steinmetz equation enjoyed a long period of consistent use in estimation, but high frequency, switching waveforms in ferrites changed its broad applicability. The Modified Steinmetz Equation (MSE), presented in [27] and [28], accounts for the non-sinusoidal

shape of switching waveforms by breaking the magnetizing current into major and minor loops, and evaluating their effects independently. It also suggests an effective frequency for use in the original Steinmetz Equation, which solves the problem equivalently. In [29], the Generalized Steinmetz Equation (GSE) is presented, which produces better accuracy at extreme duty cycles, and is simpler to use, requiring only Steinmetz Parameters α, β, and k, and the instantaneous values of the magnetic flux density and its derivative within one period. Yet another effective frequency equation for use with the original formula is presented. This work was continued in [30], where the major and minor loop idea of the MSE is included in the GSE, forming the improved GSE (iGSE). Without considering the effect of DC premagnetization on the core, this is the most accurate core loss estimation method to date. If we consider the effect of DC premagnetization, the improved iGSE (iiGSE), presented in [31] and [32], with its empirical loss map approach, is the most accurate, but requires measurement collection for the loss map and subsequent creation of a so-called 'Steinmetz Premagnetization Graph' (SPG) prior to calculation. Another model, even more accurate at extreme duty ratios and in the case of time-varying duty ratios, is presented in [33], and is called the Improved Steinmetz Equation (ISE). It proposes two models, one with constant Steinmetz parameters, and one with two sets of Steinmetz parameters, each valid at different frequencies. It further separates the excitation waveform into the sub-cycles of on and off time during one switching period, lending itself handily to the design of magnetic components in switching power converters. This formulation is itself an extension of a large project undertaken by Dartmouth University, the National Institute of Standards and Technology (NIST), and the Power Sources Manufacturers Association

(PSMA), the primary results of which are presented in [34] and [35]. This study is notable because it addresses the long-standing concern of magnetic component designers that the Steinmetz parameters obtained from manufacturer datasheets are for sinusoidal excitation, while most power electronics converters ideally generate rectangular waveforms. The study demonstrates that it is possible to apply a transformation to square wave measurement data to obtain accurate results for rectangular waveshapes of many varieties, though not all cases can be handled by this simple transformation. Nevertheless, this is an important result, and it is likely that the inclusion of such data from manufacturers would go a long way toward improving estimations of core loss. Another notable feature of the study is that all measurement data has been made publicly available for download, as described in the project report [36].

As a final note on core loss calculations, it is possible to compute core loss as the sum of hysteresis loss and eddy loss, computing each separately and summing them with an additional term, excess loss, to arrive at the total as in [37] and [38]. As noted in [31], this approach has two important disadvantages. The first is that the parameters necessary to compute the values are not always provided by manufacturers and are difficult to derive. The second is that separate computations each have their own error, and when accumulated, the errors may produce a larger error than by using a method which considers all sources of loss simultaneously. Even if both errors are small, it seems prudent to use a method which is almost always available and has only one dominant error term.

2.1.3 Complex Impedance

Complex impedance, primarily inductance, is another important parameter in transformer design. Ideally, energy is transferred from the input of the transformer to the output with no loss or storage; however, the real world is non-ideal, and just as losses occur as described above, energy is stored in the magnetic field produced by the current in the windings in any transformer. The amount of storage depends on numerous factors but can be determined by investigating the coupling achieved by the geometry of the coils and properties of the intervening media. From a circuit perspective, inductance is a quantity describing the ratio of the rate of change of current through a circuit element to the voltage across it. From an energy perspective, it is the quantity describing the ratio of the square of the rate of charge carrier motion to the total energy stored in the generated magnetic field. A single, coiled conductor has a self-inductance due to the flux that links all its turns, and a leakage inductance due to the flux produced by the coil that links only some fraction of its turns. When two coils are placed in proximity, the same quantities still exist, but mutual inductance and leakage inductance between the two coils complicate the matter. Generalizing to N coils, an $N \times N$ symmetric matrix must be constructed to keep track of all the inductance values. Adding a magnetic core to any or all the coils further increases the complexity. While magnetizing inductance, attributed to the flux linking all the transformer coils, is responsible for the base operation of the transformer, leakage inductance is a parasitic element, which reduces transformer voltage regulation, and contributes inversely to proximity losses. However, it can also be exploited to achieve desired resonance effects. It is therefore important to ensure the transformer's leakage inductance falls within an acceptable range. FEM simulation is one

means by which to predict inductance values, but analytical models exist, and are well-suited to fast calculations, with varying degrees of accuracy. The simplest transformer inductance models have very large error, especially at high frequency, at which the imaginary portion of impedance increases linearly with frequency. This necessitates careful consideration and more detailed models to properly anticipate regulation, losses, and other performance-related quantities such as switch dead time accommodation of current rise and fall intervals.

One such model, developed for round wires in [39], and extended to litz wires in [40], uses complex permeability for investigation of both leakage inductance and proximity effect losses. The results are shown to match well with FEM simulation. This method requires the winding window to be separated into distinct winding areas, then each winding is broken into rectangular cells, and the permeability is calculated for each cell, bundle-by-bundle, by weighting and distributing the permeability of the bundle throughout the cell.

An earlier model, presented in [41], considers complex impedance rather than complex permeability. It uses the method of images to demonstrate expansion of the typical formula for inductance to include a constant term due to air, a constant term due to the presence of a core, and a summation of images produced by interaction with the core. The paper demonstrates that the typical model for self-inductance has an error of 41% for the test case, even at the super low frequency of 100 Hz. This error balloons quickly at higher frequency. The method treats the core as a toroid, cut and unrolled into a cylinder, and extended infinitely by use of clever boundary conditions, as will be shown later.

This method is supported by manufacturer provision of the effective area, length, and volume of the core in question, and allows for the calculation of an arbitrary number of images, truncated at an appropriate precision by the designer. The model uses the geometric mean distance (GMD) method to determine coil-to-coil distances, which is popularly applied in this type of calculation. The paper references NIST's inductance tables, [42], produced in 1921, which enable the calculation of the inductance of multilayer coils of select configurations. The work is extended to interleaved windings in [43], and the two papers together present an excellent summary of transformer inductance prediction under nearly any imaginable case. Due to the ease of implementation and the accuracy with which it calculates leakage inductance, specifically, this method is preferred in the work presented here. A similarly thorough investigation, this time specifically for inductance, is presented in [44], where again, an accuracy target, tunable via truncation, is employed for full Bessel function cylindrical coordinate calculations of the inductance matrix. The work specifically targets high frequency, and is quite rigorous, employing superposition of the contributions of the field to the inside and outside regions of the winding window, and the core itself. The result is the complete inductance matrix, and by comparison with FEM simulation, it can be made arbitrarily accurate.

In dealing specifically with the analysis of leakage inductance in multi-winding transformers, several methods have been suggested. One method is an equivalent circuit model, presented in [45]. This method unites older approaches, namely terminal measurement and the duality between magnetic and electric circuits, and as such, is named after their combination: The Terminal-Duality Model (TDM). The method handily

performs a multi-winding transformer leakage inductance calculation via transient circuit simulation methods and matches FEM simulations to within 1% in all presented test cases. The paper does not yet account for self-inductance but provides three separate methods to calculate the leakage inductance. Another method, proposed in [46], and refined in [47], suggests that measurement can provide all the necessary information for determination of leakage inductances via matrix solutions by – perhaps paradoxically – considering the leakages to be intrinsically coupled throughout the transformer. This introduces an effective coupling coefficient between any two windings, which is readily calculated by algebraic equations based on a simple variable substitution. However, it assumes that the primary winding has perfect coupling with itself, while allowing the secondary windings to leak with respect to themselves. Since the primary winding is generally closest to the core, this is not wholly unreasonable as approximations go, but it does represent an idealization.

Other authors have contributed to leakage inductance calculation theory in various ways, the most notable of which will now be presented. A series of application-oriented papers, [48], [49], [50], and [51], deal with calculation of leakage inductance and coupling coefficients for core-type transformers, with the specific application of resistance welding equipment used for validation alongside comparison with FEM simulation results. This series culminates in a MATLAB program and includes calculations for interleaved transformers but is restricted to two-winding solutions. The calculations are approximate, but the speed and applicability to two-winding transformers suggest a potential choice for fast comparison of different winding configurations. Another pair of papers, [52], and [53], deal specifically with one attribute of leakage

inductance calculation, namely the GMD approach. Improvements in calculation under both arbitrary winding configuration and for concentric windings of equal heights are presented. The improved accuracy makes these papers attractive for use in future work. Another paper [54], applies the work from [41] to planar magnetics, which is a topic of interest in high power density applications, where footprint and profile are bottlenecks.

While transformers are primarily inductance-dominated in terms of their impedance, their construction does in fact place charges separated by various media near enough to cause capacitive effects. In [55], methods are discussed for determining the static capacitance for a pair of foil windings, and both static and dynamic capacitance between a pair of round wires. In [56], the round-wire methods from [55] are refined to account for the shape of the electric field when considering the different media between windings, proposing a parabolic shape rather than a circular segment (i.e. a different conic section). The paper also expands the computation to an arbitrary number of turns, in multiple arrangements, and provides validation of results via FEM simulations. A third paper, [57], proposes a variety of two-capacitor circuit models for analysis of two- and three-winding transformers, allowing in-depth study of resonance and other complex impedance effects in SPICE-type simulations. Simpler models exist as well, as in [58] and [59] for use as quick approximations or design guidelines.

2.1.4 Thermal Modeling

Since many of the quantities we would like to compute depend on temperature, no discussion of transformer modeling would be complete without at least some information on thermal modeling. [1] and [3] each give a simple thermal model for the entire transformer, and the latter gives some additional information about empirical

observations and derived relationships between transformer surface area, height, and heat dissipation. These simple models are very rough approximations, but in [60] a very detailed thermal model is developed for a high power, medium-frequency transformer, inclusive of all winding and core thermal paths to ambient, and considering the surface orientation of radiating elements, along with the conduction and convection paths for each winding, and each yoke and limb of the core. A thorough investigation of thermal modeling for transformer windings of both solid round wire and litz wire is presented in [61], with measurement results for validation.

Dissipation due to loss is only one effect to consider, however. It is well-known that the conductivity of copper changes at different temperatures, and so too do the properties of magnetic materials, with ferrites being no exception. Based on this change in properties, [62] gives an easy-to-use model of the acceptable current density in a wire based on a reference configuration, which needs only geometry computations to employ. In Ferroxcube's Soft Ferrite Design Tool (SFDT) (available at [63]) and in all Ferroxcube's material datasheets, curves of permeability and specific loss are presented as functions of temperature, with the interesting commonality (in most of their materials) that the elements and alloying processes used minimize loss at 100 °C. Consideration of these effects necessitates iteration, as the loss must be computed to determine the temperature rise, which may then be used to determine the temperature operating point based on an assumed ambient temperature, and the process repeated until the change between iterations is acceptably small.

2.2 Microgrid

Among those concerns regarding the proliferation of DER is variability, which causes undesirable bus voltage and frequency fluctuations in the network. This issue scales with the number of such sources, as demonstrated in [64], but can be addressed by the inclusion of energy storage solutions (ESS), as shown in [65]. Microgrids combining local collections of DER with ESS elements within a distribution network continue to gain popularity, requiring continued attention from researchers. For further general reading, [66] is recommended, giving an excellent summary and brief history of microgrid topics, including issues related to power electronics, controls, security, popularity, and more.

2.2.1 Modeling and Testbeds

Several hardware testbeds were investigated, such as the hybrid testbeds/live networks of the Alameda County Santa Rita Jail in [67] and Illinois Institute of Technology described in [68], as well as the Florida International University microgrid featured in [69] and [70]. These networks represent vital research but lack the flexibility and scalability that we desired for the testbed. The Aalborg Microgrid Programme and its family of microgrid testbeds, in particular the intelligent microgrid lab introduced in [71], was also investigated. This setup is very attractive, as it is quite flexible and offers a degree of scalability, but it still suffers from the limitations of other hardware implementations due to its inclusion of physical inverters. While such hardware testing is imperative in the broader scope of microgrid research, to allow fast, flexible testing of multi-scale microgrid solutions, we wish to remove as much of the risk, cost, and

construction or purchasing delay associated with hardware as possible. It is for these reasons that a real-time simulation-based approach has been selected.

In [72], a real-time simulation testbed was developed to address these issues, and preliminary results from testing an augmented version of the hierarchical control strategy described in [73] were presented. The testbed features a real-time simulation with a network model and "energy cells" (defined as the combination of photovoltaic (PV) generation, a smart inverter, and an ESS), Modbus communication capability for remote control via custom software, and the necessary hardware and simulation architecture for controller hardware in the loop (CHIL) support. Fig. 2 shows the high-level overview of the testbed, and Fig. 3 shows the high-level overview of the control architecture. Since the initial presentation of the basic testbed, further testing and refinement have been completed, and full details of the testbed and the results of testing amendments to the control strategy will be included. The model has been tested with differing numbers of energy cells installed for assessing its scalability. Two strategies for reference generation were implemented and tested: Measurements at a single energy cell's network bus, and independent measurements for each energy cell. The remote-control software has been designed with stability and speed in mind and allows data collection with consideration for parsing for analysis. Finally, the model has been arranged for multi-core utilization in the OPAL-RT, preparing it for future expansion. Potential applications for this testbed include validation and scalability testing of control schemes, multi-scale modeling of power electronics and microgrids, communication testing, and more.

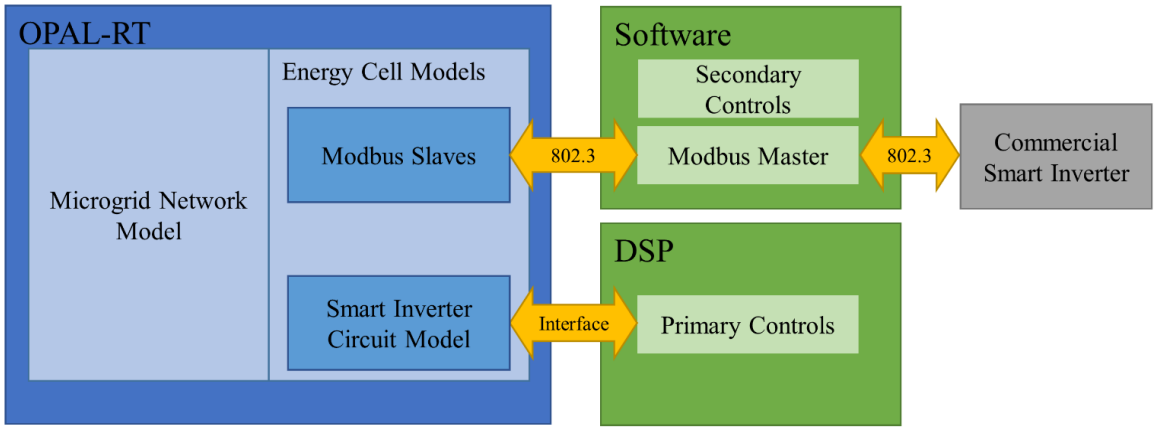

Fig. 2. High-level overview of testbed.

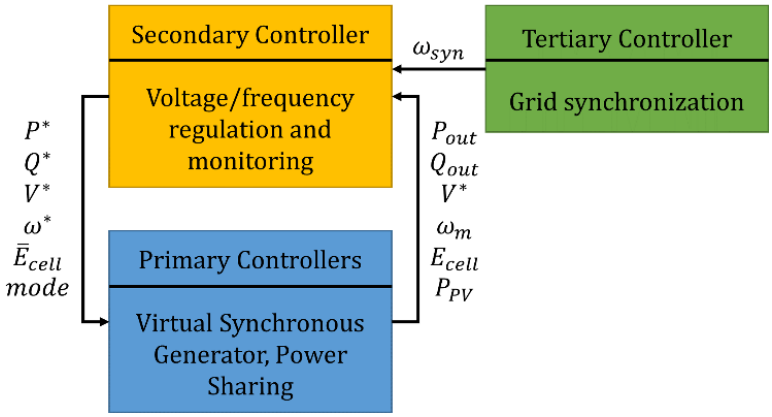

Fig. 3. High-level overview of control structure, featuring measurement and reference command signals.

2.2.2 Control

It has been demonstrated in [74] that network elements within microgrids can be controlled as a single entity and shown in [75] and [73] that this control can extend to islanded operation, wherein a breaker at the point of common coupling (PCC) is opened and no connection to the bulk electrical system is present. A comparison between virtual synchronous generator (VSG) control and droop control was performed in [76], and revisited in [77] from the perspective of the mode of operation of the converter, finding the VSG method to be superior in terms of overshoot and damping in step response, as well as having slower frequency transients, better emulating traditional generation.

Alternatives to hierarchical control have also been investigated, for example the decentralized and distributed control approach in [78].

2.2.3 Real-Time Simulation

Many technologies exist for simulation in the real-time arena. In [79], the Real Time Digital Simulator (RTDS) and National Instruments PCI eXtension for Instrumentation (NI-PXI) were used to perform power system simulation with protection hardware-in-the-loop (HIL). The design of a Real-Time Isolated Simulator (RTISim) was discussed and applied to turbine and governor simulation in [80], making use of the popular NI LabView software and incorporating HIL capability. Other published real-time simulation examples in [81], [82], and [83], and the cluster-based configuration in [84] expand the real-time simulation landscape, and still others, like ADI rtX, and Plexim's RT Box represent other possible paths. Ultimately, this work was completed with the OPAL-RT real-time simulator, which uses MATLAB and Simulink for design and features a wide variety of configurable simulation hardware expansions and a flexible licensing system. While each of these technologies has merits and demerits, our selection enables us to investigate important issues related to microgrids and DER with the desired level of flexibility and scalability.

2.3 Converters

With transformer design as a foundation, and microgrids as an application, we need to investigate the technology that connects the two: The converter. We will look briefly at the DC-DC stage of a two-stage inverter, the asymmetric half-bridge, then investigate the DC-AC stage and its control via the grid-forming inverter (GFI), and conclude the

literature review with information regarding the SST, a complete AC-AC power conversion solution featuring a high-frequency transformer as one of its key components.

2.3.1 Asymmetric Half-Bridge DC-DC Converter

While the isolated half-bridge DC-DC converter topology is very well-understood, additional literature review was performed on asymmetric duty cycle implementation for ZVS. In [85], basic quantities are provided, such as ZVS current boundary, minimum duty ratio, and average voltage transfer function. A simple waveform analysis is provided, and design equations delivered. In [86], the authors provide more detailed analysis of the switching waveforms and provide extensive results for comparison between measurement and analysis. ZVS boundary conditions are discussed in detail, and design equations are again provided. This low-voltage converter can be paired with an H-bridge to form a complete microinverter solution, excellent for managing power delivery for small PV installations.

2.3.2 Dual Active Bridge Converter

The dual active bridge (DAB) is an isolated DC-DC converter with two active H-bridges bookending a high-frequency transformer. This makes it naturally bidirectional, as either bridge can act as rectifier or inverter. An initial description of the converter with analysis of basic quantities and experimental validation is given in [87], and a more thorough analysis is given in [88]. When modeling the converter for controller design, the traditional state space averaging method described in [5] is not effective at capturing the transformer states' dynamics, since with proper design they are purely AC and have no DC steady-state component. Because of this, the generalized state space averaging method described in [89], [90], [91], and [92] is often employed to model the first

harmonic (i.e. fundamental switching frequency) content as well, as in [93], [94], [95], [96], and [97]. This method has a steady-state error due to the exclusion of higher order harmonics, which is addressed by two distinct methods in [95] and [97]. An alternative approach is to use discrete models, but this method is not suitable for modeling as part of a large system due to the high computational cost it incurs and the small time step it requires, so it will not be discussed here. A final approach is like the combination of the average model and discrete model, employing wavelets to model the converter. The Haar wavelet is a natural choice for switching waveforms, due to their piecewise constant nature, and this approach has been demonstrated in [98] to have very good accuracy, up to and including the actual switching transients typically not captured by average models for equal numbers of coefficients.

2.3.3 Grid-Forming Inverter

It is well-established by now that DER are increasing in prevalence, and that their proliferation is accompanied by impacts to stability, reliability, and controllability as compared with typical baseline generation technologies. Literature on the topic is typically presented from either a power systems perspective, in which simple inverter models are used and the network dynamics and control are given the most attention, or from a power electronics perspective, where the microgrid is represented as an infinite bus ideal AC voltage source, and inverter dynamics and control are highlighted. Neither of these types of models can fully capture the intricate dynamics and associated control problems of today's microgrid, leading to additional analysis, multiple simulations of different subsets of the overall network, and protracted hardware testing. More recently, there has been interest (see [99], [100]) in investigating the combination of the two to a

greater degree, and related work in this report aims to contribute to this budding field of study.

Possible methods of investigation include direct implementation of hardware in an existing microgrid or testbed, pure mathematical analysis, and simulation, either static, offline simulation, or real-time simulation. In the case that real-time simulation is used, issues arise from the calculation time required to simulate both dynamic power flow and transients in the network. In [101], [102], [103], [104], [105], and [106], this problem is largely resolved by using a dynamic phasor simulation, which is a hybrid approach marrying transient stability (TS) and electromagnetic transient (EMT) simulation methodologies, and which lends itself well to dynamic power flow solution.

From a control standpoint, inverters in a microgrid may be broadly classified as grid-feeding, grid-supporting, or grid-forming, depending on whether they are intended for use in grid-connected, or stand-alone/islanded configuration. Grid-feeding inverters are typically controlled to provide a set real and reactive power output and are the simplest to control. Grid-supporting inverters leverage the existing stability of the bulk electrical power network to simplify operation and control while providing basic support, but the GFI must carry the full burden of maintaining frequency and voltage stability, as they are intended to be capable of operating in stand-alone or islanded mode. In a microgrid, wherein grid-connection and access to stability-maintaining rotating machine inertia is not always a given, some augmentations must be made to the control strategy. In [73], a hierarchical control strategy is introduced, which achieves multiple objectives in the network simultaneously by employing three levels of cascaded control. In [72], this control strategy was employed with an energy storage balancing augmentation for a

moderately large network model featuring 100% DER penetration. A good summary of these control methods can be found in [107].

In [108], a fully featured state space average model is derived for an unterminated GFI and augmented to include the effect of several types of loads. While this model does not treat the multitude of operating conditions or topologies that can occur in a microgrid, its unterminated version is very well-suited to inclusion in a larger simulation framework and allows for study of both individual and generalized load cases. In contrast, [78] presents a very simplified GFI state space model that can be used in conjunction with an arbitrarily complicated network model and gives a stabilizing control strategy by employing H_∞ controller design optimization. Since the H_∞ controller design strategy operates on a generalized plant model, it is theoretically possible to adapt practically any inverter model to work with it, but due to the simplicity of the model and control strategy in [108], we will leave this adaptation for future work. Yet another example using both voltage and current control, but without regard for hierarchical controls is given by [109], wherein a middle ground is taken in terms of model complexity for both the inverter and microgrid. The paper claims to provide a stabilizing controller for any grid condition or configuration via parallel PI and PR controllers, but its controls and model do not integrate easily into the testbed used in this research.

Since microgrids are typically distribution-level networks, some phase imbalance is to be expected due to single-phase and two-phase loads. This presents a problem for many models used for analysis and controller design, which assume balanced phase quantities, and often omit the zero-sequence entirely. A novel approach to solving this problem in real-time simulation has been developed by exploiting the relationship

between phasors decomposed into their real and imaginary parts, and the synchronous reference frame. This allows one three-phase inverter model to be replaced by three single-phase inverter models without incurring significant additional computational cost, and without the loss of accuracy inherent to representation by phase-shifted duplicates of single-phase quantities.

In the relevant work described in this report the microgrid model used in [72] is expanded to include the unterminated GFI model in [108], employing the OPAL-RT platform to perform real-time simulations and assess the impact on performance and stability of including nonideal GFI models in an islanded microgrid.

2.3.4 Solid-State Transformer

The SST is fundamentally an isolated AC-AC converter made of a high-frequency transformer augmented by switching converters at each end. It combines superior voltage amplification, galvanic isolation, and enhanced control, but has a high cost and component count, with a minimum of 8 switches and a high-frequency transformer in each single-phase module for proper bidirectional functionality. However, its versatility makes it very attractive as a replacement for the standard line frequency transformer. Its output can be tightly controlled for frequency and power factor regulation, and its modular nature allows for adaptation to deal with virtually any power level and for the ability to tailor the device to handle specific problems at its installation location.

Apart from the increase in cost relative to traditional transformers due to the number of expensive semiconductor components, the high frequency transformer in the SST can adversely affect its ability to meet design goals by being its bulkiest, and most lossy component, reducing both efficiency and power density. With proper design, following

the best methodologies available, as discussed in the literature review on transformer design, these problems can be diminished significantly. With wide-bandgap GaN and SiC MOSFETs, higher switching frequency is available, which reduces the necessary size of the transformer, but at the cost of higher inductive impedance, and the possibility for increased switching losses. Additional discussion on high voltage, high power, high frequency transformer operation in SST converters is given in [110] for three phase transformers. Compounding these issues are parasitic capacitive and inductive effects of increased frequency at the circuit layout level, seen as capacitance across semiconductor components and inductance in printed circuit board (PCB) traces [111]. Also, due to the higher voltage and power level of three-phase inverters, some SST implementations call for parallel inverters, which can introduce new problems for the SST such as increased or distorted magnetic flux due to coupled transformer phase windings as discussed in [112], and circulating current or common-mode ripple current. Strategies to address the last issue are provided in [113] and more recently in [114].

In [115], [116], and [117], four basic types of SST are enumerated: the pure AC-AC SST with no DC-DC stage, two types of AC-DC-AC SST with low or high voltage DC between stages, and the AC-DC-DC-AC SST with both high and low voltage DC between stages. In the first type, a line frequency waveform is converted to high frequency, amplified by the transformer, and converted back to line frequency. The second and third types allow for a DC pick-off point for DC loads or storage, or alternatively, for a DC source, such as a DER installation. The final type has similar functionality to the previous three but allows for high-efficiency DC-DC converters like the dual/triple/quad/multi active bridge (D/T/Q/MAB), and provides more flexibility in

DC connections for sources and sinks. Additional topologies include the compact Dyna-C three-phase SST presented in [118], and the single-phase Modified DAB SST proposed in [119]. Without local loads in the energy cells in the microgrid designed here, this last topology is particularly interesting, as it provides an SST-like converter with a DC input, which would interface with the PV and storage DC link directly. There are various examples of modular, multi-level converters, which are very flexible and can be controlled via the fundamental feedback control method defined by the internal model principle, such as the well-described converter presented in [120]. A final noteworthy topology is the three-phase, four-leg SST, demonstrated in [121], [122], [123], and with soft switching in [124] and [125]. This SST topology is an improvement on the previous split DC link topology aimed at controlling circulating currents, in that the fourth output leg, assigned to the neutral return, allows for better, simpler voltage control of the three-phase output and reduces the necessary size of the DC link capacitors.

Adding the SST to a microgrid increases complexity and integrating the control of the SST into the existing control structure requires careful planning and attention to detail in order to achieve the various objectives of each controller simultaneously without interference. This is precisely why hierarchical control was developed, and why effort should be exerted to include the SST in the standardized control structure described by [73]. From the literature survey conducted, this is not yet the case, though attempts have been made at varying styles of hierarchical control. In [126], an alternative hierarchical control strategy is developed and demonstrated to address PV and ESS management concerns that the authors felt were not handled by the existing hierarchical control structure. In [127], a similar strategy is adopted for a DC microgrid, using a modular

multilevel SST, and an augmentation to the prevalent hierarchical control strategy to manage energy storage via the tertiary level of control.

Local control strategies also exist, which could potentially be coupled with the existing hierarchical control structure as was the case with the GFI model mentioned in Section 2.3.3. In [128], the phase shift and pulse width modulation (PWM) control methods are compared, with the PWM method giving a broader range of duty cycles for a single-phase DAB. A decentralized control method for bidirectional power transfer in parallel DAB is demonstrated in [129], and a slightly different version of this strategy is provided in [130].

In investigating the performance of the SST, real-time simulation of devices in a microgrid model has the same benefits as similar simulations for the GFI. An RTDS simulation featuring the IEEE 13-Node Feeder was used to investigate SST performance in [111], wherein advanced, robust controls are designed via the H_∞ and μ-synthesis methods. A real-time HIL-enabled simulation was performed in [131], for a small system featuring a matrix converter-based SST, which converts three-phase to single-phase and vice-versa. Model-predictive control (MPC) is employed to improve control relative to typical PI control by using a forward-difference Euler formula to update the state space model at each time step so that reactive power can be minimized by a cost function in the stationary reference frame. More similarly to the GFI modeling and control featured here, a dynamic average model was used in [132] for a three-phase, four-leg converter in the synchronous reference frame via space vector modulation (SVM). An OPAL-RT simulation of a small system was performed with three SST models demonstrating robust

PI control of several test cases, including short-circuit, load changes, and unbalanced operation.

With the encouraging success of these approaches, it should be possible to fully integrate the SST into the existing hierarchical control structure employed in the constructed testbed and improve the capability of the microgrid. The energy storage balancing control already implemented in [72] can be adapted to accommodate these findings, paving the way for continued integration of improvements to this exciting technology.

3 ANALYSIS AND DESIGN

Between ideation and implementation lies analysis and design. In this section we will cover the mathematics needed to design, analyze, and optimize transformers for a variety of applications, discuss the modeling, design, and control of microgrids, as well as a real-time testbed designed to quickly and safely test control methods and other devices and strategies, and conclude the main discussion with converter design and analysis for the asymmetric half-bridge, GFI, and a proposed SST. A brief section will also cover the remote-control software designed for use with the microgrid testbed described below.

3.1 Transformers

Presented with a converter design, such as the asymmetric half-bridge in Fig. 4 and Table I, the transformer is initially ideal, represented simply by a turns ratio for calculation of voltage amplification from primary to secondary. Given certain modes of operation, the inductance of the transformer may also be one of the design goals, so some nominal value of magnetizing inductance may also be used (~1 μH). The information provided here, along with voltage and current waveforms in the windings from a simulation of the circuit is generally more than enough to design the transformer.

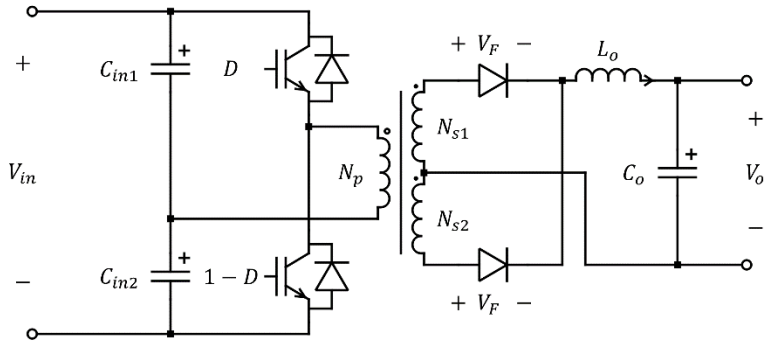

Fig. 4. Schematic of ideal asymmetric duty ratio isolated half-bridge DC-DC converter.

TABLE I
DC-DC CONVERTER DESIGN PARAMETERS

Parameter	Value(s)
Input Voltage V_{in}	27 V – 39 V
Output Voltage V_o	224 V
Output Power P_o	300 W
Diode Forward Voltage V_F	1.4 V
Switching Frequency f	200 kHz
Maximum Duty Ratio D_{max}	0.5
Input Capacitance (each) C_{in}	18.8 µF
Output Capacitance C_o	30 µF
Output Inductance L_o	100 µH
Turns Ratio $N_p: N_{s1}: N_{s2}$	1:15:15 center-tapped

Generally, the design process is as shown in the algorithm diagram in Fig. 5. With a converter application in mind, a converter is designed and simulated. This provides the design variables and waveforms produced during operation with an ideal transformer. The main path dictates the design actions and decisions, with an optional refinement loop indicated by dotted lines. Within the main design path are several inner loops, which can be iterated over for the best design. A material n is selected from the materials list of N_1 materials, which determines a number of cores $N_2(n)$ that are constructed from that material, from which core m is selected, the shape and size of which determines the possible winding structures. Among the $N_3(m)$ winding structures, structure p is selected, and calculations are performed. Iteration may then proceed over each of the previous lists. Throughout this section, a dual focus on analysis and programming application will be embraced, since the analytical methods were implemented in a transformer design script as they were discovered or derived. This approach serves as both a guide to design generally, as well as acting as a detailed user guide for the design script. Alternatively, readers may use this information to implement their own tools based on the work presented here.

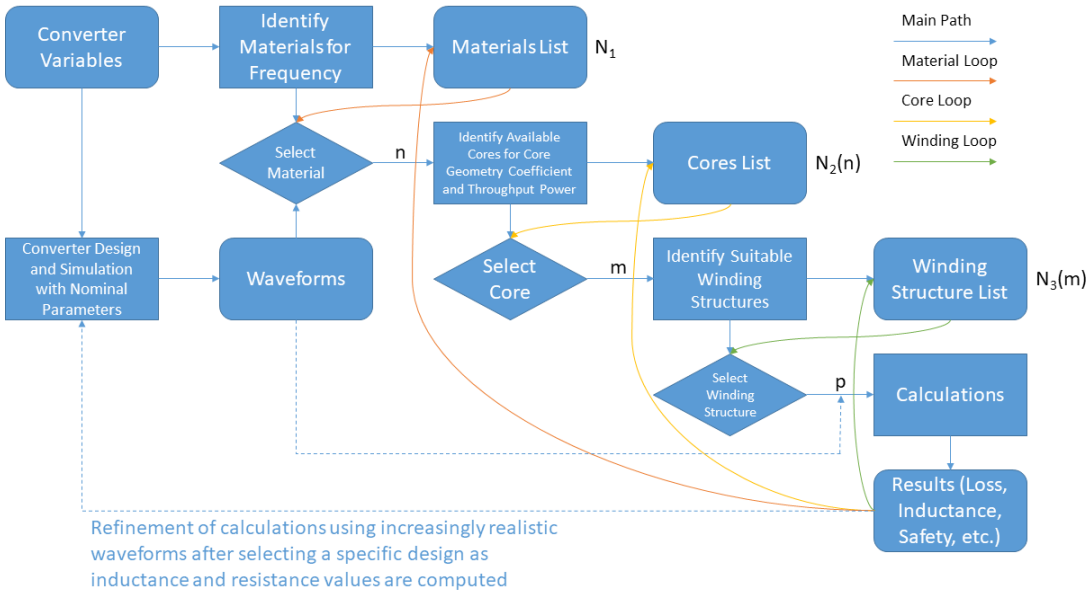

Fig. 5. Design algorithm for optimized transformer.

3.1.1 Material and Core Selection

The switching frequency restricts the material selection, and while the material also influences other parameters, it is the simplest entry point for an algorithmic design. Manufacturers of magnetic cores generally provide specific loss data as shown in the left plot in Fig. 6, where the specific loss P_V is the loss per unit volume for frequency f over a range of peak magnetic flux density $\hat{B}$. This loss data can be digitized, and the resulting data points can be curve-fitted using the Steinmetz equation in (1), since the curves are generally restricted to specific frequencies and flux density ranges and normalized to a given temperature. This allows extraction of the Steinmetz parameters, α, β, and k.

$$P_V = k f^{\alpha} \hat{B}^{\beta} \quad \left[\frac{\mathrm{W}}{\mathrm{m}^3}\right] \tag{1}$$

In this work, after digitization of loss curves for all materials within the power converter range of products offered by Ferroxcube, an automated curve-fitting program

was implemented in MATLAB to extract a set of Steinmetz parameters for each, and generate a report providing visual confirmation of both curve and surface fit, along with the parameters. It uses equation (2), which provides a better fit for loss curves that are not strictly linear on a logarithmic plot and yields the same results as equation (1) for those that are.

$$P_V = max\{k_1 f^{\alpha_1} \hat{B}^{\beta_1}, k_2 f^{\alpha_2} \hat{B}^{\beta_2}, k_3 f^{\alpha_3} \hat{B}^{\beta_3}\} \quad \left[\frac{\mathrm{W}}{\mathrm{m}^3}\right] \tag{2}$$

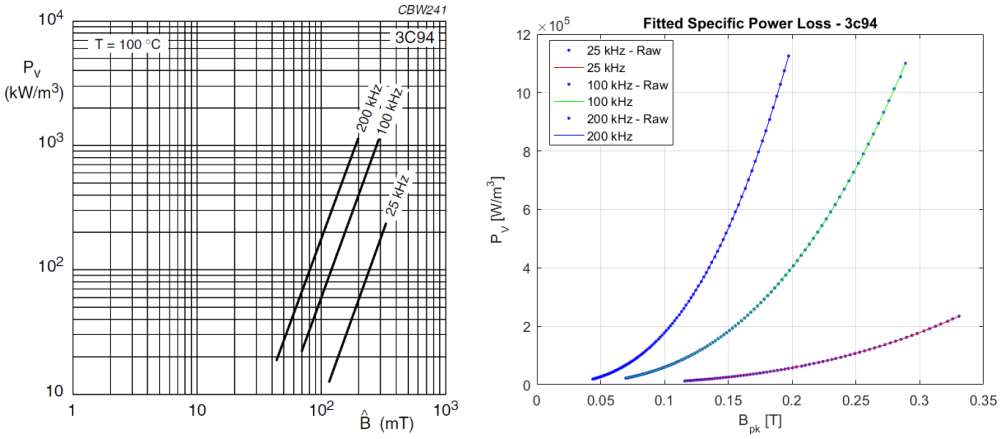

Fig. 6. Specific loss curve for Ferroxcube 3C94, left [133]. Resulting curve-fit, right.

However, there is a discrete nature to these fits due to the parametric presentation of data, and for accurate core loss prediction it is necessary to provide values for a continuous range of frequencies. Thus, a similar procedure was followed to carefully fit each dataset as a surface, allowing values to be interpolated or extrapolated as needed to fit the actual operating frequency.

The material selection subsequently restricts the core selection, making a suitable core shape and size selection with the chosen material the next logical step. There are a multitude of cores commercially available, and thus, more than one core may be suitable. To select a core, a rough assessment of the necessary core size must be made. Given an

application, the transformer must be able to achieve its intended voltage amplification ratio, handle the specified throughput power, and operate within the linear regime in terms of magnetic flux density (i.e. avoid magnetization saturation). The area product, A_p, is a quantity defined as the product of the core's effective cross-sectional area, A_e, and its window area, W_a, and gives a general guideline for core size selection via (3) [1].

$$A_p = A_e W_a = \frac{P_t}{K_f K_u f J_{RMS} \hat{B}} \quad [\text{m}]^4 \tag{3}$$

As shown in (3), the area product is a function of geometry, but can be related to a variety of other properties of interest, which will now be described. The throughput power, P_t, is the sum of the apparent power in each of the windings. The waveform factor, K_f, is associated with the frequency, f, and the peak magnetic flux density in the core, $\hat{B}$, as demonstrated by (4) [2].

$$K_f = \frac{\frac{V_{RMS}}{V_{avg}}}{\tau f} \quad [\text{cycles}]^{-1} \tag{4}$$

Equation (4) slightly obfuscates the relationship between these three variables. The form factor in the numerator can be thought to quantify the shape of the waveform in terms of the energy transferred during one zero-to-peak rise, as compared to one quarter-cycle of a square wave. The denominator represents this period by using τ, the duration during which the flux density rises from zero to its peak, or the midpoint of a square pulse. For expediency, the waveform factor is often given as 4.0 for a square wave, and 4.44 for a sine wave, but computed values are used in the design script because the computer can do the heavy lifting. Voltage quantities are used due to Faraday's law and the relationship between voltage and the rate of change of magnetic flux density, which is

roughly what $K_f f \hat{B}$ works out to, dimensionally (e.g. units of $T \cdot s^{-1}$). This clarifies the relationship stated in the previous paragraph.

The window utilization factor, K_u, is associated with the RMS current density, J_{RMS}, and is a ratio of copper area to window area. For round wires, this factor will be significantly less than one (at maximum $\sim \pi/4$ for square packing of bare wire), and for litz wire, with the additional insulation between each strand, the factor drops significantly, to a value ~0.3. Along with the three variables already discussed, this gives us a rough separation of core and window area effects in terms of power, leaving the fourth power of distance, as initially described.

The core geometry coefficient, K_g, represents a newer approach to size selection, which considers more properties, and is thus more accurate than its A_p counterpart, which appears as a constituent term. As shown in (5), it also takes the mean length of a turn, l_T, into account, and can be related to other quantities such as transformer regulation, α, and the so-called "electrical conditions", K_e, suggested in [1].

$$K_g = \frac{A_p A_e K_u}{l_T} = \frac{P_t}{2\alpha K_e} \quad [\text{m}]^5 \tag{5}$$

The factor of two in the denominator of (5) represents the assumption that $P_t = P_{in} + P_o = 2P_{in}$ (i.e. the transformer's input power P_{in} is equal to its output power P_o). Transformer regulation, α, is the percent difference of unloaded voltage V_{NL} to fully loaded voltage V_{FL} at the output terminals, as in (6). It also represents the ratio of copper loss P_{Cu} to transformer output power.

$$\alpha = \frac{V_{NL} - V_{FL}}{V_{FL}} \cdot 100 = \frac{P_{Cu}}{P_o} \cdot 100 \quad [\%] \tag{6}$$

This quantity illuminates non-idealities such as transformer winding resistance and leakage inductance, across which voltage drops occur in real world transformers. Nominally, this parameter is very small, ~0.5%–5%. For maximum transformer efficiency η_T, [6] provides some guidelines for the relationship between core and winding loss that will be provided later.

The electrical conditions, as presented in [1], are represented by an easy-to-use formula for transformer designers, but the formula includes a constant, which does not clearly illustrate its formulation. A re-derivation, included in Appendix A, was performed based on dimensional analysis. The derivation yields (7), which matches the original presentation quantitatively, but provides slightly more insight by revealing a direct proportionality to the conductivity of copper, σ_{Cu}.

$$K_e = \frac{1}{2}\sigma_{Cu}K_f^2 f^2 \hat{B}^2 \quad \left[\frac{\mathrm{W}}{\mathrm{m}^5}\right] \tag{7}$$

Employing Faraday's law again, this works out to the product of conductivity and voltage squared per distance to the fourth, or power per distance to the fifth.

The equations defined above work for most cases, where a converter is designed to operate at a given switching frequency with a steady DC excitation. However, for multi-frequency converters, for example in an SST where the input may actually be a DC value that is amplitude modulated by a sinusoidal excitation, or in the case of an inductor that has both switching frequency modulation and a sinusoidal carrier instead of a DC operating point, the equations have two primary weaknesses. First, the frequency f is no longer an adequate representation of the rate of flux density oscillation, since there are at least two excitation repetition rates depending on whether harmonics are considered.

Second, there is no single quantity defined as a waveform factor for such a composite waveform, as from either perspective (low or high frequency oscillation), the relative waveshape is time varying. This is compounded, albeit to a lesser degree, by the fact that the peak flux density per cycle is no longer constant.

A brief argument will be made here for a proposed approach to accommodate multi-frequency operation, with a complete derivation in Appendix B. Since the primary focus of this work is on transformer design, the sine carrier inductor case will not be treated, but a similar approach may be used to address it. For the case of the amplitude modulated switching signal, we can start with a very reasonable assumption that the peak flux density $\hat{B}$ due to this excitation occurs at the simultaneous peak of its constituent low- and high-frequency components, $\hat{B}_{LF}$ and $\hat{B}_{HF}$, respectively, as in (8).

$$\hat{B} = \hat{B}_{LF} + \hat{B}_{HF} \quad [\mathrm{T}] \tag{8}$$

For a line frequency or double line frequency sinusoidal modulation, which is two to five orders of magnitude slower than the typical switching frequency, the error is negligible, on the order of $\dot{B}_{LF}\tau_{sr}$, where $\dot{B}_{LF}$ is the time rate of change of the low-frequency oscillation and τ_{sr} is the time segment containing the rising portion of the symmetric switching flux waveform. Considering that the rate of change at the peak of the sinusoid is near zero, this error value is infinitesimally small, and can safely be ignored.

The second assumption is that we can approximate the throughput power in the transformer as the sum of high- and low-frequency throughput powers of all windings. In a test case with a 60 Hz sinusoid of 10% relative amplitude modulating a 20 kHz

switching frequency waveform in a two-winding transformer, the error observed was 0.16%, so this is also a reasonable assumption.

To provide a useful formula we must make one further assumption about the form of the waveform factor and frequency used in (7), considering the component contributions. We select the geometric mean values $K_{fc} = \sqrt{K_{f,LF}K_{f,HF}}$ and $f_c = \sqrt{f_o f_s}$ for this purpose, with reasoning explained in the complete derivation in Appendix B, arriving at the expression for the composite electrical conditions K_{ec} in (9).

$$K_{ec} = \frac{1}{2}\sigma_{Cu}K_{fc}^2 f_c^2 \hat{B}^2 \quad \left[\frac{\mathrm{W}}{\mathrm{m}^5}\right] \tag{9}$$

The peak flux density must also be approximated, as it is necessary for the prediction of the core size, as demonstrated above. To make this estimation, the number of turns in the transformer's voltage excitation winding must first be computed. Selection of turns ratio is generally completed during converter design, as the voltage amplification ratio is needed to complement duty ratio in achieving the appropriate output voltage. The number of turns needed in each winding can be calculated using several previously defined quantities as well as the RMS voltage V_{RMS} across that winding and manufacturer-provided effective core cross-sectional area A_e as in (10).

$$N = \frac{V_{RMS}}{K_f f A_e \hat{B}} \tag{10}$$

To compute this value prior to core selection, we first note that the quantity $A_e\hat{B}$ in the denominator is simply the peak magnetic flux $\hat{\phi}$, which by Faraday's law is the peak of the turns-scaled integral of the voltage waveform. The primary winding typically provides the voltage excitation, so we can use its waveform to compute (10) directly to determine the correct number of turns to satisfy this relationship. Later in the design

process, we use this number of turns and the turns ratio(s) of the windings to determine the necessary number of turns for all windings. In the case of a multi-winding transformer (i.e. a transformer having three or more windings on the same core), the values from the first primary winding can be used, since for proper operation of the transformer, all windings must have equal volts per turn. To use the number of turns value from (10) to compute $\hat{B}$, the mean cross-sectional area of all cores in the database is used as an initial guess, and iteratively multiplied by an increasing integer until the peak flux density is in the appropriate range for a ferrite core, ~100–500 mT.

At this point in the design process, several parameters are assumed, as in Table II. The minimum core geometry coefficient is calculated using these parameters and those derived from the waveforms provided. A list of cores exceeding this value by a relatively low margin (≤10%) is selected for iteration.

TABLE II
INITIAL TRANSFORMER DESIGN PARAMETER SELECTION

Parameter	Value
Window Utilization Factor K_u	0.3
Transformer Efficiency η_T	99%
Transformer Voltage Regulation α	0.5%

Additionally, some manufacturers have provided tools for use in determining core size and shape, such as Ferroxcube's SFDT, which is freely available at Ferroxcube's website, and which allows a user to enter specifications and receive a list of matching cores. The cores can then be sifted for throughput power capability, saturation flux density, size, shape, etc. The existence of alternative methods for selection suggests that using a combination of the methods will allow the designer to obtain the optimal design. Any transformer cores that safely satisfy constraints provided by all methods above can, upon

optimization, provide the best performance under any given set of circumstances. To this end, the SFDT is also used to add cores to the list for iteration, by again selecting a slightly higher throughput power handling capability than is needed and adding all cores within this range. For high power devices, the throughput power may be divided by an integer number of cores to accommodate the increase, but this necessarily limits the core families that may be selected to those with acceptable mating faces for stacking (e.g. only those with rectangular cross sections, such as E and U cores).

Programmatic selection of the core is not straightforward. After accounting for stacked cores if necessary, and even using a narrow range of values around the minimum core geometry coefficient, several cores may still be suitable candidates. Given that the material was selected previously, we may use the amplitude permeability at the estimated peak flux density given each core's effective cross-sectional area as a second check to promote one core to be the first choice and array the other cores to save as options for iteration. The selected core should have the closest match to the desired inductance value, if one is provided, and should otherwise simply maximize the permeability.

At this time, it is also wise to store (or access) the geometry values given on the core data sheet and compute the core's surface area for thermal modeling later in the script. To this end, models for each core type's surface area based on its geometry were derived by hand, accounting for some degree of idealization of surface shapes on every facet of the core. In the case of simple structures like the E core and toroid, this is trivial and requires no idealization. In the case of more complicated shapes, like the PQ and RM core, idealizations were made more generously. Further complicating the issue is the identification of inner and outer surfaces and their relative orientations so that

conduction, convection, and radiation may be assessed as appropriate. Currently, the thermal model in use does not account for different types of heat flow, so these distinctions are an ideal target for future work.

After this segment of the design process, the area product is calculated and used as a check to ensure that each design's window area and core cross-section are sufficient to handle the throughput power as winding selections are made.

3.1.2 Winding Design

Upon selection of a core, windings must be designed. When designing an individual transformer winding, geometry and physical construction, current density, skin depth, proximity effect, and inductance must all be considered. As a preparatory step, the number of turns in each winding must be computed before assigning winding constructions and geometry.

For each winding in the transformer, a turns ratio exists with respect to each other winding. In the case of two windings, this is a scalar value, but in the case of multi-winding transformers, a matrix of such values must be constructed. At converter design time, these values are selected to provide the correct amplification ratio(s), and we can programmatically deduce their values without additional user input from the voltage ratios amongst the provided winding waveforms. This is true even with nonideal models, in which additional drops occur due to winding resistance and reactance, because the off-nominal ratios can be constrained to purely rational values very simply with existing math libraries in modern computers (e.g. by rounding functions).

The first true step in winding design is to calculate the skin depth, as discussed in the literature review. This is accomplished by first calculating the effective frequency f_{eff} of the current waveform $i(t)$ by equation (11) [21].

$$f_{eff} = \frac{\left\{\frac{di(t)}{dt}\right\}_{RMS}}{2\pi I_{RMS}} \quad \text{[Hz]} \tag{11}$$

For the RMS current I_{RMS}, we must consider the two-norm of the DC current component I_{DC} and the RMS value of the AC variation about that component $I_{AC,RMS}$, as in (12) [21].

$$I_{RMS} = \sqrt{I_{DC}^2 + I_{AC,RMS}^2} \quad \text{[A]} \tag{12}$$

The effective frequency is used in equation (13) to arrive at the skin depth δ, which helps to guide wire selection to minimize the ratio of AC resistance R_{AC} to DC resistance R_{DC}, and which considers both the resistivity and permeability of copper, ρ_{Cu} and μ_{Cu}, respectively [21]. For the individual strand in a low number of layers, the optimal relationship considering only skin effect is expressed as in (14) [2].

$$\delta = \sqrt{\frac{\rho_{Cu}}{\pi f_{eff} \mu_{Cu}}} \quad \text{[m]} \tag{13}$$

$$\frac{d_c}{\delta} < 1.5 \leftrightarrow \frac{R_{ac}}{R_{dc}} \approx 1 \tag{14}$$

For more layers, or when also considering the proximity effect, the optimal ratio is reduced (a good rule of thumb is $d_c < \delta/4$), and when bundled conductors are used, the maximum number of strands to be bundled together must also be considered. This is discussed in more detail below.

Formulating the winding geometry requires balancing trade-offs. Many factors must be considered, such as the real-world availability of materials, physically fitting the windings within the core window, safe current density in individual conductors, optimal loss, inductance, and so on. Some general guidelines include placing the highest power winding nearest the core and winding all other coil layers around this winding, interleaving the windings, and using bifilar windings (but not bifilar wire [1]) for winding pairs of the same side (primary or secondary). In the constructed prototype and the designs created herein, it was assumed that litz wire would be used, in the configuration shown in Fig. 7.

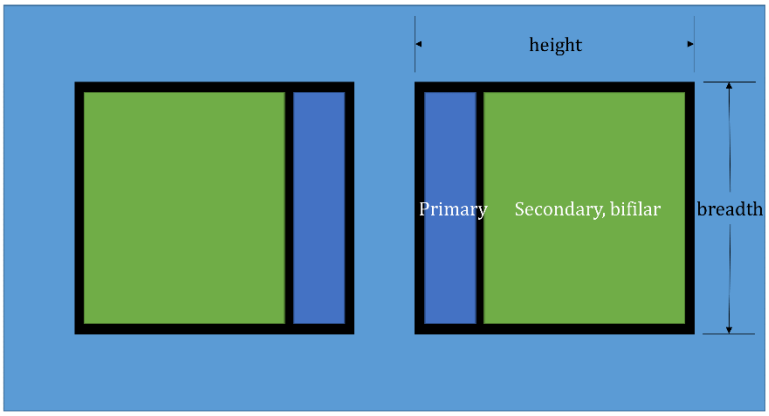

Fig. 7. Basic winding structure, showing relative positions of windings within core window.

Fitting the windings into the window requires careful (if not pessimistic) calculation of the outer diameter of a given wire construction. For litz wire, this includes consideration of the serving thickness, method of insulation, and type of litz wire (e.g. the number of twisting operations, from simply stranded type I litz, to multi-level stranding of higher type numbers). In this analysis, an outer diameter, d_o, for a given effective

bundle diameter, d_b, was arrived at by fitting data for New England Wire type II litz constructions (two stranding operations) of varying sizes as in equation (15).

$$d_o = \frac{d_b}{0.68125} \quad [\text{m}] \tag{15}$$

Using this outer diameter, the number of turns, N, and the breadth of the bobbin, b, the number of strands to fill the bobbin, n, and resulting number of bundles per layer, n_{bpl}, can be calculated for each winding, as in equations (16) [21] and (17).

$$n = \frac{k\delta^2 b}{N} \tag{16}$$

$$n_{bpl} = \left\lfloor \frac{b}{d_o} \right\rfloor \tag{17}$$

In (16), k is a constant given in Table I of [17] and is measured in mm^{-3}. When computing the optimal number of strands, care must be taken to ensure the dimensions used here match one another.

For safety, current density in bundled conductors must also be considered, or high temperature may cause damage to the resulting transformer. A safe maximum current density J_{max} of 3 A/mm^2 is typically suggested as a rule of thumb, but this does not account for the increased surface area to volume ratio in most transformer windings, nor does it consider skin or proximity effects in any capacity. In the literature review, it was noted that [62] provides an excellent, easy-to-use model based on a reference block of annealed copper and requires only geometry transformations to apply to any winding. In (18), the value computed by that model formula is used to determine the minimum safe cross-sectional area of a litz wire bundle A_{min}.

$$A_{min} = \frac{I_{RMS}}{J_{max}} \quad [\text{m}^2] \tag{18}$$

This quantity, combined with the maximum area provided by the maximum diameter due to the skin depth, provides a range of effective bundle cross-sectional areas within which the selected wire construction must fall. A list of real-world constructions available for purchase was created and is accessed to find and present possible choices by the previously mentioned design script. This presentation also considers using parallel wires in the case that the current density is too high for any single wire bundle of appropriate size. This does not directly affect the one-dimensional field geometry considered, but it does cause current crowding due to the proximity affect in the parallel conductors along the width of the window. These considerations, along with bifilar windings, and simple winding interleaving are considered when constructing the winding geometry portion of the model and employed by the functions that treat the windings later.

As discussed in the literature review, Dowell's Formula handles losses due to both types of conductor eddy effects well in terms of accuracy, given a conductor with bundle diameter much smaller than its coil diameter, and assuming primarily one-dimensional variation in MMF, radially outward from the core center. While more accurate methods exist for specific conditions, equations (19) – (22) [3] present the basic calculations necessary to arrive at the AC equivalent resistance R_{AC} via the DC resistance R_{DC}.

$$F_R = A\left[\frac{\sinh(2A)+\sin(2A)}{\cosh(2A)-\cos(2A)} + \frac{2(N_{ll}^2-1)}{3}\frac{\sinh(A)-\sin(A)}{\cosh(A)+\cos(A)}\right] \tag{19}$$

$$A = \left(\frac{\pi}{4}\right)^{0.75}\frac{d_l}{\delta}\sqrt{\eta} \tag{20}$$

$$R_{DC} = \frac{4\rho_{Cu}Nl_T}{n\pi d^2} \quad [\Omega] \tag{21}$$

$$R_{AC} = F_R R_{DC} \quad [\Omega] \tag{22}$$

This set of calculations relies on the transformation of litz wire windings into square arrangements of individual strands, of layer diameter d_l, as shown in Fig. 8.

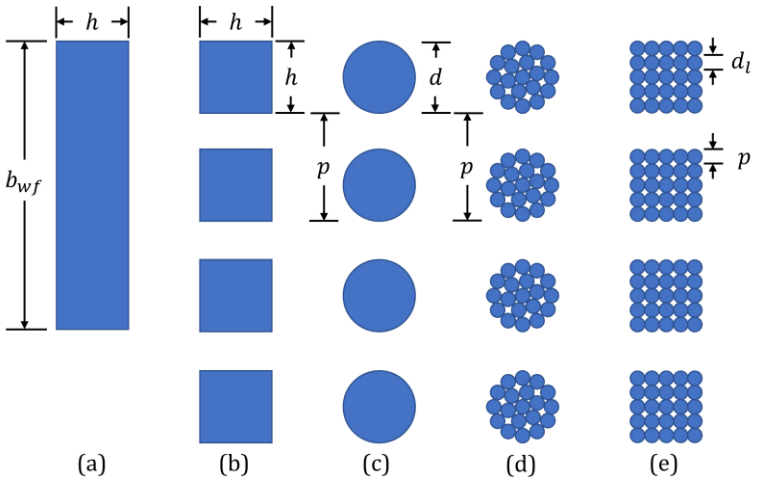

Fig. 8. Transformation of foil winding into litz-wire winding. (a) Foil winding. (b) Square wire winding. (c) Solid wire winding. (d) Round bundle of multistrand wire winding. (e) Square bundle of multistrand wire winding.

The layer diameter, or individual outer strand diameter for litz wire is given by (23) [17], which is referred to 40 AWG wire as a base value, d_r.

$$d_l(d) = d_r \alpha \left(\frac{d}{d_r}\right)^{\beta} \quad [\text{m}] \tag{23}$$

In (23), $\alpha = 1.12$ and $\beta = 0.97$ for single-build insulation, while for heavy-build insulation, values of $\alpha = 1.24$ and $\beta = 0.94$ can be used.

In (20), η is the porosity factor, which is less than 0.8 for litz wire, and is difficult to determine exactly; however, the IEC has published a standard (IEC 60317) that defines the necessary quantities for calculation of its nominal value for a given strand diameter. For litz wire of small strand diameter (less than 0.1 mm), the values fall within the range

0.7-0.8. Here, 0.75 is used for the sake of simplicity, but a lookup table can be implemented for better accuracy based on the standard.

Similarly, while there exists some actual number of layers of conductors N_l, it is nearly impossible to determine due to the stranding and twisting of litz wire; however, an effective number of layers, N_{ll}, based on a hypothetical square rearrangement, even with inclusion of a bobbin (of breadth b_b, and height h_b) is trivial to compute; a floor function was used to estimate the bundle version of it in advance in (17). The simplest presentation of this calculation, assuming a filled bobbin, is given in (24) [3].

$$N_{ll} = \frac{h_b}{d_l} = \sqrt{\frac{nNh_b}{b_b}} \tag{24}$$

Fig. 9 shows two plots of the AC-to-DC resistance ratio, both as a function of the equivalent conductor diameter normalized to the current skin depth, d/δ, where η is varied in the first, and the number of bundle layers, N_l, is varied in the second. This allows us to investigate, for example, calculation error resulting from the approximation in the prior paragraph, and different litz wire arrangements for a selected wire. It is clear from the figures that the primary geometry factors affecting the resistance of the winding at a given length are the ratio d/δ and the number of bundle layers. While it is valuable to approximate η more precisely, the difference in loss is minimal when compared to these other factors.

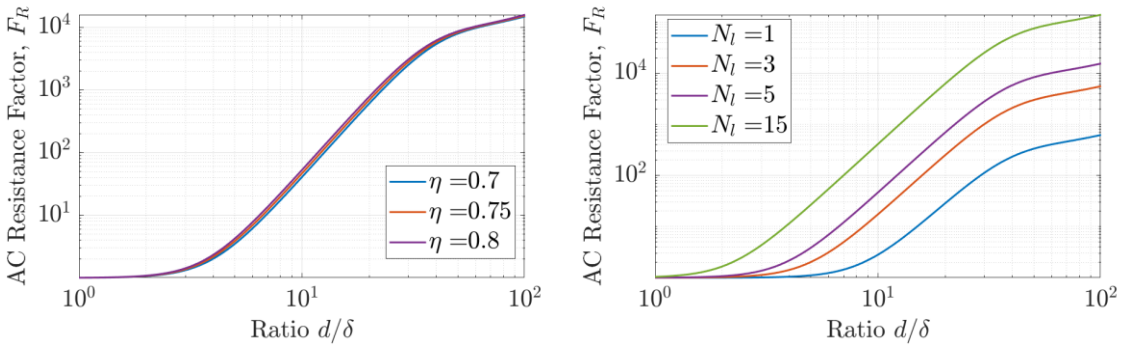

Fig. 9. AC to DC resistance factor as a function of normalized equivalent conductor diameter, varied over porosity factor with 5 layers (left), and over number of layers using a porosity factor of 0.75 (right).

As an alternative, the squared-field-derivative method (SFD) developed by researchers at Dartmouth University and provided for free as the web-based or downloadable MATLAB script known as "LitzOpt" can be used to compute the losses without having to go through the geometric manipulations discussed above. This method also works quite well in the case of one-dimensional field variation and can handle two-dimensional field variation if external FEM simulations are performed and the results are fed to the script. As noted in the literature review, this program has some deficiencies, but it offers a slightly different viewpoint and like the different methods employed for core selection, the winding selection process can only be improved by considering this perspective.

To make use of it, initially a small script was written to pick out the distinctive features of the current waveforms in the windings by considering the largest and smallest second derivatives and presenting those points as representative of the waveform. This significantly reduce the number of points, which is important since LitzOpt requires manual entry of time step durations and current values. This method worked well and enabled manual use of the online version of the tool, which features a user interface and

includes plots, tables, and diagrams of the results. However, it required additional action on the part of the user, so this method was discarded in favor of generating a formatted M-file, which is used as input in the downloadable script-based version of the tool. The transformer design tool creates this file and saves it at a user-specified location, then calls a gently modified version of LitzOpt and allows the user to load the file.

The modifications mentioned were intended to address two issues noted with the program that were likely the result of MATLAB artifacts remaining from when the program was first written. The first is that occasionally, the winding waveforms that were input would be shifted, such that the initial time period would be subsumed into the second, and the final period would be artificially lengthened to take the slack. This is visible in [134], where the waveform shown does not match the actual waveform produced by the converter under test. Some brief mention of it was made, though the cause was not correctly identified. The second issue was the display of the winding arrangement in the core window, which was occasionally offset by some nontrivial amount, making the windings appear to be inside the core. While correcting this, a light grey bobbin rectangle was also added to more accurately model the winding window.

As a final note on the investigation of winding construction, for FEM simulation purposes, an effective conductivity σ_{eff} for litz wire must be computed as in equation (25) [25].

$$\sigma_{eff} = \sigma_{Cu} \frac{d^2 n}{\frac{2\sqrt{3}}{\pi} d_l^2 n} \quad \left[\frac{\mathrm{S}}{\mathrm{m}}\right] \tag{25}$$

This equation attempts to relate the conductivity of the litz wire with an equivalent square conductor inside a square cell; this formulation fits well with the resistance

calculations discussed previously and accounts for air and insulation within that framework.

3.1.3 Inductance

With all the winding geometries sorted, it is now possible to compute the inductance matrix for the transformer. The complex self-impedance of an infinitely long solenoid is trivial to calculate. The complex impedance of a finite coil with respect to $N-1$ other finite coils sharing a common core is less so. Some brief explanation has already been given in the literature review, but in order to give a more detailed analysis, an accompanying illustration of the geometric manipulation is provided in Fig. 10, inspired by a similar figure in [41].

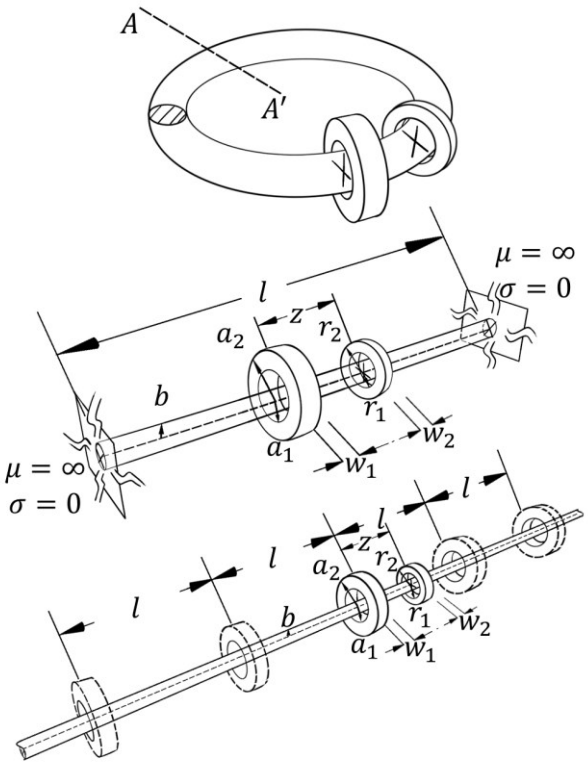

Fig. 10. Geometric core manipulation. The initial ring core is cut into a finite cylindrical rod with boundary conditions and then reflected to form an infinite core and winding images.

The equations used for calculation are given as (26) – (37) [41]:

$$Z = j\omega M_1 + Z_C \quad [\Omega] \tag{26}$$

$$Z_C = j\omega\mu_0 \frac{N_1 N_2}{h_1 w_1 h_2 w_2} \frac{2\pi}{l}\left[\frac{h_1 w_1 h_2 w_2 b^2}{2}\left(\frac{2\mu_r I_1(\Gamma_0 b)}{\Gamma_0 b I_0(\Gamma_0 b)} - 1\right) + 2S_C\right] \quad [\Omega] \tag{27}$$

$$S_C = \sum_{k=1}^{\infty} P(\beta_k a_2, \beta_k a_1) P(\beta_k r_2, \beta_k r_1) Q(\beta_k w_1, \beta_k w_2) \Phi(\beta_k) \cos(\beta_k z) \quad [\mathrm{m}]^6 \tag{28}$$

$$M_1 = \mu_0 N_1 N_2 A R \frac{2\pi}{l}\left[\frac{R}{2A} + 2S_1\right] \quad \left[\frac{\Omega \cdot \mathrm{s}}{\mathrm{rad}}\right] \tag{29}$$

$$S_1 = \sum_{k=1}^{\infty} I_1(\beta_k R) K_1(\beta_k A) \cos(\beta_k \mathrm{GMD}) \tag{30}$$

$$\Phi(\beta) = \frac{I_0(\beta b)}{K_0(\beta b)}\left[\frac{1 - \frac{I_1(\beta b)\Gamma b I_0(\Gamma b)}{\mu_r \beta b I_0(\beta b) I_1(\Gamma b)}}{1 + \frac{K_1(\beta b)\Gamma b I_0(\Gamma b)}{\mu_r \beta b K_0(\beta b) I_1(\Gamma b)}}\right] \tag{31}$$

$$\Gamma = \sqrt{\beta^2 + j\omega\mu_r\mu_0\sigma_c} \quad [\mathrm{m}]^{-1} \tag{32}$$

$$\beta_k = \frac{k2\pi}{l} \quad \left[\frac{\mathrm{rad}}{\mathrm{m}}\right] \tag{33}$$

$$\Gamma_0 = \sqrt{j\omega\mu_r\mu_0\sigma_c} \quad [\mathrm{m}]^{-1} \tag{34}$$

$$P(\beta x, \beta y) = \frac{p(\beta x) - p(\beta y)}{\beta^2} \quad [\mathrm{rad} \cdot \mathrm{m}^2] \tag{35}$$

$$p(z) = \frac{\pi z[K_1(z)L_0(z) + L_1(z)K_0(z)]}{2} \quad [\mathrm{rad}]^3 \tag{36}$$

$$Q(\beta x, \beta y) = \frac{2\left[\cos\left(\frac{\beta x - \beta y}{2}\right) - \cos\left(\frac{\beta x + \beta y}{2}\right)\right]}{\beta^2} \quad \left[\frac{\mathrm{m}}{\mathrm{rad}}\right]^2 \tag{37}$$

The number and complexity of equations bears some additional explanation. These equations can be used to calculate the total complex impedance, but in this application, only the imaginary portion is needed, so the calculated real terms are not strictly

necessary. The mutual inductance between two coils is given by (29), or alternatively read from [42] for specific coils, as mentioned in the literature review. It is made up of a constant term and a summation term, the first representing the air core mutual inductance, and the second the interactions between images. This summation term accounts for the leakage inductance between the two coils. Equation (27) gives the core static resistive impedance and the impedance due to reflection of windings and images from the core, and again, is made up of a constant core term, and a summation leakage term. The inductance matrix, then, is comprised of the sums of the constant terms from each of these two equations. The leakage inductance matrix, including self-leakage inductance on the diagonal, is comprised of the results of the summation terms. Special versions of the propagation coefficient, Γ and Γ_0, along with the imaginary portion, the phase constant β, and the wavenumber k appear in several of the equations, alongside the intrinsic permeability of free space μ_0, and the relative permeability and conductivity of the core μ_r and σ_C, respectively. The frequency dependence of the equations is explicitly included throughout via ω. I_n and K_n are modified Bessel functions of the first and second kind (nth order), and L_ν is the modified Struve function, given in (38) [135]. Together, the Bessel functions and the Struve function provide the complete solution to their associated differential equation, representing the complementary solution and the particular solution, respectively. A and R are the mean radii of coils (matching the inner and outer lowercase letter designations given to variables in Fig. 10), and the GMD is given by (39) – (45) [2], using the same orientations for height h and width w of coils as in Fig. 7.

$$L_\nu(z) = \frac{2\left(\frac{z}{2}\right)^\nu}{\sqrt{\pi}\Gamma\left(\nu+\frac{1}{2}\right)}\int_0^{\pi/2}\sinh(z\cos(\theta))\sin^{2\nu}(\theta)\,d\theta \tag{38}$$

$$\mathrm{GMD} = e^{\ln(d)-\theta} \quad [\mathrm{m}] \tag{39}$$

$$d = \sqrt{h^2 + w^2} \quad [\mathrm{m}] \tag{40}$$

$$\theta = \frac{u + v + 25}{12} - \frac{2}{3}(x + y) \tag{41}$$

$$u = \frac{w^2}{h^2}\ln\left(\frac{d^2}{w^2}\right) \tag{42}$$

$$v = \frac{h^2}{w^2}\ln\left(\frac{d^2}{h^2}\right) \tag{43}$$

$$x = \frac{w}{h}\tan^{-1}\left(\frac{h}{w}\right) \tag{44}$$

$$y = \frac{h}{w}\tan^{-1}\left(\frac{w}{h}\right) \tag{45}$$

In (38), $\Gamma(\cdot)$ represents the gamma function, not to be confused with the definition in (32). The GMD is a relatively simple way to represent multiple turns of wire as single filamentary elements, and is used in what is known as Lyle's method of equivalent filaments [2]. As mentioned in the literature review, this definition may need some revision after further study, as [52] and [53] suggest.

Using this method, the percentage of leakage inductance for an example winding configuration was calculated by sweeping the outer diameter of the litz wire from 0.1 mm to the maximum size that would allow the winding to be constructed in the core window. All calculations used the Ferroxcube E43/10/28-3F3 ferrite core, and two windings, each made of litz wire. The primary is a single parallel-distributed turn, taking up a single layer. The secondary winding, 15 turns of litz wire, was varied in its bundle outer diameter, and in arrangement within the core window. Like the resistance factor plots in Fig. 9, the 15 turns were arranged in a single layer, 3- and 5-layer rectangular

configurations, and a pancake structure (all windings in the plane orthogonal to the center leg axis). The results are presented in Fig. 11.

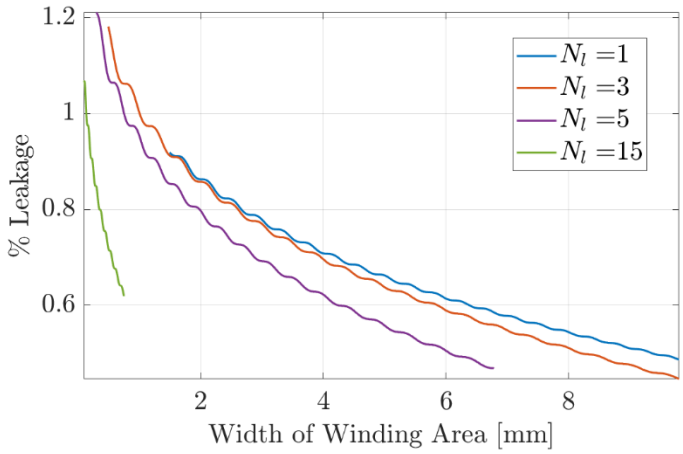

Fig. 11. Percent Leakage of 15-turn litz wire winding for various arrangements within the core window, and at varying bundle outer diameters, resulting in varying winding heights.

Manufacturer material datasheets provide the values used for calculations in this section, such as the equivalent core cross-sectional area, relative permeability, and even a value known as the "inductance factor", A_L which can be used to quickly compute the inductance of an N-turn coil. However, it is important to note potential sources of error due to assumptions and the approximations these quantities represent.

First, values describing core geometry are based on an equivalent toroidal core; in reality, cores have a variety of shapes and differing geometry measurements, and the complexity of dealing with such differences means that only FEM (or something approaching FEM) will truly account for the varying path areas, lengths, and the stark differences in shape (e.g. sharp outer corners and right-angle turns instead of a smooth, round path). On average, this is the least of the approximations, as the behavior of the magnetic material does even out over the core for excitation falling within the appropriate

operational range, since the regions of large differences are small compared to the overall magnetic path.

Noted in [41], the values provided for the inductance factor A_L assume that the winding width is equal to the magnetic path length of the core. This is an appropriate assumption for an inductor wound on the entire circumference of a toroid core, but nowhere near the correct arrangement for a multi-winding transformer on, for example, an E core center leg. Applying this approximation recklessly will lead to drastically different inductance estimations as compared with measurement, since only the constant core term will be computed, neglecting the constant air term and all the leakage terms, which are typically quite significant.

Finally, the provided permeability values must be addressed. The initial permeability, μ_i is often the first (and sometimes the only) permeability value given directly on the datasheet. For small inductors handling very little power, using this value will give acceptable results. For every other case, using this value will significantly underestimate the inductance. Plots of complex permeability, typical hysteresis curves, amplitude permeability, permeability vs. temperature, and in some cases, reversible permeability are often given, and extracting values from these curves provides much better information about how flux is generated in response to varying field excitation.

Complex permeability curves provide information for high-frequency operation, typically well above the range of operation at the base switching frequency; however, when considering harmonics of the fundamental frequency, some effects from this range will appear, most notably a change in the loss-to-storage ratio explained by the loss tangent, $\tan(\delta)$.

The example B-H curves provide several important pieces of information that can be used in various magnetic models, including the coercivity H_c and remanence B_r. Coercivity describes the field strength necessary to demagnetize the core after reaching the nonlinear region of operation where the hysteresis curve begins to take its characteristic 'S' shape. This directly complements the remanent flux density value, which represents the remaining magnetization in the core upon returning the external field excitation to zero. At every point on this curve, the slope of the line represents the permeability. Under very low field excitation, the slope of the curve at zero external field is referred to as the reversible permeability μ_{rev}. For the rest of the curve at a given temperature, the permeability clearly varies, and properly assessing the impact of this variability is critical to accurate inductance calculations. Since the behavior at the upper and lower ends of the B-H curve demonstrate transient behavior that is equal and opposite at either extreme of field strength for a good transformer design, this assessment should be primarily concerned with the behavior in the middle linear region.

The plots of amplitude permeability μ_a are the best tools for this job, because while they do not explicitly capture the time-varying behavior of the material near saturation, they do describe the slope of the main portion of the curve for a given peak flux density, from which we can derive a much more accurate inductance value. In order to use this value in calculation, datasheet extraction is performed using WebPlotDigitizer [136], and curve fitting is employed to create a model for use at design time. There are physics-based models that describe this behavior, which work very well for measured data, but they are unfortunately not of much use to a component designer without samples and copious time to test (see [137] for an example). For fast, accurate, analytical prediction of

permeability, the curves can be well-matched to a finite Gaussian series of the form in (46), which correctly captures the behavior near saturation of approaching zero without reaching it. This is a realistic assumption because it is unlikely that a static magnetic field of sufficient strength to completely align all domains in the core will be applied during any given switching cycle, so there will always be some non-zero slope in the hysteresis curve in practice.

$$\mu_a = \sum_{i=1}^{n} a_i e^{-\left(\frac{\hat{B}-b_i}{c_i}\right)^2} \tag{46}$$

Using the data from extraction and adding a final point approximating the behavior at the saturation flux density B_{sat}, (i.e. the point $(B_{sat}, 0)$) as shown in the example in Fig. 12, the amplitude permeability can be estimated and stored as a set of coefficients a_i, b_i, and c_i for $i \in \{1, 2, \dots, n\}$, improving the accuracy of inductance calculations. Refining this calculation as more information about the transformer becomes available yields better and better approximations, so this is done at the time of material selection, again after core selection, and again after winding selection to arrive at the best estimation.

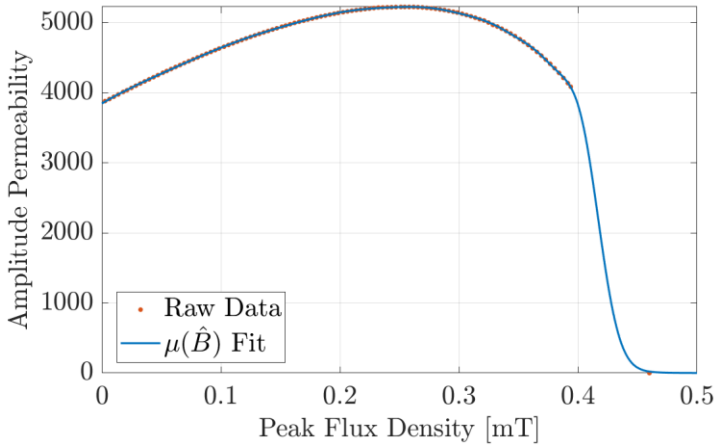

Fig. 12. Amplitude Permeability of 3C92 as a function of peak flux density.

Analysis must be verified by measurement, and since the values used in circuit analysis are fictitious (e.g. there is not actually a "leakage inductor" in the winding current path), some calculation must be performed to extract these elements from those measured. Four tests are necessary to obtain all inductance information about a given winding configuration, namely the open-circuit test, the short-circuit test, and the two series tests. In the first, each winding is measured with all other windings open-circuited to obtain the open-circuit inductance for winding i, $L_{i,OC}$. In the second, each winding is measured with one other winding short-circuited to collect the short-circuit inductance between windings i and j, $L_{ij,SC}$. Finally, a measurement is made of each winding pair connected in series-aiding configuration and series-opposing configuration (with respect to the flux generated by the right-hand rule and dot convention) for the values $L_{ij,SA}$ and $L_{ij,SO}$, respectively. These tests are performed for all possible configurations of pairs of windings to arrive at a set of values from which the analysis elements can be derived. A set of equations, (47) – (50) defines the quantities exposed by these measurements.

$$L_{i,OC} = L_i = L_{i,l} + L_m \quad [\text{H}] \tag{47}$$

$$L_{ij,SC} = L_{i,l} + L_{j,l} \quad [\text{H}] \tag{48}$$

$$L_{ij,SA} = L_i + 2M_{ij} + L_j \quad [\text{H}] \tag{49}$$

$$L_{ij,SO} = L_i - 2M_{ij} + L_j \quad [\text{H}] \tag{50}$$

In these equations, we find the self-inductance of each winding L_i comprised of its leakage inductance $L_{i,l}$ and the magnetizing inductance L_m referred to its side of the transformer, and the mutual inductance between windings i and j, $M_{ij} = M_{ji}$. Inspired by the coupled leakage model proposed in [46], and consistent with the work in [41], a mutual leakage term between a pair of windings is suggested here as a correction to (48),

which for two-winding transformers is simple to calculate, but for more windings requires the solution of a quadratic form, as in (51).

$$\vec{L}^T A \vec{L} = \vec{L}_{SC} \quad \text{[H]} \tag{51}$$

Equation (52) calculates the square root of each leakage inductance value pairwise for two given windings and is equivalent to the presentation in (51) in that configuration. More discussion on this formulation is provided in Appendix C.

$$\begin{aligned} L_{i,l} + k_{ij}\sqrt{L_{i,l}L_{j,l}} + \frac{N_i^2}{N_j^2}L_{j,l} &= L_{ij,SC} \\ \frac{N_j^2}{N_i^2}L_{i,l} + k_{ji}\sqrt{L_{i,l}L_{j,l}} + L_{j,l} &= L_{ji,SC} \end{aligned} \quad \text{[H]} \tag{52}$$

Here we have introduced a coupling coefficient, k_{ij}, between windings i and j, as seen from winding i, as well as k_{ji} in the reverse direction. The coupling coefficient is described repeatedly in literature as the fraction of total flux coupling two windings, and its complement with one is the leakage coefficient, $h = 1 - k$. This coupling factor is the geometric mean of the coupling factors for each winding, which can be derived from (47) in the form $L = hL + kL$. This formulation accounts for anisotropy in the core reluctance as well, as the values are measured for each winding configuration, inclusive of all combinations of test and short windings.

The magnetizing inductance, then, is simply the remaining fraction of the open-circuit inductance after the leakage inductance is accounted for. There are numerous ways to formulate its calculation, but for measurement presentation purposes it was simply calculated by the difference of the open-circuit inductance of the primary and the primary leakage inductance.

It should be mentioned that the preceding theoretical discussion regarding computation of inductance assumes that the material in use is isotropic and will remain that way during operation. If this is not the case, a symmetric matrix is insufficient to describe the inductance values generally. In the simplest case, one dimensional anisotropy along the magnetic path length, the inductance matrix is asymmetric and $M_{ij} \neq M_{ji}$. For three-dimensional anisotropy, a rank 3 tensor is needed, with variations along each coordinate vector represented in the new dimension. Analysis of these conditions is beyond the scope of this work, but it is important to note when talking about measurement.

Algorithmically, this is a good checkpoint, as we now have a complete transformer. It is appropriate to ensure that all consistency metrics (window area sufficiency, A_p and K_g greater than or equal to goals, peak flux density less than saturation flux density, and safe peak current density) are met. This information is quite handy for determining whether to keep a design or discard it prior to loss calculations.

3.1.4 Capacitance

In [55], the total self-capacitance C_f of a two-winding, foil-wound transformer is given by (53).

$$C_f = \frac{1}{\frac{1}{C_{ttf}} + \frac{1}{C_{tsf1}} + \frac{1}{C_{tsf2}}} \quad \text{[F]} \tag{53}$$

In (53), C_{ttf} is the sum of turn-to-turn capacitances between successive turns in the winding given by (54), C_{tsf1} is the sum of turn-to-shield capacitances of the first

winding given by (55), and C_{tsf2} is the sum of turn-to-shield capacitances of the second winding given by (56).

$$C_{ttf} = \sum_{i=1}^{8} C_i = 2\varepsilon_2 \frac{l_a l_{b5}}{d_2} + 2\varepsilon_2 \frac{l_a l_{b6}}{d_2} + 4\varepsilon_2 \frac{l_a}{\ln\left(\frac{r_2 + d_2}{r_2}\right)} \quad \text{[F]} \tag{54}$$

$$C_{tsf1} = \sum_{i=1}^{8} C_{i1} = 2\varepsilon_1 \frac{l_a l_{b5}}{d_1} + 2\varepsilon_1 \frac{l_a l_{b6}}{d_1} + 4\varepsilon_1 \frac{l_a}{\ln\left(\frac{r_1 + d_1}{r_1}\right)} \quad \text{[F]} \tag{55}$$

$$C_{tsf2} = \sum_{i=1}^{8} C_{i2} = 2\varepsilon_3 \frac{l_a l_{b5}}{d_3} + 2\varepsilon_3 \frac{l_a l_{b6}}{d_3} + 4\varepsilon_3 \frac{l_a}{\ln\left(\frac{r_3 + d_3}{r_3}\right)} \quad \text{[F]} \tag{56}$$

The structure analyzed in (54) – (56) is depicted by Fig. 13, where l_a is the width of the foil winding, into the diagram, and the corners (sections 1–4) are modeled as cylindrical capacitor sections with radii r_i, while l_{b5} and l_{b6} are the lengths of the connecting sections (sections 5–8), treated as parallel plate capacitors. The thickness and permittivity of the insulation between the two windings and between the windings and inner and outer shields are given by d_i and $\varepsilon_i = \varepsilon_{r,i}\varepsilon_0$, respectively.

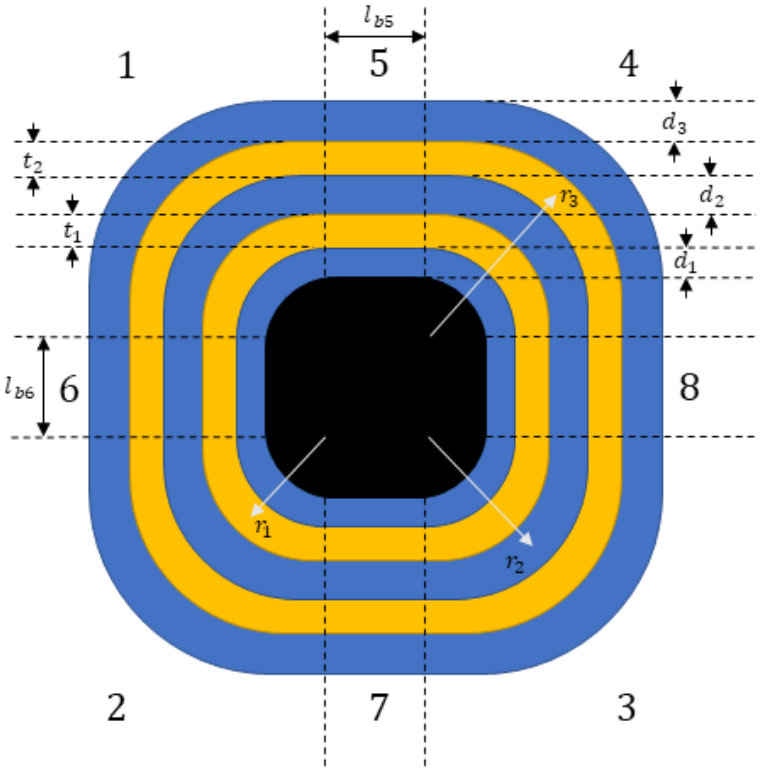

Fig. 13. Foil winding diagram, with winding divided into 8 sections: 4 cylindrical sections, and 4 parallel plate sections.

In Fig. 13, copper thickness values t_1 and t_2 have been included to clearly illustrate the total extent of each winding. Each section has its own capacitance in the sums in (54), (55), and (56), denoted C_i, C_{i1}, and C_{i2}, respectively. These capacitances are in parallel in each equation, and thus sum directly; however, as described in (53), the capacitance values resulting from each equation are in series with one another when considering the transformer's total capacitance.

We now attend to the other case presented in [55], the capacitance between a pair of round wires. Given a pair of solid, round wires with outer diameters (including insulation) d_o, and copper diameters d_c, the differential turn-to-turn capacitance of the

insulation is given by (57), while the differential turn-to-turn capacitance of the air gap is given by (58), where both are functions of the angle of observation, θ.

$$dC_{ttc}(\theta) = \frac{1}{2}\varepsilon_{s1}\, d\theta \int_0^{l_t} dl \int_{\frac{d_c}{2}}^{\frac{d_o}{2}} \frac{r}{dr} = \frac{\varepsilon_{s1} l_t}{2\ln\left(\frac{d_o}{d_c}\right)} d\theta \tag{57}$$

$$dC_{ttg}(\theta) = \varepsilon_0 \frac{\left(\frac{l_t d_o}{2}\right)}{x(\theta)} d\theta \tag{58}$$

In (57), a minor correction has been made to account for the insulation of each wire (namely the series identical capacitance factor of ½), which previously was included only in the final sum; this seems appropriate since the capacitance is given as a turn-to-turn value, rather than an elementary value. In (58), x is the effective length of the electric field path in the airgap, considering a curved path, and is given by (59). A derivation for this expression is given in Appendix D.

$$x(\theta) = \theta d_o \tan\left(\frac{\theta}{2}\right) \quad \text{[m]} \tag{59}$$

The differential expression in (58) must be numerically integrated, as no closed-form analytical expression exists due to the form of the integrand and the resulting non-removable singularities at the upper and lower limits of integration.

Finally, the differential turn-to-turn capacitance between the two wires can be calculated using (60), wherein the series capacitances of the insulation and airgap are considered.

$$dC_{tteq}(\theta) = \frac{1}{\frac{1}{dC_{ttc}} + \frac{1}{dC_{ttg}}} = \frac{\varepsilon_{s1} l_t}{2}\left(\frac{1}{\varepsilon_{r1}\theta\tan\left(\frac{\theta}{2}\right) + \ln\left(\frac{d_o}{d_c}\right)}\right) d\theta \tag{60}$$

Again, (60) has been corrected to account for the changes made to (57), as compared with the version in [55]. Equation (58) is intractable for hand-solution, and difficult to solve numerically; however, using (60), we can solve for the equivalent turn-to-turn capacitance, and solve for the air gap capacitance algebraically in reverse using (61).

$$dC_{ttg} = \frac{dC_{tteq}\, dC_{ttc}}{dC_{ttc} - dC_{tteq}} \tag{61}$$

In [56], while the mechanism for the suggested conic eccentricity is left unspecified, a parabolic electric field line description, shown to more closely match FEM simulation than the circular path, is proposed. The differential capacitance in the air portion of the path is given by (62), and in the insulation by (63), both of which require (64).

$$dC_{air} = \frac{\varepsilon_0 \frac{d_o}{2}}{\int_{-x_1}^{x_1} \sqrt{1 + \left(\frac{dy}{dx}\right)^2}\, dx} d\theta \tag{62}$$

$$dC_{ins} = \frac{\left(\varepsilon_r \varepsilon_0 \frac{d_o}{2}\right)}{\int_{x_1}^{x_2} \sqrt{1 + \left(\frac{dy}{dx}\right)^2}\, dx} d\theta \tag{63}$$

$$\frac{dy}{dx} = \frac{2x\left(\frac{d_o}{2} - \frac{d_c}{2}\right)\sin(\theta)}{\left(\frac{d_o}{2} - \frac{d_c}{2}\cos(\theta)\right)^2} \tag{64}$$

The geometry used to compute (62) – (64) is shown in Fig. 14, with x positions indicating the location of electric field excursion from the insulation and conductor x_1 and x_2, the conductor center x_3, the height from the center of the conductor at which the

electric field line at angle θ leaves, y_1, and the diameters of the bare conductor and insulated conductor, d_c and d_o.

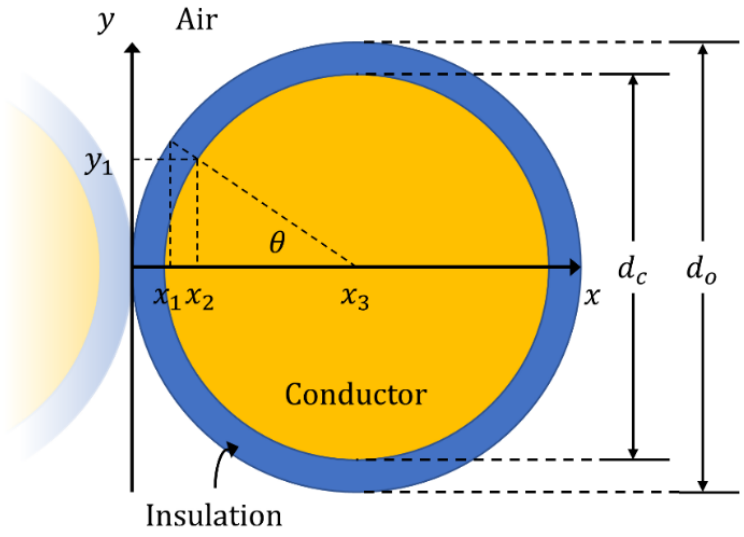

Fig. 14. Geometry used to compute static capacitance of round wire by parabolic paths.

A simple alternative approximation, based on the transformation of litz wire and round wire to foil windings requiring less additional setup but having only been tested against one case, and not at all against FEM simulation is presented in Appendix E.

3.1.5 Loss Analysis

Finally, we can calculate losses. For winding loss P_w, the typical I^2R copper loss formulation is used, but to include the AC and DC losses for a given winding, one must use the RMS current in that winding calculated in (12), DC resistance calculated for the coil in (21), and the AC resistance factor calculated in (19) as in (65) [3].

$$P_w = P_{Cu} = F_R(I_{RMS}^2 R_{DC}) \quad [\text{W}] \tag{65}$$

Core loss, as mentioned in the literature review, has various calculation methods, but herein the iGSE is implemented using another of Dartmouth's MATLAB scripts, namely 'coreloss.m' [30]. It faithfully (with a bit of unit conversion) calculates the time-average

specific core loss $\overline{P_V}$ based on Steinmetz parameters for a given piecewise-defined flux density waveform. The formulas used are given in (66) and (67) [30].

$$\overline{P_{V,i}} = \frac{1}{T_i}\int_0^{T_i} k_i \left|\frac{dB}{dt}\right|^{\alpha} \Delta B^{\beta-\alpha}\, dt \quad \left[\frac{\mathrm{W}}{\mathrm{m}^3}\right] \tag{66}$$

$$k_i = \frac{k}{(2\pi)^{\alpha-1}\int_0^{2\pi}|\cos(\theta)|^{\alpha}2^{\beta-\alpha}\, d\theta} \tag{67}$$

In (66) and (67), α, β, and k are the Steinmetz parameters obtained by curve fitting. This formula accounts for major and minor subloops within periodic waveforms (i.e. the integral is evaluated over segments containing monotonic regions of the flux density waveform and their mirror counterparts). Within such a subloop i, ΔB is the peak-to-peak change in magnetic flux density, and T_i is the segment of the total period encompassing only the period of the subloop in question. The contribution of each segment is then weighted by its duration and all weighted segments are summed to produce the total time-average specific core loss per cycle via equation (68).

$$\overline{P_V} = \sum_i \frac{T_i P_{V,i}}{T} \quad \left[\frac{\mathrm{W}}{\mathrm{m}^3}\right] \tag{68}$$

The core loss script was edited to address a major concern: the time taken to evaluate multi-frequency waveforms. Since such a waveform needs a high resolution to represent the switching frequency variation but must accommodate the duration of at least one period of the low-frequency oscillation, it tends to be quite lengthy. Operating along the waveform linearly to decompose the major and minor loops was originally done by iteration, but MATLAB is specifically designed to work with matrices and vectors, so effort was exerted to convert as many iteration operations into vector operations as possible. Care was taken to avoid using any functions not included with the base

MATLAB installation, and a significant increase in speed was observed, from tens of minutes to tens of seconds.

After calculating losses for one winding configuration, the values for the next configuration can be computed. After computing values for all winding constructions for one core, a different core model can be selected, and the winding iterations completed again. After all cores for the chosen material are investigated, another material can be selected, and the process started again. After all iterations, several complete transformers are available for optimization by desired characteristics (e.g. loss, inductance, volume, etc.). A brute force approach, wherein all possible combinations are evaluated and sifted for optimality is one possible method for optimal design; however, more sophisticated methods exist, and should be investigated.

3.1.5.1 Loss Optimization

Losses in a transformer P_L can be represented by the sum of losses in the windings P_w and losses in the core P_c, as shown by (69).

$$P_L = P_w + P_c \quad [\mathrm{W}] \tag{69}$$

Throughout the literature on the topic, it is often stated that optimal efficiency occurs when the core loss and winding loss are equal. Based on the discussion in [6], this is true only for specific materials, and only under certain conditions. With some simplifying assumptions and substitution of constants a and b for terms held constant during analysis, the total loss in the transformer can be expressed by (70).

$$P_L = P_w + P_c = \frac{a}{f^2 \hat{B}^2} + b f^{\alpha} \hat{B}^{\beta} \quad [\mathrm{W}] \tag{70}$$

Taking the partial derivatives with respect to $\hat{B}$ and f, we have (71) and (72), respectively.

$$\frac{\partial P}{\partial \hat{B}} = -\frac{2a}{f^2 \hat{B}^3} + \beta b f^{\alpha} \hat{B}^{\beta-1} \tag{71}$$

$$\frac{\partial P}{\partial f} = -\frac{2a}{f^3 \hat{B}^2} + \alpha b f^{\alpha-1} \hat{B}^{\beta} \tag{72}$$

Setting the derivatives equal to zero, we can find local minima from each equation, with (73) providing the minimum loss under fixed frequency, and (74) providing the minimum loss under fixed peak flux density.

$$P_w = \frac{\beta}{2} P_c \quad [\mathrm{W}] \tag{73}$$

$$P_w = \frac{\alpha}{2} P_c \quad [\mathrm{W}] \tag{74}$$

Under these conditions, $\alpha = \beta = 2$ ensures that equal core and winding loss provide maximum efficiency at fixed values of both f and $\hat{B}$, but this is not the case in general. Furthermore, adjusting the frequency or peak flux density for a given core and winding configuration may allow minimum loss to be achieved in theory, but saturation flux density may limit the range of allowable $\hat{B}$, while converter design almost certainly limits the freedom to choose a switching frequency. Finally, this loss analysis uses the original Steinmetz equation for core loss and a simplified version of the winding loss equation. The equations can be modified to account for more accurate derivative-based loss analysis, but this complicates the optimization process significantly, so other methods should be used to seek maximum efficiency.

Total winding loss is comprised of DC Joule heating loss P_{wDC}, and two types of AC eddy current losses: skin effect loss P_{wSE} and proximity effect loss P_{wPE}, which can be combined into P_{wAC} as in (75).

$$P_w = P_{wDC} + P_{wSE} + P_{wPE} = P_{wDC} + P_{wAC} \quad [\text{W}] \tag{75}$$

There are several ways to break these losses down, but the simplest and most straightforward is to use the I^2R conduction loss formulation with the RMS current from (12) as presented in (76).

$$P_w = I^2R = \sqrt{I_{DC}^2 + I_{AC,MS}}R_{AC} = \sqrt{I_{DC}^2 + I_{AC,MS}}F_R R_{DC} \quad [\text{W}] \tag{76}$$

Expanding on the second term in the radicand of (12) and (76), given a periodic current waveform, we can separate it into a periodic portion with zero mean, and the DC offset. The DC offset is simply the mean value of the waveform; subtracting this value yields the periodic portion, and we can compute its mean square value $I_{AC,MS}$ via (77).

$$I_{AC,MS} = I_{AC,RMS}^2 = \frac{1}{T}\int_0^T I_{AC}^2(t)\,dt \quad [\text{A}]^2 \tag{77}$$

The DC resistance of the winding is computed by (21), or as expressed by (78).

$$R_{DC} = \frac{4\rho_{Cu}N_e l_t}{\pi d^2} \quad [\Omega] \tag{78}$$

Here we are approximating the total winding length by the product of its mean length turn and the number of effective turns $N_e = N/n$.

The other factor in (76), F_R, comes from Dowell's equation given by (19), which takes a dimensionless argument A that encodes information about the diameter of a single layer of conductors in the winding window relative to the skin depth of the current in the wire and the porosity factor (the relationship between the conductor area and a square cell

of the window), previously given in (20). The skin depth is found using (13) with an effective frequency given by (11), which considers the disparity in energy transfer between a switching waveform and a sinusoid.

In Dowell's equation, we have used the effective number of layers of the winding (from conversion of litz wire to an equivalent foil winding) within the bobbin height (center leg to outer leg distance), which in the case of a filled window is given by (24). In the general case, we use the height of the winding itself, or the number of bundle layers given a square bundle configuration and the number of conductors per bundle "side", computed by taking the square root of the number of strands in the bundle, n as shown in (79).

$$N_{ll} = \frac{h_w}{d_l} = N_l\sqrt{n} = \frac{N}{N_{bpl}}\sqrt{n} = \frac{N}{\frac{b_b}{\sqrt{n}d_l}}\sqrt{n} = \frac{Nnd_l}{b_b} \tag{79}$$

With this, we have completely described the winding losses due to DC Joule heating, skin effect, and proximity effect. A complete formulation with all terms fully expanded is given by (80) – (84).

$$P_w = I_{RMS}^2 D_R S\left[\frac{\sinh(2DS)+\sin(2DS)}{\cosh(2DS)-\cos(2DS)} + N_K\frac{\sinh(DS)-\sin(DS)}{\cosh(DS)+\cos(DS)}\right] \quad [\text{W}] \tag{80}$$

$$D = \left(\frac{\pi}{4}\right)^{\frac{3}{4}} d_l(d) \quad [\text{m}] \tag{81}$$

$$F = \sqrt{\frac{\left\{\frac{di(t)}{dt}\right\}_{RMS}\mu_{Cu}\eta}{2I_{RMS}\rho_{Cu}}} \quad [\text{m}]^{-1} \tag{82}$$

$$D_R = DR_{DC} = \left(\frac{\pi}{4}\right)^{\frac{3}{4}}\frac{4\rho_{Cu}Nd_l(d)l_t}{\pi n d^2} \quad [\Omega\cdot\text{m}] \tag{83}$$

$$N_K = \frac{2}{3}\left(\left(\frac{N n d_l(d)}{b_b}\right)^2 - 1\right) \tag{84}$$

In this formulation, there are terms known due to the converter design, terms from wire and core selection, and constants. While η is not technically a constant, its value is difficult to determine exactly, and it has little effect on the resistance of the winding (and thus the loss) as shown in Fig. 9, so it will be taken as the midpoint of its typical range in litz wire, 0.75. Also note that the layer diameter has been given as a function of the strand diameter, $d_l(d)$, referring to the presentation in (23). This reduces the number of variables by one, but the presentation is more succinct as it is represented here.

As mentioned, we prefer the iGSE for core loss computation, described in Section 3.1.5. The equation relies on the availability of a waveform for the magnetic flux density in the core. This can be computed from the primary winding voltage waveform as in (85).

$$B(t) = \frac{1}{N A_e}\int_0^T v(t)\,dt - B_{DC} \quad [\mathrm{T}] \tag{85}$$

Specifically, we need the peak-to-peak magnitude of this waveform during a given monotonic segment i of a hysteresis loop with period T_i, and the magnitude of its derivative with respect to time, given by (86) and (87), respectively. Equation (87) is presented in combined units since there are two sets of dimensions, both of which relate easily to those selected (i.e. 1 Wb = 1 T·m^2 = 1 V·s).

$$\Delta B = \max_{t\in T_i} B(t) - \min_{t\in T_i} B(t) \quad [\mathrm{T}] \tag{86}$$

$$\left|\frac{dB}{dt}\right| = \left|\frac{d}{dt}\left[-\frac{1}{N A_e}\int_0^T v(t)\,dt - B_{DC}\right]\right| = \frac{1}{N A_e}|v(t)| \quad \left[\frac{\mathrm{Wb}}{\mathrm{m}^2\cdot\mathrm{s}}\right] \tag{87}$$

Assuming a simple hysteresis loop, we can compute the core loss using (66) – (68), along with the equivalent core volume V_e. A fully expanded form is presented as (88) and (89).

$$P_c = \frac{V_e}{(NA_e)^\alpha}\frac{1}{T}\int_0^T \left[\frac{k}{(2\pi)^{\alpha-1}\int_0^{2\pi}|\cos(\theta)|^\alpha 2^{\beta-\alpha}\,d\theta}\right]|v(t)|^\alpha \Delta B^{\beta-\alpha}\,dt \quad \text{[W]} \qquad (88)$$

$$\Delta B = \max_{t\in T}\left(\frac{1}{NA_e}\int_0^T v(t)\,dt - B_{DC}\right) - \min_{t\in T}\left(\frac{1}{NA_e}\int_0^T v(t)\,dt - B_{DC}\right) \quad \text{[T]} \qquad (89)$$

If we further assume that there is no DC bias or premagnetization, the equations can be reduced to (90) and (91).

$$P_c = \frac{V_e}{(NA_e)^\beta}\left[\frac{k}{2^{\beta-1}\pi^{\alpha-1}\int_0^{2\pi}|\cos(\theta)|^\alpha\,d\theta}\right](N\Delta\phi)^{\beta-\alpha}\frac{1}{T}\int_0^T |v(t)|^\alpha dt \quad \text{[W]} \qquad (90)$$

$$N\Delta\phi = \max_{t\in T}\left(\int_0^T v(t)\,dt\right) - \min_{t\in T}\left(\int_0^T v(t)\,dt\right) \quad \text{[T]} \qquad (91)$$

As before, the equations contain parameters known from converter design and variables selected during the transformer design process.

With both parts of the total transformer loss fully expanded, we can enumerate all constants, converter-specific parameters, and core and winding selection parameters, summarized in Table III.

TABLE III
LOSS EQUATION CONSTANTS, PARAMETERS, AND VARIABLES

Loss Equation	Constants	Known Parameters	Optimization Variables
Winding Loss P_w	$\rho_{Cu}, \mu_{Cu}, \eta$	$I_{RMS}, \{\mathrm{d}i(t)/\mathrm{d}t\}_{RMS}, N$	d, l_t, n, b_b
Core Loss P_c	—	$N, T, v(t)$	$V_e, A_e, k, \alpha, \beta$

To formulate the optimization problem, we begin with the objective function in (92).

$$\text{minimize } P_L = P_w + P_c \tag{92}$$

Then we express the constraints necessary to ensure safety, consistent steady-state operation, and physically feasible design in (93) – (96).

$$\left|\hat{B}\right| < B_{sat} \quad [\text{T}] \tag{93}$$

$$\widehat{J_w} = \frac{4\widehat{I_w}}{\pi d_w^2 N_{\parallel}} < J_{max}, \forall w \in W \quad \left[\frac{\text{A}}{\text{m}^2}\right] \tag{94}$$

$$\frac{N_w d_{o,w} N_{\parallel}}{N_{l,w}} < b_b, \forall w \in W \quad [\text{m}] \tag{95}$$

$$\sum_{w \in W} d_{o,w} N_{l,w} < h_b \quad [\text{m}] \tag{96}$$

Equation (93) constrains the absolute peak magnetic flux density to avoid saturation at the value B_{sat}, ensuring that the transformer will operate primarily in the linear regime, maximizing throughput power, reducing heating, and behaving predictably during steady-state operation. In (94), the peak current density in winding w is constrained to the safe current density limit for each winding in the set of all windings W to prevent electrical hazards stemming from the transformer. The windings are further constrained by (95) and (96), the former limiting the breadth of each winding to the bobbin breadth, and the latter limiting the total height of all windings to the bobbin height. Equation (95) considers the number of turns in the winding N_w, its conductor outer diameter $d_{o,w}$, the number of parallel wires $N_{\parallel}$ (occasionally necessary to meet (94)), and the number of layers in the winding $N_{l,w}$. These constraints are not exhaustive. For example, upper and lower bounds on individual variables are omitted. However, they provide a foundation for the process, which can be modified as needed for specific applications.

Some modifications will now be suggested. A second objective can be added to seek a specific inductance value by minimizing the distance between an inductance calculation and the target. The original objective function can be changed to maximize power density, specifically, by formulating the problem with the specific core loss divided by the effective volume. Mass and/or density could be added as additional variables for weight considerations for applications like electric vehicle charging and drive circuits. In some of these cases, multiple objectives need to be realized, so optimality becomes a matter of balancing trade-offs.

For multi-objective optimization, we seek Pareto optimality, in which solutions lie along the Pareto frontier such that improvement in optimality via one parameter decreases optimality by another. MATLAB's Optimization Toolbox provides solvers that optimize multiple objective functions over multiple variables, such as 'fgoalattain.m' as well as solvers that can perform the same job, like 'fsolve.m' and 'fmincon.m' when configured correctly via external function files. There are also other methods of multi-objective optimization such as evolutionary algorithms (e.g. genetic algorithms) and simulation techniques (e.g. Monte Carlo and simulated annealing), which have been employed in other work for this task.

One major problem with this approach is that solutions are difficult to constrain to real-world components. For example, there is no direct relationship between a core's volume and its cross-sectional area, due to the large number of different shapes and sizes. Results can be quite mysterious from this perspective. After optimization, we must find wires and cores that best match the optimal variables; however, this is unlikely to be possible to do exactly due to limitations on manufacturing and availability. A least-

squares minimization is the simplest approach, wherein we take the minimum two-norm of the difference between optimal parameters and parameters of wires and cores which are purchasable.

An alternative approach to this strategy is a midpoint between the complete enumeration approach used in the transformer design script and the approach described in main portion of this section. Lists of possible components (materials, cores, and wires) can be used to discretize the solution, which makes the optimization process coarser, but removes the necessity to try to match the sometimes strange solutions of the direct optimization approach to real-world purchases.

3.1.6 Thermal Model

After loss computation, the power dissipated by the core and windings can be used to compute the temperature rise in each. In [1] and again in both [3] and [6], a very simple formula for the coefficient of heat transfer in the transformer is given by (97).

$$h = 1.42\left[\frac{\Delta T}{H}\right]^{0.25} \quad \left[\frac{\mathrm{W}}{\mathrm{m}^2 \cdot {}^\circ\mathrm{C}}\right] \tag{97}$$

It uses the temperature rise ΔT and the height of the transformer H to determine this coefficient, but the process can also be reversed to find the temperature rise if the coefficient is known. [6] also gives the temperature rise in terms of this coefficient as (98), further breaking down the thermal resistance R_θ as in (99).

$$\Delta T = \frac{1}{hA_s}P_L = R_\theta P_L \quad [{}^\circ\mathrm{C}] \tag{98}$$

$$\frac{1}{R_\theta} = \frac{1}{R_{\theta_w}} + \frac{1}{R_{\theta_c}} = hA_s \quad \left[\frac{\mathrm{W}}{{}^\circ\mathrm{C}}\right] \tag{99}$$

In each source, the coefficient h is described as uncertain, and the formula contains constants without definition or derivation, so this should be used as a rough approximation only.

At the other end of the complexity spectrum, a very detailed model was noted in the literature review in [60], in which every path and means of heat transfer is investigated and validated against a Multiphysics simulation and test measurements. This level of detail is admirable and inclusion of a version of it generalized to all conditions in the design script would be an excellent goal for future development.

In this work, the model complexity is somewhere between the two ends of the spectrum, considering conduction between each winding and between the windings and the core, as well as convection for each to ambient. The model is a slight modification of that provided in [3] and appears to work well when compared with results in literature. The electrical circuit equivalent model is depicted by Fig. 15 and described by the system of equations in (100).

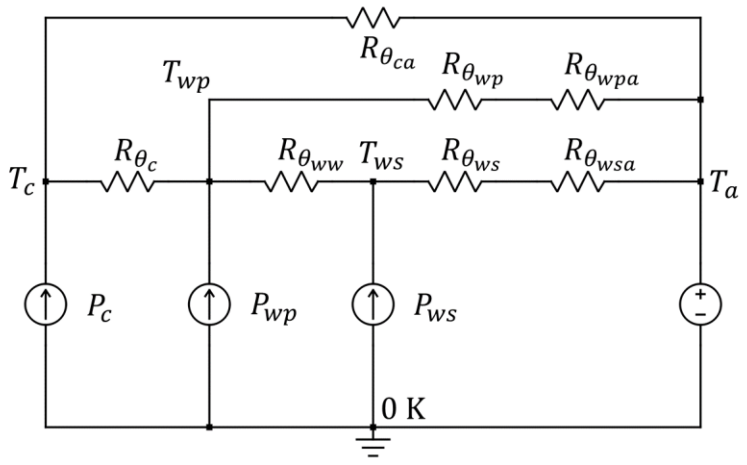

Fig. 15. Thermal model of two-winding transformer.

$$\begin{bmatrix} R_{\theta_c} + R_{\theta_{ca}} & -R_{\theta_{ca}} & 0 \\ -R_{\theta_{ww}} & R_{\theta_{ww}} + R_{\theta_c} + \dfrac{R_{\theta_c} R_{\theta_{ww}}}{R_{\theta_{peq}}} & -R_{\theta_c} \\ 0 & -R_{\theta_{seq}} & R_{\theta_{seq}} + R_{\theta_{ww}} \end{bmatrix} \begin{bmatrix} T_c \\ T_{wp} \\ T_{ws} \end{bmatrix} = R_P \begin{bmatrix} P_c \\ P_{wp} \\ P_{ws} \end{bmatrix} + R_T T_a \quad (100)$$

In (100), $R_{\theta_{peq}}$ and $R_{\theta_{seq}}$ are the thermal equivalent series resistances of the primary and secondary windings to ambient, shown in Fig. 15 as $R_{\theta_{wp}} + R_{\theta_{wpa}}$ and $R_{\theta_{ws}} + R_{\theta_{wsa}}$, respectively. The diagonal matrix R_P and column vector R_T are given by (101) and (102).

$$R_P = \begin{bmatrix} R_{\theta_c} R_{\theta_{ca}} & R_{\theta_c} R_{\theta_{ww}} & R_{\theta_{ww}} R_{\theta_{seq}} \end{bmatrix} I \quad \left[\frac{^\circ\mathrm{C}}{\mathrm{W}}\right]^2 \tag{101}$$

$$R_T = \begin{bmatrix} R_{\theta_c} & \dfrac{R_{\theta_c} R_{\theta_{ww}}}{R_{\theta_{peq}}} & R_{\theta_{ww}} \end{bmatrix}^T \quad \left[\frac{^\circ\mathrm{C}}{\mathrm{W}}\right] \tag{102}$$

Using known values for the losses P_c, P_{wp}, and P_{ws}, the ambient temperature T_a, and computed values for the thermal resistances, the temperatures of the core and windings can be computed by solving (100). For thermal management purposes, the value of $R_{\theta_{ca}}$ can be modified to include the effect of a heat sink to find an appropriate solution. For multi-winding transformers, the model is expanded as needed to include the losses and resistance to air in each winding, and the resistances between the windings. For each additional winding, one row and one column are added to the matrix on the LHS of (100), and one row is added to each vector expression on the RHS.

That said, as noted in the literature review and in several places during this analysis, the operating temperature of the core and windings change the properties of the materials from which they are constructed, including both the Steinmetz coefficients and the resistivity of the core and the copper in the windings. Since these quantities directly

impact losses, this necessitates an iterative procedure in which losses are computed at a nominal temperature, the temperature rise is computed, and the process repeated until the change in loss and/or temperature rise is below an acceptable threshold.

3.1.7 State Space Model

In order to facilitate simulation and integration of transformer models with larger microgrid simulations, a state space model of the transformer was derived. By itself, the model is just another way to evaluate transformer performance, but it has limitations since its behavior is largely dictated by the source and load to which it is connected. However, with some additional effort, an unterminated model, independent of load, can be fed source voltage and load current waveforms as inputs, or connected to other state-space models with matching inputs and outputs, and its load voltage and source current outputs will respond appropriately. This allows for modular modeling of transformers in a variety of circuits and is a good foundation for inclusion in both microgrid and converter simulations. Since a current source in series with an inductor is inconsistent, this requires moving the secondary leakage inductance to the load model. For example, for connection to a typical power electronics LC output filter, the filter inductor would absorb the leakage inductance.

The Steinmetz model of a two-winding transformer depicted in Fig. 16 is used for demonstration. This venerable model includes the primary and secondary winding leakage inductances $L_{p,l}$ and $L_{s,l}$ and AC resistances $r_p$and r_s, as well as the effect of the core via the magnetizing branch, consisting of magnetizing inductance L_m and equivalent core loss resistor R_c. With no ideal transformer between primary and secondary, values on the secondary side are referred to the primary side by the turns ratio, appearing with a

prime decoration (e.g. $L'_{s,l} = \left(N_p^2/N_s^2\right)L_{s,l}$). This referral is also applied to voltages and currents as appropriate (e.g. $v'_s = \left(N_p/N_s\right)v_s$).

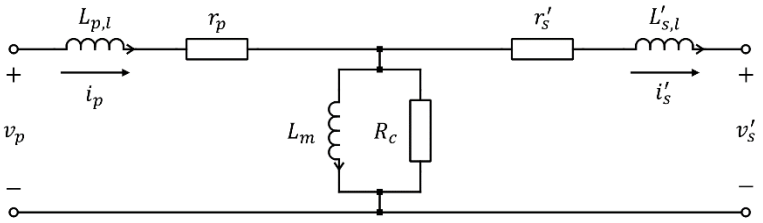

Fig. 16. Steinmetz "T-model" of a nonideal two-winding transformer, with secondary quantities referred to the primary side.

The load-terminated model for a simple two-winding transformer is given by the system of equations in (103), with the partitioned descriptor state space matrix equations followed by the state, input, and output vectors, and finally the state space matrices A, B, C, and D and descriptor matrix M.

$$\begin{gathered}
\left[\frac{\dot{\boldsymbol{x}}}{\boldsymbol{y}}\right] = \left[\begin{array}{c|c} M^{-1}A & M^{-1}B \\ \hline C & D \end{array}\right]\left[\frac{\boldsymbol{x}}{\boldsymbol{u}}\right] \\
\boldsymbol{x} = [i_{L_{p,l}} \quad i_{L_{s,l}} \quad i_{L_m}]^T \\
\boldsymbol{y} = v_s \\
\boldsymbol{u} = v_p \\
A = \begin{bmatrix} -R_c - r_p & \frac{N_s}{N_p}R_c & R_c \\ \frac{N_s}{N_p}R_c & -\frac{N_s^2}{N_p^2}R_c - r_s - Z_L & -\frac{N_s}{N_p}R_c \\ R_c & -\frac{N_s}{N_p}R_c & -R_c \end{bmatrix} \quad B = \begin{bmatrix} 1 \\ 0 \\ 0 \end{bmatrix} \\
C = [0 \quad Z_L \quad 0] \qquad D = [0] \\
M = [L_{p,l} \quad L_{s,l} \quad L_m]I
\end{gathered} \tag{103}$$

The term Z_L in (103) represents the load connected to the secondary terminals of the transformer. This value can be made arbitrarily large to observe the voltage transfer

characteristics of the transformer. The equivalent core resistance value requires the manufacturer-provided effective core length l_e, and is approximated by (104) [2].

$$R_c = \pi f^2 \sigma_c \left(\frac{\mu_c N_p}{l_e}\right)^2 \frac{l_e A_e}{2} \quad [\Omega] \tag{104}$$

An alternative to the load-terminated or unterminated models described above can be constructed by including the transformer capacitance. There are numerous formulations for transformer capacitance computation, but [57] suggests several models that may be valuable in this approach. The inclusion of a capacitance value at the terminals of the secondary removes the inconsistency of including a current input in series with an inductor, broadening the range of applications for the transformer state space model.

3.2 Microgrid

In this section we will cover the prevalent hierarchical control scheme introduced by [73], and specifically the implementation of it in the OPAL-RT real-time microgrid testbed. The testbed will be described, and various testing setups will be explained, where modifications were made to exploit the flexibility and power of the real-time simulation environment.

3.2.1 Hierarchical Control

To ensure reliable operation of the microgrid, the hierarchical control structure from [73] was used, with improved reactive power support, and with a novel energy storage balancing scheme. The hierarchy is three-tiered, with the tertiary level of control having a lower bandwidth than the secondary tier. This strategy ensures that the reference commands from the tertiary controller do not interfere with the control objectives of lower levels. The primary controllers directly influence the energy cells' smart inverter

operation via generation of setpoints, while the secondary and tertiary controllers cascade reference values to their downstream counterparts in succession, allowing multiple control objectives to be realized with relatively simple individual controller designs. Herein we will describe the control strategy and mathematical modeling used in the implementation.

3.2.1.1 Primary Control

Rather than implementing maximum power point tracking (MPPT), which is commonly used to maximize power production in inverters attached to distributed PV sources, the VSG control scheme in [76] was used to maintain stable AC bus voltage and frequency. This scheme causes the smart inverter to emulate a synchronous machine, which helps to ensure that multiple energy cells can coexist amicably in the network. The block diagram of this scheme is visualized in Fig. 17. Equations presented in this section are implemented in Simulink, as will be described in Section 3.2.5.

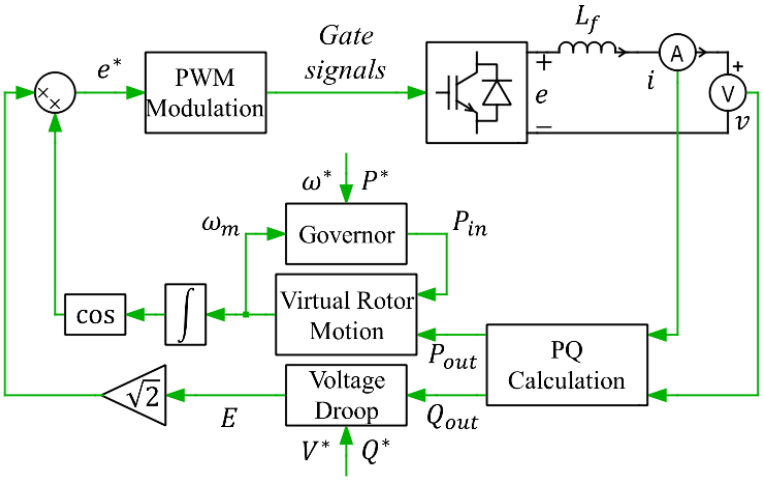

Fig. 17. Simplified VSG control block diagram; control signals in green, electrical signals in black.

The virtual rotor motion emulation is described by the swing equation in (105), with J being the virtual inertia, ω_m being the "mechanical" angular frequency of the virtual rotor, P_{in} being the virtual shaft power controlled by the governor, and P_{out} being the inverter real power output.

$$J\omega_m \frac{d\omega_m}{dt} = P_{in} - P_{out} \quad [\text{W}] \tag{105}$$

The virtual governor is emulated using the P-ω droop equation in (106), wherein P^* is the real power reference value and ω^* is the frequency reference value generated by the secondary tier of control. The reactive power is related to the bus voltage by the Q-V droop equation in (107), where E is the EMF at the VSG terminals, Q_{out} is the inverter reactive power output, Q^* is the reactive power reference command, and V^* is the voltage reference command generated by the secondary control tier.

$$P_{in} = P^* + (\omega^* - \omega_m)/m_p \quad [\text{W}] \tag{106}$$

$$E = V^* + m_q(Q^* - Q_{out}) \quad [\text{V}] \tag{107}$$

In (106), m_p is the real power droop coefficient, which defines the relationship between the virtual rotor speed and the load condition. To achieve the power sharing control objective while under islanded operation, the reactive power droop coefficient m_q in (107) has been modified such that in addition to defining the relationship between reactive power and terminal voltage, it also provides adaptive reactive power support. We define m_q as in (108) and (109), wherein m_{q0} is the typical reactive power droop coefficient and S_{rated} is the rated apparent power for the inverter.

$$m_q = m_{q0}/k \quad \left[\frac{\text{V}}{\text{VAr}}\right] \tag{108}$$

$$k = \sqrt{1 - P^{*2}/S_{rated}^2} \tag{109}$$

This formulation causes inverters generating less real power to provide more reactive power, maintaining a relatively steady apparent power output near the rated value.

Using this method incurs some nontrivial drift in the bus voltage and frequency over time. With sufficiently small droop coefficients, the steady-state error is reduced; however, the accuracy of the desired power-sharing capability is also reduced. This is addressed by the secondary controller and will be described in Section 3.2.1.2.

Regarding droop parameters, they can be selected for a given inverter by several methods. The presentation in [138] suggests the formulation in (110) and (111), and that they be made proportional to their respective power levels, such that the product of droop coefficient and power rating in each inverter is equal among all.

$$m_p = \frac{\omega_0 - \omega^*}{P_{rated} - P^*} \quad \left[\frac{\text{rad}/\text{s}}{\text{W}}\right] \tag{110}$$

$$m_{q0} = \frac{V_0 - V^*}{Q_{rated} - Q^*} \quad \left[\frac{\text{V}}{\text{VAr}}\right] \tag{111}$$

Here, V_0 and ω_0 are the nominal bus voltage and frequency, respectively. This formulation is intended to enforce power sharing between inverters. The discussion in [73] gives the parameters as (112) and (113), accounting for bidirectional real and reactive power flow.

$$m_p = \frac{\Delta\omega}{2P_{rated}} \quad \left[\frac{\text{rad}/\text{s}}{\text{W}}\right] \tag{112}$$

$$m_{q0} = \frac{\Delta V}{2Q_{rated}} \quad \left[\frac{\text{V}}{\text{VAr}}\right] \tag{113}$$

The $\Delta\omega$ and ΔV values in the numerators of these expressions are the maximum allowable deviation in frequency and voltage, respectively, while the denominator terms span the entire range of power flow of the inverter, assuming it has the same rating in each direction. This is the formulation used in the microgrid model, alongside an explicit virtual impedance in the virtual rotor computation block.

As an alternative, the presentation in [139] contracts the denominators to just the setpoints, and expands the numerators as in (114) and (115) to prepare for another term in each control equation accounting for the virtual impedance X_v, shown in (116) and (117).

$$m_p \leq \frac{\omega_{max} - \omega_{min}}{P^*} \quad \left[\frac{\text{rad}/\text{s}}{\text{W}}\right] \tag{114}$$

$$m_{q0} \leq \frac{V_{max} - V_{min}}{Q^*} \quad \left[\frac{\text{V}}{\text{VAr}}\right] \tag{115}$$

$$m_{pd} = \frac{X_v}{V^{*2}} \quad [\text{W}]^{-1} \tag{116}$$

$$m_{q0d} = \frac{X_v}{V^*} \quad [\text{VAr}]^{-1} \tag{117}$$

With these parameters, (106) and (107) must reformulated as in (118) and (119), effectively eliminating the need for a separate virtual impedance calculation.

$$\omega = \omega^* - m_p P - m_{pd}\frac{dP}{dt} \quad \left[\frac{\text{rad}}{\text{s}}\right] \tag{118}$$

$$V = V^* - \left(m_q + m_{q0d}\right)Q \quad [\text{V}] \tag{119}$$

A high-pass filter may be used instead of the derivative in (118), or the equation can be integrated to use the bus angle instead of the frequency. As a final note on droop control, acceptable ranges for the coefficients are given in IEEE Std. 1547-2018 [140],

along with specifications for contingency operation, and communication interface requirements. This standard will most certainly need to be followed carefully in any devices intended for use in real networks.

While operating under islanded conditions, the primary controller is responsible for enforcing energy storage balancing alongside the power sharing objective. To achieve this objective, the droop coefficients could both be adaptively changed, but this can cause stability issues as reported in [141]. Instead, it is proposed that the real power reference value should be adaptively changed instead, which allows both the power sharing and energy storage balance objectives to be achieved simultaneously. We first note that in the model, the energy storage of each energy cell E_{cell} is governed by the accumulated difference between the cell's PV generation P_{PV} and inverter output power as in (120).

$$E_{cell}(t) = E_{cell}(0) + \int_0^t \left(P_{PV}(\tau) - P_{out}(\tau)\right) d\tau \quad \text{[J]} \tag{120}$$

If this value is measured at each energy cell, and its mean across all energy cells, $\bar{E}_{cell}$, is computed at each time step by the secondary controller, then the real power reference value can be computed in the frequency domain by (121).

$$P^*(s) = G_{cP}(s)(\bar{E}_{cell} - E_{cell}) \tag{121}$$

The term G_{cP} represents a simple PI controller, which ensures that the energy cells maintain their stored energies near the average across all inverters in the network. This will improve reliability for the microgrid in the case that demand exceeds PV generation without grid support.

In grid-connected operation, energy cell setpoints for real and reactive power are commanded directly, enabling the operator to schedule DER for economic dispatch or contingency resolution purposes.

3.2.1.2 Secondary Control

The secondary tier of control is responsible for coordinating minimization of bus voltage and frequency deviation by providing reference values for primary controllers. As mentioned in the primary controller description, the bus voltage and frequency values experience drift over time due to small droop coefficients. Therefore, low-bandwidth controllers are needed to restore them to nominal by providing adaptive voltage and frequency reference values. The bus voltage reference is computed in the frequency domain by (122).

$$V^*(s) = G_{cV}(s)(V_0 - V) + V_0 \tag{122}$$

Here, the feedback error between the nominal bus voltage V_0 and the bus voltage measurement V is the input to a PI controller, G_{cV}. Similarly, the VSG rotor speed reference is provided by (123).

$$\omega^*(s) = G_{c\omega}(s)\big(\omega_0 + \omega_{syn} - \omega_m\big) + \omega_0 \tag{123}$$

Here we use another PI controller $G_{c\omega}$ to minimize the error between the system frequency ω_0 and the frequency at the terminals of the inverter. The term ω_{syn} is the output of the tertiary controller, which is used to synchronize the voltage angles at the PCC between the microgrid and the bulk power system.

In the initial implementation in [72], the reference values in (122) and (123) were generated based on measurements at a single, arbitrary inverter bus and relayed to all primary controllers. This strategy is simple and effective but does lead to some

inaccuracy in reference tracking. To address this concern, the controller was modified such that its measurements and calculations were performed independently for each energy cell, improving reference tracking across the microgrid. This is a more complicated (and less centralized) control strategy but it reaps benefits from improved voltage reference following and an increase in reliability should communication be interrupted between the energy cells and the central controller; only the average stored energy computation would be affected in such a case.

One notable tradeoff of this amendment is observed in the bandwidth of the PI controller in (121), previously in the hundreds of microradians per second range. Upon implementation of the new controller, this bandwidth was too slow to maintain energy storage balance as the power produced by each energy cell adapted to the dynamic state of the network and had to be increased to the milliradians per second range.

3.2.1.3 Tertiary Control

The tertiary controller is responsible for maintaining synchronism at the PCC between the microgrid and the bulk power system. This is achieved by taking measurements of the voltage angles at the grid side and microgrid side of the PCC breaker, denoted by θ_g and θ_{PCC}, respectively. The ω_{syn} term in (123) is calculated in the frequency domain by (124).

$$\omega_{syn}(s) = G_{c\omega_{syn}}(s)\left(\theta_g - \theta_{PCC}\right) \tag{124}$$

Here, we have used PI controller $G_{c\omega_{syn}}$ to minimize the error between the measured angles and compute the resulting frequency deviation. This controller is ideally sited at the PCC substation, and communicates with the secondary controller to ensure successful

grid-connected operation of the microgrid or assist in synchronization when reconnecting to the grid after a contingency or other islanding event.

3.2.2 Testbed Description

With the mathematical model of the control strategy established, we will introduce the testbed configuration and simulation models used to implement and test the control strategy, inclusive of the microgrid network model, energy cell model, and the various controller models.

The testbed consists of an OPAL-RT real-time simulator, a remote computer capable of running the remote-control software, and a digital controller board programmed to act as the primary controller for an energy cell. Optionally, the remote-control software can also be modified to communicate with commercial smart inverters, making this a true multi-platform real-time simulation testbed.

The network is modeled in the phasor domain to reduce the computational burden incurred by typical EMT or TS simulations. However, this method does not capture transients between steady-state conditions, so for accuracy and speed, a hybrid EMT-TS simulation, like those described in [101] and [102] is implemented. The OPAL-RT is capable of real-time simulation using phasor domain TS simulation via its ePHASORsim component, and EMT simulation via its eMEGAsim component to make a more accurate model for approximately the same computational burden, while retaining the ability to interact with the system realistically during simulation.

3.2.3 Microgrid Model

The IEEE 123 Node Test Feeder [142] was used as the microgrid network model, as its size and topology allow for interesting events and interactions, while remaining

relatively easy to take in. The voltage regulators described in the reference are omitted from the model implementation since the energy cells provide that functionality. Two primary configurations were used for testing, one with three energy cells, and the other with ten energy cells. Their locations, along with the location of the PCC are as shown in Fig. 18.

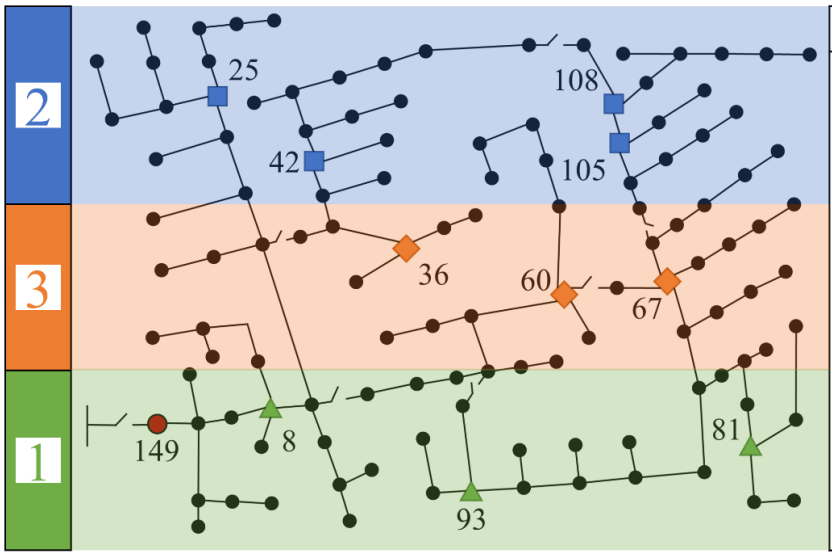

Bus	Feature	Zone
8	EC1	1
25	EC2	2
36	EC4	3
42	EC5	2
60	EC6	3
67	EC3	3
81	EC7	1
93	EC8	1
105	EC9	2
108	EC10	2
149	PCC	-

Fig. 18. IEEE 123 Node Test Feeder topology with PCC location, PV generation zones, and energy cell (EC) locations highlighted.

3.2.3.1 OPAL-RT Model

The model was constructed in Simulink with the help of OPAL-RT's RT-LAB blockset, and compiled and coordinated using RT-LAB. Initially, the model featured one console subsystem for user control and monitoring, and one for the model; however, during its expansion the network-related and energy cell-related model components were separated into two subsystems, each of which was allotted a single processor core during simulation in the OPAL-RT. While this does introduce some nontrivial overhead due to cross-core synchronization, the net effect is positive considering the effective increase in simulation time step budget for each subsystem. The simplified energy cell subsystem

block diagram is shown in Fig. 19, while the simplified network subsystem block diagram is shown in Fig. 20.

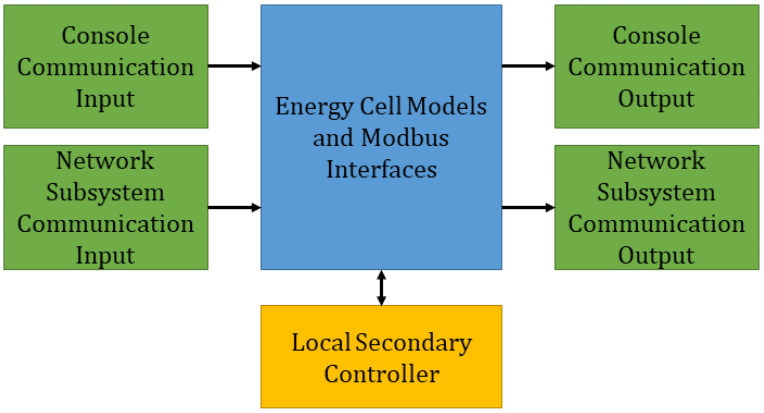

Fig. 19. Simplified energy cell subsystem block diagram.

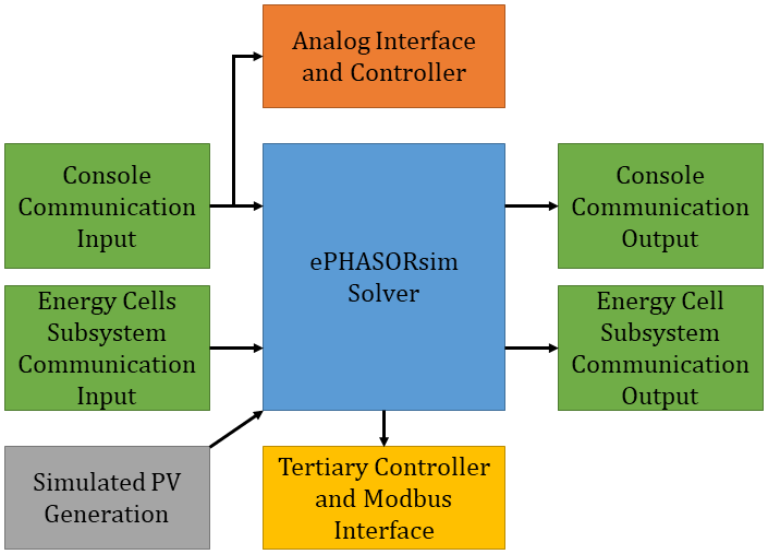

Fig. 20. Simplified network subsystem block diagram.

The console subsystem allows the user to interact with the model in real time, affording access to signal plotting and control inputs. It has also been configured to show the Modbus register values in real-time and have consolidated all data writing blocks there. This is valuable because the console runs on the host machine (i.e. the computer

used to interface with the OPAL-RT), so plotting and data writes do not have to compete with computation for processor time during simulations.

The primary components of the network model subsystem are the ePHASORsim Solver block, the subsystem communication interfaces, the simulated PV generation architecture, the analog controller interface and supporting simulation controller, and the tertiary controller and its Modbus communication interface.

The ePHASORsim Solver block performs the phasor domain TS computations, and accepts as inputs the PCC breaker control signal, the utility grid model phase voltages, switching signals for a subset of the system load, and phase currents from the energy cells. It outputs the bus voltages needed by the energy cell models and the analog controller interface in phasor form. As is the case with many network solvers, the ePHASORsim block can be supported by a backing spreadsheet detailing the network topology.

The subsystem communication interfaces negotiate the transfer of signals between the various subsystems. Notably, there are OPAL-RT-specific blocks associated with synchronizing the input from the other subsystems, necessary to ensure deterministic operation of the simulation.

PV generation is simulated by reading three PV curves obtained from [143] from file and scaling them to the appropriate power level for the simulation using a factor of 1000. The data in these files spans 24 hours, but a timescale compression of 100 is used to reduce simulation time to 14.4 minutes.

The analog controller interface scales and routes the signals measured from an attached interface board connected to a digital controller board for CHIL. The controller

associated with this interface implements a binary file specific to the FPGA device used; in this case, the VC707 FPGA is mounted in the OPAL-RT rack and used to include the CHIL simulation of a primary controller.

As discussed in Section 3.2.1, a tertiary controller is included in the network model, which requires the bus voltage angles on either side of the PCC. Since the voltages output by the ePHASORsim block are in phasor form, it is trivial to extract the voltage angle at any given bus. In a real-world application, a PLL would be necessary to provide similar functionality for the tertiary controller.

3.2.3.2 Timing Considerations

Real-time simulation relies on a fixed time step during which all computations must be completed; failure to complete any computation during the time step produces an overrun, which delays computation of the next time step. For small, intermittent overruns the net effect is negligible, but when overruns become larger or more frequent, this can cause the simulation to stall as the delay accumulates. To avoid overruns, the step size needs to be selected based on careful consideration of the simulation at hand. The model uses a time step of $T_s = 100\ \mu s$, increased fourfold from the initial design value. This increase was necessary to accommodate both the synchronization overhead of multicore computation, as well as the increased burden of additional energy cell buses in the ten-inverter case. The three-energy cell test cases have maximum time steps of approximately 45 µs, but the ten-cell case operates at a maximum time step of 57 µs; 100 µs was chosen to make it an even integer multiple of the original time step, which simplified parameter tuning. As many blocks as possible use a matching sampling time within the simulation,

and wherever this was not possible, rate transition blocks were used as needed to coordinate the timing.

Several of the generated signals in this subsystem, most notably the PV generation, which is read from a file, do not pass through any blocks that produce a state. This is untenable for cross-core synchronization, as one subsystem would be left waiting on the other to complete computation indefinitely. To solve this problem, a transport delay block with a delay greater than or equal to the sampling time of the simulation time step must be inserted between the generated signal and the communication interface, as discussed in [144].

3.2.4 Energy Cell Model

Within the Energy Cell Models and Modbus Interfaces subsystem, it is necessary to extract phasor form values for use in the network simulation. It is possible to use the fast Fourier transform (FFT) as in [101] or curve fitting as in [102] to extract these values. However, a dynamic phasor modeling method has been chosen instead, described by [103], [104], and [105] to complement the hybrid simulation. This method neatly avoids the computational overhead caused by FFT or curve fitting methods, and allows a higher step size, since the frequency spectrum is centered at DC, as shown in [105].

To demonstrate the application of the dynamic phasor model, we can use the grid filter featured in Fig. 17. Its time domain equation is given by (125).

$$\frac{di}{dt} = -\frac{R_f}{L_f} i + \frac{1}{L_f}(e - v) \tag{125}$$

From this, we can extract the real and imaginary parts of the phasors in rectangular form as shown in (126) where we have used subscript d for the real part, and subscript q

for the imaginary part, enabling these models to interact with the network via magnitude and angle computation.

$$\begin{bmatrix} \dot{\imath}_d \\ \dot{\imath}_q \end{bmatrix} = \begin{bmatrix} -\frac{R_f}{L_f} & \omega_0 \\ -\omega_0 & -\frac{R_f}{L_f} \end{bmatrix} \begin{bmatrix} i_d \\ i_q \end{bmatrix} + \begin{bmatrix} \frac{1}{L_f} & 0 \\ 0 & \frac{1}{L_f} \end{bmatrix} \begin{bmatrix} e_d - v_d \\ e_q - v_q \end{bmatrix} \tag{126}$$

3.2.4.1 OPAL-RT Model

The Energy Cell Models and Modbus Interfaces subsystem contains the computation and transformation blocks necessary to provide a phasor domain representation, as well as the primary controller, and the supporting controls needed for selecting the appropriate reference commands based on the grid connection status. In Fig. 19, there is little functional difference from similar components described in the discussion of the network model. Each energy cell model features its own Modbus communication interface and the necessary scaling and routing architecture to enable it. Within, an RT-LAB Modbus block is backed by an Excel spreadsheet detailing the various input and output register addresses and communication details.

As reported in [76], both the droop coefficients and the output impedance affect system stability. It was necessary to simulate the system iteratively while adapting the values of the droop coefficients during design to produce a stable system. The output impedance of the energy cells is determined by the grid filter in Fig. 17, which is typically designed for harmonic compensation; here a virtual impedance control strategy has been implemented as described in [145] by placing a static inductive impedance in series accordingly. The power outputs of the inverters are brought to the specified load level of the network by scaling their currents by a factor of 10, and each energy cell is

connected to its network bus by an ideal transformer implemented as a gain of 4160/480 in the simulation. The resulting design specifications are given in Table IV.

TABLE IV
ENERGY CELL SPECIFICATIONS

Parameter	Value
Power Rating, S_{rated}	$300\ \text{kVA}$
Nominal Voltage, V_0	$480\ \text{V}_{\text{L-L}}$
Droop Coefficient, m_p	$5\ (\text{mrad/s})/\text{kW}$
Droop Coefficient, m_{q0}	$50\ \text{mV/kVAr}$
Output Impedance, Z_0	$0.1 + j0.8\ \Omega$
Virtual Inertia, J	$5 \cdot S_{rated}/(2\pi 60)^2$
Nominal Storage Level, E_0	$S_{rated} \cdot 10\ \text{min}$

3.2.4.2 Timing Considerations

While most blocks in this subsystem are sampled with the same period as the simulation time step, there are two notable exceptions. The sampling time of the Modbus block is the same as the time step for the simulation, which simplifies synchronization of signals within the simulation itself; however, in the backing Excel spreadsheet, the polling period (or sample time) of the Modbus communication is set to 10 ms. This is an integer divisor of the secondary controller sampling period of 200 ms, designed to ensure that data within the simulation is made available as quickly as possible without putting additional computational burden on this portion of the simulation.

In the simulated secondary controller, zero order hold blocks are used to emulate the secondary controller delay, so that both the input to and output from the PI controllers described previously are held for 200 ms.

3.2.5 Controller Modeling

Here we will describe the configuration and models for individual controllers and discuss their implementations.

3.2.5.1 Local Control

In this work, we refer to a secondary controller as "local" or "remote" from the perspective of the energy cells for which it is responsible. The local controller is implemented in Simulink directly alongside the model and was the first to be designed; it is therefore most appropriate to explain the controller design here.

During the design of the controller models, a first-order approximation to the plant models for voltage, frequency, and power were made based on the response of each to step reference commands. Plant models are represented by their dominant first order response and take the form of (127) with gain g and pole p. The exception to this is the grid frequency synchronization controller $G_{c\omega_{syn}}$, which contributes to the reference value for the closed-loop system comprised of $G_{\omega^*\to\omega}$ and $G_{c\omega}$. PI controllers are designed for a desired open-loop bandwidth and phase margin and take the form of (128). In (127) and (128), X is a placeholder for the value being controlled, and is one of P, V, ω, or ω_{syn}.

$$G_{X^*\to X}(s) = g/(s+p) \tag{127}$$

$$G_{cX}(s) = K_p + K_i/s \tag{128}$$

Reactive power reference tracking is provided by a simple integral controller with a gain of $K_i = 0.001$. While a phase margin of $60°$ is usually sufficient, since a communication delay is involved, an additional $30°$ was added to the desired phase margin in the case of both voltage and frequency controllers. Controller block diagrams are illustrated by Fig. 21, and step responses for each plant are shown in Fig. 22. Table V gives the parameters for each plant model and controller, as well as the bandwidth ω_g and phase margin ϕ_g of the open-loop transfer function representing their series combination.

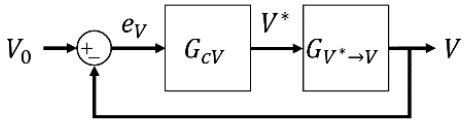

a

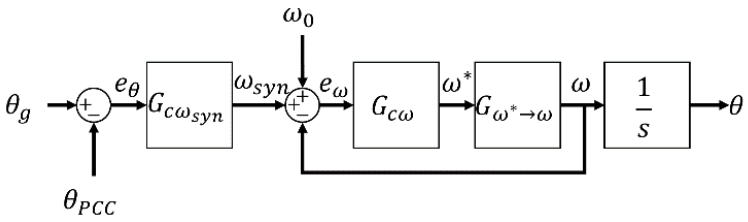

b

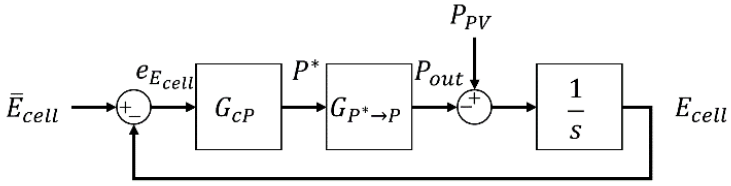

c

Fig. 21. (a) voltage control loop, (b) frequency control loop, and (c) power and energy control loop.

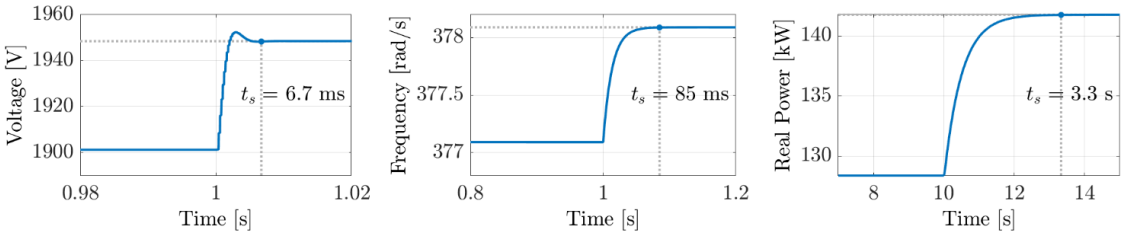

a b c

Fig. 22. Step responses and settling times of uncontrolled system for (a) voltage, (b) frequency, and (c) real power output.

TABLE V
PLANT, CONTROLLER, AND OPEN-LOOP PARAMETERS

Plant	k	p	Controller	K_p	K_i	Open-Loop	ω_g [rad/s]	ϕ_g [°]
$G_{P^*\to P}$	1	1.5	G_{cP}	0.039	0.004396	L_P	0.003	91.4
$G_{V^*\to V}$	415	750	G_{cV}	0.0047	3.6	L_V	2	90
$G_{\omega^*\to\omega}$	58.8	58.8	$G_{c\omega}$	0.034	2	L_ω	2	90
$L_\omega/(1+L_\omega)$	–	–	$G_{c\omega_{syn}}$	0.176	0.016	$L_{\omega_{syn}}$	0.0163	99.7

3.2.5.2 Remote Control

The remote controller is implemented in software via a continuous loop with a period of 200 ms. Since we are receiving measurements and sending commands in a discrete fashion, a typical Tustin transformation was used to convert the controllers' continuous transfer functions from the s-domain to the z-domain. Rearranging the resulting equation in terms of error e and control output u, we arrive at a discrete time domain difference equation for sample k, like that in (129).

$$u[k] = u[k-1] + \left(K_p + \frac{T_s}{2}K_i\right)(e[k] - e[k-1]) \tag{129}$$

This lends itself very well to such an implementation, as it requires only a handful of constants and a simple buffer of one sample for the output and error of the variable being controlled.

Since the Modbus protocol standard [146] dictates only that register values be 16-bit integers and does not mandate that they be either signed or unsigned, it is up to the implementer to choose. The OPAL-RT Modbus block uses unsigned 16-bit integers (UINT16) for its registers, and thus, the remote-control software does as well. For accurate measurement and commands to be exchanged, values must be separated from their signs, and scaled to within the UINT16 range of 0–65535. For signed values, the

convention used is to extract the sign of the value as ± 1, then add one to it, producing a zero for negative numbers and a two for positive numbers.

Three sets of registers are used for communication: Input registers for measurements, and both read and write holding registers for commands. Table VI gives a complete list of the registers and scaling values used in the model. In communication between the OPAL-RT and the remote computer, energy quantities are presented in MJ, rather than kWh. The quantity $status$ is a binary switch where one represents remote control, and zero represents local control, and the quantity $mode$ is a binary switch where one represents islanded mode, and zero represents grid-connected mode. The holding registers (block 40001–49999) are arranged with the write addresses for remote control in the first eight, and the read addresses for local control in the next eight.

TABLE VI
MODBUS REGISTER MAP AND SCALING FACTORS

Quantity	Register	Scaling Factor	Quantity	Register	Scaling Factor
$\lvert V_a \rvert$	30001	1	P^*	40002	0.001
$1 + sgn(\angle V_a)$	30002	1	Q^*	40003	0.001
$\lvert \angle V_a \rvert$	30003	100	$sgn(\delta_\omega) + 1$	40004	1
$\lvert I_a \rvert$	30004	1	$\lvert \delta_\omega \rvert$	40005	1000
$1 + sgn(\angle I_a)$	30005	1	$sgn(\delta_E) + 1$	40006	1
$\lvert \angle I_a \rvert$	30006	100	$\lvert \delta_E \rvert$	40007	1
$1 + sgn(P)$	30007	1	$\bar{E}_{cell}$	40008	10
$\lvert P \rvert$	30008	0.001	$mode$	40009	1
$1 + sgn(Q)$	30009	1	P^*	40010	0.001
$\lvert Q \rvert$	30010	0.001	Q^*	40011	0.001
$1 + sgn(\omega_0 - \omega)$	30011	1	$sgn(\delta_\omega) + 1$	40012	1
$\lvert \omega_0 - \omega \rvert$	30012	1000	$\lvert \delta_\omega \rvert$	40013	1000
P_{PV}	30013	0.001	$sgn(\delta_E) + 1$	40014	1
E_{cell}	30014	10	$\lvert \delta_E \rvert$	40015	1
$status$	40001	1	$\bar{E}_{cell}$	40016	10

3.2.6 Microgrid Model with Complete GFI Model

Including a more detailed inverter model requires amendments; a brief description of the changes to the microgrid network model from previous sections will be given here along with a summary of operating conditions. The microgrid is operated only in islanded mode, thus only two tiers of the hierarchical control strategy are active, with the tertiary controller inactive as grid frequency synchronization is unnecessary. The voltage and frequency are measured at the energy cells' buses independently, rather than using measurements from a single energy cell to drive the secondary controllers. The inverter model from [108] replaces the relatively simple model in use previously. To accommodate this replacement, the filter model used to generate the output current via the inverter terminal voltage reference generated by virtual impedance control and the bus voltage resulting from the dynamic power flow solution was modified to include the capacitance C_f and damping resistance R_d present in the new inverter model. However,

this modification is non-trivial, since any AC impedance time constant τ must be greater than the simulation time step T_s for convergence. The time step must be sufficiently large to allow completion of all computations in the simulation, so this bounds the RC time constant from below as in (130).

$$T_s < \tau = R_d C_f \quad [\text{s}] \tag{130}$$

Since the filter is not typically designed with simulation in mind, this may not be the case. An alternative approach to filter redesign is to use a constant frequency domain impedance term $Z(s)$, evaluated at the system frequency ω_s, as in (131).

$$Z(j\omega_s) = R_d + \frac{1}{j\omega_s C_f} \quad [\Omega] \tag{131}$$

This approach trades accuracy at harmonic frequencies for convergence in the case where a specific filter configuration is required. Given IEEE 519 [147] specifications, at the bus voltage used in this network of 4160 V, voltage distortion must be less than 3% (~125 V) for individual harmonics, and less than 5% (~208 V) overall. Since we are using the filter model to determine the current produced by the energy cells, it is important to be aware of the error this approximation incurs. Assuming the worst case (4.99% THD_V, with all odd harmonics between 3 and 49 present, distributed according to the $1/h$ rule), the total current distortion is 0.2% of the output current for $R_d = 1.96\ \Omega$ and $C_f = 10\ \mu\text{F}$. Since we are not modeling harmonic distortion, this represents the error in the current computation due to this impedance approximation, which is acceptably small.

3.3 Converters

Here we will describe the various converters used to investigate transformers and microgrid applications, including the asymmetric half-bridge DC-DC stage of a microinverter, the DAB, the GFI, which is designated as such by its control method, and finally the SST design, intended for use in the microgrid testbed described previously.

3.3.1 Asymmetric Half-Bridge DC-DC Converter

The isolated half-bridge DC-DC converter is originally a buck-derived topology. In this application, it is employed in a boost configuration. It is nearly identical in operation to the full-bridge converter, but one switching pole pair has been replaced with capacitors, which ideally hold half of the input voltage each. This yields the voltage transfer function in equation (132) [4], [5].

$$\frac{V_o}{V_{in}} = \frac{1}{2} D \frac{N_2}{N_1} \tag{132}$$

This assumes a symmetric duty cycle; D is applied to both switches, referred to the rectified voltage on the secondary side of the circuit, with a dead time between switch activations to ensure that the pole pair is not shorted across its input, and to allow commutation time between inductance and capacitance through the diodes on the output side. Since the capacitors hold the voltage applied to the primary winding of the transformer at half the input voltage, the turns ratio amplifies this voltage instead, and the output voltage is as given in (132).

The asymmetric duty cycle version of this converter instead applies D to one switch, and $1 - D$ to the other, while retaining the protective dead time. This yields the voltage transfer function in equation (133) [85], [86].

$$\frac{V_o}{V_{in}} = 2D(1-D)\frac{N_2}{N_1} \tag{133}$$

This allows switching loss to be greatly reduced, as the converter can now achieve ZVS. ZVS relies on bringing the voltage across a switch to zero, ideally, prior to turning it on or off, such that the loss incurred while switching is minimized. This is achieved by draining charge from the parasitic switch capacitance via some commutating current. Draining the charge from these parasitic elements allows the switch voltage to be reduced such that ZVS can occur, but clearly there is a minimum current necessary to do so within a given time. This boundary for the asymmetric half-bridge is given by (134) [85], [86]:

$$I_0 = \frac{N_1^2 V_o}{4N_2^2 D^2}\sqrt{\frac{C_e}{L_c}} = \frac{1}{2}\frac{N_1}{N_2}(I_{S1} + I_{S2}) \quad \text{[A]} \tag{134}$$

In (134), C_e is the parallel combination of the switch capacitances, and L_c is the commutating inductance, typically the leakage inductance of the transformer referred to the primary side if no additional inductance is required to achieve ZVS. Designing the transformer to achieve ZVS is then a matter of designing the leakage inductance and turns ratio to satisfy (134). Under the assumption that the current derivative in the primary winding is a constant during the dead time, we can use the inductor voltage equation to find the necessary inductance for dead time, Δ, and starting current, I_1, as given by equation (135). A derivation of this equation is provided in Appendix F. Fig. 23 shows the relationship between the dead time and resulting inductance over a range of common values.

$$L_c^2 + \left(\frac{2N_1 V_{L_c}}{N_2 I_1}\Delta - \frac{N_1^4 C_e V_o^2}{16N_2^4 D^4 I_1^2}\right)L_c + \frac{N_1^2 V_{L_c}^2}{N_2^2 I_1^2}\Delta^2 = 0 \tag{135}$$

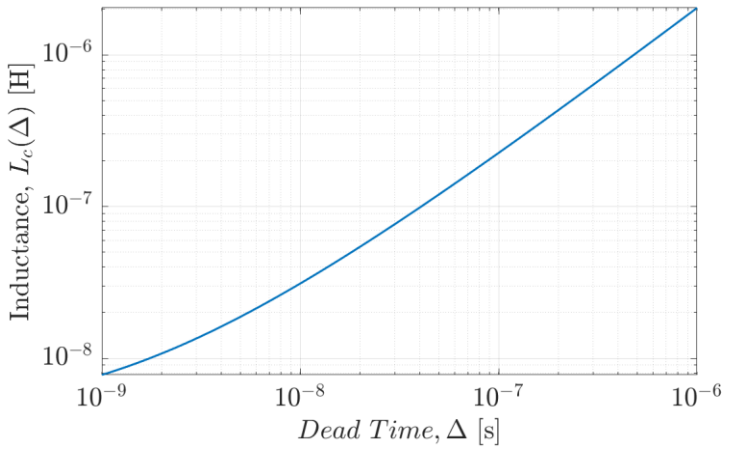

Fig. 23. Necessary commutating inductance for given dead time in the converter design described by Table I.

3.3.2 Dual Active Bridge Converter

The DAB is typically depicted in a simple form for analytical purposes, wherein the transformer is represented by an inductor representative of the total leakage inductance, with a 1:1 turns ratio, and with most other nonidealities neglected. In some cases, additional nonideal elements are included. For example, in [97] the winding resistance is included, in [93] the output capacitor's equivalent series resistance (ESR) is included, while in [96] winding resistance, and the magnetizing branch are each included, along with ESR of the input and output capacitors. Since such models already exist in published literature, the model used here goes further and simplifies less in order to truly examine the transformer states in a way not yet published, and which is in line with the transformer state space model given in Section 3.1.7.

The schematic of the DAB as modeled is shown in Fig. 24.

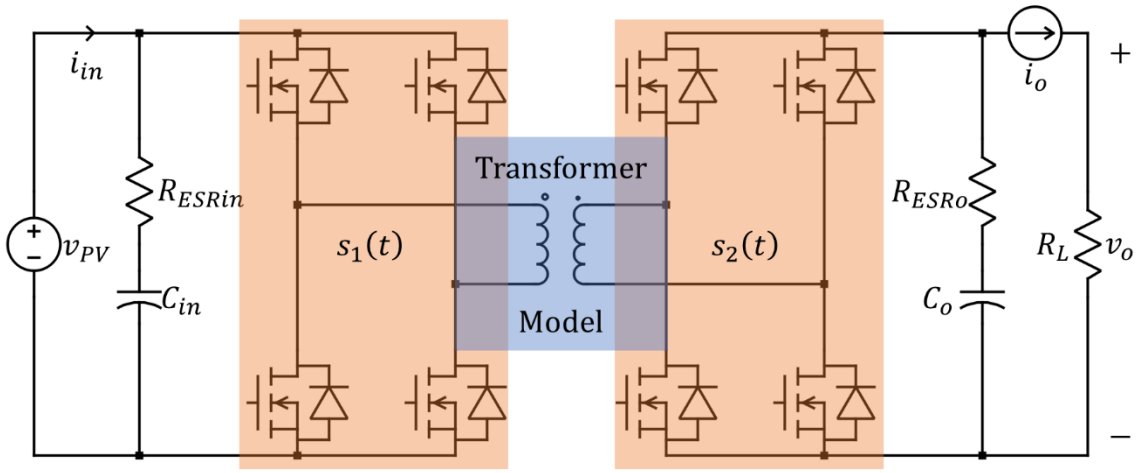

Fig. 24. Schematic of dual active bridge converter showing inputs and outputs, transformer model, switching function regions, input and output impedances, and load resistor.

The converter is designed to process 600 kW, which is a concern that must be addressed. Since the throughput power of the included transformer is the sum of the apparent power in each winding, the transformer is to handle over a megawatt of power, which is quite the tall order. This power level is atypical for high-frequency transformers, and rather ambitious even for medium-frequency transformers often seen in higher power SST designs. In order to handle this throughput power, a multi-winding transformer is designed, with five parallel primary windings and five parallel secondary windings. Each primary winding is excited by the same voltage source, and each carries one fifth of the current, reducing the apparent power in each winding proportionally. They have also been interleaved to reduce the proximity effect factor to less than one, significantly reducing the overall loss. In order to handle the high magnetic field intensity that these windings will produce, E cores have been stacked to share the burden so that the flux density is within acceptable levels. Still, an active thermal management solution will almost certainly be required in the final design. Justification for these choices can be

found in Section 3.1, and numerical values resulting from the design are provided in Section 4.3.3.

This DAB is part of an array of five such converters used to form the DC-DC stage of a novel modular SST topology to be used in the microgrid described in Section 3.2. The parallelization of the parasitic elements in the transformer windings represents one of the only significant idealizations of the model, with the other being that the output capacitances across the MOSFETs used for each bridge are not included. The first choice was made because it reduces the number of states significantly, and because the windings are wound parallel on the same core, so their operation is intrinsically linked. The second choice was made because the output voltage is approximately equal to the reflected input voltage, and so ZVS should always occur as per [128], even when using a simple phase shift control scheme.

The schematic of the transformer and its parallelized version are shown in Fig. 25.

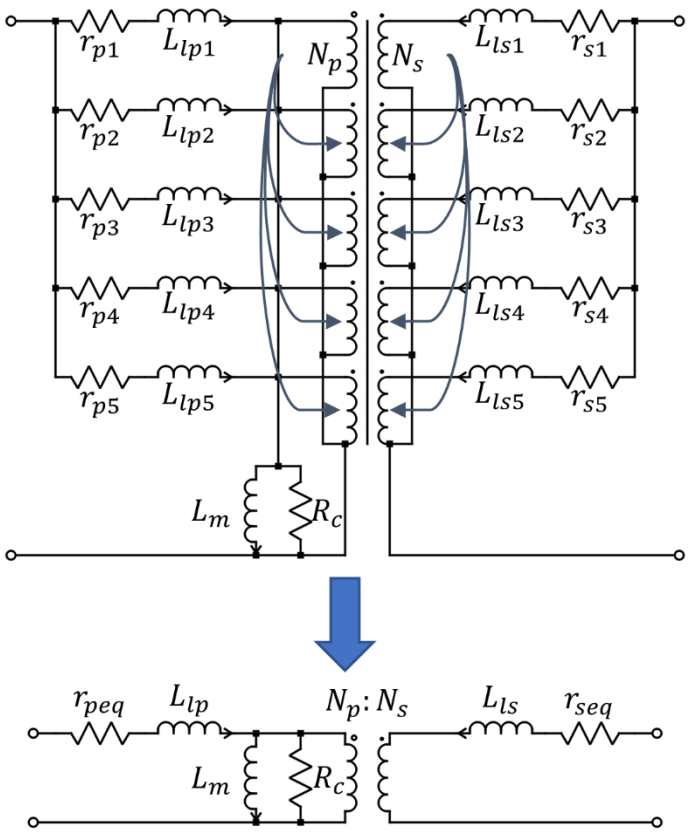

Fig. 25. Schematic of five-winding transformer and parallelized version demonstrating terminal associations and current directions.

The resulting transformer impedance, inclusive of MOSFET on-resistance, is given by (136).

$$z_T = r_{peq} + jx_p - \frac{R_c x_m \left(x_s' - j r_{seq}'\right)}{R_c\left(r_{seq}' - x_s'\right) + j\left(r_{seq}' + R_c - x_s'\right)x_m} \quad [\Omega] \qquad (136)$$

In (136), r_{peq} is the primary winding resistance in series with the on-resistance of both conducting switches in the input bridge ($2r_{on}$), x_p is the primary leakage reactance, R_c is the equivalent core loss resistance, x_m is the magnetizing reactance, x_s' is the referred secondary leakage reactance, and r_{seq}' is the referred secondary winding resistance in series with the on-resistance of both conducting switches in the output

bridge ($2r'_{on}$). For the sake of completeness, it should be noted that these reactances are computed as the product of the operating frequency and the inductance, e.g. $x = \omega_s L$.

Typically, the first step in control design for the DAB is to compute the output power in terms of the control variable, which for a single phase shift can be computed by (137).

$$P_{DAB} = \frac{\frac{N_2}{N_1} V_{in} V_o}{\omega_s L_s} \phi \left(1 - \frac{\phi}{\pi}\right) \quad [\text{W}] \tag{137}$$

In this case, since many nonidealities not typically included in the model are used, this formulation is not accurate enough to determine the correct phase shift angle at which the bridges must operate, and using it resulted in poor performance. Ultimately, (137) is simply an idealization of the power flow equation between the nodes in a two-node network given by (138).

$$P_{ij} = |V_i||V_j|\left(\Re\{Y_{ij}\}\cos(\delta_{ij}) + \Im\{Y_{ij}\}\sin(\delta_{ij})\right) \quad [\text{W}] \tag{138}$$

The formulation in (137) computes a quantity that is typically referred to as the "DC power flow" at one of these nodes, expressed as $P_i = |V_i||V_j|(B_{ij}\delta_{ij})$, where B_{ij} is the imaginary part of the admittance matrix connecting the two nodes, and $\delta_{ij} = \theta_i - \theta_j$ is the difference in phase angle between the two nodes. While it is referred to as a DC quantity, this is only because it takes the form of a resistive power flow in a DC circuit; in reality, this power flow occurs at the fundamental frequency. In the case of the DAB, this frequency is taken as the switching frequency, the angle difference represents the angle contributed by the series and shunt elements between the nodes, and the power flow itself is the time-averaged value over each switching cycle of the converter.

Thus, to compute the phase angle, we need only reformulate (136) as the admittance, including the effect of the capacitors and their ESR (e.g. $z = R_{ESR} - jx_C$) as in (139),

and apply (138). Including the capacitive branches ensures that their contribution to the phase angle is considered when using DC values for the voltages at input and output, as they introduce a phase shift due to the current they draw that is not otherwise captured.

$$Y_{DAB} = y_{in} + \frac{1}{(z_T + z_o)^*} \quad [\text{S}] \tag{139}$$

With a steady DC input voltage, the term $y_{in} = 1 \,/\, \left(R_{ESRin} - jx_{C_{in}}\right)^*$ can be neglected, because no current is drawn by the input capacitor since its voltage is a DC value equal to the source voltage. However, since it is possible that this model may be applied to other situations where the input voltage is time-varying, it is included here for completeness. Per convention, the superscript asterisk $(\cdot)^*$ denotes the complex conjugate. The resulting equation is given by (140), where the value of δ_{DAB} is given by (141).

$$P_{DAB} = \frac{N_2}{N_1} V_{in} V_o (\Re\{Y_{DAB}\} \cos(\delta_{DAB}) + \Im\{Y_{DAB}\} \sin(\delta_{DAB})) \phi \left(1 - \frac{\phi}{\pi}\right) \quad [\text{W}] \tag{140}$$

$$\delta_{DAB} = \tan^{-1}\left(\frac{\Im\{Y_{DAB}\}}{\Re\{Y_{DAB}\}}\right) \quad [\text{rad}] \tag{141}$$

Conventional state space modeling for switching converters is not possible because they assume different topologies as the switches connect different portions of the network together. State space averaging is typically employed, wherein these discrete states are weighted by the nominal duty ratio and linearized about that operating point. In this case, the approach still falls short, as the transformer states have no DC steady-state average values, and the impact they have on the system is lost. This necessitates the use of generalized state space averaging, wherein some finite truncation of the Fourier series of the state waveforms is used to approximate the behavior in an average sense. Sources in

literature typically provide a model with the first harmonic approximation (FHA), where only the switching frequency average values and the DC average values are used to represent the quantities of interest. However, when investigating the operation of the basic model in PLECS, very strong second harmonic content was observed in the input current and output voltage, which were selected as outputs of the state space model. It was for this reason that the second harmonic approximation (SHA) was used instead. The five states that exist in the full model are expanded to 25 to accommodate the DC, fundamental real and imaginary, and second harmonic real and imaginary average values for each. Similarly, the two outputs are expanded to ten to accommodate their Fourier coefficients. The input voltage and output current, selected as the two inputs to the system, are assumed to be DC or much slower than the switching frequency, so they are not expanded. The state space model for this converter is provided in the system of equations in (142), and its complete derivation is given in Appendix G.

$$
\begin{gathered}
\begin{bmatrix}\dot{\boldsymbol{x}}\\ \boldsymbol{y}\end{bmatrix} = \left[\begin{array}{c|c} M^{-1}A & M^{-1}B \\ \hline C & D \end{array}\right]\begin{bmatrix}\boldsymbol{x}\\ \boldsymbol{u}\end{bmatrix} \\
\boldsymbol{x} = [\boldsymbol{x}_0^T \quad \boldsymbol{x}_{1R}^T \quad \boldsymbol{x}_{1I}^T \quad \boldsymbol{x}_{2R}^T \quad \boldsymbol{x}_{2I}^T]^T \\
\boldsymbol{y} = [\boldsymbol{y}_0^T \quad \boldsymbol{y}_{1R}^T \quad \boldsymbol{y}_{1I}^T \quad \boldsymbol{y}_{2R}^T \quad \boldsymbol{y}_{2I}^T]^T \\
\boldsymbol{u} = [v_{PV} \quad i_o]^T \\
A = \begin{bmatrix} A_{00} & 2A_{sR} & 2A_{sI} & 0 & 0 \\ A_{sR} & A_{00} & M_i\omega_s & A_{sR} & A_{sI} \\ A_{sI} & -M_i\omega_s & A_{00} & -A_{sI} & A_{sR} \\ 0 & A_{sR} & -A_{sI} & A_{00} & 2M_i\omega_s \\ 0 & A_{sI} & A_{sR} & -2M_i\omega_s & A_{00} \end{bmatrix} \quad B = \begin{bmatrix} B_0 \\ B_{1R} \\ B_{1I} \\ 0 \\ 0 \end{bmatrix} \\
C = \begin{bmatrix} C_{00} & 2C_{sR} & 2C_{sI} & 0 & 0 \\ C_{sR} & C_{00} & 0 & C_{sR} & C_{sI} \\ C_{sI} & 0 & C_{00} & -C_{sI} & C_{sR} \\ 0 & C_{sR} & -C_{sI} & C_{00} & 0 \\ 0 & C_{sI} & C_{sR} & 0 & C_{00} \end{bmatrix} \quad D = \begin{bmatrix} D_0 \\ 0 \\ 0 \\ 0 \\ 0 \end{bmatrix} \\
M = \bigoplus_{i=1}^{5} M_i
\end{gathered}
\tag{142}
$$

The equations in (142) define a 25-state, 2-input, 10-output system, and are composed of matrices given by (143) – (153).

$$A_{00} = \begin{bmatrix} -\frac{1}{R_{ESRin}} & 0 & 0 & 0 & 0 \\ 0 & -(r_{peq} + R_c) & R_c & -\frac{N_2}{N_1}R_c & 0 \\ 0 & R_c & -R_c & \frac{N_2}{N_1}R_c & 0 \\ 0 & -\frac{N_2}{N_1}R_c & \frac{N_2}{N_1}R_c & -\left(r_{seq} + \frac{N_2^2}{N_1^2}R_c + R_{ESRo}\right) & 0 \\ 0 & 0 & 0 & 0 & -\frac{1}{2R_{ESRo}} \end{bmatrix} \quad (143)$$

$$A_{sR} = \begin{bmatrix} 0 & 0 & 0 & 0 & 0 \\ 0 & 0 & 0 & 0 & 0 \\ 0 & 0 & 0 & 0 & 0 \\ 0 & 0 & 0 & 0 & s_{2R} \\ 0 & 0 & 0 & -s_{2R} & 0 \end{bmatrix} \quad (144)$$

$$A_{sI} = \begin{bmatrix} 0 & 0 & 0 & 0 & 0 \\ 0 & 0 & 0 & 0 & 0 \\ 0 & 0 & 0 & 0 & 0 \\ 0 & 0 & 0 & 0 & s_{2I} \\ 0 & 0 & 0 & -s_{2I} & 0 \end{bmatrix} \quad (145)$$

$$B_0 = \begin{bmatrix} 1/R_{ESRin} & 0 \\ 0 & 0 \\ 0 & 0 \\ 0 & 0 \\ 0 & \frac{R_L - R_{ESRo}}{2R_{ESRo}} \end{bmatrix} \quad (146)$$

$$B_{1R} = \begin{bmatrix} 0 & 0 \\ 0 & 0 \\ 0 & 0 \\ 0 & 0 \\ 0 & \frac{R_L - R_{ESRo}}{2}s_{2R} \end{bmatrix} \quad (147)$$

$$B_{1I} = \begin{bmatrix} 0 & 0 \\ s_{1I} & 0 \\ 0 & 0 \\ 0 & 0 \\ 0 & \frac{R_L - R_{ESRo}}{2} s_{2I} \end{bmatrix} \tag{148}$$

$$C_{00} = \begin{bmatrix} -\frac{1}{R_{ESRin}} & 0 & 0 & 0 & 0 \\ 0 & 0 & 0 & 0 & \frac{1}{2} \end{bmatrix} \tag{149}$$

$$C_{sR} = \begin{bmatrix} 0 & 0 & 0 & 0 & 0 \\ 0 & 0 & 0 & -\frac{R_{ESRo} s_{2R}}{2} & 0 \end{bmatrix} \tag{150}$$

$$C_{sI} = \begin{bmatrix} 0 & s_{1I} & 0 & 0 & 0 \\ 0 & 0 & 0 & -\frac{R_{ESRo} s_{2I}}{2} & 0 \end{bmatrix} \tag{151}$$

$$D_0 = \begin{bmatrix} \frac{1}{R_{ESRin}} & 0 \\ 0 & \frac{R_L - R_{ESRo}}{2} \end{bmatrix} \tag{152}$$

$$M_i = [C_{in} \quad L_{lp} \quad L_m \quad L_{ls} \quad C_o]I \tag{153}$$

In (142), the $\oplus$ operator represents the n-ary matrix direct sum, which is a succinct way to represent a block diagonal matrix composed of the individual square matrix elements M_i given by (153). In (143) – (153), the real and imaginary parts of the harmonic switching functions are given by (154) – (156).

$$s_{1I} = -\frac{2}{\pi} \tag{154}$$

$$s_{2R} = -\frac{2\sin(\phi)}{\pi} \tag{155}$$

$$s_{2I} = -\frac{2\cos(\phi)}{\pi} \tag{156}$$

A further distinction between this model and those in literature is that the output variables are not taken as the states. Driving specific state variables is a valid objective, considering how much the performance of the DAB depends on them. However, this DAB is only one module of an SST, and must be interfaced with the GFI. It is for this reason that the output current was selected as an input, since the microgrid demand will drive the current draw through the GFI, and thus through the DAB. The input voltage is taken to be a fixed DC value, so we have the latitude to select the input current i_{in} as an output, which would likewise be important to the designer of the DC portion of the SST. To maintain the correct bus voltage at the GFI terminals, the proper HV DC link voltage must be maintained, so the output voltage v_o of the DAB is a natural second choice for one of its outputs.

Since the outputs in $\boldsymbol{y}$ are complex, some manipulation is required in order to use them to evaluate the performance of the DAB. Each of the ten output values of the model corresponds to a variable in the SHA output equation (157).

$$\begin{bmatrix} i_{in} \\ v_o \end{bmatrix} \approx \begin{bmatrix} i_{in0} \\ v_{o0} \end{bmatrix} + 2\begin{bmatrix} i_{in1R} & -i_{in1I} \\ v_{o1R} & -v_{o1I} \end{bmatrix}\begin{bmatrix} \cos(\omega_s t) \\ \sin(\omega_s t) \end{bmatrix} + 2\begin{bmatrix} i_{in2R} & -i_{in2I} \\ v_{o2R} & -v_{o2I} \end{bmatrix}\begin{bmatrix} \cos(2\omega_s t) \\ \sin(2\omega_s t) \end{bmatrix} \quad (157)$$

In a closed-loop control scenario, the duty ratio (or phase shift) would also be an input, and we would perturb and linearize the system around its equilibrium point; however, the stand-alone model is operated in open-loop in simulation with a fixed duty ratio. The process to generate the linearized small signal equations is well-established in literature and can be found in the sources cited in the literature review. In the full SST model, closed-loop control is employed, and it will be discussed in Section 3.3.4.1.

The comparison of waveforms generated by the PLECS model and the SHA model are given in Section 4.3.2.

In [95] and [97], a discrepancy is noted between the output power due to the phase shift computed in (137) and simulation results of the FHA model. The explanation for this is that the truncation of the Fourier series omits the contribution of higher order harmonics, reducing the overall power produced by the converter model, thus introducing a steady-state error. To address this, each of the references provides a correction method, the former by directly modifying the state equations, and the latter by modifying the duty ratio (or equivalently, the phase shift). The second method was selected for use in this model, and the result of its application will be demonstrated along with the operation of the model in Section 4.3.2.

As a final note on the modeling of the DAB, it was mentioned in the literature review that the Haar wavelet has been shown to have excellent accuracy for fewer coefficients than the generalized state space average model (see [98]). This method was not discovered until late in the work presented here, so its application to the modeling process was not examined in detail. Nevertheless, future research should include detailed investigation of this approach due to its relative simplicity and high accuracy.

3.3.3 Grid-Forming Inverter

The unterminated GFI state space average model in [108] is given by the system of equations in (158), beginning with the partitioned state and output matrix equations, then the state, output, and input vectors $\boldsymbol{x}$, $\boldsymbol{y}$, and $\boldsymbol{u}$, and concluding with the state space matrices A, B, C, and D. Fig. 26 shows the schematic of the inverter, with salient quantities labeled, and with the simplifying expression for r_{eq}, which includes

semiconductor on-resistance r_{on}, shown. The convention for representing time-varying values, e.g. $x(t) = X + \tilde{x}(t)$, where the capital letter represents the DC portion and the tilde represents the small-signal portion is used, but with the lowercase representing the dynamic portion without adornment for compact presentation. Since the inverter is three-phase, the synchronous reference frame is used to represent all relevant values via their d- and q-axis components as indicated by appropriate subscripts. Table VII gives the component values.

$$\begin{bmatrix} \dot{\boldsymbol{x}} \\ \boldsymbol{y} \end{bmatrix} = \left[\begin{array}{c|c} A & B \\ \hline C & D \end{array}\right] \begin{bmatrix} \boldsymbol{x} \\ \boldsymbol{u} \end{bmatrix}$$

$$\boldsymbol{x} = \begin{bmatrix} i_{L_d} & i_{L_q} & v_{C_{fd}} & v_{C_{fq}} \end{bmatrix}^T$$

$$\boldsymbol{y} = [i_{in} \quad i_{L_d} \quad i_{L_q} \quad v_{od} \quad v_{oq}]^T$$

$$\boldsymbol{u} = [v_{in} \quad i_{od} \quad i_{oq} \quad d_d \quad d_q]^T$$

$$A = \begin{bmatrix} -\frac{r_{eq}}{L} & \omega_s & -\frac{1}{L} & 0 \\ -\omega_s & -\frac{r_{eq}}{L} & 0 & -\frac{1}{L} \\ \frac{1}{C_f} & 0 & 0 & \omega_s \\ 0 & \frac{1}{C_f} & -\omega_s & 0 \end{bmatrix} \quad B = \begin{bmatrix} \frac{D_d}{L} & \frac{R_d}{L} & 0 & \frac{V_{in}}{L} & 0 \\ \frac{D_q}{L} & 0 & \frac{R_d}{L} & 0 & \frac{V_{in}}{L} \\ 0 & -\frac{1}{C_f} & 0 & 0 & 0 \\ 0 & 0 & -\frac{1}{C_f} & 0 & 0 \end{bmatrix} \tag{158}$$

$$C = \begin{bmatrix} \frac{3D_d}{2} & \frac{3D_q}{2} & 0 & 0 \\ 1 & 0 & 0 & 0 \\ 0 & 1 & 0 & 0 \\ R_d & 0 & 1 & 0 \\ 0 & R_d & 0 & 1 \end{bmatrix} \quad D = \begin{bmatrix} 0 & 0 & 0 & \frac{3I_{L_d}}{2} & \frac{3I_{L_q}}{2} \\ 0 & 0 & 0 & 0 & 0 \\ 0 & 0 & 0 & 0 & 0 \\ 0 & -R_d & 0 & 0 & 0 \\ 0 & 0 & -R_d & 0 & 0 \end{bmatrix}$$

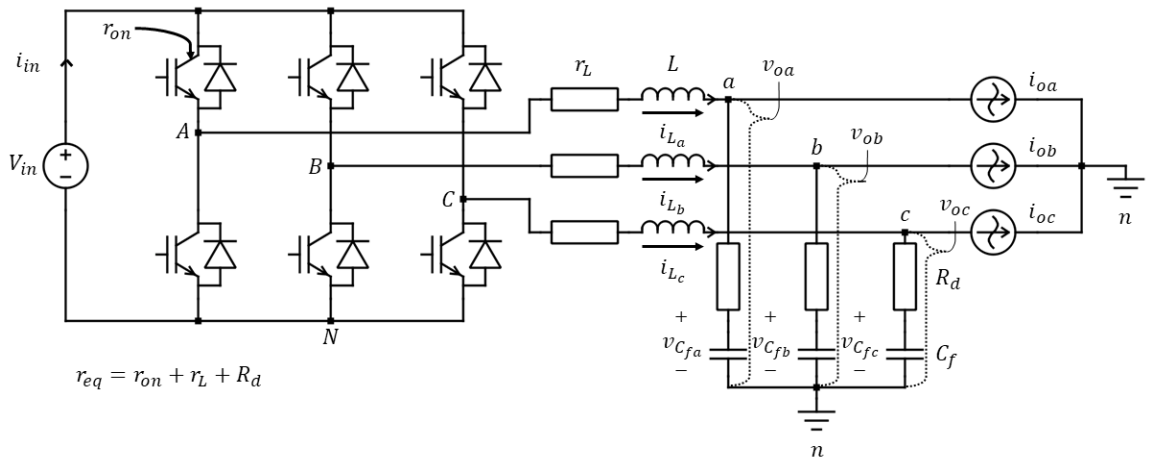

Fig. 26. GFI topology represented by state space model in (158).

TABLE VII
GRID-FORMING INVERTER COMPONENT VALUES

Component	Value
Semiconductor On-resistance, r_{on}	10 mΩ
Inductor Resistance, r_L	100 mΩ
Filter Inductance, L	2 mH
Damping Resistance (including ESR), R_d	1.96 Ω
Filter Capacitance, C_f	10 μF

We consider the source V_{in} to be the DC link portion of a two-stage converter, at the output of a DC-DC converter, at the connection to the ESS. It is assumed that this voltage is controlled to be very nearly DC, and so a DC signal is used as the first input (i.e. $v_{in}(t) = V_{in} + 0$). With this configuration, both the PV-generated power and any power sourced from the storage solution are managed by the inverter, simplifying the simulation process and integrating easily with the existing microgrid testbed architecture.

The power flow simulation is phasor-based, so these phasors must be converted to the synchronous reference frame if they are to be used with the inverter model. The IEEE 123-Node Test Feeder represents a distribution-level network, and thus it contains some single-phase and two-phase lines and loads. This causes unbalanced phase quantities and means that zero sequence components are present in the system. The inverter model used

is not designed with unbalanced phases in mind, so the real and imaginary parts of the phase voltage and current phasors are used as the dq-axis quantities in three identical parallel pseudo-single-phase converter models. This allows the simulation to capture the unbalanced behavior and requires little additional computational overhead, representing a balanced choice between the tradeoff of accuracy and speed.

Alternatives to this method were considered, such as decomposing the system using symmetrical components and transforming to synchronous frame as in [122], re-deriving the model to account for the zero sequence components, or simply duplicating the phase a quantities to approximate a balanced system while accepting the inherent error. The first method introduces additional computational overhead due to the necessary conversions to achieve separation of symmetrical components. The second method may provide superior modeling fidelity and accuracy but would require extended analytical effort for approximately the same result. The third method was deemed too rough an approximation, and despite its simplicity it is less attractive for its loss of accuracy.

A final consideration for the handling of unbalanced conditions is that of power computation. In [148], it is demonstrated that the typical computation for three-phase power in the synchronous reference frame under unbalanced conditions does not capture the oscillating power introduced by the unbalanced quantities. An offline simulation was constructed to examine the three simulation strategies and compare their accuracy with a reference signal featuring this oscillation. Unbalanced current was generated with amplitudes $\{1, 1.09, 0.85\}$ * 510.3 A for phases a, b, and c, respectively at a power factor of 0.89 leading. The steady-state result of simulation can be seen in Fig. 27. The

absolute percentage error is shown in Fig. 28, where the mean absolute percentage error (MAPE) is given, demonstrating the effectiveness of the approach in context.

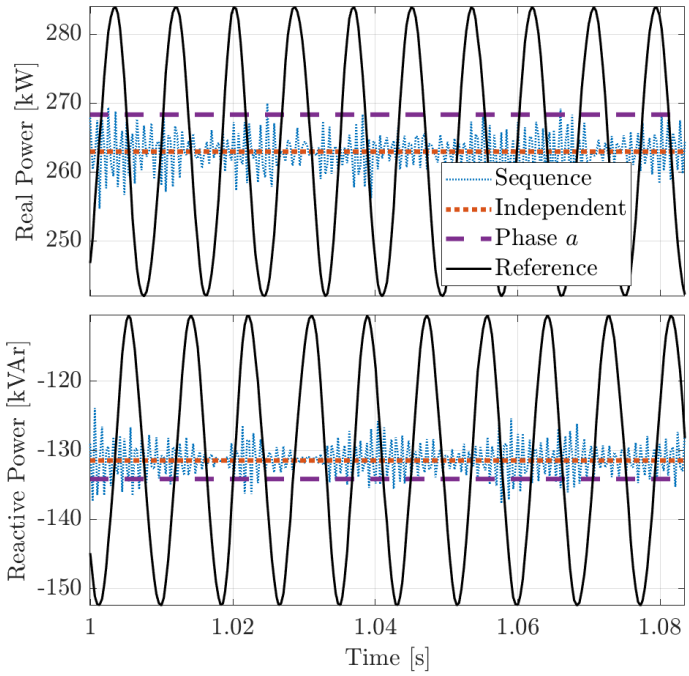

Fig. 27. Simulation results comparing sequence decomposition, independent phase control, and phase a duplication to reference.

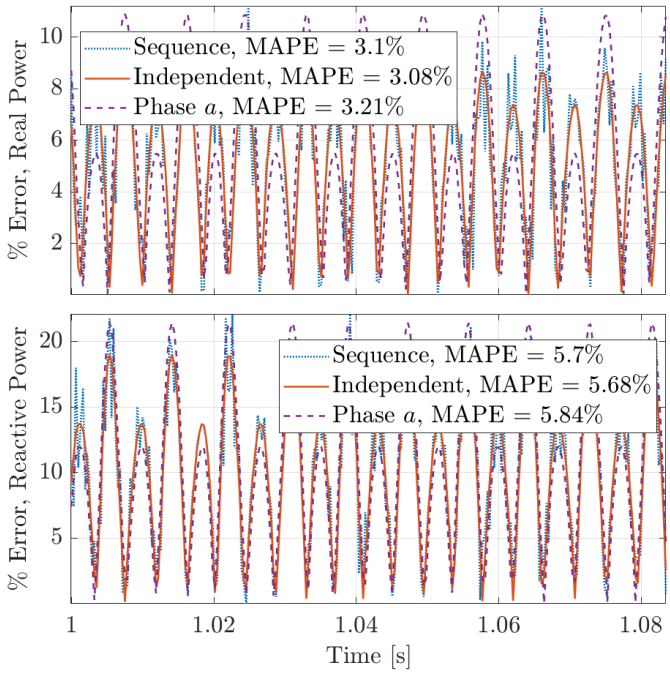

Fig. 28. Absolute percentage error from simulation in Fig. 27, with mean absolute percentage error (MAPE) shown for each method.

To complete the model and begin controller design, the final quiescent operating point values must be determined. Using (159) to obtain the equilibrium state values $\boldsymbol{X}$, (160) was employed to generate the steady-state output values $\boldsymbol{Y}$ presented alongside their input counterparts $\boldsymbol{U}$ in Table VIII.

$$\boldsymbol{X} = -A^{-1}B\boldsymbol{U} \tag{159}$$

$$\boldsymbol{Y} = C\boldsymbol{X} + D\boldsymbol{U} \tag{160}$$

TABLE VIII
STEADY-STATE INPUT AND OUTPUT VALUES

Model Input	Value	Model Output	Value
Input Voltage, V_{in}	1 kV	Input Current, I_{in}	307.5 A
Output Current, I_{od}	456.4 A	Inductor Current, I_{Ld}	456.5 A
Output Current, I_{oq}	228.2 A	Inductor Current, I_{Lq}	229.7 A
Duty Ratio, D_d	0.1322	Output Voltage, V_{od}	387.3 V
Duty Ratio, D_q	0.1836	Output Voltage, V_{oq}	−2.302 V

3.3.3.1 Control Design

Control objectives include step reference command following for the output voltage using the duty ratio as the control input, a minimum phase margin of 60° with up to 30° of additional phase to account for communication delay, and high-frequency roll-off to avoid switching frequency noise on the order of 10 kHz and above. Plant analysis for the transfer function matrix P_{dv_o} from $\boldsymbol{d} = \left[d_d, d_q\right]^T$ to $\boldsymbol{v}_o = \left[v_{od}, v_{oq}\right]^T$ using the values in Table VII and Table VIII reveals repeated poles at 7447 and 6695 rad/s and repeated zeros at the same locations along with a high-frequency pair at 51.02 krad/s. Analysis also indicates that $\text{rank}\big(\mathcal{O}(A, C)\big) = \text{rank}\big(\mathcal{C}(A, B)\big) = 4$, and thus the inverter states are both observable from the output and controllable from the input. To control the inverter without interference from switching events, a unity gain crossover frequency ω_g of about one decade below the typical switching frequency was targeted; however, this is on the order of 6280 rad/s (~1 kHz), which is too close to the resonant peak introduced by the poles for guaranteed stability, so the desired ω_g was lowered by another two decades to 62.8 rad/s.

The final control block diagram for the microgrid with the GFI model is shown in Fig. 29, with color coding to separate the microgrid model, inverter model and associated

controller, and hierarchical controllers. Values with superscript asterisks are controller reference values, while the subscript 0 indicates a nominal value.

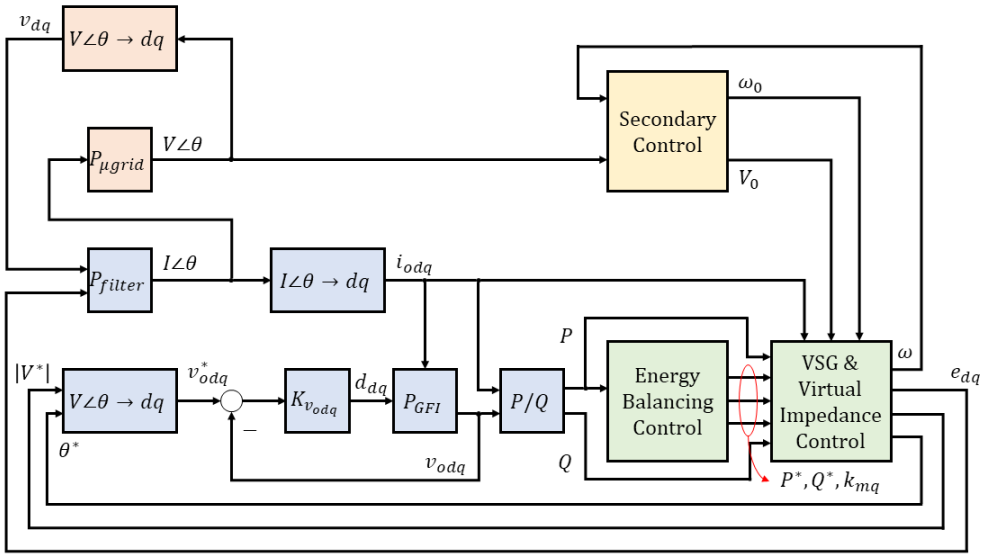

Fig. 29. Control block diagram with microgrid model in orange, inverter model and control in blue, primary control in green, and secondary control in yellow.

The final controller $K_{v_{odq}}$ that was designed to interface with the existing hierarchical control was surprisingly simple. Given the above limitations on bandwidth, an iterative PID controller design process was initiated using the dominant plant transfer functions in (161) – (163), wherein the integral controller was designed first to begin placing ω_g at its desired location by augmenting the transfer functions with $1/s$ and solving for the appropriate gain. Note that $P_{d_q v_{oq}} = P_{d_d v_{od}}$ and $P_{d_d v_{oq}} = -P_{d_q v_{od}}$. When including the high frequency terms to design the proportional and derivative portions of the controller, it was discovered that this simple integral controller, implemented in the dq reference frame, was stabilizing for the full plant model with only minor gain adjustments necessary. Not only does it stabilize the plant, but it has a 90° phase margin at ω_g,

promising robust performance even under nominal communication delay, a relevant concern in a system with a central controller. Furthermore, while the plant indicates cross-coupling between the off-diagonal elements of P_{dv_o}, their impact is immaterial in simulation, as will be shown in Section 4.2.4. Thus, the controller is given by (164), where I is the 2x2 identity matrix.

$$P_{d_d v_{od}} \approx \frac{10^6(s + 5 \times 10^4)(s^2 + 10^3 s + 5 \times 10^7)}{(s^2 + 10^3 s + 4 \times 10^7)(s^2 + 10^3 s + 6 \times 10^7)} \tag{161}$$

$$P_{d_q v_{od}} \approx \frac{-4 \times 10^8(s + 30)(s + 10^5)}{(s^2 + 10^3 s + 4 \times 10^7)(s^2 + 10^3 s + 6 \times 10^7)} \tag{162}$$

$$P_{dv_o} = \begin{bmatrix} P_{d_d v_{od}} & P_{d_q v_{od}} \\ -P_{d_q v_{od}} & P_{d_d v_{od}} \end{bmatrix} \tag{163}$$

$$K_{v_{odq}} = \frac{0.062648}{s} I \tag{164}$$

A Bode plot of the open loop transfer function $L = P_{dv_o} K_{v_{odq}}$ is shown in Fig. 30, with the pertinent points highlighted. The high-frequency roll-off region begins at 633 rad/s, so it meets the design goal and has the added benefit of rejecting oscillatory behavior from the resonant peak. The step response of the closed loop transfer function from reference to output is shown in Fig. 31, with the 10%–90% rise time t_r and the settling time $t_s = 5\tau$ indicated on the plot. No oscillation or overshoot is present in the response. Since the reference generation is sampled at 200 ms intervals due to the emulation of communication delay in the microgrid testbed, all commands appear as successive step functions from the controller's perspective.

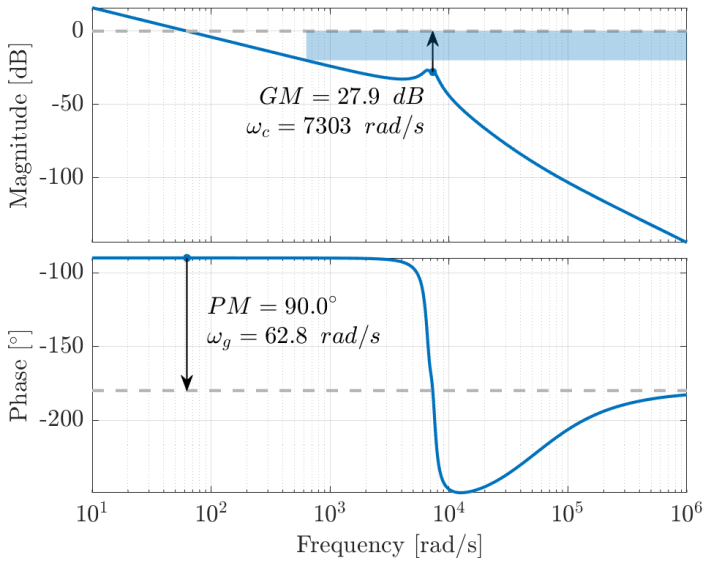

Fig. 30. Open-loop response of $L = P_{dv_o} K_{v_{odq}}$ with integral control, highlighting the unity gain and imaginary phase crossover frequencies, and the high-frequency roll-off exclusion region ($|L| \leq -20\ dB$).

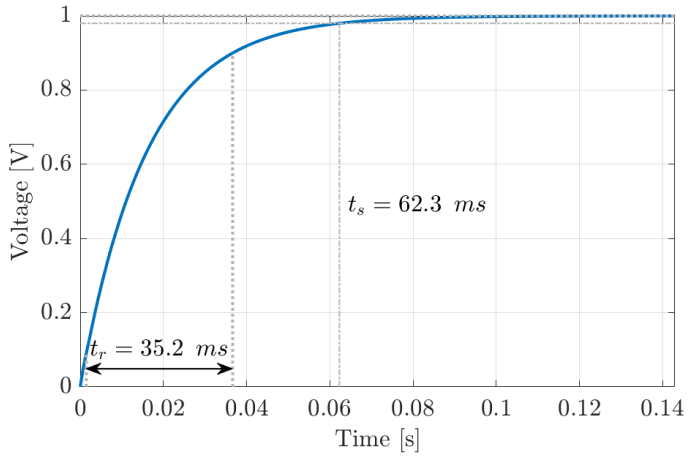

Fig. 31. Unit step response of closed-loop system $L/(1 + L)$ from reference to output featuring rise time t_r and settling time t_s.

3.3.4 Solid-State Transformer

We now have all the requisite fundamentals to discuss the design of a novel SST and its inclusion in large-scale simulation. A simple choice for SST integration into the microgrid model would be to directly replace existing ideal transformers (implemented as

gains) with SST converters. However, it may be advantageous from the perspectives of real-world cost, control complexity, and computational budget in simulation to simply remove the gain and use one of the multi-stage SST implementations, replacing the ideal transformer and incorporating the GFI simultaneously instead. To that end, the following SST-based energy cell configuration is proposed.

Fig. 32 shows the stages of the SST-based energy cell in block diagram form, with the DC portion assumed to be in place as in the previous discussion of the microgrid model, and with the DAB array, HV DC Link, and three-phase GFI models and controller design described previously, with necessary modifications discussed here.

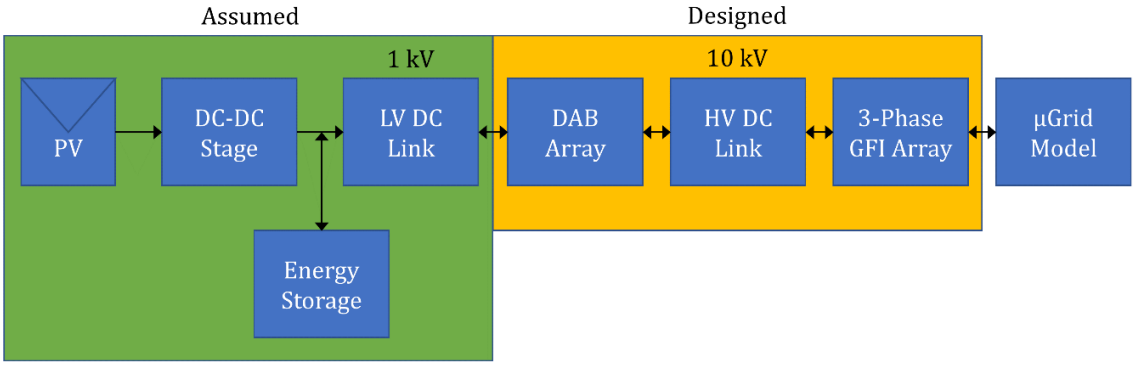

Fig. 32. Truncated SST energy cell block diagram, featuring DC source portion assumed to be in-place, and DC-AC portion designed here.

Of course, this is not a full SST as it is not truly an AC-AC converter; however, it is not much different in that regard from the Modified DAB SST demonstrated in [119], and still employs many of the SST features expounded on in the literature review. The DAB array is a set of five parallel input, series output DAB converters, each featuring a high-frequency transformer designed for minimum loss as described in Section 3.3.2. The DAB array amplifies the LV DC Link voltage of 1 kV to 10 kV across the distributed HV DC Link. A parallel array of GFI models like those in Section 3.3.3, designed to interface

directly with the microgrid model, providing line-to-line RMS output at 4160 V, and integrated with the hierarchical control strategy completes the SST.

The DC link current is controlled by the GFI array to meet the demand of the microgrid, while the DC link voltage is held constant by the DAB array. Each of the five DAB converters is connected in parallel to the DC source voltage, and thus splits the current evenly at the input. Half of the output power is processed by each GFI in the array.

Two important issues with the parallel GFI array must be considered. First, the voltage stress across the switches is very high at 10 kV. This can be dealt with by using an emerging technology: The 15kV SiC MOSFET, discussed in [149], which provides the necessary support as well as a very comfortable safety margin. An alternative strategy would be to use a multi-level converter, where switches take on only $1/(n-1)$ of the total voltage across the input for n levels, but investigation of this alternative is left for future work. The second issue is that if any unbalanced phase quantities exist, they will induce circulating currents that may disrupt the operation of the converter. The fourth leg described by [121] – [125] can be controlled for just this purpose, and may need to be investigated further if the existing control strategy is insufficient in practice to attend to the problem. This requires implementation of a 3D space vector PWM (3DSVM), as described by [150] (note that this is one variation on this theme among many), and which also appears in [121] for the same application. However, at the time of simulation, the control strategy already in place from previous GFI designs is capable of handling unbalanced quantities without losing stability, and the effect of imbalance on system performance is thus minimized.

Fig. 33 depicts the simplified truncated SST circuit diagram. Simulations demonstrating its operation are provided in Section 4.3.3.

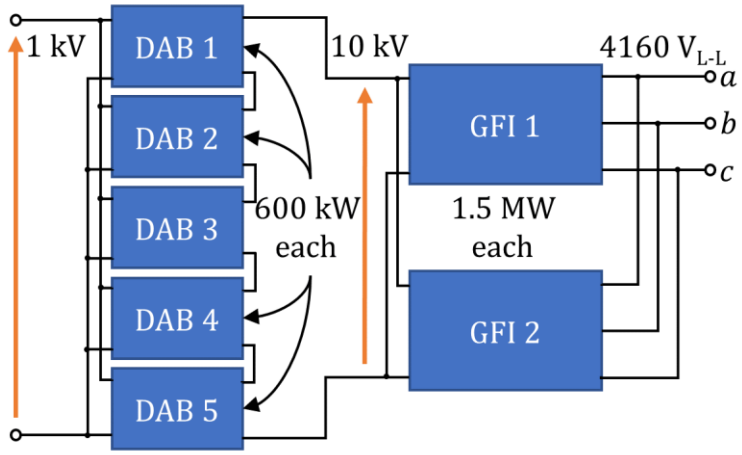

Fig. 33. Simplified SST diagram featuring parallel-series array of DAB converters and parallel GFI array.

3.3.4.1 DAB and GFI Model Modifications

When simulating this model with a time step of 100 µs, high frequency signals like those generated by the DAB model will not be represented. Instead, we can approximate the operation using the RMS value of the output voltage, since the voltage is assumed to be DC in the GFI model. To compute this value for the SHA model, we use the sum of squares of each RMS component, as in (165).

$$V_{Link} = \sqrt{v_{o0}^2 + 2(v_{o1R}^2 + v_{o1I}^2) + 2(v_{o2R}^2 + v_{o2I}^2)} \quad [\text{V}] \qquad (165)$$

A better approach is to truncate the harmonic states and their derivatives, forming a low-frequency model directly from the full model. The reason for this is that reducing the size of the state space matrix reduces the number of states, which yields additional time step budget. Furthermore, the reduction of the model in this way preserves the impact of

switching harmonics via the B and D matrices, so this information is not lost. To perform this truncation, from (142), we take A_{00}, B_0, C_{00}, and D_0.

However, this only considers the open-loop model. The same process can be applied to the closed-loop model to reduce the order and preserve the DC impact of the switching harmonics, but the formulation of this model has not yet been discussed. In the state space averaging approach, the duty ratio is used to weight the individual topological matrices formed by the switching action, such that the average model considers the intermediate value about which the switching waveform oscillates. In the generalized state space averaging approach, this still roughly describes the process, but since the waveforms are now nonlinear, and not piecewise linear as in the state space average model, some additional steps must be taken. In [97], the formal process of taking partial derivatives of each function is applied, and this is the most generally applicable approach. However, in [93], an approach similar to the standard state space averaging method of perturbation and linearization is applied, which is more familiar and more accessible to researchers who have not studied nonlinear control theory. This method was used in this work and will now be described.

The first step to include the duty ratio as an input is to identify the correct perturbation approximation to apply to the switching functions. Given that the switching function $s_1(t)$ does not have 0, $1R$, $2R$, or $2I$ components, and its only component is linear, its small signal form is identical to its large signal form. Focusing attention on $s_2(t)$, the affected variables are $i_{L_{ls}}$, v_{C_o}, and v_o. Thus, only these equations will differ from those in the large signal model. Ignoring the constant proportionality terms for the sake of simplicity, the harmonic forms of s_2 are sine and cosine terms with the duty ratio

as inputs. When perturbing the duty ratio, we have $d(t) = D + \tilde{d}(t)$, so for example, the sine term is written using the angle sum identity from trigonometry as (166).

$$\sin(\pi d) = \sin\left(\pi\left(D + \tilde{d}\right)\right) = \sin(\pi D)\cos\left(\pi\tilde{d}\right) + \cos(\pi D)\sin\left(\pi\tilde{d}\right) \tag{166}$$

Since we are attempting to control a small perturbation about the steady state value, we can employ the small angle approximation, which for a small angular value ε is stated for sine as $\sin(\varepsilon) \approx \varepsilon$ and for cosine as $\cos(\varepsilon) \approx 1$. Thus, (166) becomes approximately (167).

$$\sin(\pi d) \approx \sin(\pi D) + \cos(\pi D)\left(\pi\tilde{d}\right) \tag{167}$$

A similar process is followed for the cosine terms using the appropriate identity. Perturbing the states similarly yields the general form $x(t) = X + \tilde{x}(t)$, so the product of the switching function first real harmonic and the state variables at harmonic k takes the form of (168).

$$\langle s_2\rangle_{1R}\langle x\rangle_k \approx \sin(\pi D)\,X + \cos(\pi D)\left(\pi\tilde{d}\right)X + \sin(\pi D)\,\langle\tilde{x}\rangle_k + \underbrace{\cancel{\cos(\pi D)\left(\pi\tilde{d}\right)\langle\tilde{x}\rangle_k}}_{0} \tag{168}$$

Here we neglect the product of the perturbations, since it is assumed to be much smaller than the other terms. A similar process is followed for the first imaginary harmonic terms, and for the output terms in turn. The resulting state space model is produced directly by taking the product of new switching perturbation matrices like those described by (144) and (145) with the steady state values obtained by equations of the form of (159) and (160). The small signal model is then truncated as described above in order to model the DAB in real-time simulation.

The GFI model also requires modification in order to operate at its new, higher output values. Specifically, due to the higher reactive power output, the filter needs to be

redesigned, not just for harmonic attenuation, but also to reduce the voltage drop and amend the reactive power of the filter series and shunt branches, respectively. Failure to do so results in wild instability, excited within a few milliseconds of simulation start. Following the wisdom in [4] and [5], the filter was redesigned with component values given in Section 4.3.3, producing stable operation. As a result, the controller requires re-tuning to accommodate these changes, but the design process is the same so it will not be described again. Note that the grid-side inductor is not included in the model for the SST.

3.4 Remote Control Software

The remote-control software was written in Visual Basic .NET (VB.NET) using Visual Studio 2017. This GUI-based program utilizes the GPL3-licensed EasyModbusTCP.NET v5.5 library, available at [151], which allows Modbus protocol communication over TCP/IP.

The software is written using object-oriented programming (OOP) principles, and classes for the energy cell, tertiary controller, connection, and control loop are defined. The asynchronous programming paradigm is used liberally, with both UI elements and communication methods making use of asynchronous callbacks as appropriate. The program is highly modular and is thus malleable enough to be adapted to any reasonably similar future use. For example, it was designed with the ability to communicate with devices other than the OPAL-RT, so long as they are capable of Modbus over TCP/IP, by simply changing the register addresses and scaling factors to match those of the device. The codebase is too large to include in this report, but access to it is discussed in Appendix H.

3.4.1 Building Blocks

UI aside, the primary components of the software are the connection, energy cell, tertiary controller, and control loop classes.

The connection object is the entry point for an energy cell or tertiary controller, and instantiating one signals the user's intention to monitor and/or control one of the two, differentiated by a checkbox. The connection is built with the ability to detect and correct connectivity issues autonomously, and is defined by the user with its name, IP address, port, and device ID specified by [146].

The energy cell object contains all the necessary measurement and control variables, scaling factors, and both synchronous and asynchronous methods needed for data retrieval via the connection and other administrative tasks such as invalid data detection. Each distinct energy cell has a unique connection object as a property, and connection information and events are shared between the two, with event handlers responsible for autonomous operation. The tertiary controller object is like the energy cell object, but with only two register variables for the sign and magnitude of ω_{syn}, and only one method to read them.

The control loop object performs the bulk of the work that is not UI related. A high-precision timer is started upon object instantiation when entering the software's control interface that runs at a period T_s of 200 ms and calls all necessary read and write methods within each energy cell and tertiary controller asynchronously and in parallel during each iteration. The UI allows energy cells to be monitored in local control mode and polls the holding registers associated with the local control signals to maintain continuity upon remote control mode activation. It also allows the user to manually assign values for P^*

and Q^* while in grid-connected mode. Since computation of control signals via (129) requires measurement values, the asynchronous tasks are awaited prior to computation. Since the communication and computation tasks are all initiated asynchronously and in parallel, it would be possible to enter a race condition for the average energy storage value needed for the real power reference, so VB.NET's SyncLock is used to prevent this.

3.4.2 Timing Considerations

To select the loop period, some simple arithmetic and engineering judgement were used. The largest single request from the software master to the OPAL-RT slave is 14 registers, at two bytes each. With the associated Modbus and TCP/IP packet overhead of 64 bytes, the packet size amounts to approximately 92 bytes. With an average 32-byte ping time of 34 ms, which was observed from the remote computer used during testing, taking congestion into account by using a safety margin of half the observed rate, we can assume transmission at approximately 500 bytes per second. Roughly, this gives a 200 ms window in which to complete calculation for communication in each iteration of the control loop. We can generalize this approximation using the number of registers $n_{registers}$ and average ping time t_{ping} in milliseconds as in (169).

$$T_s \approx \frac{(2\ [\text{bytes}]) * n_{registers} + 64\ [\text{bytes}]}{\frac{1}{2}\left(\frac{32\ [\text{bytes}]}{t_{ping}}\right)} \quad [\text{s}] \tag{169}$$

The time between successive operations, which are read-read for local control, and read-write for remote control, was measured during testing. The measurements were all within 100 ms of the 101.6 ms average which illustrates the sufficiency of the selected

value of T_s. The slight excursion from 100 ms on average is most likely due to the time to write to the standard input/output buffer for logging purposes.

4 EXPERIMENTAL AND SIMULATION RESULTS

Here we will present validation of the previous analyses for each topic in turn. We will fist cover the results of testing an initial transformer design, as well as reporting on a re-design carried out with the transformer design software mentioned previously, specifically for the 300 W micro-inverter constructed during work on the Power America project in 2016. Validation of transformer inductance and loss calculations will be demonstrated via both FEM simulation and measurement. To further illustrate the performance of the transformer optimization methods suggested, experimental results from selected literature will be used as a litmus test. The design of the DAB converter's matrix transformer will be described, and results of simulation testing will be presented. Simulation results from testing different scenarios in the microgrid testbed will be presented and discussed in context. The results of PLECS simulation of the designed 300 W micro-inverter, including closed-loop control will be presented. A set of energy storage component waveforms from the simulation will be explained in detail for the same converter. The stand-alone version of the DAB designed for the SST will be compared with its SHA model, and finally, all simulation results of the proposed SST design will be presented to demonstrate its functionality.

4.1 Transformers

Several transformers were built and tested in the DC-DC stage of the 300 W micro-inverter, with a variety of cores and winding configurations. The design and construction of these transformers prompted and supported the creation of the transformer design script intended for continued use in design and analysis of future transformers. The final transformer settled on for use in the prototype circuit represents a best attempt to hand-

design and wind a transformer, and its analysis will illuminate some of the functionality of the design script. Comparisons of some of the script results with FEM and experiment will also be provided. A first-pass design of a new transformer for the circuit will be presented at the end of the section to demonstrate the value of the design functionality of the tool. The script itself will not be include here since it is composed of over ten thousand lines of code, but access to it will be discussed in Appendix H.

The prototype transformer, pictured in Fig. 34, consists of a single-turn primary with six parallel 405/44 litz wires, and a bifilar-wound pair of secondary windings, each composed of 15 turns of 165/42 litz wire, wound on a Ferroxcube E43/10/28 made of 3F3 MnZn material.

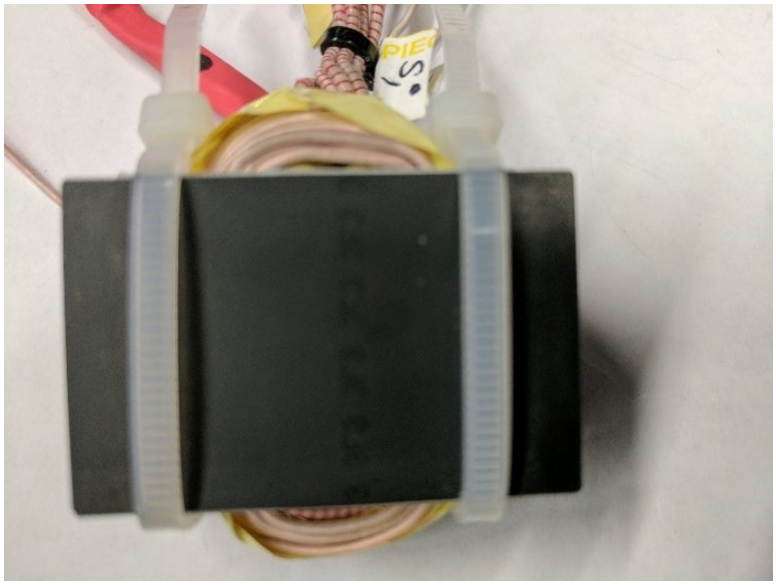

Fig. 34. Prototype transformer, E43/10/28-3F3

Fig. 35 depicts the 2D cross-sectional half-model used in ANSYS Maxwell for FEM analysis, and Fig. 36 shows a representative flux density vector and magnetic vector equipotential (field line) plot. Maxwell Circuit Editor (MCE) was used to define the

winding excitation externally by constructing the DC-DC stage circuit as shown in the schematic in Fig. 37.

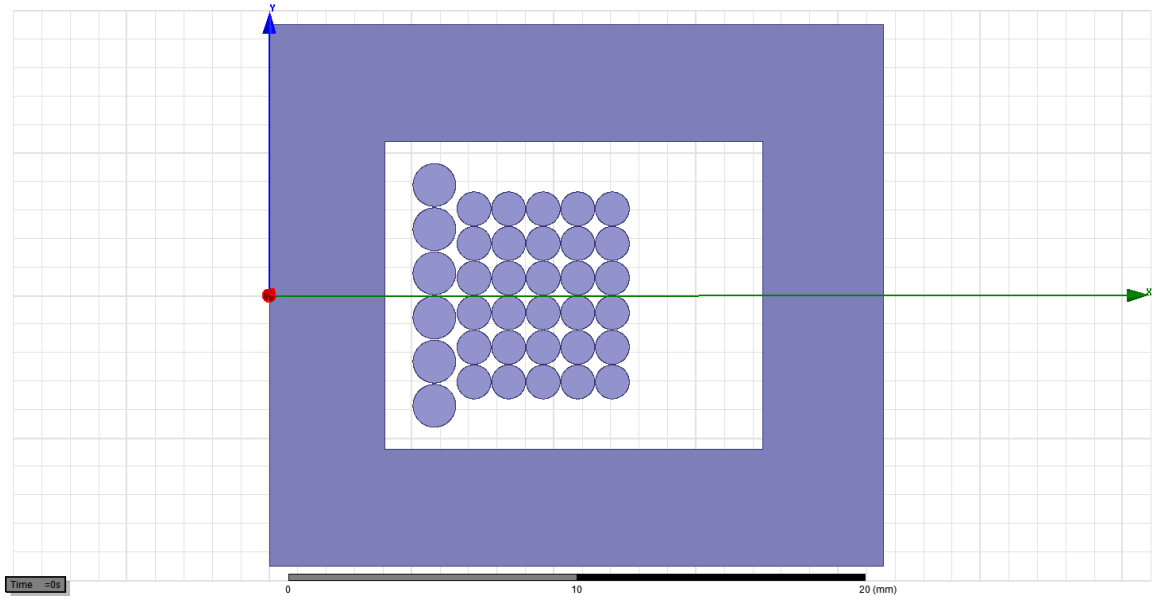

Fig. 35. 2D cross-sectional half-model of prototype transformer used in FEA.

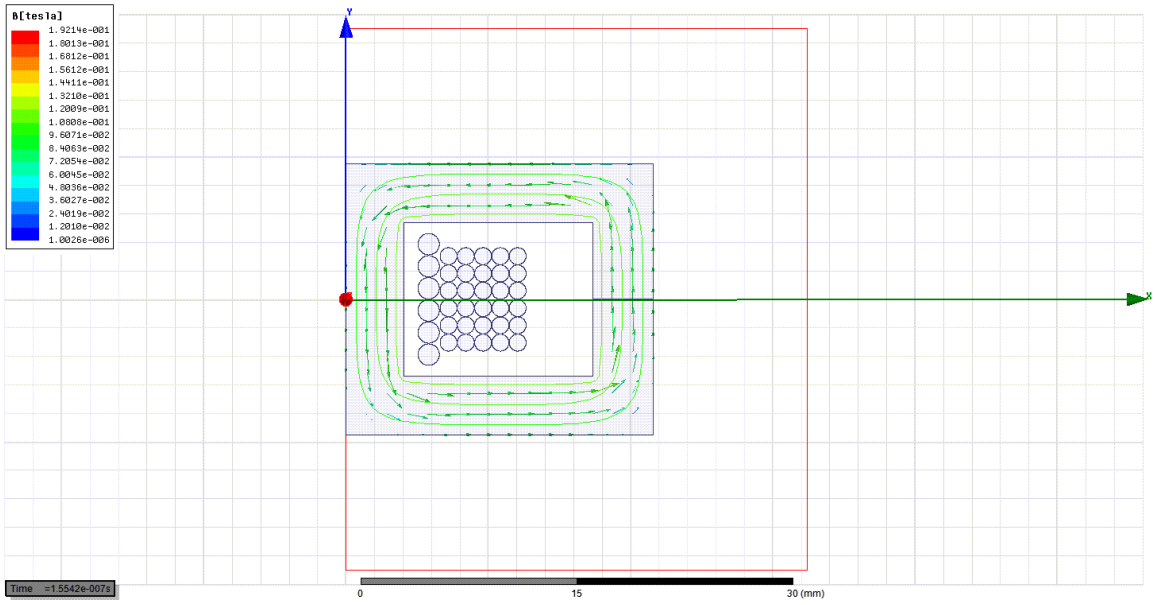

Fig. 36. Representative flux density vector and magnetic vector equipotential lines.

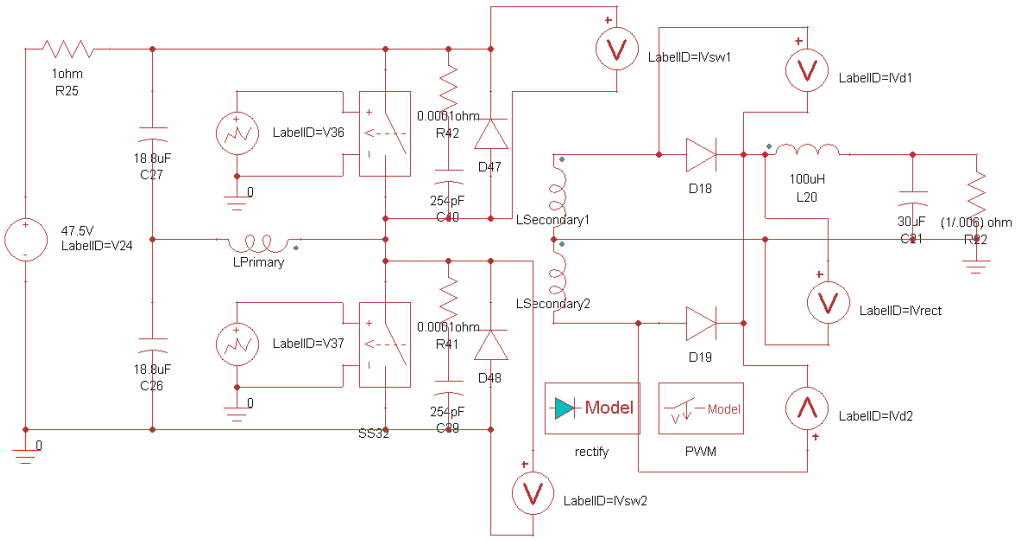

Fig. 37. Asymmetric half-bridge schematic used for winding excitation in Maxwell.

Measurements of the transformer loss values were analytically extracted from experiments with the DC-DC stage prototype, using a Yokogawa WT500 Power Analyzer, which is accurate to 0.1%. The impedance measurements were made with an OMICRON Lab Bode 100 network analyzer which is accurate to 0.1 dB for magnitude and 0.1° for phase. The measurement setup used to collect losses is depicted in Fig. 38, while the measurement configuration for impedance is depicted in Fig. 39. The results of all measurements, simulation, and analysis are presented in Table IX and Table X for comparison.

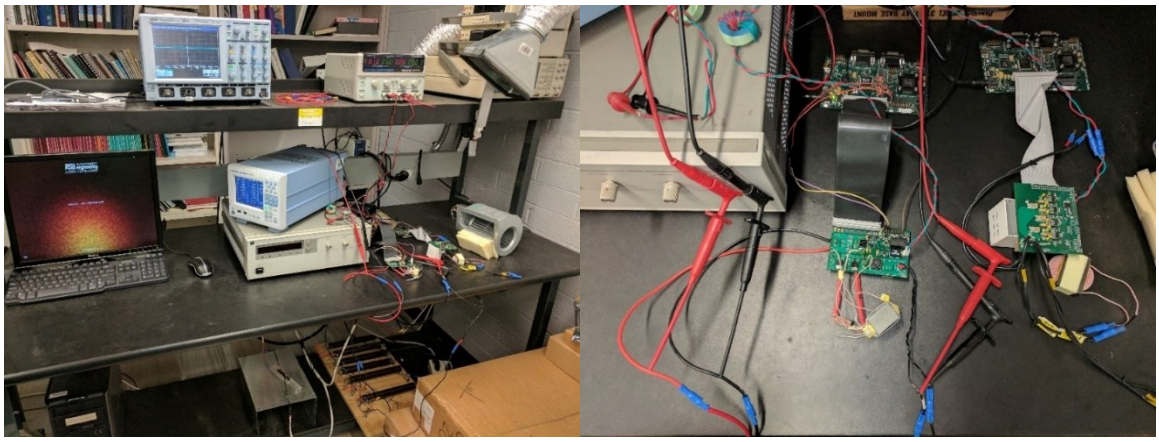

Fig. 38. (left) Overall power measurement setup featuring oscilloscope, power analyzer, DC sources, and blower, and (right) closer view of measurement connections, both stages of inverter, and DSP control/measurement connections.

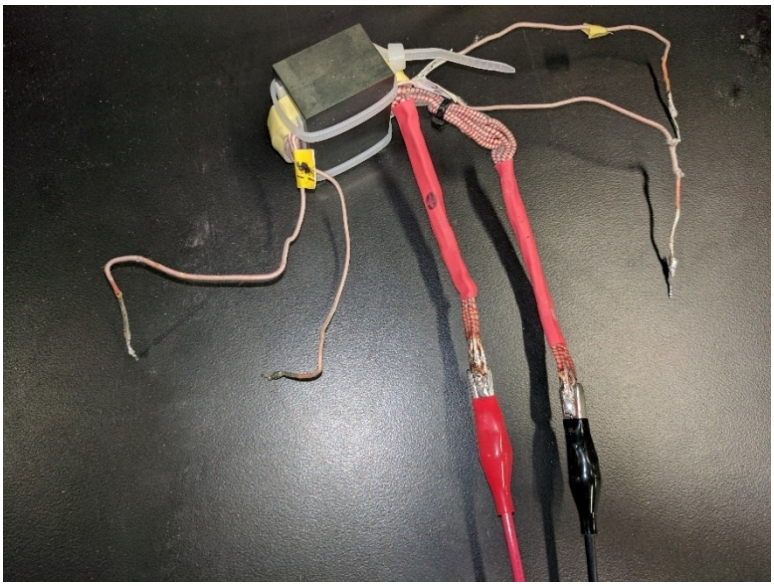

Fig. 39. Impedance measurement connection, single port measurement method, primary winding.

Loss measurements were made of the DC-DC stage prototype and the total loss was broken down by analysis into component contributions. The transformer loss was taken as the difference between the total loss and the loss in the four semiconductors, namely the two switches and the two diodes. Their total loss at 69 % load (207 W) was calculated to be 3.16 W, and the total DC-DC stage loss was measured to be 10.74 W. This yields

the experimental value in Table IX, where analytical loss values are compared with measurement, inclusive of efficiency.

TABLE IX
LOSS VALUES OF TRANSFORMER PROTOTYPE

Loss Quantity	Analytical	Measured
Copper Loss P_{Cu}	1.11 W	–
Core Loss P_c	6.36 W	–
Total Loss P_L	7.46 W	7.58 W
Transformer Efficiency η_T	96.4%	96.3%

Inductance measurements were performed on the transformer directly. The inductance was measured with a frequency sweep from 10 Hz to 40 MHz and sampled at 200 kHz. Inductance measurements were made for each winding with the other two windings open-circuited, and with one other winding short-circuited, for all such combinations. Further measurements were made with each of the winding pairs in series-aiding and series-opposing flux configurations to form a complete set of transformer inductance measurements. The resulting inductance measurements were then used to calculate the main inductance and leakage inductance matrices as described in Section 3.1.3. The values for the fictitious circuit elements used for analysis and simulation are provided in Table X.

TABLE X
INDUCTANCE VALUES OF TRANSFORMER PROTOTYPE

Inductance Quantity	Analytical	FEM	Measured
Magnetizing (ref. to Primary) L_m	5.71 µH	5.02 µH	5.37 µH
Primary Leakage $L_{p,l}$	94.88 nH	99.04 nH	94.73 nH
Secondary Leakage (each) $L_{s,l}$	6.75 µH	8.08 µH	5.97 µH
Total Leakage (ref. to Primary) L_l	124.88 nH	134.95 nH	121.26 nH

Resistance measurements were also performed; however, the sensitivity of the measurement hardware was insufficient to collect accurate measurements. The network

analyzer is only capable of measuring resistance values of greater than 500 mΩ by default and can be configured with additional equipment to measure resistance as low as 20 mΩ. Both values exceed the expected DC resistance of the windings, and only cover the AC resistance of one of the two secondary windings. Thus, it falls to the overall loss measurements to validate the analytical results.

FEA as described above yielded values for inductance, core loss, current density, and Ohmic loss. Ferroxcube 3F3 material was modeled using the same data obtained from the datasheet for the material described previously. The litz wire was modeled using the effective conductivity method described in (25). Since 2D transient simulations in Maxwell do now allow insulation boundary conditions, the conductor bundles are physically displaced by 50 microns and 25 microns for the primary and secondary, respectively, to avoid any short-circuit behavior. Despite the care and attention to detail employed in the modeling, there were some unexpected behaviors observed in simulation.

The loss values calculated by FEA were unfortunately useless, as Maxwell does not calculate eddy effects directly for stranded windings under transient simulation, and instead relies on the quotient of the integral of the square of current density in the volume of the conductor and its conductivity. While this is the definition of Ohmic loss, for this application there are two main problems with this simulation strategy. First, the transformer (in 2D simulation) is only modeled to the depth of the core, and thus necessarily excludes a significant portion of the windings, and completely neglects the winding terminal excursions (‘flags’). In the case of the primary winding, this represents a significant deviation from reality as the flags alone comprise approximately 80% of the

winding length. Second, litz wire is not a solid conductor, nor is it a standard stranded conductor, hence the effective conductivity definition as described above. The resulting Ohmic loss values were on the order of 10% of those expected per both measurement and analysis. This is around the magnitude expected for DC losses in the windings alone. Finally, the flux density achieved only about 80% of its peak value obtained via analysis, which in turn reduced the core loss values. This is likely due to transient behavior, as only the first cycle of operation was simulated. The winding currents do not reach their steady-state peak values, which further suggests that this is the case. It is possible that given longer simulation time, the transient effects would even out, and steady-state operation would be achieved, allowing the value to rise toward the anticipated value. Initial values were set in the MCE circuit description, but not all initial conditions were available for editing, and thus, some starting transient behavior is to be expected. Despite these issues, FEM simulation is a promising tool and with more experience, future FEM simulations with 3D models can account for these issues and enable deeper understanding.

The transformer design script was also used to design a set of seven transformers. Of the seven transformers designed, five of them were close enough to commercially available products to attempt construction. The best transformer design in terms of loss is presented in the following tables. It is comprised of an ETD 29/16/10 core made of 3C96 MnZn, with windings arranged as shown in Fig. 7. The primary winding is one layer of eight parallel strands of 200/38 litz wire (number of strands/strand AWG) with an effective AWG of 6. The secondary windings are three layers of five bifilar turns (ten total turns per layer) of 165/42 litz wire, with an equivalent AWG of 20. Table XI gives

the inductance values of the design. Table XII shows the losses and efficiency. Table XIII provides consistency check information.

TABLE XI
INDUCTANCE VALUES OF DESIGNED TRANSFORMER

Inductance Quantity	Value
Magnetizing L_m	1.327 µH
Primary Leakage $L_{p,l}$	71.46 nH
Secondary Leakage (each) $L_{s,l}$	5.23 µH
Total Leakage (ref. to primary) L_l	94.7 nH

TABLE XII
LOSS VALUES OF DESIGNED TRANSFORMER

Loss Quantity	Value
Copper Loss P_{Cu}	1.198 W
Core Loss P_c	1.718 W
Total Loss P_L	2.916 W
Transformer Efficiency η_T	99.03%

TABLE XIII
VALIDATION OF CONSISTENCY WITH GOALS

Consistency Parameter	Value	Goal
Core Geometry Coefficient K_g	4655.4 mm^5	3130.0 mm^5
Area Product A_p	10199.0 mm^4	68640 mm^4
Peak Magnetic Flux Density $\hat{B}$	177.4 mT	500 mT
Peak Current Density $\hat{J}$	2.212 A/mm^2	3.000 A/mm^2

In initial attempts to construct this transformer, several problems were encountered. First, many models of transformer core are unavailable commercially due to their lack of popularity. Some of the cores and winding constructions suggested by analysis were unavailable, and those cores with the same form factor were not always available in the material suggested. Second, after attempts to wind several transformers by hand, it was decided that the transformer should be constructed at the machine shop; however, when winding by machine, space to wind and stability of wound wire must be considered. Winding several layers of secondary over a single layer of primary, for example, must

still allow the primary winding terminations to exit the bobbin without disturbing the layer structure.

4.1.1 Measurement Results from Literature

Since the results of the design script were only tested against the measurements from a single transformer prototype, skepticism regarding the accuracy and effectiveness of the formulations used within is justifiable. Likewise, the computations in the optimization method discussed in 3.1.5.1 were not validated against any hardware. Throughout the creation of the design script, each new computation method was tested against the results given in the literature from which it was taken to ensure that it correctly reproduced any test cases provided. However, further validation was desired, and to that end literature was scoured for suitable measurement test cases with which to validate the script's results.

Throughout the sources in the literature review, some degree of hardware measurement was present in numerous papers, but to ensure that a large enough pool was available for testing, additional sources were sought out. More than 40 sources with measurement results were collected, and from this list, every source which had a description of its test setup, a description of the transformer design specifications, and tabular or graphical results were retained. Initially this resulted in 11 sources, with common reasons for exclusion being lack of explanation of measurement setup, incomplete or missing transformer design information, or lack of usable data. Investigating the remaining sources in greater detail, six were removed due to scrutiny revealing that the provided information was less complete than initially assessed. The

remaining five sources will be cited, described in detail, and the method of data extraction and results of comparing analysis to measurement will be presented.

For plotted data, a full screen zoomed screenshot was taken on a 2560×1440 resolution monitor and imported into WebPlotDigitizer. The axes were calibrated, and points were placed on the plot to match the presented data. The "pixel error", or the error in digitization of the data due to discrete positioning of data samples in the digitization software is derived from the transformation equations given in the form of (170).

$$\begin{aligned} x_{data} &= \varepsilon_x x_{px} + \varepsilon_{yx} y_{px} + \varepsilon_{x,offset} \\ y_{data} &= \varepsilon_{xy} x_{px} + \varepsilon_y y_{px} + \varepsilon_{y,offset} \end{aligned} \tag{170}$$

This information is available directly from the software after calibrating the axes and is useful in determining the accuracy of extracted data, which in most cases is quite high. One of the plots that was finally selected for use, in Source 3, was from a scanned copy of the original paper, which appears to be the only available version. The scanning process was not perfect, and the plot is slightly misaligned, introducing error in each dimension for each axis. In the tables in this section, a comma-delimited pair representing the self-error (e.g. the error in x data relative to the x-axis calibration) will be given for the data if no skew was detected, and pairs of sums will be given for the skewed case, representing the x and y contribution to each error in extracted data (e.g. $\varepsilon_x + \varepsilon_{yx}$, $\varepsilon_{xy} + \varepsilon_y$). Since the placement of points is accurate up to one half pixel, the values given represent $\varepsilon_x/2$ and $\varepsilon_y/2$, or in the case of the skewed plot, those values and $\varepsilon_{yx}/2$ and $\varepsilon_{xy}/2$. The offset is ignored because it does not contribute to the error and is only used to place the axes relative to the user interface image coordinates.

4.1.1.1 Source 1

In [29], an amplified signal generator was used to produce sinusoidal voltage input at 20 kHz with variable third harmonic content. The transformer was immersed in an oil bath held at 100 °C by a hot plate, and the input current and output voltage were measured with a 200 MHz sampling rate.

The transformer was constructed on a Philips TX39/20/13 toroidal core made of 3C85 material, with a primary winding of six turns of 7/38 litz wire, and a secondary of six turns of 7/38 litz wire, evenly distributed along the core's circumference.

The data is presented in several figures, the first few of which compare the source's proposed calculation method to data from a prior source. The fifth figure is a linear plot of the total core loss at a phase angle of 0° while the third harmonic was varied. The sixth figure is a linear plot of the total core loss at a fixed 70% third harmonic component contribution while the phase angle was varied. These last two plots are used.

Results of comparison with extracted data for these two figures are presented in Fig. 40 and Fig. 41. The pixel error and the error of the two estimation methods with respect to the extracted data are presented in Table XIV.

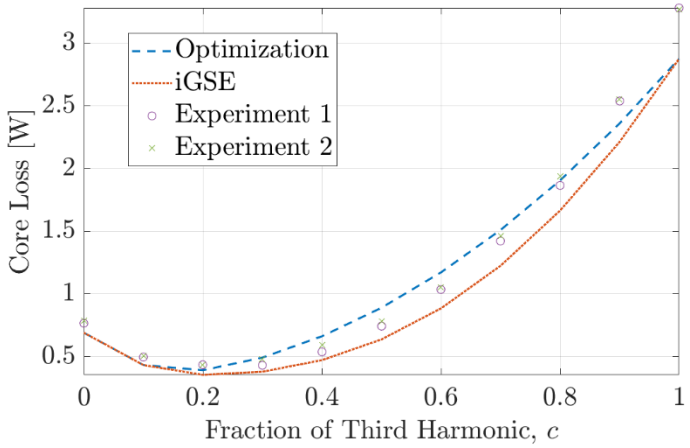

Fig. 40. Results for optimization method and iGSE vs. data extracted from Fig. 5 in Source 1.

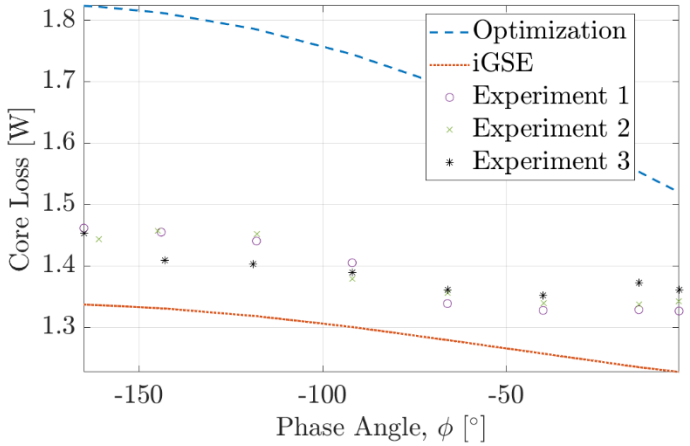

Fig. 41. Results for optimization method and iGSE vs. data extracted from Fig. 6 in Source 1.

TABLE XIV
ERROR INFORMATION FOR SOURCE 1

Case	Pixel Error [x/px, y/px]	Method	MAPE [%]
1	3.589e-4, 1.592e-3	Optimization	10.47
		iGSE	17.18
2	0.079, 9.1e-4	Optimization	17.96
		iGSE	7.90

In Fig. 40, the optimization method has some deviation in shape from the measured data but overestimates the loss for a significant fraction of the points. The estimation method used in the paper has objectively worse results from both a shape and value standpoint,

especially when compared with the iGSE. It should be noted that the Steinmetz coefficient values used for estimation were different from those used in this source. The values in the source were hand-tuned from measurement by the process suggested in [152], while those used in this analysis were extracted as described in Section 3.1.1.

In Fig. 41, the optimization method again deviates in shape and overestimates the loss, while the iGSE computes a much closer value but does not follow the shape and underestimates the loss.

While the error in estimation of core loss is not insignificant, it should be placed in context. If we assume the transformer design to be 99% efficient and dominated by core loss, the errors presented here have smaller than 0.2% impact on the estimated efficiency value at the power level deduced from that figure. At 98% efficiency, the impact increases to just less than 0.4%. For a highly efficient transformer design, this inaccuracy is negligible. Furthermore, in the case of the formula used in the optimization method, the values have been overestimated, meaning that the core will perform better than expected.

4.1.1.2 Source 2

In [28], the actual measurement setup is not specified directly, but rather given as a citation to the measurement standards CECC 25300 and CECC 25000, which are behind a paywall, and not made available through the university's library services. Fortunately, [153] describes the measurement setup in more detail. The input to the transformer was a closely measured and controlled square wave voltage at 20 kHz that produced a triangular flux waveform with a variable dead time between pulses, resulting in a variable repetition rate or variable duty ratio as desired.

The transformer was described only well enough to compute core losses, as the winding construction was completely omitted. The selected core was a Philips E42/42/15 made from 3C85 material.

The data is presented in two figures, excluding the plots of excitation and results for the ferromagnetic material tested in the source. The first figure is a logarithmic plot of the specific core loss as the repetition rate was varied. The second figure is a linear plot of the total core loss as the duty ratio was varied.

Results of comparison with extracted data for these two figures are presented in Fig. 42 and Fig. 43. The pixel error and the error of the two estimation methods with respect to the extracted data are presented in Table XV.

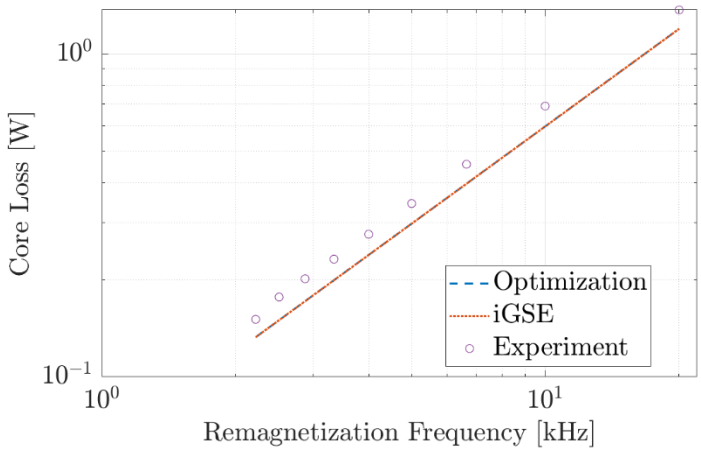

Fig. 42. Results for optimization method and iGSE vs. data extracted from Fig. 6 in Source 2.

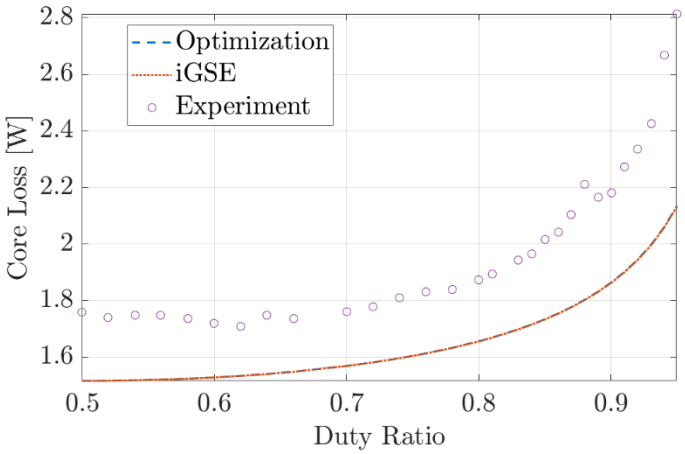

Fig. 43. Results for optimization method and iGSE vs. data extracted from Fig. 8 in Source 2.

TABLE XV
ERROR INFORMATION FOR SOURCE 2

Case	Pixel Error [x/px, y/px]	Method	MAPE [%]
1	6.190e-4, 1.541e-3	Optimization	15.70
		iGSE	15.71
2	1.506e-4, 7.205e-4	Optimization	16.37
		iGSE	16.37

In Fig. 42, the shape of the plot is almost identical to measurement, but with a slight offset. In Fig. 43, the offset persists, but the shape is again very similar, even at higher duty ratio, which is typically a problematic mode of operation for core loss prediction. The two methods used for prediction agree almost exactly in both cases because there are no minor loops in the flux waveform, which is one of the stated assumptions of the optimization method. Again, the Steinmetz coefficients used were different, and for the same reason as in the first source, so the predicted values here differ from those in the source. The effect on efficiency prediction is very close to that in the first source, again assuming a 99 % efficient transformer design. However, a key difference here is that the effect of DC premagnetization on the core has been corrected empirically in the results in

the source, whereas the methods used for prediction here cannot since they are not based on measurement, which is required for such a correction.

4.1.1.3 Source 3

In [30], a setup like that in the first source is used to excite and measure the transformer, which was also the same one used in that source. This is not surprising considering that the students who produced each paper worked in the same lab, under the same PI. It is appropriate to note that this source contains the original publication of the iGSE.

The data is presented as a linear plot of the total core loss as the proportion of the third harmonic component was varied. It is very nearly identical (or perhaps truly identical) to the data from the first source, but it was extracted separately and thus the results will be presented in the same manner.

Results of comparison with extracted data for this figure is presented in Fig. 44. The pixel error and the error of the two estimation methods with respect to the extracted data are presented in Table XVI.

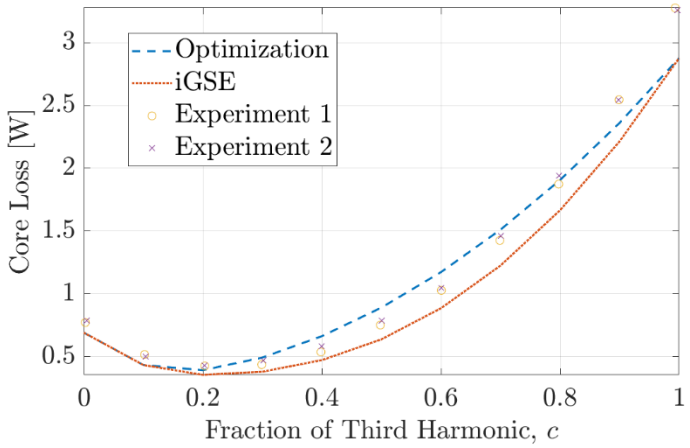

Fig. 44. Results for optimization method and iGSE vs. data extracted from Fig. 4 in Source 3.

TABLE XVI
ERROR INFORMATION FOR SOURCE 3

Case	Pixel Error [x/px, y/px]	Method	MAPE [%]
1	4.674e-4+4.208e-6, 2.254e-6+1.707e-3	Optimization iGSE	10.49 16.99

That there is any difference in the iGSE computation compared to the results in the source is only due to the difference in Steinmetz parameters, which have been consistently taken from [152] in the results from this group. The difference between the MAPE in sources 1 and 3 are explained by either different measurements in the two papers, or by difference in data extraction, or both, as indicated by the slight offset in pixel errors between the two cases. As noted in the introduction in this section, this is due in part to the skewed printing of the plot, which introduces error in both axes for each conversion, though the error from the orthogonal axis is at least two orders of magnitude less in each case.

4.1.1.4 Source 4

In [134], a full-bridge converter was used to excite a transformer in-circuit at 150 kHz with a 0.75 duty ratio rectangular waveform for the main portion of the tests including the

thermal measurements used to deduce the relative losses, while small signal excitation was used to measure the impedance values.

The selected transformer was constructed from a Ferroxcube ETC39/20/13 made from 3C96 material, with a primary of 28 turns of 500/46 litz wire, and a secondary of 14 turns of 1100/46 litz wire, with 1 mm spacing between the two windings for leakage inductance for ZVS.

The results are presented variously, with most data including loss and impedance values given in tabular form, with some additional plots showing the tabulated data graphically in the case of harmonic impedance or the measured output waveforms.

Since there is only one case at a single operating condition, the results of comparison with the data from the source are presented directly in Table XVII. Also, only the absolute percentage error is used instead of the mean of that error, which is identical for a single point.

TABLE XVII
ERROR INFORMATION FOR SOURCE 4

Method\Quantity	Core Loss	Winding Loss
Measurement [W]	0.0733	5.47
Optimization [W]	0.0231	3.24
APE [%]	217.08	40.78
iGSE [W]	0.0231	–
APE [%]	217.14	–

In this case, the losses are quite different from those measured in the source. For the core loss, one factor is the temperature of operation. The core was measured at 36.9 °C for the thermal model computations that were made to determine the winding losses. This value is less than 40 % of the minimum loss temperature value for 3C96 material on the Celsius scale, and ferrite losses (specifically in Ferroxcube's materials) increase quadratically

with distance from 100 °C, by the formula shown in (171) from the SFDT help document [63], which is normalized such that $k_T(100\ ℃) = k$.

$$k_T(T) = k(k_{t2}T^2 - k_{t1}T + k_{t0}) \tag{171}$$

The computed core loss value in the source is also lower than the measured loss, and since it was used to compute the winding loss, it contributes some error; however, this error is quite small, as can be seen from the large difference in loss values between the windings and core.

The winding loss computed by the optimization equation is lower than the measured value in part because the length of the windings is unknown. The length of each wire was used to compute the mean length turn in the source, but without that information, the opposite process was followed to determine the length here. The mean length turn of each winding was computed from the available information about the core and the arrangement of windings in the core window, including a 5% increase in length for litz wire twisting of strands. If this value is hand-tuned or solved in reverse by matching the DC resistance values provided, the result can be made arbitrarily close to the measured value. This has not been done in the presentation here because it would not demonstrate how sensitive the computations are to these parameters.

Given the throughput power of this transformer of 420 W, its efficiency from measurement is 98.68 %, while the computed efficiency is 99.22 %. This is just over half a percent efficiency difference, in an approximate model without complete information about the transformer design, which is an acceptable result. When using the full transformer design script, the values are quite a bit closer, with core loss at 0.0362 W, winding loss at 4.23 W, and an efficiency value of 98.82 %, which is a difference of only

0.14 %, though it is an underestimation of the loss. The design script uses much more sophisticated methods to compute the geometry, construction, and arrangement of the windings, so this demonstrates a high sensitivity of winding loss to physical arrangement.

4.1.1.5 Source 5

In [34], a two-winding measurement method was employed with a full bridge and blocking capacitor for excitation of the primary, and a measurement winding for current and voltage at the secondary. A separate sense winding was used for flux computations, and the entire assembly was immersed in an oil bath to maintain an 80 °C operating temperature. The tests were performed to determine the viability of applying transformations to square excitation measurement data, rather than sinusoidal measurement data typically provided by manufacturers.

The transformer was constructed from a Magnetics, Inc. 442206-TC toroid core made of R material, with a five-turn primary and a five-turn secondary, both of unspecified construction.

The data is downloadable in raw form in various file formats, meaning that no data extraction error needs to be considered. Within the source, this data is presented as a series of figures, which were used to format the results.

Among all the plots, only square wave measurement data was compared. Fig. 45 shows the results of comparison with data for the loss vs. peak flux plot, and Fig. 46 shows the results of comparison with data for the loss vs. on-time plot. Fig. 47 gives the MAPE of comparison for all data as a function of the frequency of operation, while Fig. 48 gives the MAPE of comparison for all data as a function of the on-time.

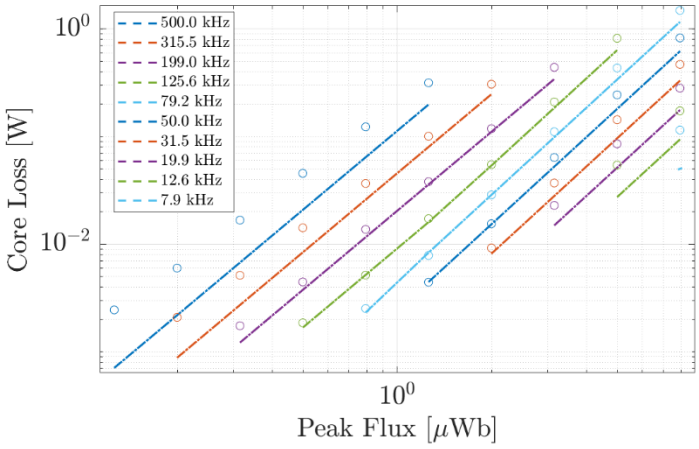

Fig. 45. Results for optimization method and iGSE vs. data from Source 5.

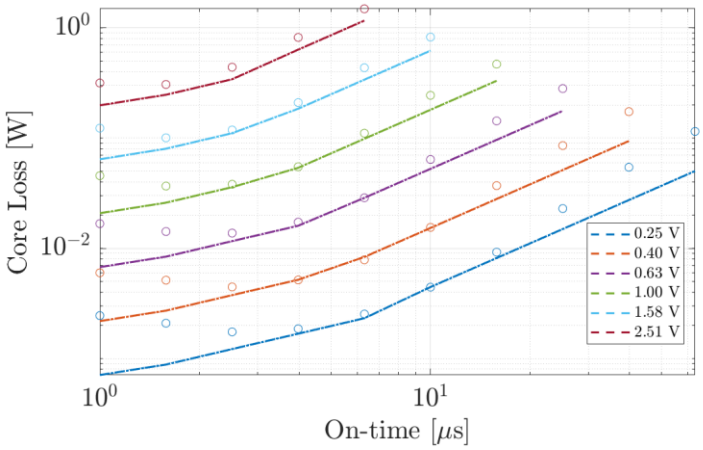

Fig. 46. Results for optimization method and iGSE vs. data from Source 5.

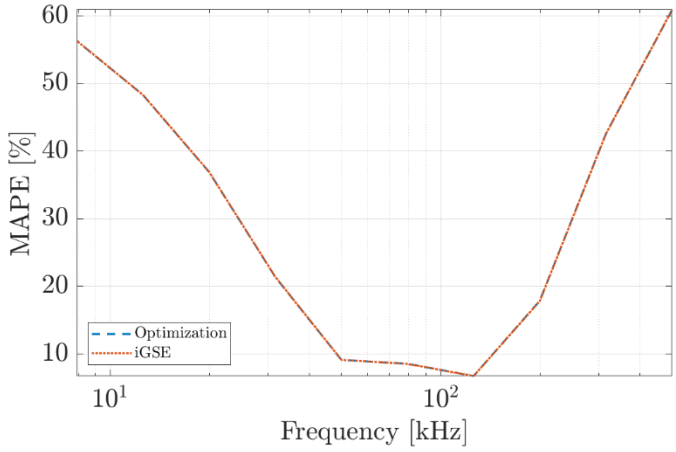

Fig. 47. Error for optimization method and iGSE vs. data from Source 5.

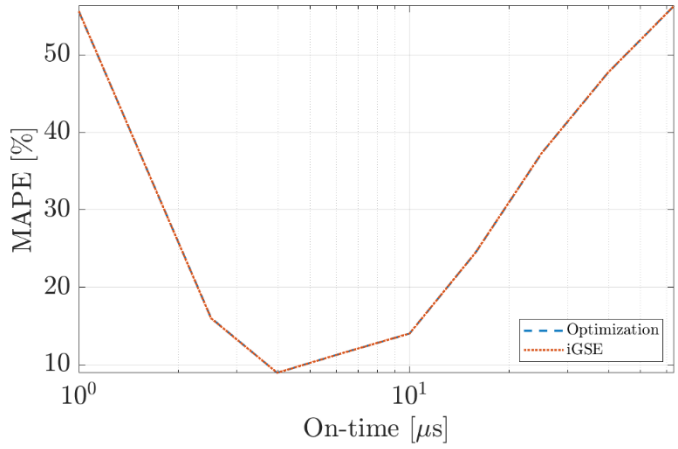

Fig. 48. Error for optimization method and iGSE vs. data from Source 5.

This data makes it clear that very short or very long pulses of constant excitation cause extreme differences in loss in ferrite cores when compared with sinusoidal operation, and when compared with pulses near the center frequency (geometric mean frequency) of a material specified by the manufacturer. This can be seen in the plots in Fig. 47 and Fig. 48, where the manufacturer data gives this frequency implicitly via four curves as $f_c = \sqrt[4]{500 * 200 * 100 * 25}$ kHz ≈ 125 kHz, which corresponds to a period of about 8 µs, or a square wave on-time of about 4 µs. Whether this is the result of manufacturer measurement method, intrinsic material properties, or the curve-fitting process used for parameter extraction is unknown and may be worth investigating.

The core was measured at 80 °C, which again introduces error into the computation methods used here, though it is not the same as the Ferroxcube case. Magnetics Inc. materials have a wider range of minimum loss temperatures. Regardless, a better coefficient modeling method, inclusive of thermal effects should be employed for highest accuracy.

While relatively few sources were able to provide enough information to reproduce their results, the accuracy of the loss estimations appears to be high enough to be useful under the right conditions from those that were. Notable weaknesses include the sensitivity to DC bias and premagnetization, sensitivity to accuracy of predictions of geometry and physical parameters, sensitivity to temperature, and sensitivity to deviation from the center frequency value specified by the manufacturer in the provided loss data from which Steinmetz parameters are extracted. These issues, along with the sensitivity to extreme duty ratios are responsible for the difficulty in predicting losses at design time.

4.2 Microgrid Test Cases

The results in this section are predominantly obtained from five tests of the control strategy outlined in Section 3.2.1 and will be presented as consistently as possible for ease of comparison. The exception is the sixth test, where a step change in real power output reference is applied while the CHIL DSP acts as the primary controller, which is distinct from the others. The five main tests are:

1. A step change in the reference command for real power while in grid-connected mode to demonstrate the power sharing capability of the energy cells.
2. A step change in the reference command for reactive power while in grid-connected mode.
3. A step change in load while in islanded mode, performed by sending an enable command to previously disabled loads at five buses to demonstrate voltage and frequency regulation capability.

4. A 24-hour test of PV generation in islanded mode to demonstrate dynamic power sharing and energy storage balancing capabilities.
5. A demonstration of the tertiary controller's ability to synchronize angle and frequency with the grid while in islanded mode in preparation for reconnection.

There are three PV generation profiles available, so they are distributed in zones as shown in Fig. 18; this distribution also applies to reference commands, which are also in sets of three for simplicity and consistency with the base case. There is a mix of results obtained while using the local central controller and the remote-control software as the secondary control tier. Each will be identified next.

For brevity, we will refer to the base case from [72] as Scenario A, the case with ten energy cells under the original control scheme as Scenario B, and the case with independent control of three inverters as Scenario C. For the fourth test, two additional scenarios, namely D and E, will demonstrate the functionality of the GFI model described in Section 3.3.3. Scenarios B and C each test a single variation on Scenario A for rigor's sake. While ten energy cells participate in generation in Scenario B, the data from the additional energy cells has been omitted for visual clarity; however, their effect can still be seen in the reduced power output in comparison with results from Scenarios A and C. Scenarios A, D, and E were all performed with the local controller acting as the secondary tier of control, while Scenarios B and C used the remote-control software.

4.2.1 Test 1 – Real Power Step Change

This test demonstrates the response to a step change in the real power reference command issued to the first energy cell while operating with the PCC breaker closed. The

total system load is 3490 kW + 1925 kVAr. Three initial real power commands, {1000, 800, 500} kW and three initial reactive power commands, {0, 0, 0} VAr are given to the energy cells at the start of the simulation. A step change to 1200 kW is issued, and the responses are shown in Fig. 49.

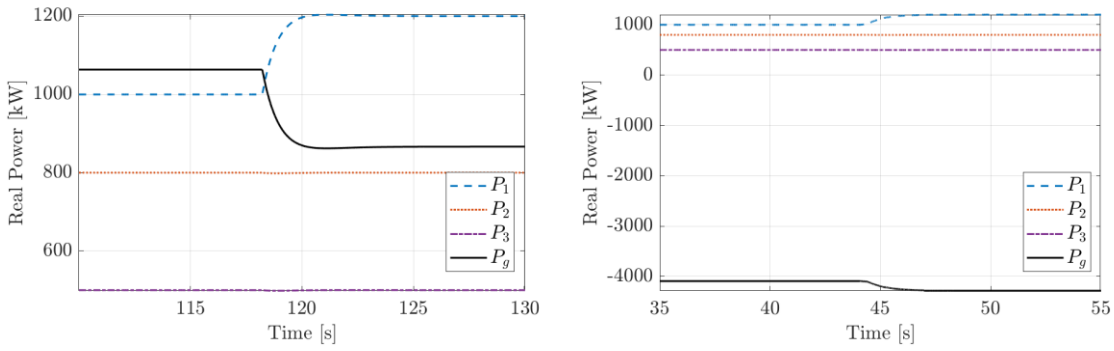

a b

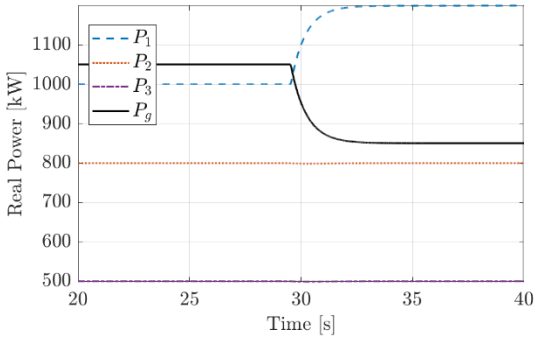

c

Fig. 49. Test 1 results for (a) Scenario A, (b) Scenario B, and (c) Scenario C.

All reference commands are followed as given, within no more than about two seconds of being issued.

4.2.2 Test 2 – Reactive Power Step Change

Like Test 1, this test demonstrates a step response in grid-connected mode, but for reactive power reference command. The same initial real and reactive power commands are issued, and the first reactive power command is changed to 100 kVAr. The responses are shown in Fig. 50.

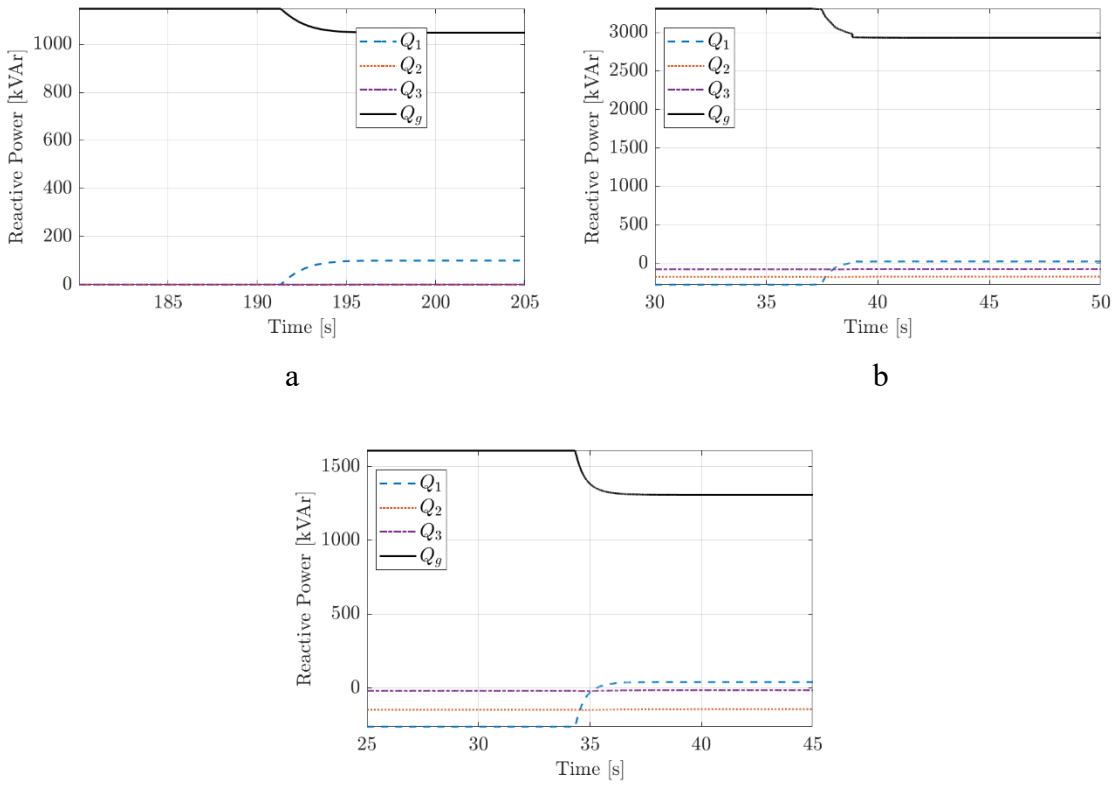

Fig. 50. Test 2 Results for (a) Scenario A, (b) Scenario B, and (c) Scenario C.

In this situation, the results for Scenario B and Scenario C differ slightly from those in Scenario A. The reactive power reference commands are not followed as well when under remote control while in grid-connected mode, including the initial commands of 0 kVAr. Many model revisions were made prior to noticing the error, so it is possible that a destructive change is responsible, since the communication itself does not introduce the error, as will be seen in following test results. Nevertheless, the command to increase reactive power output was followed to some extent; minimizing the error under these conditions will be an important task for future research.

4.2.3 Test 3 – Load Step Change

This test demonstrates the resilience of the system to step changes in load while in islanded mode, with the PCC breaker open. The total system load is initialized without loads at buses 47, 48, 49, 65, and 76, with 2951 kVA in service. The excluded loads, comprising 840 kW and 600 kVAr in total, is switched in during simulation. As generation adjusts to demand, the bus voltage and frequency of the first energy cell are measured and presented in Fig. 51. Both voltage and frequency dips are restored to nominal in each case, maintaining stable operation.

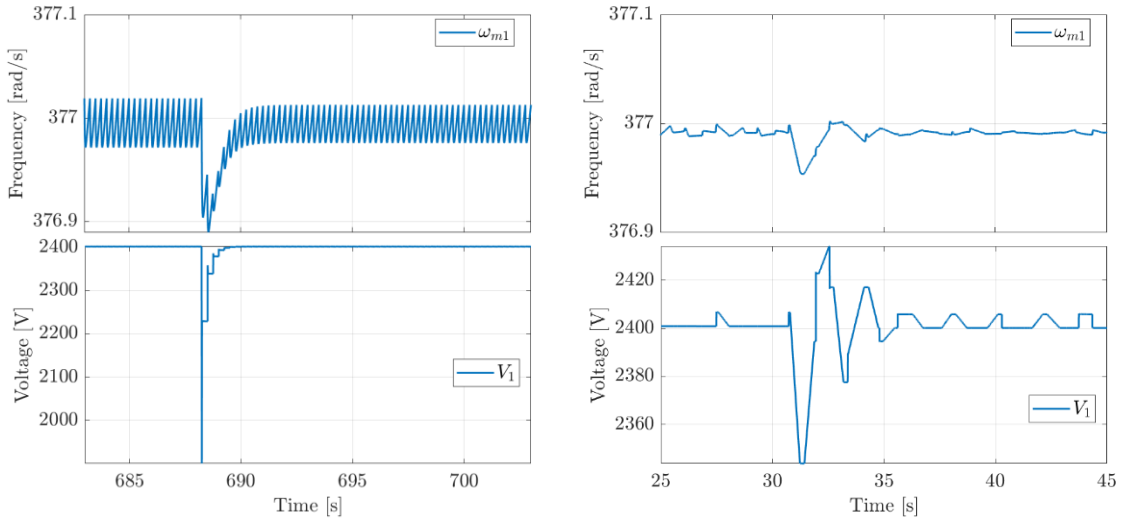

a

b

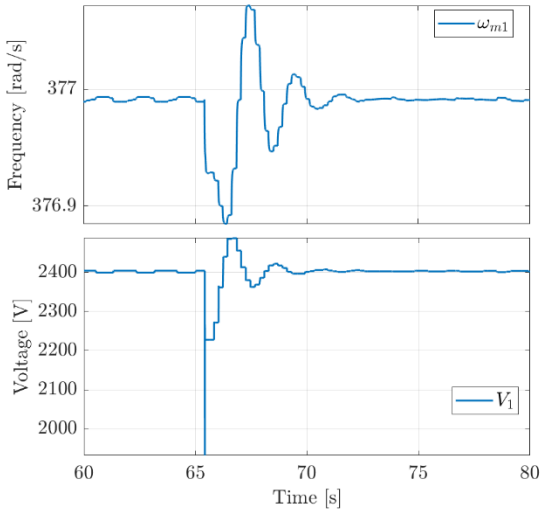

c

Fig. 51. Test 3 results for (a) Scenario A, (b) Scenario B, and (c) Scenario C.

Changes made to the model to support remote-control operation maintained approximately the same response time but introduced a slow, damped oscillation while at the same time diminishing the fast, steady-state oscillation of the previous control mode seen in the measured frequency. This is likely due to the change in integral gain discussed in Section 3.2.1.2.

4.2.4 Test 4 – 24-hour PV Generation Simulation

Fig. 52 depicts the three PV generation profiles used in this test, which demonstrates the dynamic power sharing and energy storage balancing capability of the system while in islanded mode. The PV generation profiles are based on one-day historical data of three real power plants from [143], but their power values are scaled to match the system load level. The real power generation, reactive power generation, and energy storage of the first three cells in the network, as well as the total power generated by all energy cells with a reference line for the static power flow solution from [142] are shown in Fig. 53. The energy storage balancing scheme maintains the stored energy in each energy cell very close to the average, while the reactive power adapts to serve demand and maintain stable apparent power generation.

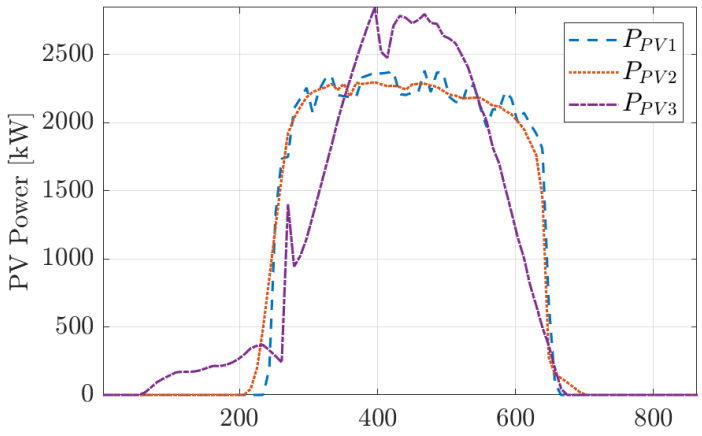

Fig. 52. 24-Hour (864 s) PV generation profile used in simulation.

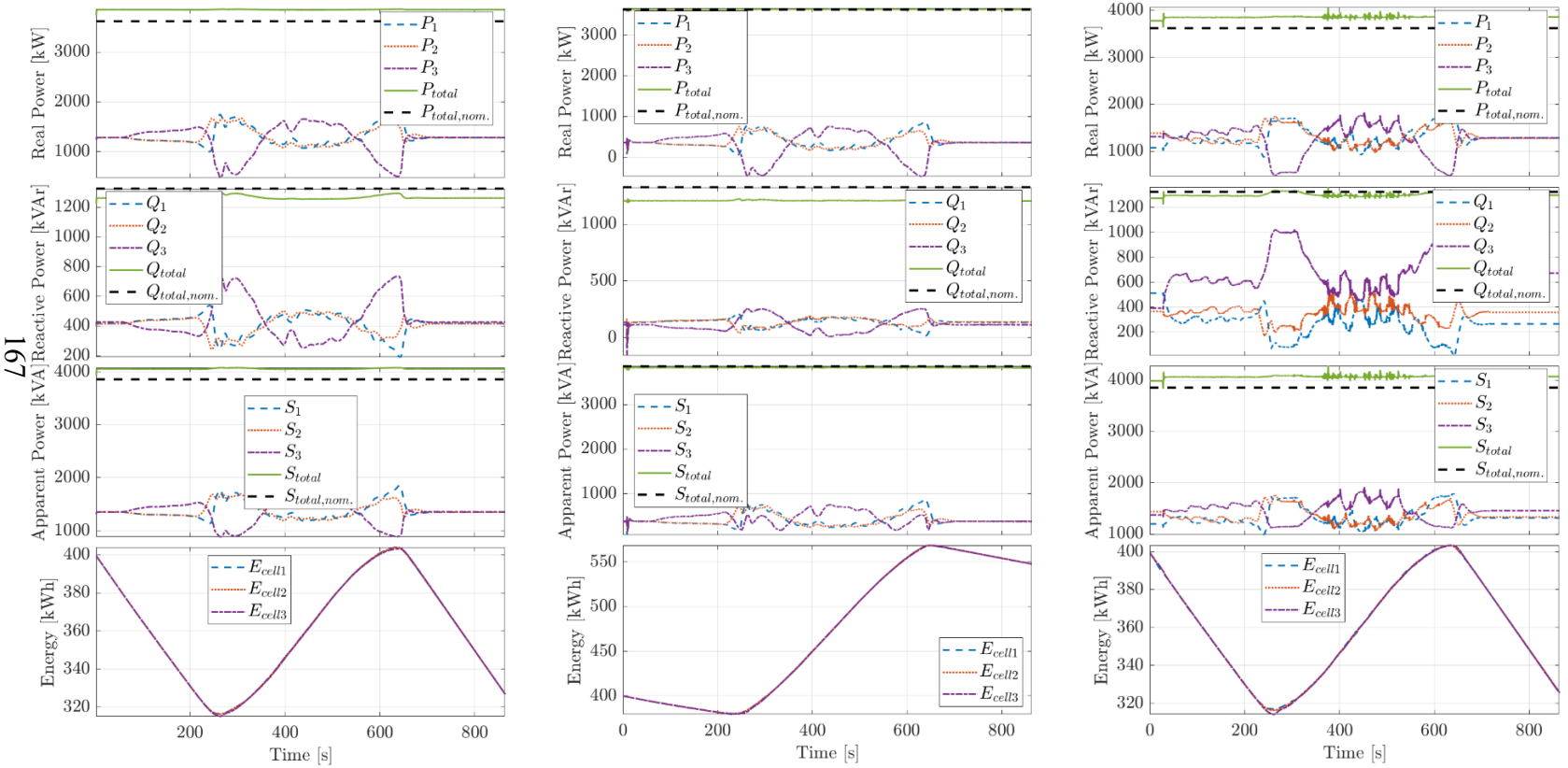

Fig. 53. Test 4 results for (a) Scenario A, (b) Scenario B, and (c) Scenario C. Note that only three of ten total energy cells' values are presented in (b), hence the lower individual values but similar totals.

Scenario C's independent control scheme introduces some interesting pseudo-oscillations into the power sharing. The energy cells' outputs no longer follow the PV curves in Fig. 52, instead drifting up and down in value while maintaining steady mean apparent power output. In Scenarios B and C, the time at which the remote-control software was ordered to take control is visible as a slight dip and spike near the start of the measurement. While the software was programmed to monitor the local controller's commands in order to reduce this sort of disturbance, the local controller has no such capability, and so during the transition it behaves erratically for a brief period prior to deactivation. Additional investigation into making the hand-off smooth from both ends is an important future task for continued research.

Test 4 was also chosen to determine the viability of simulating both the microgrid network and the GFI model simultaneously. As in the previous tests, energy cell currents are scaled by a factor of 10 to bring them to the appropriate level for the IEEE 123-Node Test Feeder, and each energy cell is connected to its network bus by an ideal transformer implemented as a gain of 4160/480 in the simulation.

Fig. 54 shows the power outputs of the energy cells under these conditions along with the energy cells' energy storage levels during the simulation. All energy cells are initialized with 80% of nominal energy storage value, or $E_{cell} = 0.8E_0$ from Table IV.

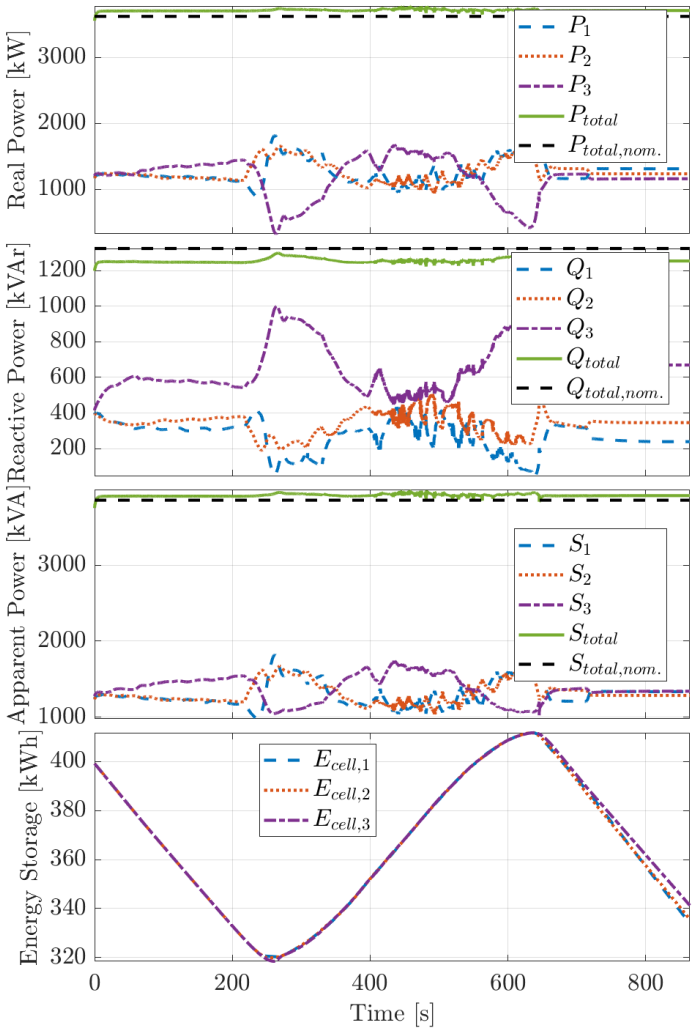

Fig. 54. Test 4 results for Scenario D, with the GFI state space model in place.

The system performs admirably with the inverter model, slightly exceeding the apparent power provided by the grid in the power flow solution given in [142] due to topology changes and storage requirements. In Fig. 54, some deviation in storage homogeneity is visible at the tail end of the simulation where energy cell 3 loses some of its agency to freely adjust its power output while meeting system demand due to lack of generation.

The line-to-neutral bus voltage on the grid side of the ideal transformer and its reference value for the first energy cell are shown in Fig. 55 for the period during which

PV generation is ramping up (approximately 240 s – 290 s). There is significant controller effort during this period as the hierarchical control continuously adjusts all references to meet demand, maintain energy storage balance, and drive bus voltage and frequency deviation to zero.

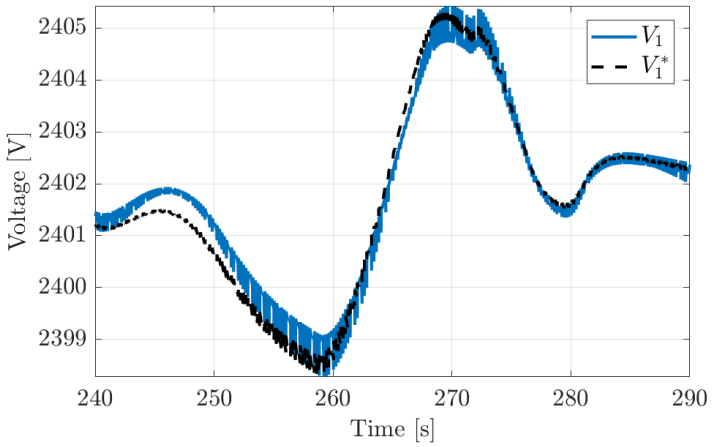

Fig. 55. Phase a bus voltage V_1 and reference value V_1^* for first energy cell during high reference volatility period.

For the same period, the reference tracking error is plotted in Fig. 56 as a percentage of the reference command value. The maximum percent error is quite small, on the order of 0.025 %, demonstrating the suitability of the integral controller for this task.

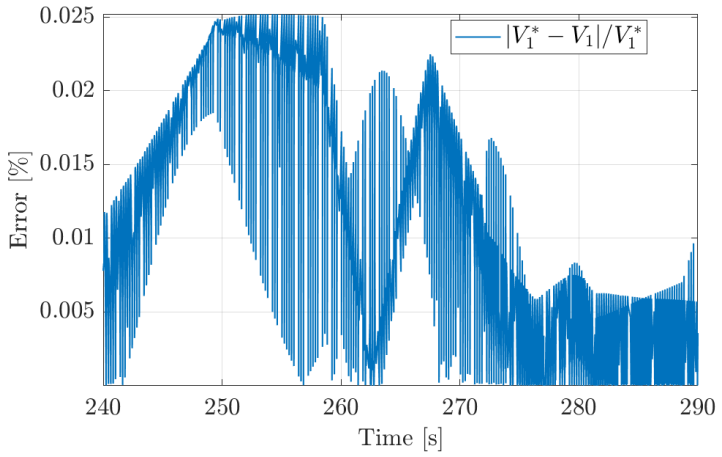

Fig. 56. Percentage error, relative to reference, for first energy cell during period shown in Fig. 55.

A subset of this period is shown in Fig. 57 giving a close view of the response to voltage setpoints during the largest oscillations, when the primary voltage controller is attempting to follow the secondary controller's reference as it adjusts for changing reactive power output.

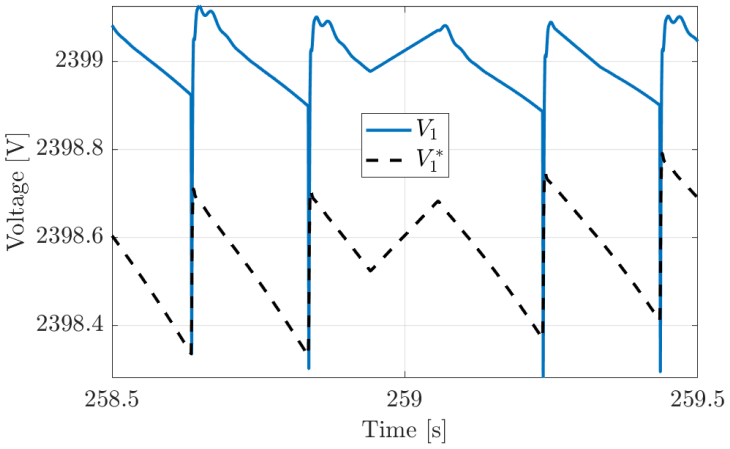

Fig. 57. Close up of largest variation in bus voltages during transient period in Fig. 55.

Fig. 57 shows that the inverter's output voltage undergoes what appears to be a classic undershoot phenomenon, typical of systems with right-half-plane zeros. Since none were observed during plant analysis and the simple controller did not add any, it is

possible that this is the result of leaving the cross-terms uncontrolled. Other possibilities include unforeseen interactions with the output impedance of the network (viewed from the inverter), and numerical error. However, this does not impose large error in the reference tracking, nor excite instability, so it can be neglected.

While it is reasonable to assume that all energy cells would maintain their storage levels near the average value during normal operation due to the energy balancing control scheme in place, contingencies and nonidealities arise in real world scenarios, and so it is valuable to examine the system operation under different initial storage values. Therefore, the system was initialized with storage values $E_{cell,1} = 0.5E_0$, $E_{cell,2} = 0.7E_0$, and $E_{cell,3} = 0.8E_0$, and the simulation was run again to determine the stability of the model and controller under more taxing conditions. The results from the previous scenarios can be compared with the results depicted in Fig. 58, which show the power and energy profiles observed in this fifth scenario.

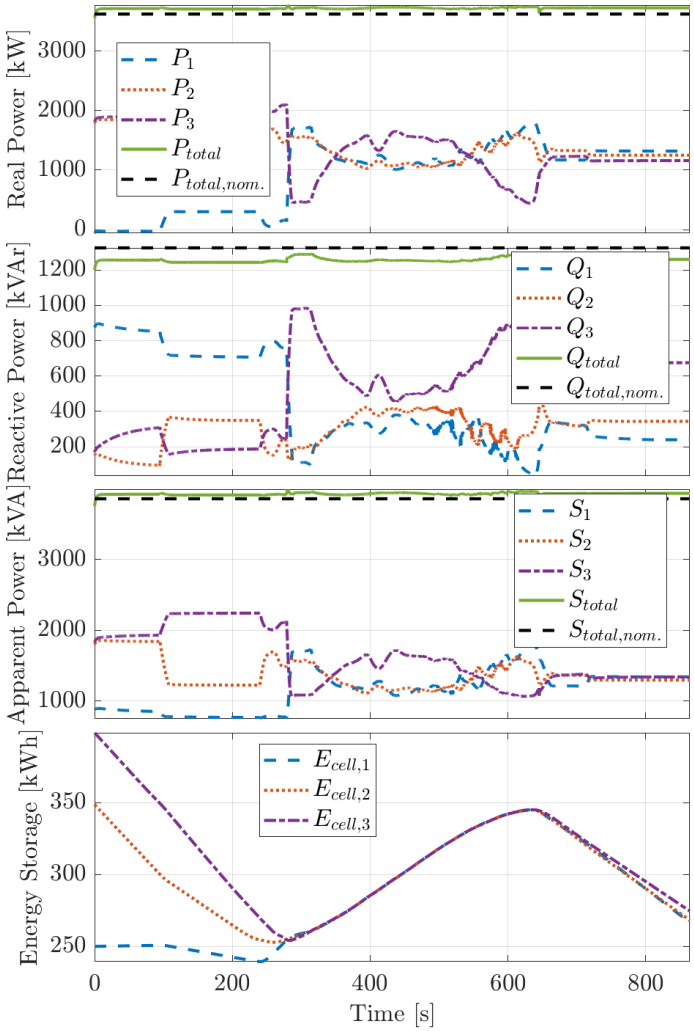

Fig. 58. Test 4 results for Scenario E, with modified initial energy storage values.

Again, the inverters respond adequately to demand, and the control system is further able to regain the energy storage balance after its challenging start. During the first 100 seconds of the simulation, the first energy cell is fed real power slowly by the others from their own storage capacities, with more power delivered from the third energy cell, but as PV generation begins to ramp up, the three cells are quickly brought to the average value. The performance afterward is largely the same as in the previous scenario.

4.2.5 Test 5 – Grid Synchronization

This test demonstrates the capability of the secondary and tertiary controllers to synchronize the microgrid frequency and angle with that of the utility grid. Grid synchronization is activated at 60 s, whereupon the phase difference is compensated within approximately one minute. The results are shown in Fig. 59.

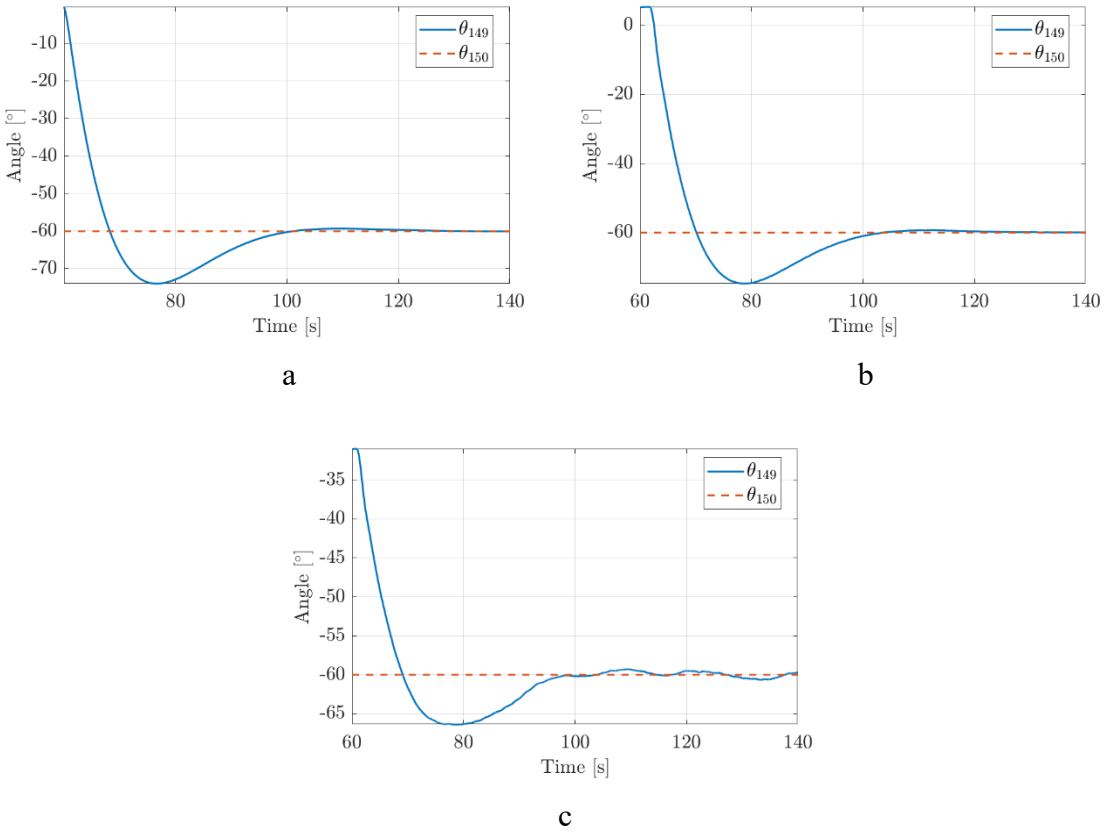

Fig. 59. Test 5 results for (a) Scenario A, (b) Scenario B, and (c) Scenario C.

In the case of Scenario C, a slight oscillation is introduced in the steady-state value, while the angle is corrected slightly faster. Under independent control, the energy cells must exert more effort to arrive at the same value, and because they are all adjusting independently, the final goal is a moving target. Slowing down the secondary controller would most likely reduce this oscillation but would also decrease the response time.

Also visible in these results is the difference in PCC bus voltage angle between the three scenarios. While consistent from run-to-run under the same conditions, the three scenarios each have a different impact on the microgrid-side PCC angle.

4.2.6 DSP Primary Controller Test

Fig. 60 shows the result of a step change to the real power reference command of an energy cell with the DSP acting as its primary controller while in grid-connected operation. The energy cell primary controller is implemented in a TI EZDSP F28335, and is used to control the inverter power stage circuit being simulated in Opal-RT. The inverter voltage and current values are scaled and generated at the Opal-RT analog output to mimic the signals generated by the sensors in the real circuit, which can be read by the hardware. The PWM control signals are generated by the hardware and sent back to the Opal-RT through its digital input ports.

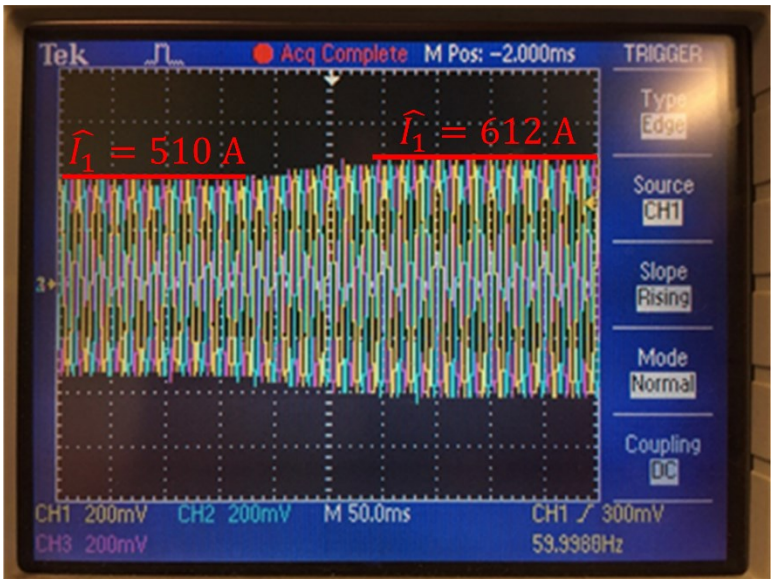

Fig. 60. Inverter current waveform response to real power step change with DSP acting as primary controller.

The measured current waveform amplitude increases commensurate with expectation. Annotations have been added to the figure as estimates of the peak current levels of the waveform based on the power levels used in this CHIL reproduction of Test 1.

4.3 Converters

Results from designed converters will be presented here. The asymmetric half-bridge simulations will be explained, followed by the results of comparison of the SHA model of the DAB with its full model, and results of simulation of the proposed SST, both in PLECS and in the OPAL-RT.

4.3.1 Asymmetric Half-Bridge

The converter presented in Section 3.3.1, with parameters as in Table I, was constructed in PLECS, and non-idealities modeled. The simulation was verified to produce the appropriate output and closed-loop control was designed for the DC-DC stage as mentioned. The DC-AC stage is controlled in open loop, with an ideal sinusoid reference. A pertinent subset of converter schematics is given, alongside the resulting transformer waveforms and a stacked waveform timing plot.

The overall micro-inverter schematic from PLECS is presented in Fig. 61. The PV source is modeled as a simple DC voltage source and resistor, as shown in the schematic in Fig. 62. The DC-AC stage is a standard H-bridge inverter with LC filter, and the closed-loop control of the system is achieved by an outer loop featuring a PI controller for the input voltage reference, and an inner PI controller loop for the duty ratio. Neither the DC-AC stage, nor the control scheme is the focus of this section, so detailed explanations of those will be omitted. The DC-DC stage schematic implemented in PLECS is illustrated in Fig. 63.

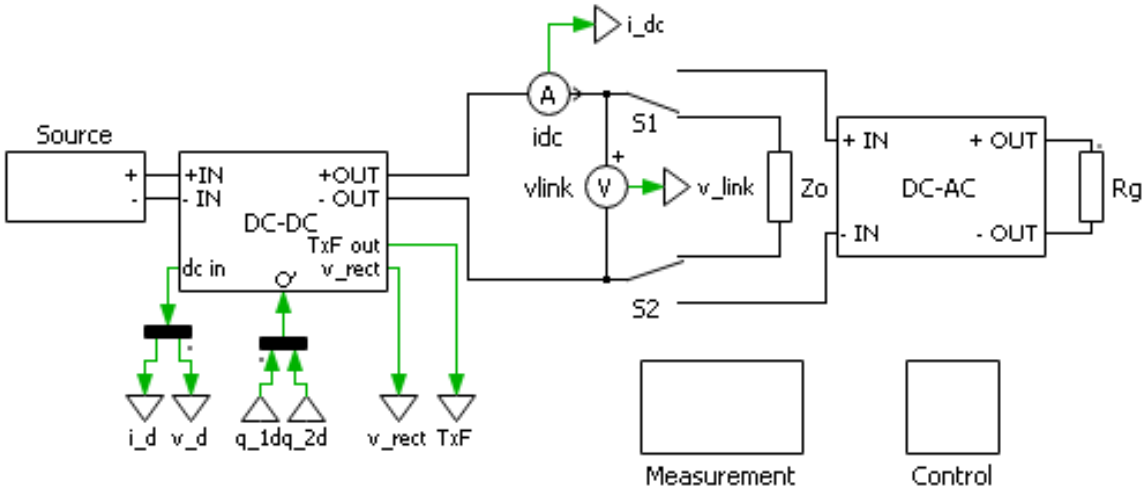

Fig. 61. Complete microinverter system schematic.

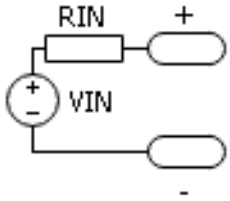

Fig. 62. PV panel source model.

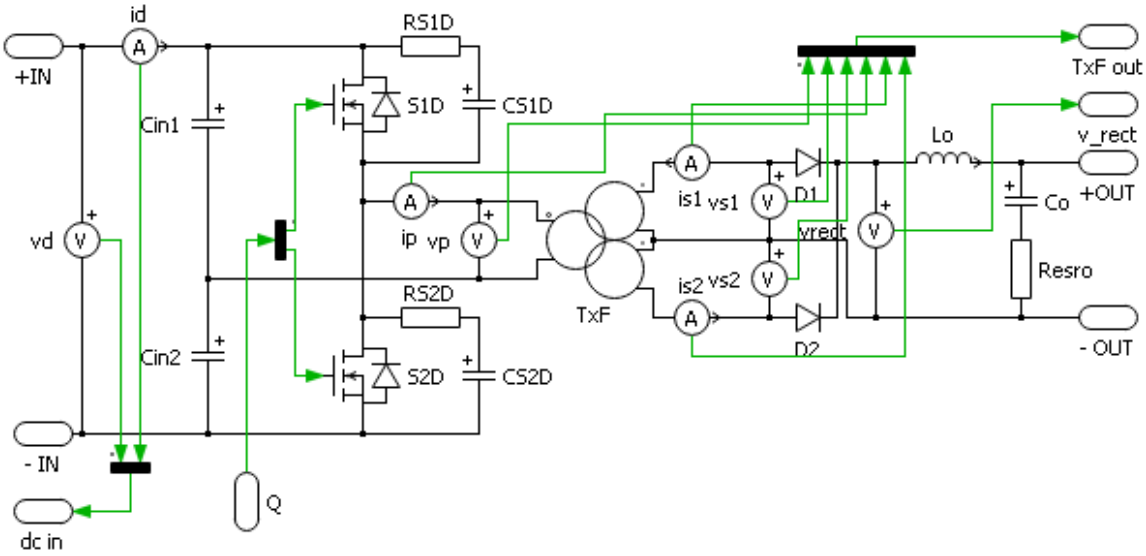

Fig. 63. PLECS schematic of DC-DC stage of micro-inverter.

The transformer voltage and current waveforms for one cycle are given in Fig. 66. It is noteworthy that the primary and secondary voltage waveforms do not appear to have

the same shape; however, this is explained by the simulation method of the transformer model used. The transformer is modeled as shown in Fig. 64, and using MATLAB to calculate the voltage drop across the leakage inductors in all three windings, the waveform resulting from the difference between those drops and the waveforms measured at the terminals reveals that the ideal transformer inside the model is operating as expected. This is shown in Fig. 65, in which the magnetizing current has been calculated in simulation from the difference between turns ratio-scaled terminal currents, and its finite difference computed in MATLAB to determine the voltage at the ideal transformer terminals. The same voltage has also been calculated by subtracting the voltage dropped across the leakage inductance from the primary terminals, and by similar means, the voltage at the ideal transformer terminals on the secondary side. The results are all well-matched, ignoring some small numerical errors from finite difference approximation. Finally, we note that the diodes restrict the flow of current on the secondary side, which is assumed positive into the dotted terminal as in Fig. 64. This rectification, along with the output filter inductor maintains unidirectional power flow into the load, as shown in Fig. 66.

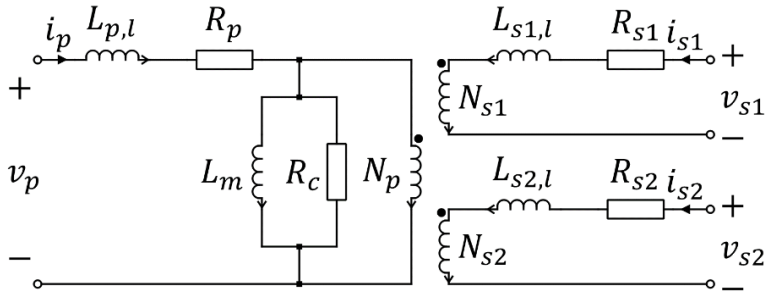

Fig. 64. Internal model of transformer used in PLECS simulation, featuring salient quantities.

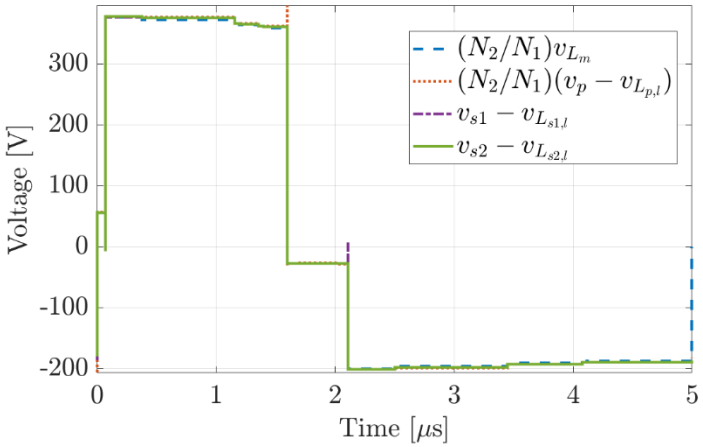

Fig. 65. Ideal transformer voltage inclusive of leakage effects, referred to secondary.

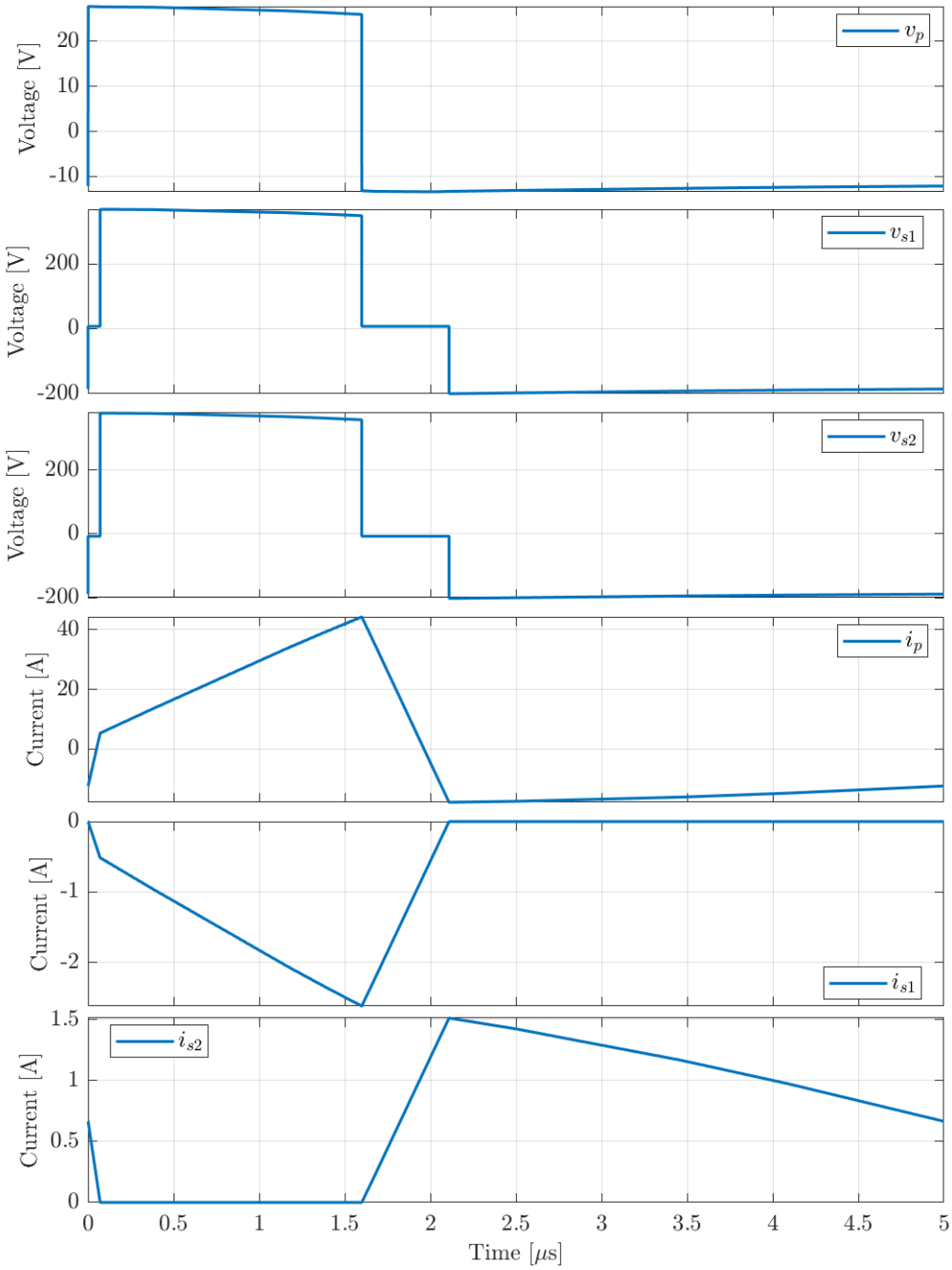

Fig. 66. Transformer voltages and currents in all windings for one cycle at 200 kHz.

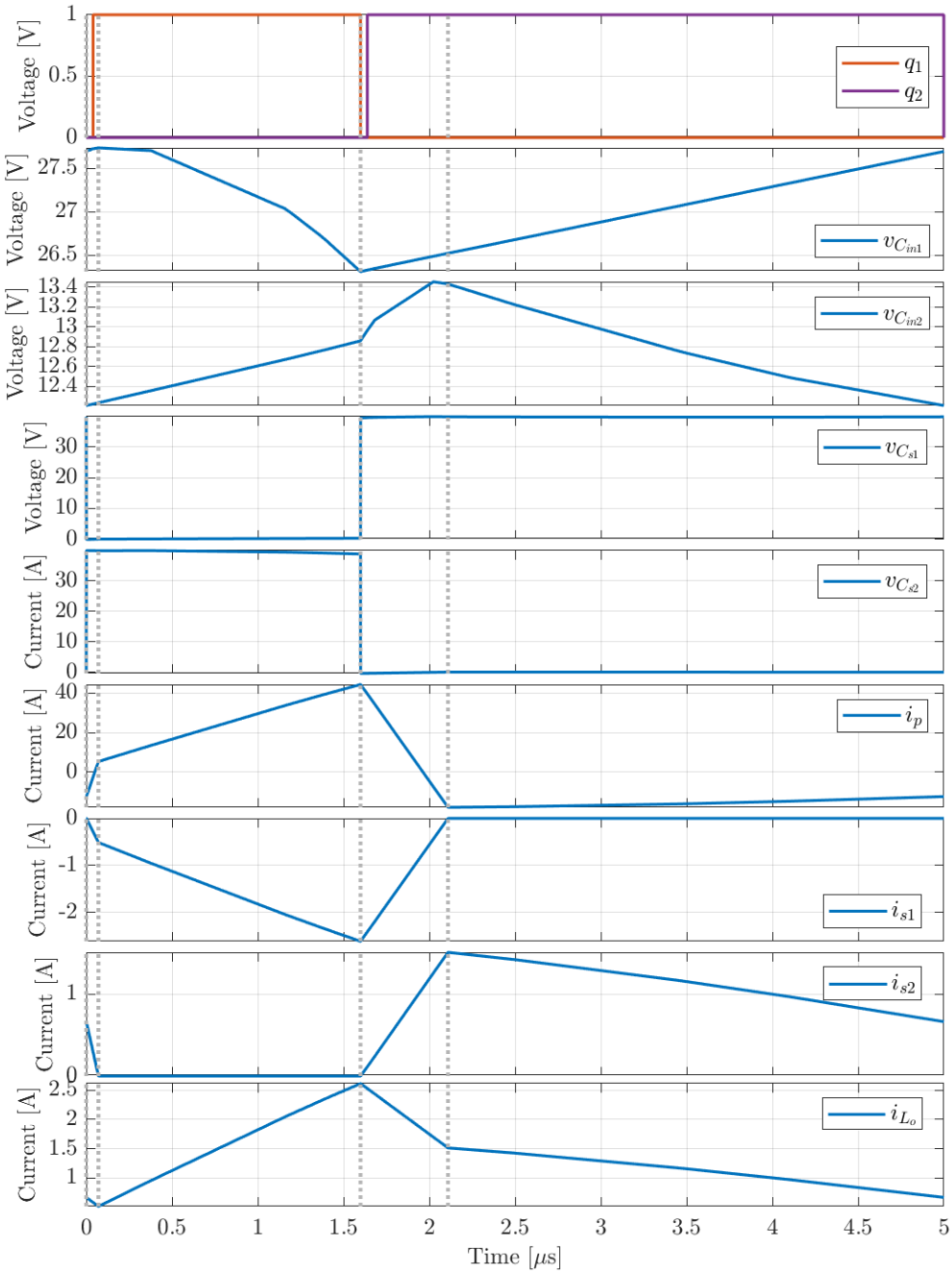

Fig. 67. Waveforms demonstrating timing with respect to energy storage elements in DC-DC stage.

In Fig. 67, the waveforms for the various energy storage components in the DC-DC stage of the microinverter are shown, lumping all winding inductances in with their respective windings. We can roughly partition the waveforms for one switching cycle into four intervals:

1. Diode commutation interval 1
2. Power transfer interval 1
3. Diode commutation interval 2
4. Power transfer interval 2

In steady-state, interval 1 begins when the lower switch opens, and includes the switch dead time and the closure of the upper switch. It ends when the lower diode becomes reverse-biased and stops conducting. When the lower switch opens, the primary winding current must now flow into the switch capacitances (and antiparallel diodes across the switches), bringing the voltage across the upper switch to zero for its imminent closure. Before the interval ends, the primary winding current changes direction and begins to store energy in its magnetic field again, as indicated by the current direction change in the primary winding waveform. The upper secondary winding begins storing energy while the lower secondary winding spends its remaining stored energy on the load through the output inductor.

Interval 2 begins when the lower diode stops conducting and encompasses the first power transfer interval. The primary winding current increases throughout the interval, bolstering its magnetic field energy storage while transferring power to the secondary side of the circuit, which is handled by the upper primary winding, and handed off to the load through the output inductor.

Interval 3 starts when the upper switch is opened and begins with another short current transient as the lower switch voltage is brought to zero for its imminent closure. It includes the dead time between the upper and lower switch transition, as well as the lower switch closure mentioned above. During this interval, the primary winding exhausts its stored energy and switches direction again, while current through the upper secondary winding drops to zero, and current in the lower secondary winding rises from zero. The output inductor maintains the current direction while sacrificing some of its stored energy to the load. The interval ends when the upper diode is reverse-biased.

The second power transfer interval, interval 4, begins when the upper diode is reverse-biased and ends when the lower switch opens. The primary winding transfers its stored energy to the output side through the lower secondary winding and through the output inductor, ultimately being delivered to the load.

ZVS is achieved in this simulation, as is clearly demonstrated in Fig. 68. For both switches, the drain-source voltage is brought to zero or just below prior to the turn-on signal at the gate. This reduces the switching loss during the initial switch conduction, when an inrush of current would create a spike in power loss, were the voltage still in transition. This exchange of capacitor charge, and thus, voltage, is made possible by the inductance in the transformer. Since inductance resists the change of current flow, the inductance in the transformer must be sufficient to maintain at least the minimum current necessary to drain charge off the parasitic capacitance of the switch in question for the duration of the dead time between switching events. The application of equation (135) for this converter with 40 ns of dead time results in a minimum inductance of 98.5 nH.

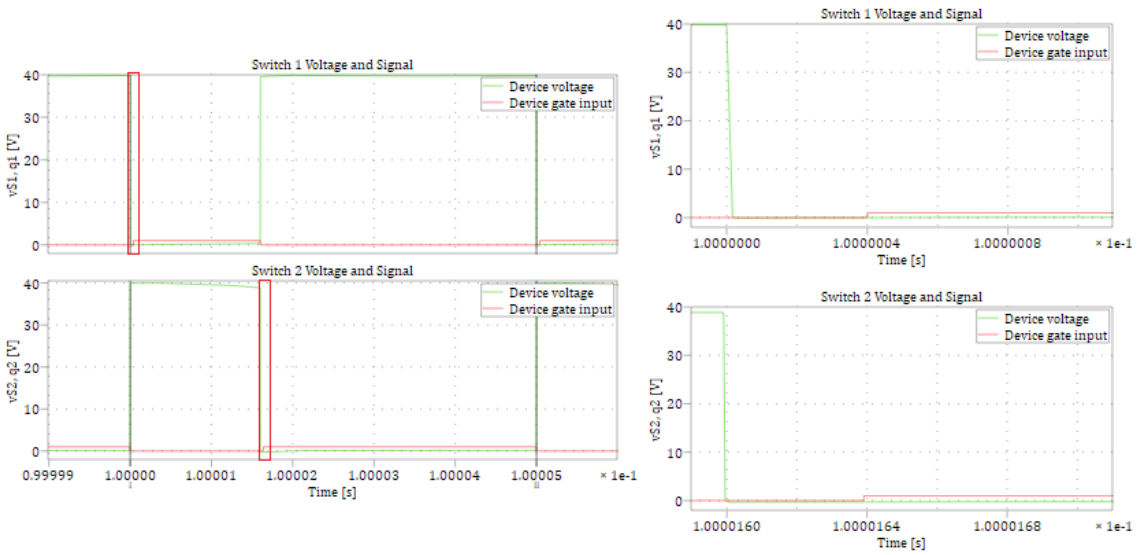

Fig. 68. Switch drain-source and gate signal voltages from PLECS simulation. Outlines on the left correspond to zoomed views on the right.

4.3.2 Stand-alone DAB

In order to test the SHA model of the DAB, the converter circuit was constructed in PLECS and an explicit state space representation was created, as shown in Fig. 69. This allows measurement and comparison of the states, which is not possible using a transfer function or state space block.

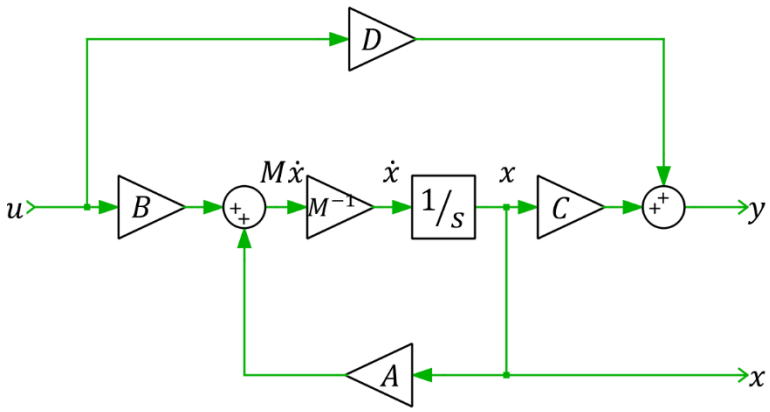

Fig. 69. Explicit state space model used in PLECS simulation.

The results of a representative cycle of operation for the states under open-loop control are shown in Fig. 70. The harmonic analysis for the same period is shown in Fig. 71.

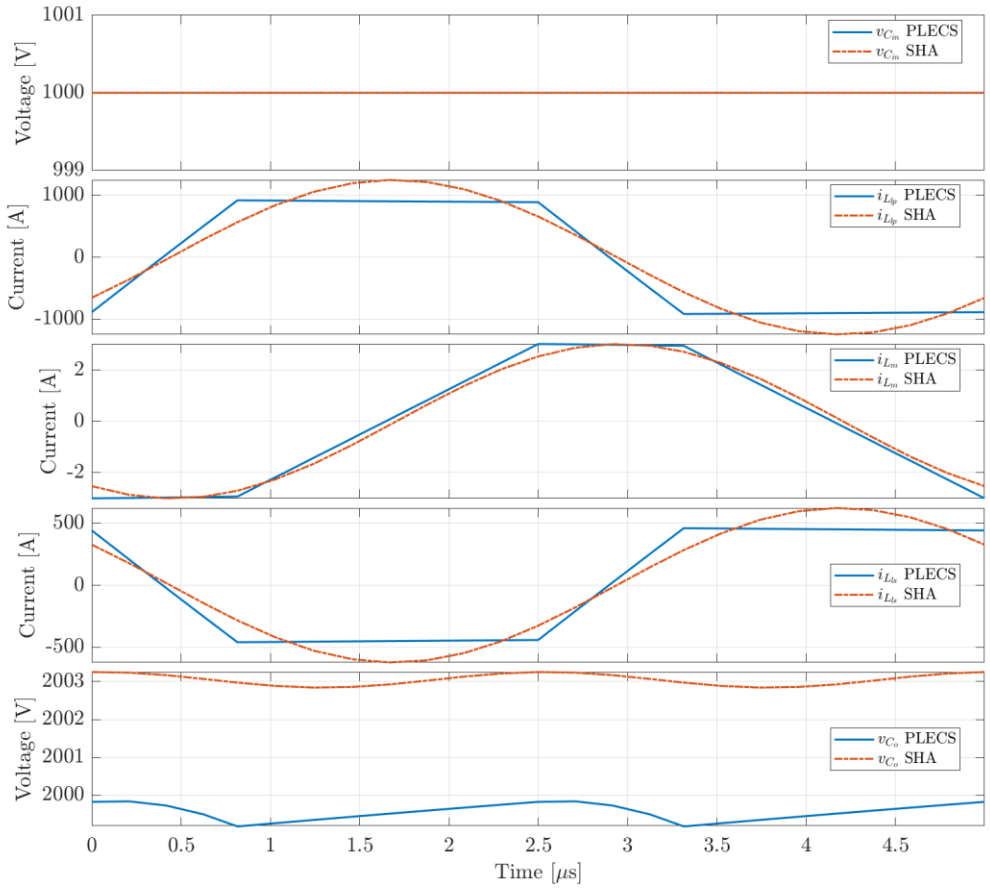

Fig. 70. DAB state dynamics in stand-alone simulation under open-loop control.

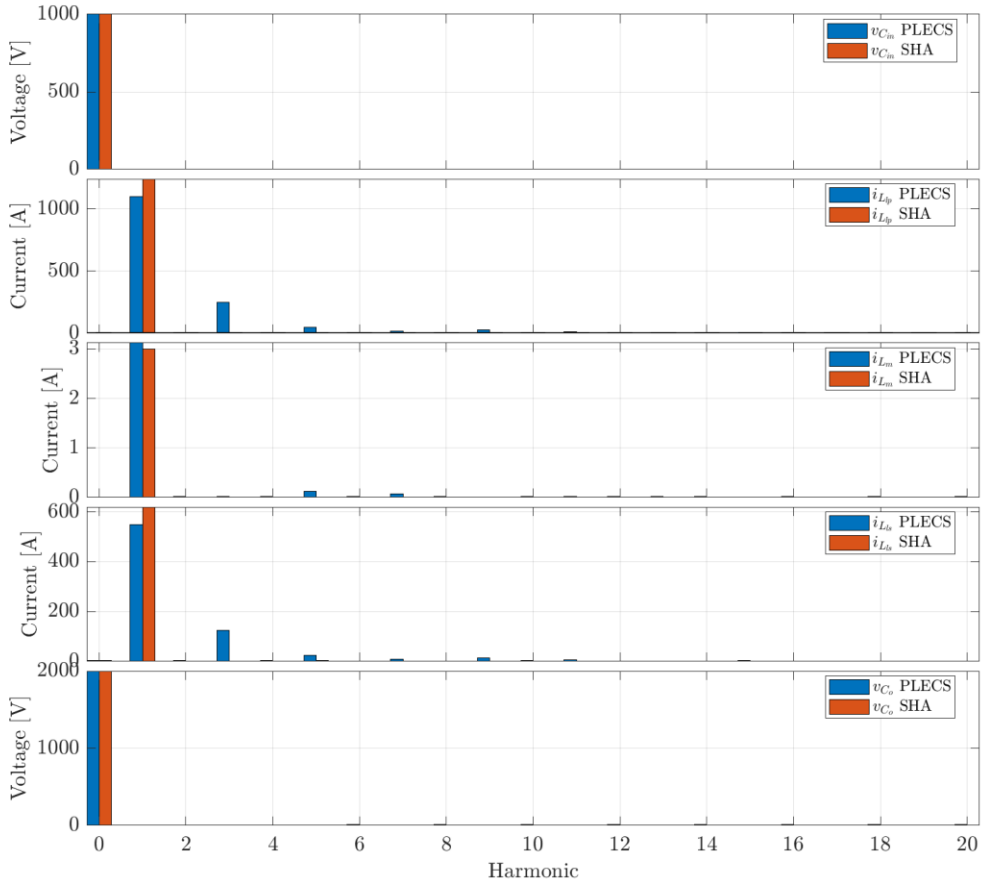

Fig. 71. DAB state harmonic analysis in stand-alone simulation under open-loop control.

The results show that the SHA predicts the behavior of the circuit well, and that it attempts to absorb the higher order harmonics into the highest represented harmonic via the correction from [97]. This makes the first harmonic larger than the simulated value, as can be seen in the plots in Fig. 71 for the transformer currents.

The results of a representative cycle of operation for the outputs under open-loop control are shown in Fig. 72. The harmonic analysis for the same period is shown in Fig. 73.

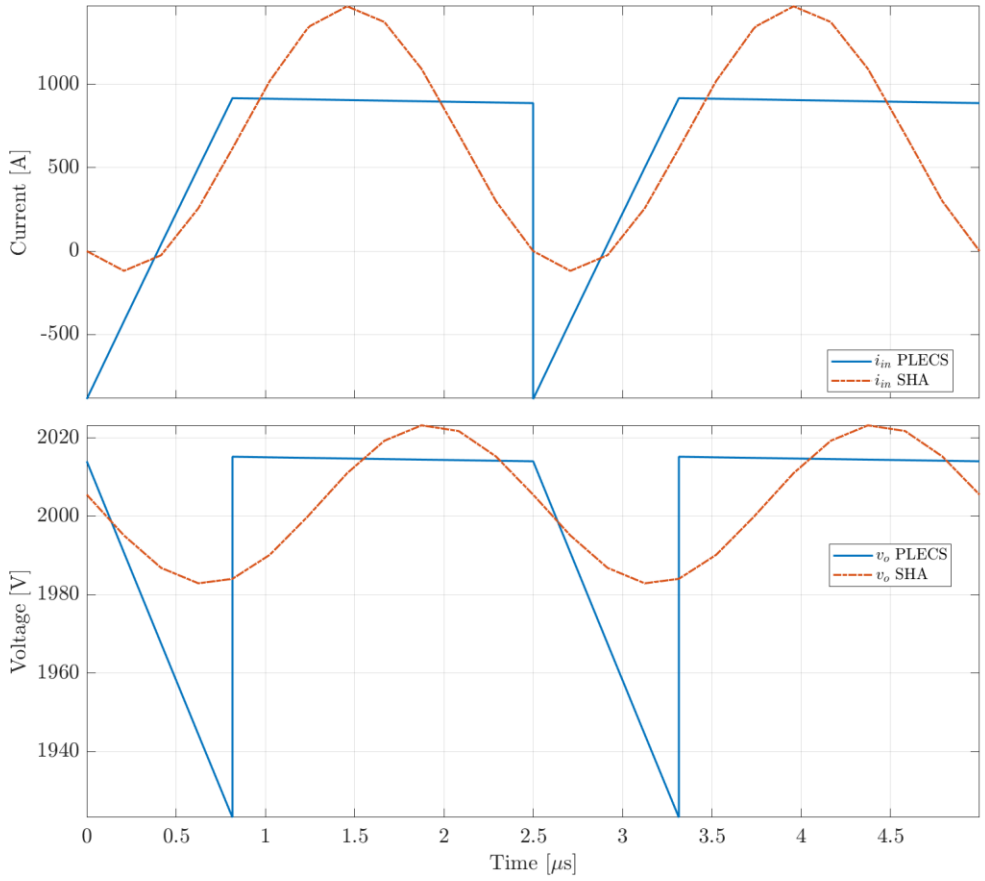

Fig. 72. DAB output dynamics in stand-alone simulation under open-loop control.

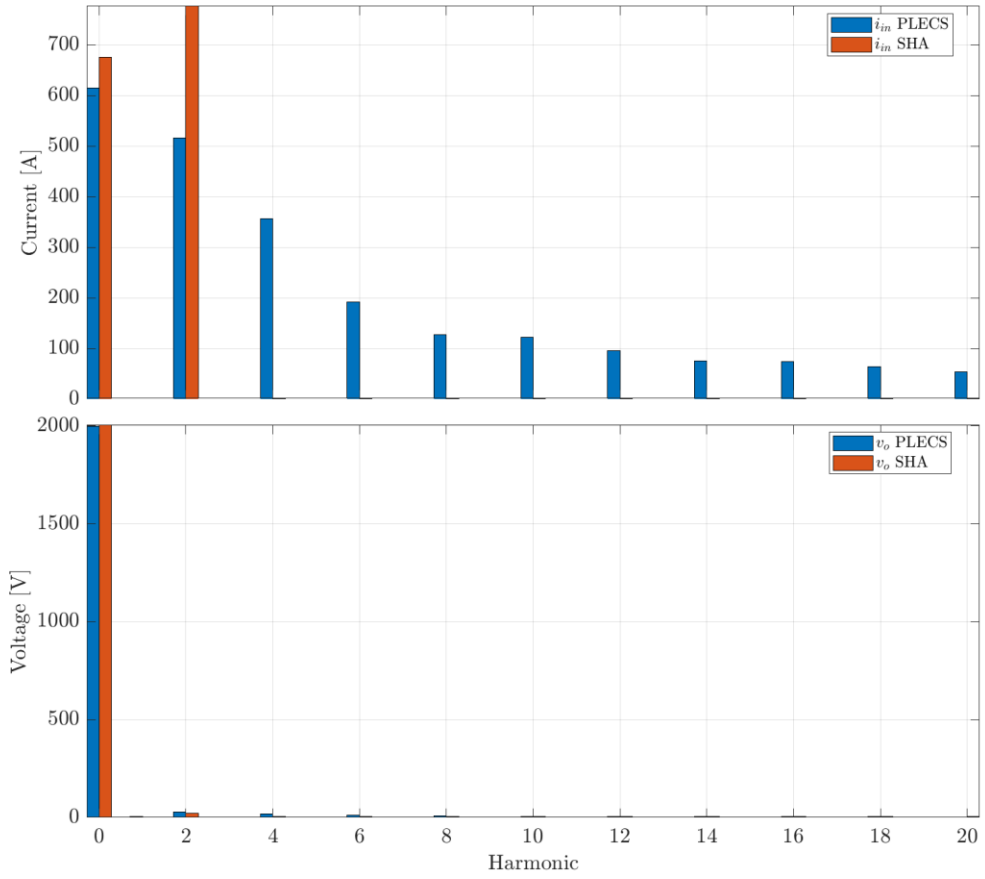

Fig. 73. DAB output harmonic analysis for stand-alone simulation under open-loop control.

Here the input current has significant even harmonic component contribution, but only the second harmonic has been modeled, as described in Section 3.3.2. The correction equation again attempts to capture higher order harmonics in the highest harmonic represented, but it appears to fall short of its goal in the case of the current. In the voltage case, while the values are much smaller, it is readily apparent from the waveshapes in Fig. 72 that there is still significant error. This correction, while a step in the right direction, is inadequate for the level of model detail and its harmonic order.

For the sake of brevity, the component values have been withheld, and will be given along with the description of the SST in the following section.

4.3.3 Truncated SST

The PLECS simulation in the previous section was expanded to include the parallel GFI models to form the complete modular truncated SST topology (Fig. 33) in order to demonstrate its functionality under both open- and closed-loop control of the DAB. Since this is a simple offline simulation without any microgrid elements, sine-triangle PWM open-loop control was employed to manage the output voltage of the GFI. Table XVIII gives the component values used in simulation.

TABLE XVIII
TRUNCATED SST SIMULATION COMPONENT PARAMETERS

Simulation Component	Value
LV DC Input Voltage, V_{in}	1 kV
DAB MOSFET On-Resistance, r_{on}	10 mΩ
GFI MOSFET On-Resistance, r_{sw}	10 mΩ
LV DC Link Capacitance, C_{in}	100 µF
HV DC Link Capacitance, C_o	391 µF
LV DC Link Capacitor ESR, R_{ESRin}	1 mΩ
HV DC Link Capacitor ESR, R_{ESRo}	100 mΩ
Transformer Magnetizing Inductance, L_m	282.98 µH
Transformer Equivalent Core Resistance, R_c	1495.9 Ω
Transformer Primary Impedance (comb.), Z_p	$0.7075 + j553.8$ mΩ
Transformer Secondary Impedance (comb.), Z_s	$0.003 + j2.294$ Ω
Transformer Turns Ratio, $N_1 : N_2$	$1 : 2$
Filter Inductor Series Resistance, r_L	20 mΩ
Filter Inductance, L	20 mH
Filter Capacitor Damping Resistance, R_d	2 Ω
Filter Capacitance, C_f	7 µF

The transformer winding values are given in Table XVIII in the parallel-combined form shown in the bottom of Fig. 25, but in the simulation the transformer was modeled in full, so Table XIX gives the complete list of winding resistance and leakage inductance values

used, as computed by the transformer design script. Windings are numbered by increasing distance from core center leg. The transformer is constructed from a pair of Ferroxcube E100/60/28 cores (in E-E configuration) made of 3C90 material, with five parallel primary windings, each with three turns of 660/38 type II litz wire, and five parallel secondary windings, each with six turns of 420/38 type II litz wire.

TABLE XIX
INDIVIDUAL IMPEDANCE VALUES FOR DAB TRANSFORMER WINDINGS

		Winding				
Side	Quantity	1	2	3	4	5
Primary	Resistance [mΩ]	2.72	3.17	3.62	4.07	4.52
	Inductance [μH]	1.97	2.07	2.20	2.35	2.51
Secondary	Resistance [mΩ]	11.1	12.9	14.7	16.5	18.3
	Inductance [μH]	8.12	8.52	9.05	9.81	10.54

Tests results are given below, with discussion to follow. Fig. 74 shows the open-loop state dynamics over a representative cycle of the DAB switching frequency. Fig. 75 gives the harmonic analysis of the states over the period in Fig. 74. In these figures, the output capacitor measurements were taken with a periodic average filter set to average values over a 5 μs period.

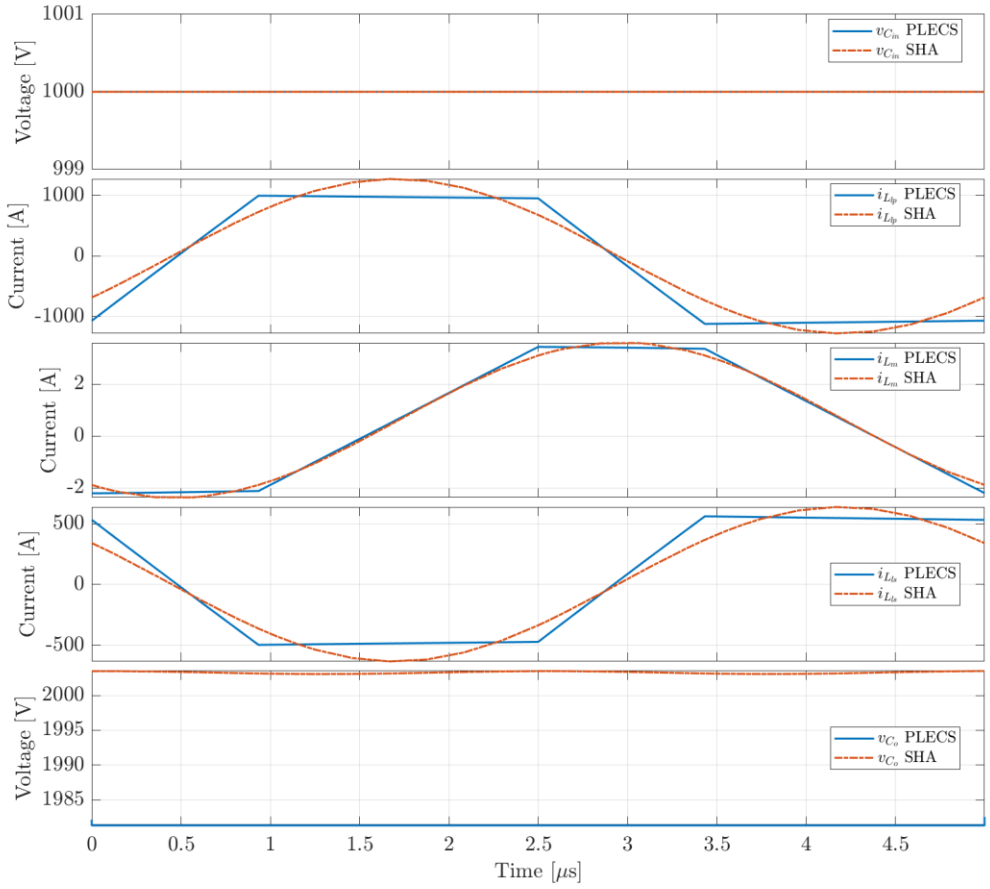

Fig. 74. DAB state dynamics during DAB switching period under open-loop control in full SST model.

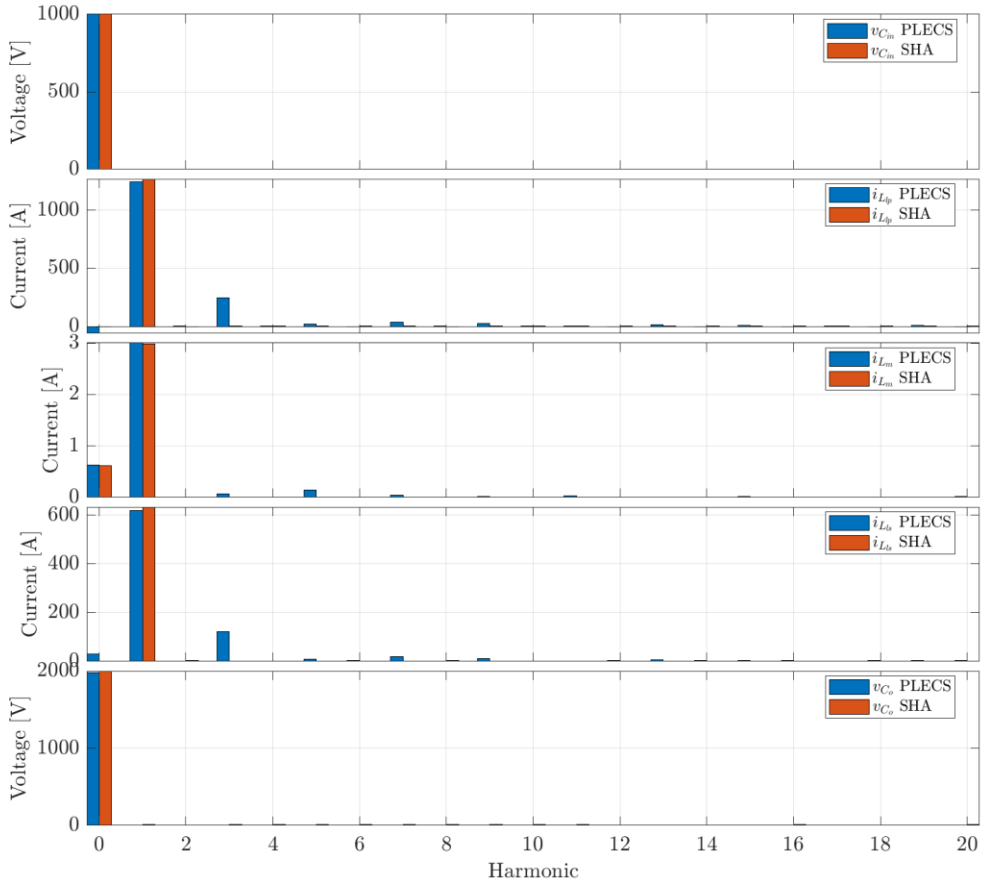

Fig. 75. DAB harmonic analysis during DAB switching period under open-loop control in full SST model.

Under open-loop control in the full model, the correction equation has not been applied to the base duty ratio, hence the much closer match seen in the harmonics. The correction is applied to the closed-loop control duty ratio, and its effect will be seen in the next set of figures. The reason for the large offset seen in the output capacitor voltage in Fig. 74 is two-fold. The correction has not been applied, which reduces the accuracy, but this effect is minimal as shown by the DC component of the output capacitor voltage in Fig. 75. The impact of the output voltage ripple due to the GFI switches makes up the difference, and it is not shown in the harmonic analysis because it is one twentieth of the

frequency of the fundamental for the DAB. It can be seen in the next set of figures, which features the period shown in Fig. 74 as the first 5 µs.

Fig. 76 shows the closed-loop state dynamics over a period of the GFI switching frequency, while Fig. 77 shows the output of the DAB during the same period.

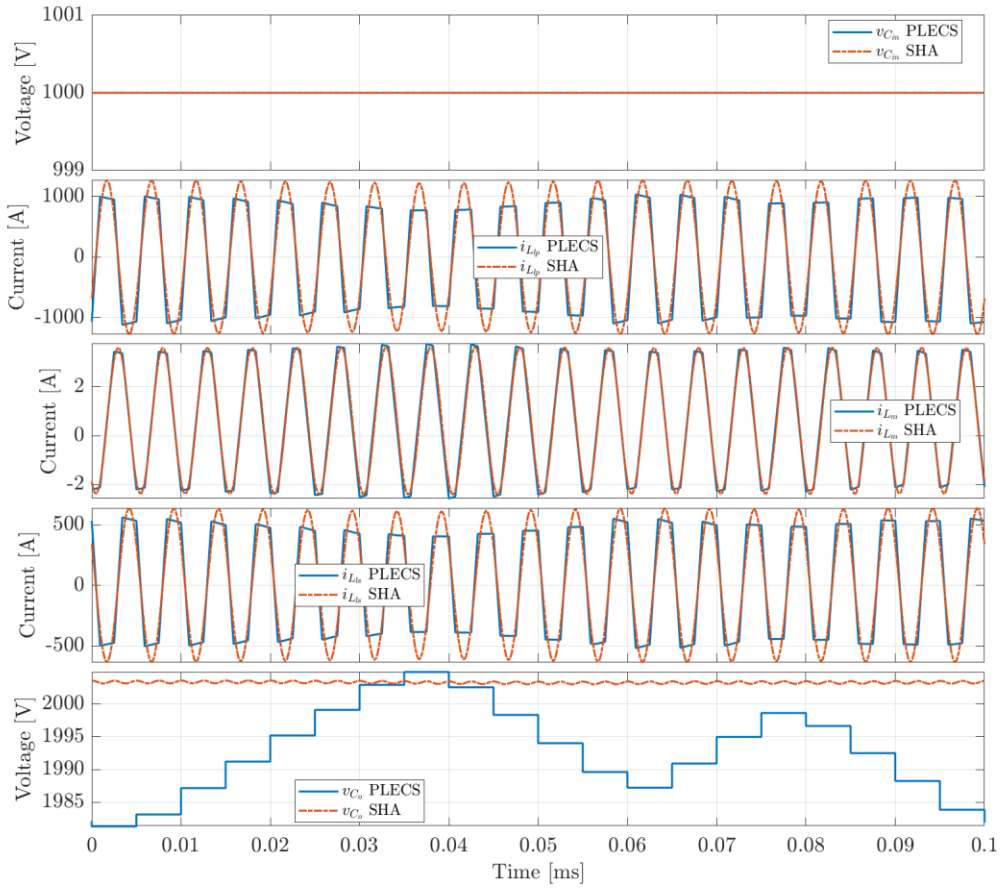

Fig. 76. DAB state dynamics during GFI switching period under closed-loop control in full SST model.

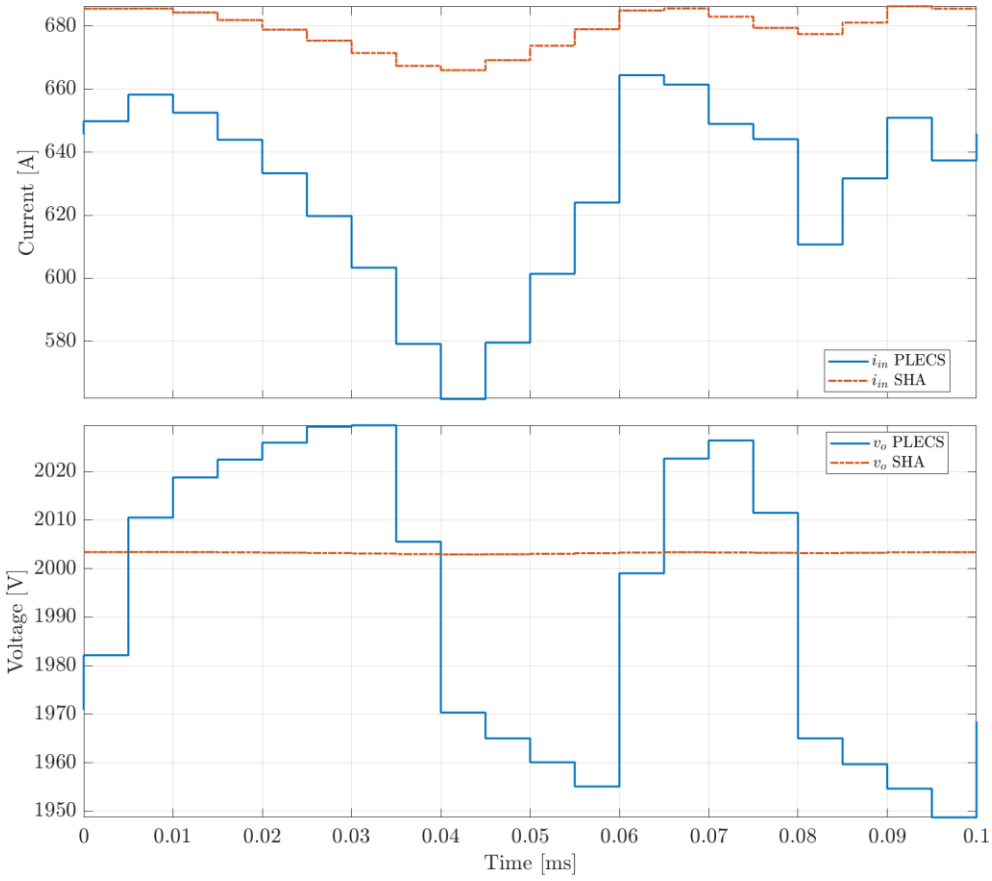

Fig. 77. DAB output dynamics during GFI switching period under closed-loop control in full SST model.

These figures demonstrate the result of applying the correction to the duty ratio under closed-loop control, wherein the values are increased to account for the higher order harmonics. With closed-loop control of only the output voltage, the input current deviates significantly from the desired steady-state DC value of 600.74 A. Since the prior stage of the energy cell is not modeled in detail, this should have little impact on the overall simulation, but for future research, an inner and outer loop control structure should be designed to more closely regulate this current.

The real power outputs of the DAB and GFI and their averages are shown in Fig. 78.

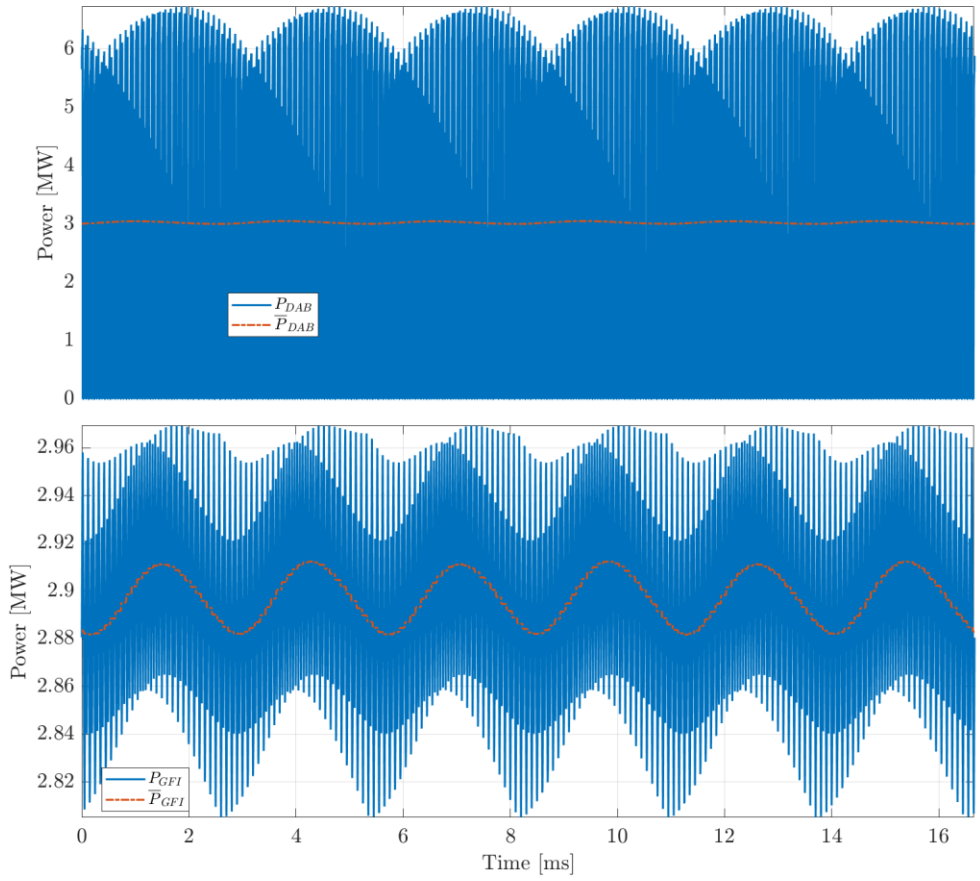

Fig. 78. DAB and GFI output powers and their averages over a single line frequency cycle under closed-loop control of the DAB and open-loop control of the GFI in full SST model.

The DAB under closed-loop control produces its 3 MW rated power output with only a slight ripple due to the GFI array's influence. Since the GFI is under open-loop control, it produces whatever power it can produce given the DAB output and the losses incurred in the switches and filter components. This is rectified in the full simulation, wherein both stages are tightly controlled. Furthermore, the output of any given energy cell is never at rated value during the simulated conditions, so this is not a cause for concern from a generation standpoint, nor from a component rating standpoint. Nevertheless,

future work with such a model should ensure that components are appropriately rated to handle the expected throughput power in each stage, as has been done here.

In order to simulate the model in the OPAL-RT, it was noted previously that the SHA model of the DAB needed adjustment to provide values suitable for simulation at 100 µs time step. The initial plant is stable but has a negative gain. The resulting closed-loop controller was designed to have approximately the same bandwidth as the controller for the GFI and has similar performance with pure integral control with a gain of -1.216. Fig. 79 shows the bode plot of the open loop system, while Fig. 80 demonstrates the step response of the closed-loop system.

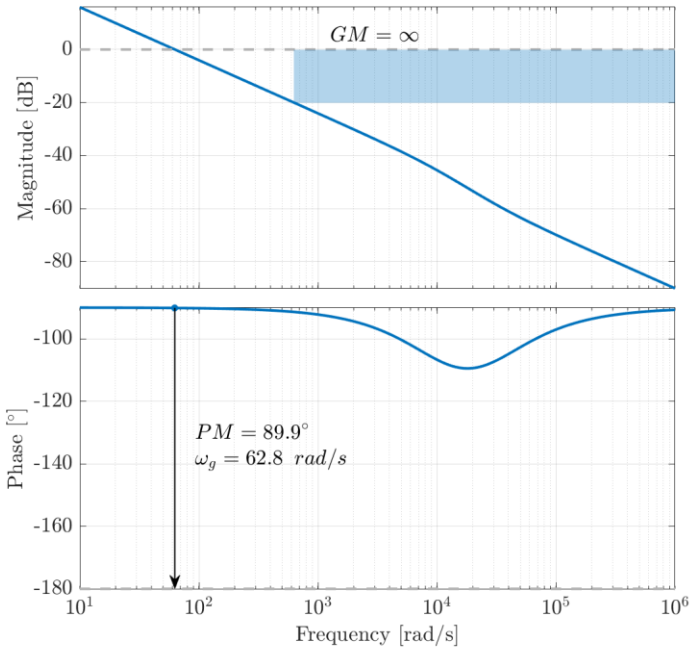

Fig. 79. Open-loop response of L_{DAB} with integral control, highlighting the unity gain crossover frequency and its phase margin, the infinite gain margin, and the high-frequency roll-off exclusion region ($|L_{DAB}| \leq -20$ dB).

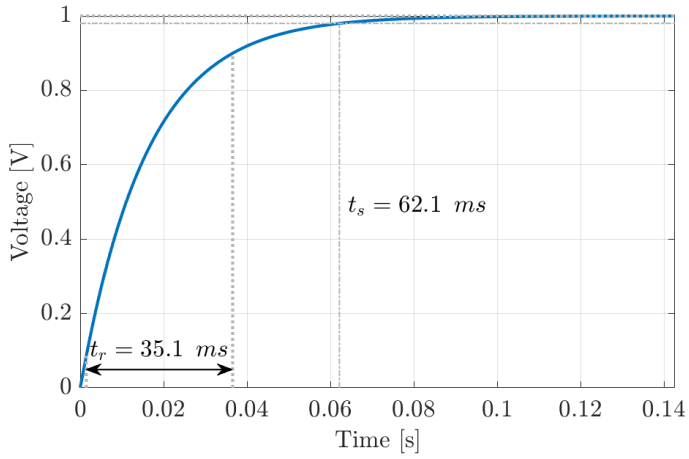

Fig. 80. Unit step response of closed-loop system $L_{DAB}/(1 + L_{DAB})$ from reference to output featuring rise time t_r and settling time t_s.

The stability of the closed-loop system is evidenced by the infinite gain margin in the forward path and the large phase margin at unity gain. Compared with the step response for the GFI, the rise time and settling time are on the order of one simulation time step faster.

The changes to the filter in the GFI model also required a change in controller design to ensure that the new resonant frequency produces no detrimental impacts on operation. This is achieved very simply by adding an additional pole to the existing integral controller at approximately half the resonant frequency. The resulting open-loop frequency response is shown in Fig. 81, while the closed-loop step response is given in Fig. 82.

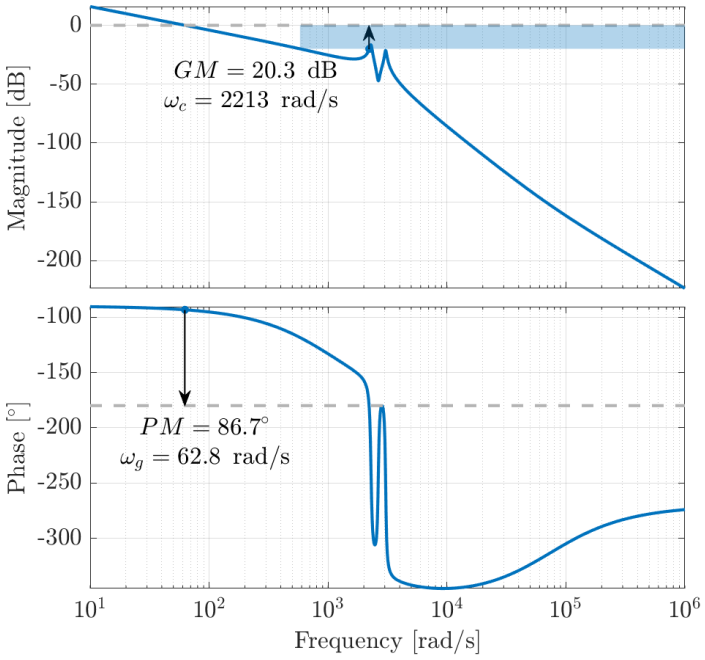

Fig. 81. Open-loop response of L_{GFI} (d-axis) with redesigned control, highlighting the unity gain crossover frequency and its phase margin, imaginary phase crossover and gain margin, and high-frequency roll-off exclusion region ($|L_{GFI}| \leq -20$ dB).

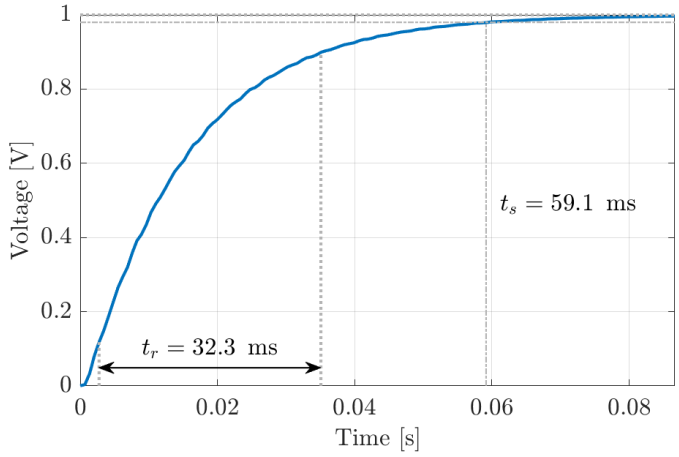

Fig. 82. Unit step response of closed-loop system $L_{GFI}/(1 + L_{GFI})$ (d-axis) from reference to output featuring rise time t_r and settling time t_s.

The result of implementing the truncated SST model in the OPAL-RT microgrid model is presented in Fig. 83, with the typical presentation from Test 4, the 24-hour PV generation simulation.

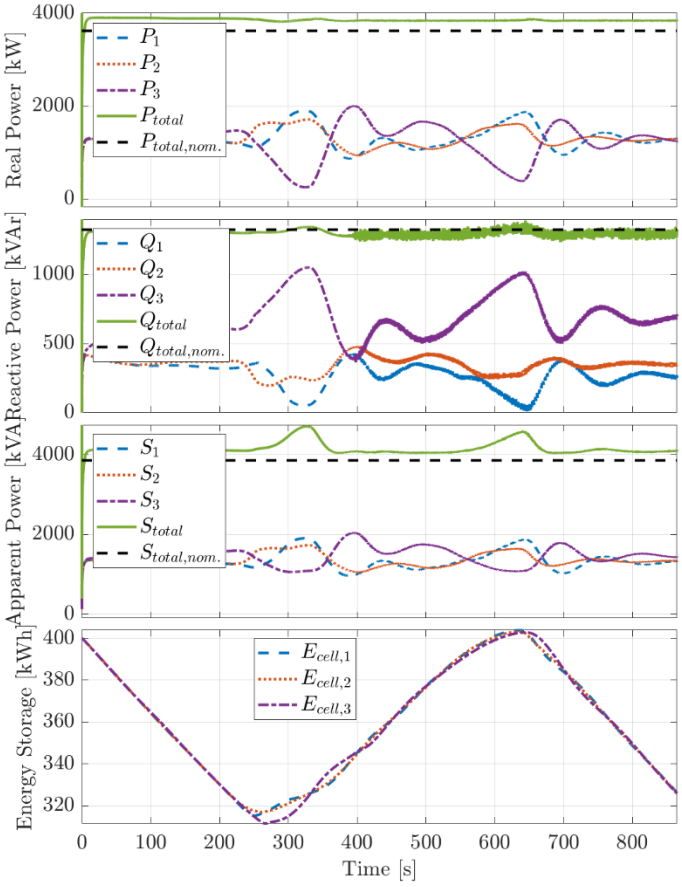

Fig. 83. Real-time simulation results for truncated SST in microgrid testbed under 24-hour PV generation simulation conditions.

Comparing these results with Fig. 53(a) and Fig. 54, three distinct differences are apparent. First, the curves are much smoother, owing to the changes in droop parameters that were necessary at the increased power and voltage levels, according to (112) and (113). Second, the reactive power becomes noisy about halfway through the simulation. The overall impact of this noise on apparent power is much less, but still noticeable. Finally, the energy storage balancing controller has more trouble maintaining the average value across all energy cells, which is also due to the changes in droop parameters.

However, these deviations are transient, and the overall reference tracking is still effective.

Even with these differences, the model still produces approximately the same total apparent power level as previous simulations, with exceptions at the high variability periods during the morning sunrise and evening sunset, where the droop parameters reduce the tracking effectiveness of the real and reactive power setpoint generation controllers.

5 FUTURE WORK

In order to prepare for the exciting future of microgrids, everything from the arrangement and control of large-scale components such as the energy cells described in this report, down to the individual circuit components that compose them must be designed with efficiency, power density, and stable operation in mind. The truncated SST topology presented here is certainly no different, and careful planning, analysis, and design practices, rooted in the teachings of state-of-the-art published material have been employed to ensure that it is of the highest quality, and is fit for the smart grid of the future.

There is still work to be done, and a short list of topics for continued research in these areas will be presented here for future researchers' convenience.

5.1 High-Frequency Transformers

- Design script development, including more detailed thermal modeling and iterative loss and inductance computations inclusive thereof, additional winding construction options such as foil, round wire, and planar windings, and continued validation of results, specifically the novel results for multi-frequency operation.
- Optimization method improvements, possibly including optimization over only purchasable components, but at least with automatic comparison over said components. Manual comparison is time-consuming and prone to error.

5.2 Microgrid Modeling and Control

- Improved PV source modeling, inclusive of DC-DC storage and LV DC link interfaces.
- Improved model reduction techniques for controller design in the presence of detailed controller models. The simple technique used for system identification for the original testbed model is not possible when including the complete SST model, as the number of states is too high.
- Analysis of controller type selection, specifically for use with VSG and virtual impedance implementations. Simple PI controllers for secondary controls may not provide the requisite response time and reference tracking when detailed models are included.

5.3 Converter Design and Analysis

- Improved generalized state space averaging modeling for arbitrary order to improve accuracy at higher order harmonics. A method has been referred to in literature (see [92]), but no implementation was provided.
- Investigation of wavelet applications to converter modeling in state space. It has been demonstrated that it is possible for simple converters, but further validation is necessary before it is generally applicable.

With this list and the work completed so far, I am confident that the task of designing and safely testing the future intelligent microgrid can be accomplished, contributing valuable research to the power engineering community, and making a small dent in the boundary of human knowledge [154].

REFERENCES

[1] W. T. McLyman, Transformer and Inductor Design Handbook, Boca Raton: CRC Press, 2011.

[2] W. G. Hurley and W. H. Wölfle, Transformers and Inductors for Power Electronics, Chichester: John Wiley & Sons Ltd., 2013.

[3] M. K. Kazimierczuk, High-Frequency Magnetic Components, Chichester: John Wiley & Sons, Ltd., 2014.

[4] N. Mohan, T. M. Undeland and W. P. Robbins, Power Electronics, Hoboken: John Wiley & Sons, Inc., 2003.

[5] R. W. Erickson and D. Maksimović, Fundamentals of Power Electronics, New York: Kluwer Academic Publishers, 2004.

[6] W. G. Hurley, W. H. Wölfle and J. G. Breslin, "Optimized Transformer Design: Inclusive of High-Frequency Effects," *IEEE Transactions on Power Electronics,* vol. 13, no. 4, pp. 651-659, 1998.

[7] J. Mühlethaler, J. W. Kolar and A. Ecklebe, "Loss Modeling of Inductive Components Employed in Power Electronic Systems," in *IEEE International Conference on Power Electronics & ECCE Asia*, Jeju, 2011.

[8] C. R. Sullivan, "Aluminum Windings and Other Strategies for High-Frequency Magnetics Design in an Era of High Copper and Energy Costs," in *IEEE Applied Power Electronics Conference*, Anaheim, 2007.

[9] X. Tang and C. R. Sullivan, "Optimization of Stranded-Wire Windings and Comparison with Litz Wire on the Basis of Cost and Loss," in *IEEE Power Electronics Specialists Conference*, Aachen, 2004.

[10] C. R. Sullivan, "Prospects for Advances in Power Magnetics," in *International Conference on Integrated Power Electronics Systems*, Berlin, 2016.

[11] R. Petkov, "Optimum Design of a High-Power, High-Frequency Transformer," *IEEE Transactions on Power Electronics,* vol. 11, no. 1, p. 33–42, 1996.

[12] C. Versèle, O. Deblecker and J. Lobry, "Multiobjective optimal design of transformers for isolated switch mode power supplies," in *SPEEDAM 2010*, Pisa, 2010.

[13] C. Versèle, O. Deblecker and J. Lobry, "A computer-aided design tool dedicated to isolated DC-DC converters based on multiobjective optimization using genetic algorithms," *COMPEL,* vol. 31, no. 2, p. 583–603, 2012.

[14] H. Qin, J. W. Kimball and G. K. Venayagamoorthy, "Particle swarm optimization of high-frequency transformer," in *36th Annual Conference on IEEE Industrial Electronics Society*, Glendale, 2010.

[15] C. R. Sullivan and R. Y. Zhang, "Analytical Model for Effects of Twisting on Litz-Wire Losses," in *IEEE Workshop on Control and Modeling for Power Electronics*, Santander, 2014.

[16] X. Nan and C. R. Sullivan, "Simplified High-Accuracy Calculation of Eddy-Current Loss in Round-Wire Windings," in *IEEE Power Electronics Specialists Conference*, Aachen, 2004.

[17] C. R. Sullivan, "Optimal Choice for Number of Strands in a Litz-Wire Transformer Winding," *IEEE Transactions on Power Electronics,* vol. 14, no. 2, pp. 283-291, 1999.

[18] C. R. Sullivan, "Computationally Efficient Winding Loss Calculation with Multiple Windings, Arbitrary Waveforms, and Two-Dimensional or Three-Dimensional Field Geometry," *IEEE Transactions on Power Electronics,* vol. 16, no. 1, pp. 142-150, 2001.

[19] C. R. Sullivan, "Cost-Constrained Selection of Strand Diameter and Number in a Litz-Wire Transformer Winding," *IEEE Transactions on Power Electronics,* vol. 16, no. 2, pp. 281-288, 2001.

[20] J. D. Pollock, T. Abdallah and C. R. Sullivan, "Easy-To-Use CAD Tools for Litz-Wire Winding Optimization," in *Applied Power Electronics Conference and Exposition*, Miami Beach, 2003.

[21] C. R. Sullivan and R. Y. Zhang, "Simplified Design Method for Litz Wire," in *Applied Power Electronics Conference and Exposition*, Fort Worth, 2014.

[22] F. A. Holguín, R. Prieto, R. Asensi and J. A. Cobos, "Power Losses Calculations in Windings of Gapped Magnetic Components," in *IEEE Applied Power Electronics Conference and Exposition*, Fort Worth, 2014.

[23] W. G. Hurley, E. Gath and J. G. Breslin, "Optimizing the AC Resistance of Multilayer Transformer Windings with Arbitrary Current Waveforms," *IEEE Transactions on Power Electronics,* vol. 15, no. 2, pp. 369-376, 2000.

[24] J.-H. Jung, "Bifilar Winding of a Center-Tapped Transformer Including Integrated Resonant Inductance for LLC Resonant Converters," *IEEE Transactions on Power Electronics,* vol. 28, no. 2, pp. 615-620, 2013.

[25] H. Rossmanith, M. Doebroenti, M. Albach and D. Exner, "Measurement and Characterization of High Frequency Losses in Nonideal Litz Wires," *IEEE Transaction on Power Electronics,* vol. 26, no. 11, pp. 3386-3393, 2011.

[26] C. P. Steinmetz, "On the Law of Hysteresis," *Transactions of the American Institute of Electrical Engineers,* vol. IX, no. 1, pp. 1-64, 1892.

[27] M. Albach, T. Dürbaum and A. Brockmeyer, "Calculating Core Losses in Transformers for Arbitrary Magnetizing Currents A Comparison of Different Approaches," in *IEEE Power Electronics Specialist Conference*, Baveno, 1996.

[28] J. Reinert, A. Brockmeyer and R. W. A. A. De Doncker, "Calculation of Losses in Ferro- and Ferrimagnetic Materials Based on the Modified Steinmetz Equation," *IEEE Transactions on Industry Applications,* vol. 37, no. 4, pp. 1055-1061, 2001.

[29] J. Li, T. Abdallah and C. R. Sullivan, "Improved Calculation of Core Loss with Nonsinusoidal Waveforms," in *IEEE Industry Applications Society*, Chicago, 2001.

[30] K. Venkatachalam, C. R. Sullivan, T. Abdallah and H. Tacca, "Accurate Prediction of Ferrite Core Loss with Nonsinusoidal Waveforms Using Only Steinmetz Parameters," in *IEEE Workshop on Computers in Power Electronics*, Mayaguez, 2002.

[31] J. Mühlethaler, J. Biela, J. W. Kolar and A. Ecklebe, "Core Losses under DC Bias Condition based on Steinmetz Parameters," in *IEEE International Power Electronics Conference*, Sapporo, 2010.

[32] J. Mülethaler, J. Biela, J. W. Kolar and A. Ecklebe, "Core Losses Under the DC Bias Condition Based on Steinmetz Parameters," *IEEE Transactions on Power Electronics,* vol. 27, no. 2, pp. 953-963, 2012.

[33] S. Barg, K. Ammous, H. Mejbri and A. Ammous, "An Improved Empirical Formulation for Magnetic Core Losses Estimation Under Nonsinusoidal Induction," *IEEE Transactions on Power Electronics,* vol. 32, no. 3, pp. 2146-2154, 2017.

[34] C. R. Sullivan, J. H. Harris and E. Herbert, "Core loss predictions for general PWM waveforms from a simplified set of measured data," in *Twenty-Fifth Annual IEEE Applied Power Electronics Conference and Exposition*, Palm Springs, 2010.

[35] E. Herbert, "User-friendly Data for Magnetic Core Loss Calculations," 10 November 2008. [Online]. Available: http://fmtt.com/Coreloss2009.pdf. [Accessed 21 September 2019].

[36] E. Herbert, "Magnetic Core Losses," The Power Sources Manufacturers Association, Mendham, 2012.

[37] G. Bertotti, Hysteresis in Magnetism, London: Academic Press, 1998.

[38] W. A. Roshen, "A Practical, Accurate and Very General Core Loss Model for Nonsinusoidal Waveforms," *IEEE Transactions on Power Electronics,* vol. 22, no. 1, p. 30–40, 2007.

[39] X. Nan and C. R. Sullivan, "A Two-Dimensional Equivalent Complex Permeability Model for Round-Wire Windings," in *IEEE Poower Electronics Specialists Conference*, Recife, 2005.

[40] X. Nan and C. R. Sullivan, "An Equivalent Complex Permeability Model for Litz-Wire Windings," in *IEEE Industry Applications Society*, Saratoga Springs, 2005.

[41] W. G. Hurley and D. J. Wilcox, "Calculation of Leakage Inductance in Transformer Windings," *IEEE Transactions on Power Electronics,* vol. 9, no. 1, pp. 121-126, 1994.

[42] F. W. Grover, "Tables for the Calculation of the Inductance of Circular Coils of Rectangular Cross Section," *Scientific Papers of the Bureau of Standards,* vol. 18, no. 1, pp. 451-487, 1922.

[43] Z. Ouyang, J. Zhang and W. G. Hurley, "Calculation of Leakage Inductance for High-Frequency Transformers," *IEEE Transactions on Power Electronics,* vol. 30, no. 10, pp. 5769-5775, 2015.

[44] M. Eslamian and B. Vahidi, "Computation of the Inductance Matrix of Axisymmetric Windings for Very Fast Transients Studies in Transformers," *Computation and Mathematics in Electrical and Electronic Engineering,* vol. 33, no. 6, pp. 2082-2100, 2014.

[45] C. Álvarez-Mariño, F. de León and X. M. López-Fernández, "Equivalent Circuit for the Leakage Inductance of Multiwinding Transformers: Unification of Terminal and Duality Models," *IEEE Transactions on Power Delivery,* vol. 27, no. 1, pp. 353-361, 2012.

[46] C. P. Schultz, "A Contribution to the Theory of Multiple Winding Transformers," in *IEEE Southeastcon*, Atlanta, 2009.

[47] C. P. Schultz, "The Coupled Leakage Model of a Multiple Winding Transformer," in *IEEE Southeastcon*, Nashville, 2011.

[48] R. Doebbelin, R. Herms, C. Teichert, W. Schaetzing and A. Lindemann, "Analysis Methods and Design of Transformers with Low Leakage Inductance for Pulsed Power Applications," in *IEEE European Conference on Power Electronics and Applications*, Aalborg, 2007.

[49] R. Doebbelin, M. Benecke and A. Lindemann, "Calculation of Leakage Inductance of Core-Type Transformers for Power Electronics Circuits," in *IEEE Power Electronics and Motion Control*, Poznan, 2008.

[50] R. Doebbelin, C. Teichert, M. Benecke and A. Lindemann, "Computerized Calculation of Leakage Inductance Values of Transformers," *PIERS Online,* vol. 5, no. 8, pp. 721-726, 2009.

[51] R. Doebbelin and A. Lindemann, "Leakage Inductance Determination for Transformers with Interleaving of Windings," *PIERS Online,* vol. 6, no. 6, pp. 527-531, 2010.

[52] V. V. Kantor, "Methods of Calculating Leakage Inductance of Transformer Windings," *Russian Electrical Engineering,* vol. 80, no. 4, pp. 224-228, 2009.

[53] V. V. Kantor, "Computation of Leakage Inductance for Complex Windings of Transformers by a Method of Geometric Mean Distances," *Russian Electrical Engineering,* vol. 82, no. 5, pp. 253-259, 2011.

[54] W. G. Hurley and M. C. Duffy, "Calculation of Self and Mutual Impedances in Planar Magnetic Structures," *IEEE Transactions on Magnetics,* vol. 31, no. 4, pp. 2416-2422, 1995.

[55] X. Liu, Y. Wang, J. Zhu, Y. Guo, G. Lei and C. Liu, "Calculation of Capacitance in High-Frequency Transformer Windings," *IEEE Transactions on Magnetics,* vol. 52, no. 7, 2016.

[56] N. B. Chagas and T. B. Marchesan, "Analytical Calculation of Static Capacitance for High-Frequency Inductors and Transformers," *IEEE Transactions on Power Electronics,* vol. 34, no. 2, p. 1672–1682, 2019.

[57] H. Zhang, S. Wang, Y. Li, Q. Wang and D. Fu, "Two-Capacitor Transformer Winding Capacitance Models for Common-Mode EMI Noise Analysis in Isolated DC-DC Converters," *IEEE Transactions on Power Electronics,* vol. 32, no. 11, p. 8458–8469, 2017.

[58] L. Dalessandro, F. d. S. Cavalcante and J. W. Kolar, "Self-Capacitance of High-Voltage Transformers," *IEEE Transactions on Power Electronics,* vol. 22, no. 5, p. 2081–2092, 2007.

[59] M. K. Kazimierczuk and A. Massarini, "Self-Capacitance of Inductors," *IEEE Transactions on Power Electronics,* vol. 12, no. 4, pp. 671-676, 1997.

[60] M. Mogorovic and D. Dujic, "Thermal modeling and experimental verification of an air cooled medium frequency transformer," in *19th European Conference on Power Electronics and Applications*, Warsaw, 2017.

[61] M. Jaritz and J. Biela, "Analytical model for the thermal resistance of windings consisting of solid or litz wire," in *15th European Conference on Power Electronics and Applications*, Lille, 2013.

[62] W. G. Odendaal and J. A. Ferreira, "A thermal model for high-frequency magnetic components," *IEEE Transactions on Industry Applications,* vol. 35, no. 4, p. 924–931, 1999.

[63] Ferroxcube International Holding B.V., "Design Help-Ferroxcube," Ferroxcube, April 2010. [Online]. Available: https://www.ferroxcube.com/en-global/design_tool/index. [Accessed June 2016].

[64] Y. T. Tan and D. S. Kirschen, "Impact on the Power system of a Large Penetration of Photovoltaic Generation," in *2007 IEEE Power Engineering Society General Meeting*, Tampa, 2007.

[65] H. Sugihara, K. Yokoyama, O. Saeki, K. Tsuji and T. Funaki, "Economic and Efficient Voltage Management Using Customer-Owned Energy Storage Systems in a Distribution Network With High Penetration of Photovoltaic Systems," *IEEE Transactions on Power Systems,* vol. 28, no. 1, p. 102–111, 2013.

[66] A. Hirsch, Y. Parag and J. Guerrero, "Microgrids: A review of technologies, key drivers, and outstanding issues," *Renewable and Sustainable Energy Reviews,* vol. 90, p. 402–411, 2018.

[67] E. Alegria, T. Brown, E. Minear and R. H. Lasseter, "CERTS Microgrid Demonstration with Large-Scale Energy Storage and Renewable Generation," *IEEE Transactions on Smart Grid,* vol. 5, no. 2, p. 937–943, 2014.

[68] M. E. Khodayar, M. Barati and M. Shahidehpour, "Integration of High Reliability Distribution System in Microgrid Operation," *IEEE Transactions on Smart Grid,* vol. 3, no. 4, p. 1997–2006, 2012.

[69] V. Salehi, A. Mohamed, A. Mazloomzadeh and O. A. Mohammed, "Laboratory-Based Smart Power System, Part I: Design and System Development," *IEEE Transactions on Smart Grid,* vol. 3, no. 3, p. 1394–1404, 2012.

[70] V. Salehi, A. Mohamed, A. Mazloomzadeh and O. A. Mohammed, "Laboratory-Based Smart Power System, Part II: Control, Monitoring, and Protection," *IEEE Transactions on Smart Grid,* vol. 3, no. 3, p. 1405–1417, 2012.

[71] L. Meng, M. Savaghebi, F. Andrade, J. C. Vasquez, J. M. Guerrero and M. Graells, "Microgrid central controller development and hierarchical control implementation in the intelligent microgrid lab of Aalborg University," in *2015 IEEE Applied Power Electronics Conference and Exposition*, Charlotte, 2015.

[72] R. S. Mongrain, Z. Yu and R. Ayyanar, "A Real-time Simulation Testbed for Hierarchical Control of a Renewable Energy-based Microgrid," in *2019 IEEE Texas Power and Energy Conference*, College Station, 2019.

[73] J. M. Guerrero, J. C. Vasquez, J. Matas, L. García de Vicuna and M. Castilla, "Hierarchical Control of Droop-Controlled AC and DC Microgrids—A General Approach Toward Standardization," *IEEE Transactions on Industrial Electronics,* vol. 58, no. 1, p. 158–172, 2011.

[74] D. Pudjianto, C. Ramsay and G. Strbac, "Virtual power plant and system integration of distributed energy resources," *IET Renewable Power Generation,* vol. 1, no. 1, p. 10–16, 2007.

[75] J. M. Guerrero, J. C. Vasquez, J. Matas, M. Castilla and L. Garcia de Vicuna, "Control Strategy for Flexible Microgrid Based on Parallel Line-Interactive UPS Systems," *IEEE Transactions on Industrial Electronics,* vol. 56, no. 3, p. 726–736, 2009.

[76] J. Liu, Y. Miura and T. Ise, "Comparison of Dynamic Characteristics Between Virtual Synchronous Generator and Droop Control in Inverter-Based Distributed Generators," *IEEE Transactions on Power Electronics,* vol. 31, no. 5, p. 3600–3611, 2016.

[77] R. Ofir, U. Markovic, P. Aristidou and G. Hug, "Droop vs. virtual inertia: Comparison from the perspective of converter operation mode," in *2018 IEEE International Energy Conference*, Limassol, 2018.

[78] C. Kammer and A. Karimi, "Decentralized and Distributed Transient Control for Microgrids," *IEEE Transactions on Control Systems Technology,* vol. 27, no. 1, p. 311–322, 2019.

[79] A. Saran, S. K. Palla, A. K. Srivastava and N. N. Schulz, "Real time power system simulation using RTDS and NI PXI," in *2008 40th North American Power Symposium*, Calgary, 2008.

[80] A. Parizad, H. Reza Baghaee, G. B. Gharehpetian and A. Yazdani, "RTISim: A New Real-Time Isolated Simulator for Turbine-Governor System of Industrial Power Plants," in *2018 IEEE International Conference on Environment and Electrical Engineering*, Palermo, 2018.

[81] V. Venkataramanan, A. Srivastava and A. Hahn, "Real-time co-simulation testbed for microgrid cyber-physical analysis," in *2016 Workshop on Modeling and Simulation of Cyber-Physical Energy Systems*, Vienna, 2016.

[82] M. J. Stanovich, I. Leonard, K. Sanjeev, M. Steurer, T. P. Roth, S. Jackson and M. Bruce, "Development of a smart-grid cyber-physical systems testbed," in *2013 IEEE PES Innovative Smart Grid Technologies Conference*, Washington, DC, 2013.

[83] L. Yang, Y. Ma, J. Wang, J. Wang, X. Zhang, L. M. Tolbert, F. Wang and K. Tomsovic, "Development of converter based reconfigurable power grid emulator," in *2014 IEEE Energy Conversion Congress and Exposition*, Pittsburgh, 2014.

[84] L.-F. Pak, M. O. Faruque, X. Nie and V. Dinavahi, "A versatile cluster-based real-time digital simulator for power engineering research," *IEEE Transactions on Power Systems,* vol. 21, no. 2, p. 455–465, 2006.

[85] P. Imbertson and N. Mohan, "Asymmetrical Duty Cycle Permits Zero Switching Loss in PWM Circuits with No Conduction Loss Penalty," *IEEE Transactions on Industry Applications,* vol. 29, no. 1, pp. 121-125, 1993.

[86] T. Ninomiya, N. Matsumoto, M. Nakahara and K. Harada, "Static and Dynamic Analysis of Zero-Voltage-Switched Half-Bridge Converter with PWM Control," in *IEEE Power Electronics Specialists*, Cambridge, 1991.

[87] M. N. Kheraluwala, R. W. Gascoigne, D. M. Divan and E. D. Baumann, "Performance characterization of a high-power dual active bridge DC-to-DC converter," *IEEE Transactions on Industry Applications,* vol. 28, no. 6, p. 1294–1301, 1992.

[88] C. Mi, H. Bai, C. Wang and S. Gargies, "Operation, design and control of dual H-bridge-based isolated bidirectional DC-DC converter," *IET Power Electronics,* vol. 1, no. 4, p. 507–517, 2008.

[89] S. R. Sanders, J. M. Noworolski, X. Z. Liu and G. C. Verghese, "Generalized averaging method for power conversion circuits," *IEEE Transactions on Power Electronics,* vol. 6, no. 2, p. 251–259, 1991.

[90] A. Emadi, "Modeling and analysis of multiconverter DC power electronic systems using the generalized state-space averaging method," *IEEE Transactions on Industrial Electronics,* vol. 51, no. 3, p. 661–668, 2004.

[91] P. Ngamkong, P. Kochcha, K. Areerak, S. Sujitjorn and K. Areerak, "Applications of the generalized state-space averaging method to modelling of DC-DC power converters," *Mathematical & Computer Modelling of Dynamical Systems,* vol. 18, no. 3, p. 243–260, 2012.

[92] U. Javaid and D. Dujić, "Arbitrary order generalized state space average modeling of switching converters," in *IEEE Energy Conversion Congress and Exposition*, Montreal, 2015.

[93] H. Qin and J. W. Kimball, "Generalized Average Modeling of Dual Active Bridge DC-DC Converter," *IEEE Transactions on Power Electronics,* vol. 27, no. 4, p. 2078–2084, 2012.

[94] F. Zhang, M. M. Ur Rehman, R. Zane and D. Maksimović, "Improved steady-state model of the dual-active-bridge converter," in *IEEE Energy Conversion Congress and Exposition*, Montreal, 2015.

[95] S. S. Shah and S. Bhattacharya, "Large & small signal modeling of dual active bridge converter using improved first harmonic approximation," in *IEEE Applied Power Electronics Conference and Exposition*, Tampa, 2017.

[96] K. Zhang, Z. Shan and J. Jatskevich, "Large- and Small-Signal Average-Value Modeling of Dual-Active-Bridge DC-DC Converter Considering Power Losses," *IEEE Transactions on Power Electronics,* vol. 32, no. 3, p. 1964–1974, 2017.

[97] J. A. Mueller and J. W. Kimball, "An Improved Generalized Average Model of DC-DC Dual Active Bridge Converters," *IEEE Transactions on Power Electronics,* vol. 33, no. 11, p. 9975–9988, 2018.

[98] F. Ponci, E. Santi and A. Monti, "Discrete-Time Multi-Resolution Modeling of Switching Power Converters Using Wavelets," *SIMULATION,* vol. 85, no. 2, p. 69–88, 2009.

[99] A. Vinayagam, K. S. V. Swarna, S. Y. Khoo, A. t. Oo and A. Stojcevski, "PV Based Microgrid with Grid-Support Grid-Forming Inverter Control-(Simulation and Analysis)," *Smart Grid and Renewable Energy,* vol. 8, p. 1–30, 2017.

[100] A. Naderipour, Z. Abdul-Malek, V. K. Ramachandaramurthy, A. Kalam and M. R. Miveh, "Hierarchical control strategy for a three-phase 4-wire microgrid under unbalanced and nonlinear load conditions," *ISA Transactions to be published,* 2019.

[101] A. A. van der Meer, M. Gibescu, M. A. M. M. van der Meijden, W. L. Kling and J. A. Ferreira, "Advanced Hybrid Transient Stability and EMT Simulation for VSC-HVDC Systems," *IEEE Transactions on Power Delivery,* vol. 30, no. 3, p. 1057–1066, 2015.

[102] F. Plumier, P. Aristidou, C. Geuzaine and T. Van Cutsem, "Co-Simulation of Electromagnetic Transients and Phasor Models: A Relaxation Approach," *IEEE Transactions on Power Delivery,* vol. 31, no. 5, p. 2360–2369, 2016.

[103] H. Ye and K. Strunz, "Multi-Scale and Frequency-Dependent Modeling of Electric Power Transmission Lines," *IEEE Transactions on Power Delivery,* vol. 33, no. 1, p. 32–41, 2018.

[104] Z. Miao, L. Piyasinghe, J. Khazaei and L. Fan, "Dynamic Phasor-Based Modeling of Unbalanced Radial Distribution Systems," *IEEE Transactions on Power Systems,* vol. 30, no. 6, p. 3102–3109, 2015.

[105] F. Gao and K. Strunz, "Frequency-adaptive power system modeling for multi-scale simulation of transients," in *IEEE PES General Meeting*, Providence, 2010.

[106] Z. Yu, Y. Tang, T. Yao and R. Ayyanar, "Dynamic simulation of CIG in large unbalanced distribution systems using an open source tool," *IET Generation, Transmission & Distribution,* vol. 13, no. 9, p. 1638–1645, 2019.

[107] A. M. Bouzid, J. M. Guerrero, A. Cheriti, M. Bouhamida, P. Sicard and M. Benghanem, "A survey on control of electric power distributed generation systems for microgrid applications," *Renewable and Sustainable Energy Reviews,* vol. 44, p. 751–766, 2015.

[108] M. Berg, T. Messo and T. Suntio, "Frequency Response Analysis of Load Effect on Dynamics of Grid-Forming Inverter," in *2018 International Power Electronics Conference*, Niigata, 2018.

[109] S. F. Zarei, H. Mokhtari and M. A. Ghasemi, "Enhanced control of grid forming VSCs in a micro-grid system under unbalanced conditions," in *2018 9th Annual Power Electronics, Drives Systems and Technologies Conference*, Tehran, 2018.

[110] C.-k. Leung, S. Dutta, S. Baek and S. Bhattacharya, "Design considerations of high voltage and high frequency three phase transformer for Solid State Transformer application," in *2010 IEEE Energy Conversion Congress and Exposition*, Atlanta, 2010.

[111] T. Yao, Robust Control of Wide Bandgap Power Electronics Device Enabled Smart Grid, Tempe: Arizona State University, 2017.

[112] B. Cougo, T. Meynard and G. Gateau, "Parallel Three-Phase Inverters: Optimal PWM Method for Flux Reduction in Intercell Transformers," *IEEE Transactions on Power Electronics,* vol. 26, no. 8, p. 2184–2191, 2011.

[113] T.-P. Chen, "Common-Mode Ripple Current Estimator for Parallel Three-Phase Inverters," *IEEE Transactions on Power Electronics,* vol. 24, no. 5, p. 1330–1339, 2009.

[114] K. Li, Z. Dong, X. Wang, C. Peng, F. Deng, J. Guerrero and J. Vasquez, "New Strategy for Eliminating Zero-sequence Circulating Current between Parallel Operating Three-level NPC Voltage Source Inverters," *Journal of Power Electronics,* vol. 18, no. 1, p. 70–80, 2018.

[115] Y. Jiang, Modeling of Solid State Transformer for the FREEDM System Demonstration, Tempe: Arizona State University, 2014.

[116] X. She, A. Q. Huang and R. Burgos, "Review of Solid-State Transformer Technologies and Their Application in Power Distribution Systems," *IEEE Journal of Emerging and Selected Topics in Power Electronics,* vol. 1, no. 3, p. 186–198, 2013.

[117] S. D. Falcones Zambrano, A DC-DC Multiport Converter Based Solid State Transformer Integrating Distributed Generation and Storage, Tempe: Arizona State University, 2011.

[118] A. Prasai, H. Chen, R. Moghe, Z. Wolanski, K. Chintakrinda, A. Zhou, J. C. Llambes and D. Divan, "Dyna-C: Experimental results for a 50 kVA 3-phase to 3-phase solid state transformer," in *2014 IEEE Applied Power Electronics Conference and Exposition*, Fort Worth, 2014.

[119] S. Zengin and M. Boztepe, "Modified dual active bridge photovoltaic inverter for solid state transformer applications," in *2014 International Symposium on Fundamentals of Electrical Engineering*, Bucharest, 2014.

[120] Y. Li, J. Han, Y. Cao, Y. Li, J. Xiong, D. Sidorov and D. Panasetsky, "A modular multilevel converter type solid state transformer with internal model control method," *International Journal of Electrical Power & Energy Systems,* vol. 85, p. 153–163, 2017.

[121] I. Vechiu, O. Curea and H. Camblong, "Transient Operation of a Four-Leg Inverter for Autonomous Applications With Unbalanced Load," *IEEE Transactions on Power Electronics,* vol. 25, no. 2, p. 399–407, 2009.

[122] A. Shri, J. Popovic, J. A. Ferreira and M. B. Gerber, "Design and control of a three-phase four-leg inverter for solid-state transformer applications," in *2013 15th European Conference on Power Electronics and Applications*, Lille, 2013.

[123] T. Yang, R. Meere, O. Feely and T. O'Donnell, "Performance of 3-phase 4-wire solid state transformer under imbalanced loads," in *2014 IEEE PES T&D Conference and Exposition*, Chicago, 2014.

[124] H. Chen and D. Divan, "Soft-Switching Solid-State Transformer (S4T)," *IEEE Transactions on Power Electronics,* vol. 33, no. 4, p. 2933–2947, 2018.

[125] H. Chen and D. Divan, "Design of a 10-kV·A Soft-Switching Solid-State Transformer (S4T)," *IEEE Transactions on Power Electronics,* vol. 33, no. 7, p. 5724–5738, 2018.

[126] B. Shi, Z. Zhao, Y. Zhou, W. Zhao, Y. Zhou, S. Wei, G. Feng and Y. Shen, "A Novel Hierarchical Control Scheme for Solid-State Transformer Interfaced PV and Storage System," in *2018 21st International Conference on Electrical Machines and Systems*, Jeju, 2018.

[127] X. Yu, X. She, X. Ni and A. Q. Huang, "System Integration and Hierarchical Power Management Strategy for a Solid-State Transformer Interfaced Microgrid System," *IEEE Transactions on Power Electronics,* vol. 29, no. 8, p. 4414–4425, 2014.

[128] C. Nan, Dual Active Bridge Converter with PWM Control in Solid State Transformer Application, Tempe: Arizona State University, 2012.

[129] D. Sha, W. Yuan, G. Xu, F. You and J. Chen, "Parallel-connected bidirectional current-fed dual active bridge DC-DC converters with decentralized control," in *2016 IEEE Energy Conversion Congress and Exposition*, Milwaukee, 2016.

[130] X. Dong, S. Yong and S. Jianhui, "Modeling and control of parallel dual-active-bridge converter in PET," in *2018 13th IEEE Conference on Industrial ELectronics and Applications*, Wuhan, 2018.

[131] Y. Liu, W. Wang, Y. Liu and S. Bayhan, "Real-time implementation of finite control set model predictive control for matrix converter based solid state transformer," *International Journal of Hydrogen Energy,* vol. 42, no. 28, p. 17976–17983, 2017.

[132] J. A. Martinez-Velasco, S. Alepuz, F. González-Molina and J. Martin-Arnedo, "Dynamic average modeling of a bidirectional solid state transformer for feasibility studies and real-time implementation," *Electric Power Systems Research,* vol. 117, p. 143–153, 2014.

[133] Ferroxcube, "3C94 Material specification," 1 September 2008. [Online]. Available: http://www.ferroxcube.com. [Accessed 29 July 2016].

[134] J. D. Pollock, Optimizing Winding Designs for High-Frequency Magnetic Components, Hanover: Dartmouth College, 2008.

[135] E. W. Weisstein, "Modified Struve Function," Wolfram Research, Inc., 2017. [Online]. Available: http://mathworld.wolfram.com/ModifiedStruveFunction.html. [Accessed 22 January 2017].

[136] A. Rohatgi, "WebPlotDigitizer," October 2015. [Online]. Available: http://arohatgi.info/WebPlotDigitizer. [Accessed 12 August 2016].

[137] R. Szewczyk, "Technical B-H saturation magnetization curve models for SPICE, FEM and MoM simulations," *Journal of Automation, Mobile Robotics and Intelligent Systems,* vol. 10, no. 2, p. 3–8, 2016.

[138] M. C. Chandorkar, D. M. Divan and R. Adapa, "Control of Parallel Connected Inverters in standalone AC Supply Systems," *IEEE Transactions on Industry Applications,* vol. 29, no. 1, p. 136–143, 1993.

[139] Y. Sun, X. Hou, J. Yang, H. Han, M. Su and J. M. Guerrero, "New Perspectives on Droop Control in AC Microgrid," *IEEE Transactions on Industrial Electronics,* vol. 64, no. 7, p. 5741–5745, 2017.

[140] IEEE Standards Association, *IEEE Std 1547-2018, IEEE Standard for Interconnection and Interoperability of Distributed Energy Resources with Associated Electric Power Systems Interfaces,* New York: IEEE, 2018.

[141] E. A. A. Coelho, P. C. Cortizo and P. F. D. Garcia, "Small-signal stability for parallel-connected inverters in stand-alone AC supply systems," *IEEE Transactions on Industry Applications,* vol. 38, no. 2, p. 533–542, 2002.

[142] IEEE PES AMPS DSAS Test Feeder Working Group, "Resources | PES Test Feeder," [Online]. Available: http://sites.ieee.org/pes-testfeeders/resources/. [Accessed 25 April 2019].

[143] Arizona State University, "EIS: Energy Information Systems," [Online]. Available: https://eis.asu.edu/flex/index.html. [Accessed 20 May 2018].

[144] OPAL-RT, "Real-time HIL RCP FPGA Knowledge Base | OPAL-RT," [Online]. Available: https://www.opal-rt.com/support-knowledge-base/?article=AA-01047. [Accessed 25 April 2019].

[145] J. M. Guerrero, L. Garcia de Vicuna, J. Matas, M. Castilla and J. Miret, "Output impedance design of parallel-connected UPS inverters with wireless load-sharing control," *IEEE Transactions on Industrial Electronics,* vol. 52, no. 4, p. 1126–1135, 2005.

[146] *V1.1b3: Modbus Application Protocol Specification,* 2012.

[147] IEEE Standards Association, *IEEE Std 519-2014, IEEE Recommended Practice and Requirements for Harmonic Control in Electric Power Systems,* New York: IEEE, 2014.

[148] R. Reginatto and R. A. Ramos, "On electrical power evaluation in dq coordinates under sinusoidal unbalanced conditions," *IET Generation, Transmission & Distribution,* vol. 8, no. 5, p. 976–982, 2014.

[149] A. Q. Huang, Q. Zhu, L. Wang and L. Zhang, "15 kV SiC MOSFET: An enabling technology for medium voltage solid state transformers," *CPSS Transactions on Power Electronics and Applications,* vol. 2, no. 2, p. 118–130, 2017.

[150] M. A. Perales, M. M. Prats, R. Portillo, J. L. Mora, J. I. Leon and L. G. Franquelo, "Three-dimensional space vector modulation in abc coordinates for four-leg voltage source converters," *IEEE Power Electronics Letters,* vol. 1, no. 4, p. 104–109, 2003.

[151] Rossmann Engineering, "EasyModbusTCP Modbus Library for .NET/Java and Python – Communication library and professional tools for industrial communication," [Online]. Available: http://easymodbustcp.net/en/. [Accessed 25 April 2019].

[152] S. Mulder, "Power ferrite loss formulas for transformer design," *Power Conversion & Intelligent Motion,* vol. 21, no. 7, p. 22–31, 1995.

[153] V. J. Thottuvelil, T. G. Wilson and H. A. Owen, Jr., "High-Frequency Measurement Techniques for Magnetic Cores," *IEEE Transactions on Power Electronics,* vol. 5, no. 1, p. 41–53, 1990.

[154] M. Might, "The illustrated guide to a Ph.D.," [Online]. Available: http://matt.might.net/articles/phd-school-in-pictures/. [Accessed 24 August 2019].

[155] V. S. Pour Mehr, A. Mohammed, A. Mazloomzadeh and O. Mohammed, "Laboratory-based smart power system, Part I: Design and system development," in *2013 IEEE Power & Energy Society General Meeting*, Vancouver, 2013.

[156] V. S. Pour Mehr, A. Mohammed, A. Mazloomzadeh and O. Mohammed, "Laboratory-based smart power system, part II: Control, monitoring, and protection," in *2013 IEEE Power & Energy Society General Meeting*, Vancouver, 2013.

APPENDIX A

RE-DERIVATION OF ELECTRICAL CONDITIONS

The formulation of the core geometry coefficient given in [1] includes a term referred to as the "Electrical Conditions", represented by K_e. The term includes a pair of constant factors, the product of which is 0.145×10^{-4}, and without any supporting derivation or explanation, and without units declared, the source of the constants is unclear. When attempting to improve the accuracy of predictions made for transformer values, especially losses, a clear understanding of all expressions will allow for better optimization, as the contribution of each parameter can be considered individually. To that end, the source of the constants and the unit dimensions were derived by examining the core geometry equation and its constituent parts, via dimensional analysis.

We will begin with the definitions provided in (5) and (6) for core geometry coefficient, K_g, and voltage regulation, α, repeated here as $(A.1)$ and $(A.2)$ for convenience, and the equation for electrical conditions, K_e, in [1] with unknown units represented by $[\mathcal{U}]$ given by $(A.3)$.

$$K_g = \frac{W_a A_c^2 K_u}{l_T} \quad [\text{cm}]^5 \tag{A.1}$$

$$\alpha = \frac{P_t}{2K_g K_e} 100 \quad [\%] \tag{A.2}$$

$$K_e = 0.145 K_f^2 f^2 B_{pk}^2 10^{-4} \quad [\mathcal{U}] \tag{A.3}$$

From the formula for α, since throughput power, P_t, is in [W], so must be the product $K_g K_e$, shown dimensionally in $(A.4)$.

$$[\text{cm}]^5[\mathcal{U}] = [\text{W}] \rightarrow [\mathcal{U}] = \frac{[\text{W}]}{[\text{cm}]^5} \tag{A.4}$$

However, given waveform factor, K_f in $[\text{cycles}]^{-1}$, frequency, f in $\left[\frac{\text{cycles}}{\text{s}}\right]$, and peak magnetic flux density, B_{pk} in [T], and assuming that the constants are dimensionless (represented by [#]), we find the contradiction in $(A.5)$.

$$\frac{[\text{W}]}{[\text{cm}]^5} = [\#][\text{cycles}]^{-2}\frac{[\text{cycles}]^2}{[\text{s}]^2}[\text{T}]^2[\#] = \frac{[\text{T}]^2}{[\text{s}]^2}$$
$$\rightarrow \frac{[\text{kg}][\text{m}]^2}{[\text{cm}]^5[\text{s}]^2} \neq \frac{[\text{kg}]^2}{[\text{A}]^2[\text{s}]^6} \qquad (A.5)$$

Clearly, the two provided constants are not dimensionless. We can rewrite the expression above, and it set equal to $[\mathcal{U}] = [\mathcal{U}_1][\mathcal{U}_2]$ to solve for the units of each constant and the units of the expression in general, as shown in $(A.6)$.

$$[\mathcal{U}_1][\mathcal{U}_2] = \frac{[\text{A}]^2[\text{s}]^6[\text{kg}][\text{m}]^2}{[\text{s}]^3[\text{kg}]^2[\text{cm}]^5} = \left(\frac{[\text{A}]^2[\text{s}]^3}{[\text{kg}][\text{cm}]^3}\right)\left(\frac{[\text{m}]^2}{[\text{cm}]^2}\right) \qquad (A.6)$$

Arranged this way, 10^{-4} is associated with the second term, and is a simple unit conversion factor, leaving the remaining unit term associated with the first constant, which can be taken as a conductivity in the range of millions of Siemens per meter. The units for each constant are provided in $(A.7)$.

$$[\mathcal{U}_1] = \frac{[\text{A}]^2[\text{s}]^3}{[\text{kg}][\text{cm}]^3} = \frac{[\text{MS}]}{[\text{m}]}, \quad [\mathcal{U}_2] = \frac{[\text{m}]^2}{[\text{cm}]^2} \qquad (A.7)$$

Redistributing the various factors and expressing all variables in their SI base units, we arrive at the final expression with appropriate units, and discover the conductivity of copper hiding in the first constant, as shown in (7), and repeated here as $(A.8)$.

$$K_e = \frac{1}{2}\sigma_{Cu}K_f^2 f^2 B_m^2 \quad \left[\frac{\text{W}}{\text{m}^5}\right] \qquad (A.8)$$

This formulation requires that α be expressed as a proper fraction rather than just the numerator of such a fraction (e.g. we now say that 5% = 0.05, not 5 as it was previously).

Similarly, K_g is now expressed in base SI units of $[\mathrm{m}]^5$. It is better suited to an SI-consistent design and analysis script such as the one written during this work, in that unit conversions need only happen if they suit presentation, rather than attempting to manage varying degrees of unit conversion throughout the code. Finally, it allows a glimpse into the construction of the core geometry coefficient that was previously hidden from view for simplicity's sake.

APPENDIX B

DERIVATION OF CORE GEOMETRY COEFFICIENT FOR COMPOSITE WAVEFORMS

To predict the necessary size of a transformer core operated under composite excitation, where the switching waveform is amplitude modulated by a low-frequency oscillation, as would be the case in an SST where the input voltage is polluted by line frequency oscillation, a new definition for the core geometry coefficient is needed. The old definition considers a single frequency and a single waveform factor, which are no longer applicable to this case.

To begin the derivation, an expression for the throughput power P_t in the transformer is given in $(B.1)$ in terms of the apparent power VA in winding w for each winding in the set of windings W.

$$P_t = \sum_w VA_w, \forall w \in W \quad [\mathrm{W}] \tag{B.1}$$

For two windings with excitation as described above, this can be approximated by$(B.2)$, where the high-frequency and low-frequency components of each value have been denoted by subscripts HF and LF, respectively.

$$\begin{aligned} P_t &= VA_1 + VA_2 \\ &= V_{1,RMS} I_{1,RMS} + V_{2,RMS} I_{2,RMS} \\ &= \sqrt{V_{1,LF,RMS}^2 + V_{1,HF,RMS}^2}\sqrt{I_{1,LF,RMS}^2 + I_{1,HF,RMS}^2} \\ &+ \sqrt{V_{2,LF,RMS}^2 + V_{2,HF,RMS}^2}\sqrt{I_{2,LF,RMS}^2 + I_{2,HF,RMS}^2} \\ &\approx \sum_w VA_{w,LF} + VA_{w,HF} \\ &= P_{t,LF} + P_{t,HF} \quad [\mathrm{W}] \end{aligned} \tag{B.2}$$

An error of ~0.16% was observed in the test case with a 60 Hz sine modulating a 20 kHz switching waveform, with the sine wave having a relative peak magnitude of 10%, so this is a reasonable approximation for cases with no more than this level of

pollution. Further analysis is needed to determine a boundary above which the approximation is no longer acceptable.

From the definition of the core geometry coefficient, considering independent contributions of each component, the expressions are given by $(B.3)$.

$$\begin{aligned} K_{g,LF} &= \frac{P_{t,LF}}{2\alpha K_{e,LF}} \\ K_{g,HF} &= \frac{P_{t,HF}}{2\alpha K_{e,HF}} \end{aligned} \quad [\mathrm{m}]^5 \qquad (B.3)$$

Using the approximation in $(B.2)$, the core geometry coefficient for the composite waveform is approximated by $(B.4)$.

$$\begin{aligned} K_g &= \frac{P_t}{2\alpha K_e} \\ &\approx \frac{1}{2\alpha}\left[\frac{P_{t,LF} + P_{t,HF}}{K_e}\right] \\ &= \frac{1}{K_e}\left[K_{e,LF}K_{g,LF} + K_{e,HF}K_{g,HF}\right] \quad [\mathrm{m}]^5 \end{aligned} \qquad (B.4)$$

Furthermore, we define the electrical conditions for each component as in $(B.5)$, where the switching frequency f_s denotes the high-frequency, and the low frequency of the pollution signal is denoted by f_0, each with a waveform factor denoted by the HF or LF subscript, as appropriate.

$$\begin{aligned} K_{e,LF} &= \frac{1}{2}\sigma_{Cu}K_{f,LF}^2 f_0^2 \hat{B}_{LF}^2 \\ K_{e,HF} &= \frac{1}{2}\sigma_{Cu}K_{f,HF}^2 f_s^2 \hat{B}_{HF}^2 \end{aligned} \quad \left[\frac{\mathrm{W}}{\mathrm{m}^5}\right] \qquad (B.5)$$

To get the low-frequency and high-frequency components of the peak magnetic flux density, we use the fraction of the power in the given winding relative to the total throughput power, thus each is expressed as in $(B.6)$.

$$\hat{B}_{LF} = \hat{B}\frac{P_{t,LF}}{P_t} \quad [\mathrm{T}] \qquad (B.6)$$
$$\hat{B}_{HF} = \hat{B}\frac{P_{t,HF}}{P_t}$$

This follows from the assumption that the peak of the total waveform occurs at the simultaneous peaks of the component waveforms, as shown in $(B.7)$.

$$\hat{B} = \hat{B}_{LF} + \hat{B}_{HF} = \hat{B}\frac{P_{t,LF} + P_{t,HF}}{P_t} \quad [\mathrm{T}] \qquad (B.7)$$

As discussed in the main text, this assumption is almost certain to be valid, considering the large difference in frequencies, and considering that the derivative of the sinusoid near its peak is almost zero.

Dividing the expressions for electrical conditions at each frequency through, we obtain the relationship in $(B.8)$.

$$\frac{K_{e,LF}}{K_{e,HF}} = \left(\frac{K_{f,LF}f_0}{K_{f,HF}f_s}\right)^2 \left(\frac{P_{t,LF}}{P_{t,HF}}\right)^2 \qquad (B.8)$$

Rearranging WLOG, the expression for the low-frequency throughput power in $(B.9)$ is obtained.

$$P_{t,LF} = \sqrt{\frac{K_{e,LF}}{K_{e,HF}}}\left(\frac{K_{f,HF}f_s}{K_{f,LF}f_0}\right)P_{t,HF} \quad [\mathrm{W}] \qquad (B.9)$$

Substituting the RHS of this expression into the expression for K_g, the core geometry coefficient is now expressed by $(B.10)$.

$$K_g = \frac{1}{2\alpha}\left[\frac{1}{K_e}P_{t,HF}\left(1 + \sqrt{\frac{K_{e,LF}}{K_{e,HF}}}\left(\frac{K_{f,HF}f_s}{K_{f,LF}f_0}\right)\right)\right]$$
$$= K_{g,HF}\left[\frac{K_{e,HF}}{K_e}\left(1 + \frac{P_{t,LF}}{P_{t,HF}}\right)\right]$$

$$= K_{g,HF}\left[\frac{K_{e,HF}}{K_e}\right]\left[\frac{P_t}{P_{t,HF}}\right] \quad [\mathrm{m}]^5 \tag{B.10}$$

The same process can be followed by substituting the alternative rearrangement of $(B.10)$ to arrive at an expression for the low-frequency component as in $(B.11)$.

$$\begin{aligned} K_g &= K_{g,LF}\left[\frac{K_{e,LF}}{K_e}\left(1+\frac{P_{t,HF}}{P_{t,LF}}\right)\right] \\ &= K_{g,LF}\left[\frac{K_{e,LF}}{K_e}\right]\left[\frac{P_t}{P_{t,LF}}\right] \quad [\mathrm{m}]^5 \end{aligned} \tag{B.11}$$

Setting the expressions in $(B.10)$ and $(B.11)$ equal, we arrive at the relationship between K_g, K_e, and P_t for each component of the composite waveform relative to one another as expressed by $(B.12)$.

$$\frac{K_{g,HF}}{K_{g,LF}} = \frac{K_{e,LF}P_{t,HF}}{K_{e,HF}P_{t,LF}} \rightarrow \frac{K_{g,HF}K_{e,HF}}{K_{g,LF}K_{e,LF}} = \frac{P_{t,HF}}{P_{t,LF}} \tag{B.12}$$

For a given throughput power, the product K_gK_e is a constant. Furthermore, the relationship for this constant among frequency components of a transformer waveform is determined by the ratio of the throughput powers in each frequency component. However, K_g and K_e for the total waveform remain unknown, despite their product being known.

Summing the two expressions for K_g, we arrive at the expression in $(B.13)$.

$$\begin{aligned} 2K_g &= \frac{P_t}{K_e}\left[\frac{K_{g,LF}K_{e,LF}}{P_{t,LF}} + \frac{K_{g,HF}K_{e,HF}}{P_{t,HF}}\right] \\ \rightarrow K_g &= \frac{P_t}{2K_e}\left[\frac{P_{t,HF}K_{g,LF}K_{e,LF} + P_{t,LF}K_{g,HF}K_{e,HF}}{P_{t,LF}P_{t,HF}}\right] \quad [\mathrm{m}]^5 \end{aligned} \tag{B.13}$$

Noting that the summands in the numerator of the term in brackets are equal, we could make either substitution such that we obtain the proportionality relationship in $(B.14)$.

$$\frac{K_g K_e}{P_t} = \frac{K_{g,LF} K_{e,LF}}{P_{t,LF}} = \frac{K_{g,HF} K_{e,HF}}{P_{t,HF}} = \frac{1}{2\alpha} \tag{B.14}$$

Applying the definition for the electrical conditions, we can substitute the expression for peak magnetic flux density in terms of the frequency components from $(B.7)$ as shown in $(B.15)$.

$$K_e = \frac{1}{2}\sigma_{Cu} K_f^2 f^2 \left(\hat{B}_{LF} + \hat{B}_{HF}\right)^2 \quad \left[\frac{\mathrm{W}}{\mathrm{m}^5}\right] \tag{B.15}$$

However, there is no single waveform factor or frequency in the composite waveform. It is also the case that the electrical conditions must not be a simple sum of those for the frequency components, because the peak magnetic flux density is the square of such a sum, as shown in $(B.16)$.

$$K_e = \frac{1}{2}\sigma_{Cu} K_f^2 f^2 \left(\hat{B}_{LF}^2 + 2\hat{B}_{LF}\hat{B}_{HF} + \hat{B}_{HF}^2\right) \quad \left[\frac{\mathrm{W}}{\mathrm{m}^5}\right] \tag{B.16}$$

Substituting the expressions for each component in the center term, and the individual expressions for their electrical conditions, we arrive at the expression in $(B.17)$.

$$\begin{aligned} K_e &= \frac{1}{2}\sigma_{Cu} K_f^2 f^2 \left(\frac{2K_{e,LF}}{\sigma_{Cu} K_{f,LF}^2 f_0^2} + 2\hat{B}^2 \frac{P_{t,LF} P_{t,HF}}{P_t^2} + \frac{2K_{e,HF}}{\sigma_{Cu} K_{f,HF}^2 f_s^2}\right) \\ &= \left(\frac{K_f f}{K_{f,LF} f_0}\right)^2 K_{e,LF} + \sigma_{Cu} K_f^2 f^2 \hat{B}^2 \frac{P_{t,LF} P_{t,HF}}{P_t^2} + \left(\frac{K_f f}{K_{f,HF} f_s}\right)^2 K_{e,HF} \\ &= 2\frac{P_{t,LF} P_{t,HF}}{P_t^2} K_e + \left(\frac{K_f f}{K_{f,LF} f_0}\right)^2 K_{e,LF} + \left(\frac{K_f f}{K_{f,HF} f_s}\right)^2 K_{e,HF} \quad \left[\frac{\mathrm{W}}{\mathrm{m}^5}\right] \end{aligned} \tag{B.17}$$

We can rearrange this expression to collect the K_e terms, to arrive at $(B.18)$.

$$\begin{aligned} K_e &= \left[\frac{P_t^2}{P_t^2 - 2P_{t,LF} P_{t,HF}}\right]\left[\left(\frac{K_f f}{K_{f,LF} f_0}\right)^2 K_{e,LF} + \left(\frac{K_f f}{K_{f,HF} f_s}\right)^2 K_{e,HF}\right] \\ &= \left[\frac{P_t^2}{P_{t,LF}^2 + P_{t,HF}^2}\right]\left[\left(\frac{K_f f}{K_{f,LF} f_0}\right)^2 K_{e,LF} + \left(\frac{K_f f}{K_{f,HF} f_s}\right)^2 K_{e,HF}\right] \quad \left[\frac{\mathrm{W}}{\mathrm{m}^5}\right] \end{aligned} \tag{B.18}$$

Now a large assumption must be made, which simplifies the design process significantly, and is consistent with the methods described in the main text for the base switching frequency case making it suitable for implementation in the design script, but which will require more justification. This justification is provided below. That said, if we suppose that the term $K_f f$ is the geometric mean of the related products in the component expressions, we arrive at the new expression in $(B.19)$.

$$K_e = \left[\frac{P_t^2}{P_{t,LF}^2 + P_{t,HF}^2}\right]\left[\frac{K_{f,HF} f_s}{K_{f,LF} f_0} K_{e,LF} + \frac{K_{f,LF} f_0}{K_{f,HF} f_s} K_{e,HF}\right] \quad \left[\frac{\mathrm{W}}{\mathrm{m}^5}\right] \tag{B.19}$$

Substitution of the expressions in $(B.5)$ into $(B.19)$ results in $(B.20)$ (units omitted for formatting purposes).

$$K_e = \frac{1}{2}\sigma_{Cu}\left[\frac{P_t^2}{P_{t,LF}^2 + P_{t,HF}^2}\right]\left[K_{f,LF} f_0 K_{f,HF} f_s \hat{B}^2 \frac{P_{t.LF}^2}{P_t^2} + K_{f,LF} f_0 K_{f,HF} f_s \hat{B}^2 \frac{P_{t.HF}^2}{P_t^2}\right] \tag{B.20}$$

This simplifies readily to $(B.21)$, defining the electrical conditions for the composite waveform in a familiar and pleasant way.

$$K_e = \frac{1}{2}\sigma_{Cu} K_{f,LF} f_0 K_{f,HF} f_s \hat{B}^2 \quad \left[\frac{\mathrm{W}}{\mathrm{m}^5}\right] \tag{B.21}$$

With this we can find K_g for the composite waveform, given by $(B.13)$. If we further suppose that $K_f = \sqrt{K_{f,LF} K_{f,HF}}$ and $f = \sqrt{f_0 f_s}$, we have completed the derivation, and can write (9). Additional explanation and justification will now be provided.

The waveform factor in cycles^{-1} (or "per cycle") relates the positive, rising portion of the flux waveform to its rate of repetition. For dimensional analysis, we can rearrange the expression for K_e as $(B.22)$.

$$K_e = \frac{1}{2}\left(K_f f \hat{B}\right)\left(\sigma_{Cu} K_f f \hat{B}\right) \quad \left[\frac{\mathrm{W}}{\mathrm{m}^5}\right] \tag{B.22}$$

By careful examination, we can recognize this as the complex power density of the transformer, akin to the per unit volume magnitude of the Poynting vector, as shown in $(B.23)$.

$$\left[\frac{\mathrm{W}}{\mathrm{m}^5}\right] = \left[\frac{\mathrm{S}}{\mathrm{m}}\right]\left[\frac{\mathrm{T}}{\mathrm{s}}\right]\left[\frac{\mathrm{T}}{\mathrm{s}}\right] = \left[\frac{1}{\Omega \cdot \mathrm{m}}\right]\left[\frac{\mathrm{V} \cdot \mathrm{s}}{\mathrm{m}^2 \cdot \mathrm{s}}\right]\left[\frac{\mathrm{V} \cdot \mathrm{s}}{\mathrm{m}^2 \cdot \mathrm{s}}\right] = \left[\frac{1}{\mathrm{m}^3}\right]\left[\frac{\mathrm{V}}{\mathrm{m}}\right]\left[\frac{\mathrm{A}}{\mathrm{m}}\right] \qquad (B.23)$$

For a single frequency, this relates the apparent power and the physical dimensions of the transformer. For the composite waveform, it is less clear how this relationship is defined.

The core geometry coefficient is a guideline for core selection and is constructed to help relate electrical properties to physical properties during the design process. The approach described here places the values for the electrical conditions of the composite waveform between those of the component waveforms due to the geometric mean assumption, and similarly for the core geometry coefficient. For equal throughput power in a composite waveform and a single-frequency waveform, this fits the theory well since the reduction in contribution from the high-frequency component would not be compensated exactly by contribution of the low-frequency component replacing it in the new waveform. Furthermore, lower frequency excitation requires a larger core, but since its contribution is much smaller than that of the high-frequency component, the increase in size will necessarily be less than if the low-frequency component dominated the waveform.

Representing the core geometry coefficient expression as a sum of the scaled components by a rearrangement of $(B.13)$, we arrive at $(B.24)$.

$$K_g = \left[\frac{P_t}{P_{t,LF}}\right]\left[\frac{K_{e,LF}}{K_e}\right]K_{g,LF} + \left[\frac{P_t}{P_{t,HF}}\right]\left[\frac{K_{e,HF}}{K_e}\right]K_{g,HF}$$

$$= \left[\frac{P_t}{P_{t,LF}}\right]\left[\frac{K_{f,LF}f_0}{K_{f,HF}f_s}\right]\left[\frac{P_{t,LF}^2}{P_t^2}\right]K_{g,LF} + \left[\frac{P_t}{P_{t,HF}}\right]\left[\frac{K_{f,HF}f_0}{K_{f,LF}f_s}\right]\left[\frac{P_{t,HF}^2}{P_t^2}\right]K_{g,HF}$$
$$= \left[\frac{P_{t,LF}}{P_t}\right]\left[\frac{K_{f,LF}f_0}{K_{f,HF}f_s}\right]K_{g,LF} + \left[\frac{P_{t,HF}}{P_t}\right]\left[\frac{K_{f,HF}f_0}{K_{f,LF}f_s}\right]K_{g,HF} \quad [\mathrm{m}]^5 \qquad (B.24)$$

We see that each component K_g term is scaled by the fraction of the total power it represents, and by the ratio of the two components, like-to-unlike. In each term, we are examining the power repetition rate at the frequency in which we are interested as a fraction of the total power at the repetition rate of the frequency in which we are not interested.

Equation $(B.24)$ weights the terms both by the ratios of their rates of repetition to one another, and by their relative power contributions, which can also be expressed in terms of energy delivery. The low-frequency weighting term is representative of the energy delivered by the low-frequency waveform during each cycle of the high-frequency waveform as a fraction of the total energy delivered during each cycle of its repetition and vice-versa. This is formally expressed by $(B.25)$.

$$\left.\begin{aligned}\frac{P_{t,LF}}{K_{f,HF}f_s} &= W_{LF/HF}\\ \frac{K_{f,LF}f_0}{P_t} &= \frac{1}{W_{TOT/LF}}\end{aligned}\right\} \rightarrow \left[\frac{P_{t,LF}}{P_t}\right]\left[\frac{K_{f,LF}f_0}{K_{f,HF}f_s}\right] = \frac{W_{LF/HF}}{W_{TOT/LF}}$$
$$\left.\begin{aligned}\frac{P_{t,HF}}{K_{f,LF}f_0} &= W_{HF/LF}\\ \frac{K_{f,HF}f_s}{P_t} &= \frac{1}{W_{TOT/HF}}\end{aligned}\right\} \rightarrow \left[\frac{P_{t,HF}}{P_t}\right]\left[\frac{K_{f,HF}f_0}{K_{f,LF}f_s}\right] = \frac{W_{HF/LF}}{W_{TOT/HF}} \qquad (B.25)$$

Using these expressions, we can write the core geometry coefficient as $(B.26)$.

$$K_g = \frac{W_{LF/HF}}{W_{TOT/LF}}K_{g,LF} + \frac{W_{HF/LF}}{W_{TOT/HF}}K_{g,HF} \quad [\mathrm{m}]^5 \qquad (B.26)$$

The energy transferred by the low-frequency waveform during every cycle of the high-frequency waveform $W_{LF/HF}$, relative to the fraction of the total energy transferred per cycle of the low-frequency waveform $W_{TOT/LF}$ scales the low-frequency waveform's core geometry coefficient $K_{g,LF}$, while the energy transferred by the high-frequency waveform during every cycle of the low-frequency waveform $W_{HF/LF}$, relative to the total energy transferred per cycle of the high-frequency waveform $W_{TOT/HF}$ scales the high-frequency core geometry coefficient $K_{g,HF}$.

APPENDIX C

LEAKAGE INDUCTANCE FROM MEASUREMENT

Measurements of transformer leakage inductance are primarily obtained by short-circuit tests, and the measured value is generally taken as the sum of the leakage inductance of the winding measured and the leakage inductance of the winding shorted, referred to the measured side. In [41], we see that there is a leakage inductance for each winding, and a leakage inductance between each pair of windings; this mutual leakage is not discovered from the standard calculations. Furthermore, the standard measurement overestimates inductance values for the one winding, while underestimating values for the other winding. In [46], the author suggests a method of calculating these inductance values from voltage and current measurements by assuming that the primary winding has no self-leakage (i.e. assuming that the primary winding inductance represents the magnetizing inductance, and that the winding is perfectly coupled with itself), and using that assumption to define effective coupling factors between all windings that allow the solution of the system of differential equations $v = L\, di/dt$. Since this solves the differential equations, it must have a basis in fact, but the initial assumption seems to conflict with the findings in [41]. To resolve this conflict, a revision to the calculations applied to standard inductance measurement is proposed such that values arrived at by analysis can be compared directly with those measured, and so that any leakage inductance effects can be predicted as accurately as possible.

Having taken a complete set of inductance measurements as described in Section 3.1.3, we suppose that we can model leakage flux as a coupled phenomenon between windings during a short-circuit test, and that it is proportional to the leakage flux. Using the same form for this term as the mutual inductance, we can adjust the traditional measurement calculation as in (52), repeated for convenience as $(C.1)$.

$$\begin{aligned} L_{i,l} + k'_{ij}\sqrt{L_{i,l}L_{j,l}} + \frac{N_i^2}{N_j^2}L_{j,l} &= L_{ij,SC} \\ \frac{N_j^2}{N_i^2}L_{i,l} + k'_{ji}\sqrt{L_{i,l}L_{j,l}} + L_{j,l} &= L_{ji,SC} \end{aligned} \quad \text{[H]} \qquad (C.1)$$

The middle term does not actually represent anything within the circuit model used for analysis. What it does represent is a mathematical construct, absorbing the difference in measurement values due to physical nonidealities and allowing the leakage values to be determined in a least squares sense. The values obtained from this formula match expectation via experiment and FEM simulation. From the perspective of the circuit model, the formula describing a given short circuit measurement is of the form shown in $(C.2)$.

$$L_{ij,SC} = L_{i,l} + k_j \frac{N_i^2}{N_j^2}L_{j,l} \quad \text{[H]} \qquad (C.2)$$

In $(C.2)$, k_j is the coupling coefficient of winding j to itself. More investigation of sources of measurement error is required to relate these two equations as one provides agreeable values, while the other provides an agreeable theoretical foundation.

An alternative consideration is that when measuring complex impedance, the dominant quantity associated with the imaginary term (inductance or capacitance) will be displayed by standard measurement hardware. Thus, another possible explanation for the mismatch of leakage inductance measurement with analysis is the capacitance, which has the opposite effect on impedance with respect to frequency. Furthermore, since analysis considers only discrete impedance elements, neglecting the complicated interactions of multiple equivalent series-parallel combinations of inductance and capacitance may also contribute.

APPENDIX D

FORMULATION OF ARC LENGTH OF ELECTRIC FIELD PATH IN STATIC ROUND WIRE CAPACITANCE COMPUTATION

While still an approximation, the presentation in [55] of the static capacitance between turns of solid, round wire is more accurate than the straight-line path approximations commonly used in capacitance estimation. The approximation neglects the effects of the boundary between copper and insulation, and again between insulation and air, but does more closely estimate the path of the electric field between conductors than straight-line paths. Since the formula for the length of the path presented in [55] is novel, it seems strange that no derivation was provided. That will be remedied here.

Under the explicit assumption that the field lines extend radially outward from the conductor along the surface normal, and are not refracted at the interfaces between media, the smoothest transition between two adjacent conductors' surfaces occurs for circular arcs, with circles arranged as in Fig. D. 1. Since the derivative of the electric field must be continuous in a homogenous medium (such as air), this path is well-supported by field theory, and serves as a good basis considering the assumptions stated. To determine the arc length of these field lines, simple trigonometric identities are sufficient.

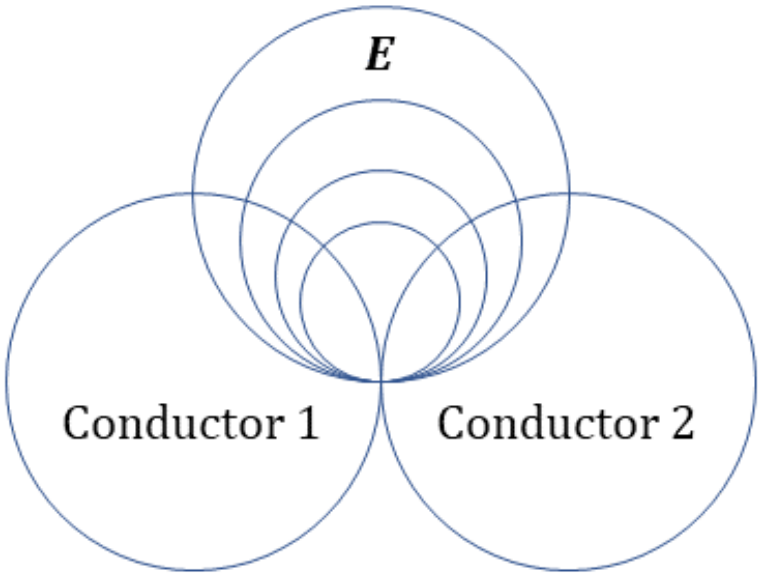

Fig. D. 1. Geometric representation of electric field lines between adjacent round conductor surfaces.

In Fig. D. 2(a), the necessary angles and the diameter of the identical, adjacent conductors (shown from center-to-center) are illustrated, and the triangle formed by the intersections of the circle representing the selected field line with the conductor's outer diameter and the center of the conductor is shown cut such that two right triangles are formed, with the right angle on the shared diameter. We shall refer to this isosceles triangle, shown in detail in Fig. D. 2(b), with the radii of the conductors as its equal legs as T_1.

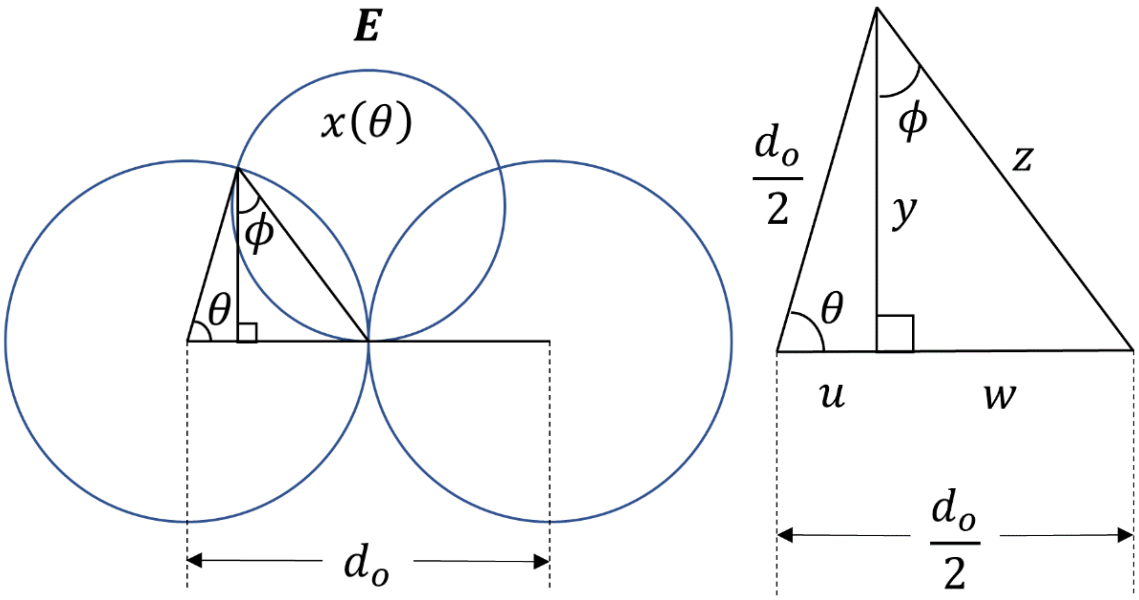

Fig. D. 2. Trigonometric representation of a single field line at angle θ. (a) Angles needed for computation, and depiction of center-to-center distance, d_o. (b) Right triangles formed from isosceles triangle comprised of radii subtending θ and the adjoining chord.

We note that the length of the line segment $y = (d_o/2)\sin(\theta) = z\sin(\pi/2 - \phi)$.

By the law of sines, $(D.1)$ is also true.

$$\frac{z}{\sin(\theta)} = \frac{d_o}{2\sin\left(\frac{\pi}{2} - \theta + \phi\right)} \qquad (D.1)$$

Solving these two expressions for z and equating them, we arrive at $(D.2)$.

$$\frac{d_o\sin(\theta)}{2\sin\left(\frac{\pi}{2} - \phi\right)} = \frac{d_o\sin(\theta)}{2\sin\left(\frac{\pi}{2} - \theta + \phi\right)} \qquad (D.2)$$

From $(D.2)$, it is clear that $\sin(\pi/2 - \phi) = \sin(\pi/2 - \theta + \phi)$, and therefore the arguments must be equal, indicating that $\phi = \theta/2$. Since two legs of T_1 are tangent to the field line circle, bisecting the angle θ will split the circle into two congruent semicircles. Extending the bisecting line to form a new right triangle with d_o as its base yields the

diameter d of the circle as the height of the leg opposite the angle $\theta/2$, as shown in Fig. D. 3.

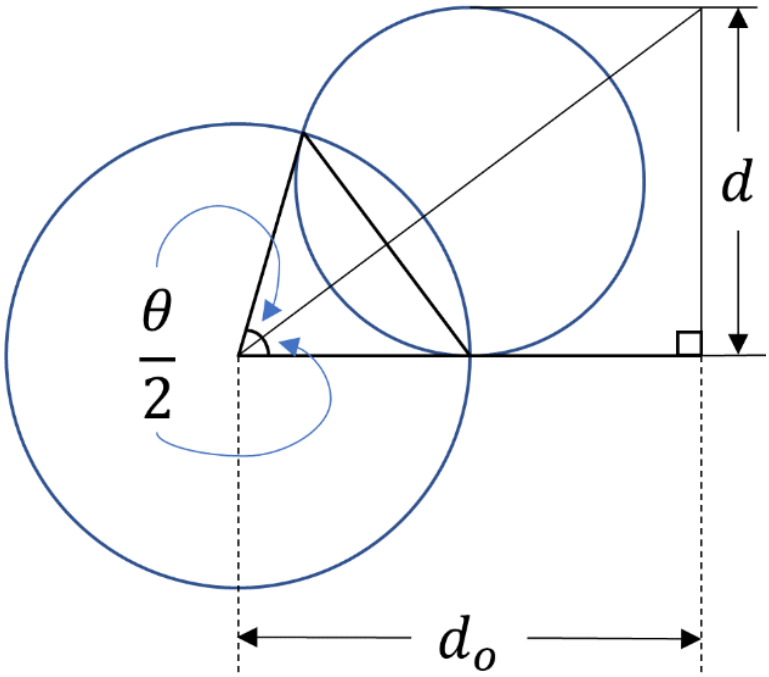

Fig. D. 3. Illustration of bisection of electric field line circle and resulting diameter.

We must now represent the angle subtended by arc $x(\theta)$ in terms of θ. In Fig. D. 4, the necessary angles are shown to illustrate that the angle subtended by the arc is 2θ. Therefore, the length of the arc $x(\theta)$ can be described by the product of the radius of the field line circle and the angle θ subtended by the arc, as stated in $(D.3)$, giving us (59).

$$x(\theta) = r2\theta = \frac{1}{2}\left(d_o \tan\left(\frac{\theta}{2}\right)\right)2\theta = d_o\theta \tan\left(\frac{\theta}{2}\right) \quad \text{[m]} \qquad (D.3)$$

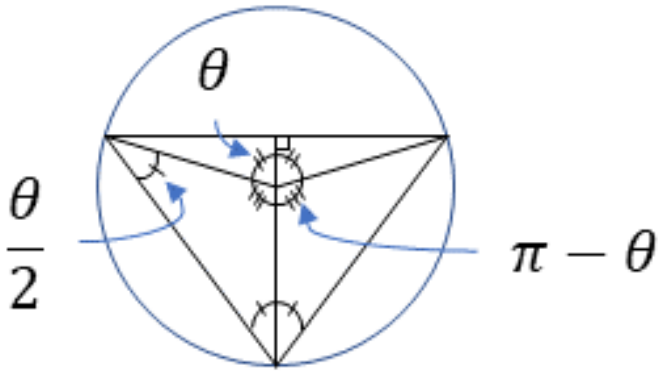

Fig. D. 4. Final geometric illustration, showing angle subtended by arc $x(\theta)$, and all interior angles.

APPENDIX E

ROUND WIRE TRANSFORMATION FOR CAPACITANCE

In [3], a transformation method from solid round wire, stranded wire, and Litz wire to equivalent copper foil is presented. The method is typically applied to the cross-sectional portion of the windings in the core window area of the transformer for resistance and loss calculation; however, it may extend to the transformation from the other case presented in [55]: the capacitance between a pair of round wires.

To transform the round wire to an equivalent foil winding following the process in [3], we first transform the round wires to square wires, then transform the square wires to equivalent foil windings. Given a round wire with coper area $A_r = \pi r^2$, we form the square winding of equivalent area by defining the side length, $t = \sqrt{A_r} = \sqrt{\pi} r$. For capacitance calculation, the center-to-center (or edge-to-edge) distance between round conductors, including insulation, $p = t + t_i = d_o$, where t_i is the insulation thickness, should be preserved, despite differences between r and t. Given the number of circular or square conductor turns per layer, N_l, we have the winding layer area $A_l = N_l A_r$, from which we can derive the width of the foil winding l_a from the area of the copper in the window, $A_f = t l_a = A_l$. The final term in the transformation is the porosity factor, $\eta = 2r/p$, which accounts for the ratio of conductor-to-nonconductor area.

We must also consider the windings along their length, since (53) – (56) present sectioned capacitance estimation formulas. The length of the round wire windings is stated as a single value l_t, which apparently assumes a purely circular winding pattern. Assuming the same configuration, we can use the cylindrical capacitance expressions from (54), as in $(E.1)$. The reason (55) and (56) are not also converted, is that the round wire capacitance computation in [55] does not include turn-to-shield capacitances.

$$C_{ttf} = \sum_{i=1}^{8} C_i = 4\varepsilon_2 \frac{l_a}{ln\left(\frac{r_2 + d_2}{r_2}\right)} \quad [\text{F}] \qquad (E.1)$$

Multiplying this result by $\pi\eta$ gives the total capacitance of the windings for the equivalent surface areas of the transformed conductors.

Litz wire can be transformed to an equivalent round wire winding, as in [3], by similarly equating the copper area and total area of the wire, including insulation and serving. Various constructions of Litz wire exist, but most have a porosity factor between 0.7 and 0.8. In this case, the total copper area, $A_{Cu,L}$ is the product of the number of strands, N_s, and the individual strand copper wire area, $A_{Cu,s}$. Using the porosity factor, η_L we can compute the total area of the bundle of Litz wire, $A_L = A_{Cu,L} \,/\, \eta_L$. These values, in turn, give the transformed round wire equivalent radii, which can be used in (57) and (60) to allow the computation of $(61)(58)$.

Given the same round wire configuration provided in [55] (two wires, wound concentrically), with a copper radius of 0.4 mm and an outer radius, including insulation, of 0.41 mm, a capacitance value of 114.76 pF was obtained via FEM in [55]. Using the method presented in [55], the value was found to be 115.56 pF. Using the transformation here, the value is 118.95 pF, a 3.14% overestimation.

Using a common Litz wire construction, type II with 165 strands of 42 AWG wire per bundle as an example, after transformation we have a total copper area of 0.5199 mm^2, a total area of 0.6932 mm^2, with corresponding copper radius of 0.4068 mm, and outer radius of 4.698 mm. The resulting equivalent insulation thickness is 0.0629 mm, which accounts for the increased insulation of individually insulated wires and the outer serving

of the wire. The static capacitance of the transformed Litz wire is 42.90 pF, using the same relative permittivity and winding turn length as in the previous round wire case.

While more investigation is necessary to determine the general applicability, this is a reasonably accurate method of approximation for the case tested, and while it does not provide the level of accuracy that other methods in this report do, it may be an easy way to make a fast initial estimate of capacitance in a transformer winding without involving FEM. The main draw of this approach is that the geometry portion of these computations will ostensibly already be performed during resistance and loss computations.

APPENDIX F

MINIMUM COMMUTATING INDUCTANCE FOR ZVS IN ASYMMETRIC HALF-BRIDGE

To determine the inductance necessary to ensure ZVS in the asymmetric half-bridge, we begin with equation (134) for the minimum boundary of the output current, repeated here as $(F.1)$ for convenience, and the equation for the voltage across an inductor given by $(F.2)$.

$$I_0 = \frac{N_1^2 V_o}{4N_2^2 D^2}\sqrt{\frac{C_e}{L_c}} \quad [\text{A}] \tag{F.1}$$

$$v_L = L\frac{di_L}{dt} \quad [\text{V}] \tag{F.2}$$

As voltage develops across an inductor, the current through it responds according to its inductance; larger inductance limits the rate of change, while smaller inductance allows faster change. The output filter inductor and the magnetizing inductance are much larger than the leakage inductance, so during this interval the threat of dropping below minimum current comes from the leakage. If we assume that the interval is short enough that the current derivative will be a constant, we can approximate the inductor voltage equation for the commutating inductance by $(F.3)$.

$$V_{L_c} = L_c\frac{N_1}{N_2}\frac{(I_0 - I_1)}{\Delta} \quad [\text{V}] \tag{F.3}$$

In $(F.3)$, the output current, I_1, at the beginning of the dead time, Δ, and its difference with the minimum output current are scaled by the turns ratio, N_1/N_2. Solving for the minimum output current as in $(F.4)$, we can then equate the two expressions as demonstrated by $(F.5)$.

$$I_0 = \frac{N_1}{N_2}\frac{V_{L_c}\Delta}{L_c} + I_1 \quad [\text{A}] \tag{F.4}$$

$$I_1 + \frac{N_1}{N_2}\frac{V_{L_c}\Delta}{L_c} = \frac{N_1^2}{N_2^2}\frac{V_o}{4D^2}\sqrt{\frac{C_e}{L_c}} \quad [\mathrm{A}] \qquad (F.5)$$

To find the voltage across the commutating inductance, V_{Lc}, we note that the ideal case has the transformer terminals shorted during this interval. In the non-ideal case, as we have seen, there is a small voltage developed across the magnetizing inductance and thus, across the ideal transformer terminals contained within the T-model. This voltage, however, is ~10% of the terminal voltage at most, and for a first-order approximation we can assume it is zero; this is an advantageous approximation as it is a worse case from the perspective of the current derivative, which is directly proportional to this voltage. With our assumption that the full winding voltage is dropped across the commutating inductance, we can solve equation (135), presented again here for convenience as $(F.6)$.

$$L_c^2 + \left(\frac{N_1}{N_2}\frac{2V_{L_c}}{I_1}\Delta - \frac{N_1^4}{N_2^4}\frac{C_e V_o^2}{16D^4 I_1^2}\right)L_c + \frac{N_1^2}{N_2^2}\frac{V_{L_c}^2}{I_1^2}\Delta^2 = 0 \qquad (F.6)$$

APPENDIX G

DERIVATION OF SECOND HARMONIC APPROXIMATION GENERALIZED AVERAGE STATE SPACE MODEL OF DUAL ACTIVE BRIDGE

To derive the model, we begin with the differential equations for the full model of the DAB along with the equations for its outputs, given by $(G.1)$ – $(G.7)$.

$$C_{in}\dot{v_{C_{in}}}(t) = -\frac{1}{R_{ESRin}}v_{C_{in}}(t) + \frac{1}{R_{ESRin}}V_{PV} \tag{G.1}$$

$$L_{lp}\dot{\imath_{L_{lp}}}(t) = -\left(r_{peq} + R_c\right)i_{L_{lp}}(t) + R_c i_{L_m}(t) - \frac{N_s}{N_p}R_c i_{L_{ls}}(t) + s_1(t)V_{PV} \tag{G.2}$$

$$L_m\dot{\imath_{L_m}}(t) = R_c i_{L_{lp}}(t) - R_c i_{L_m}(t) + \frac{N_s}{N_p}R_c i_{L_{ls}}(t) \tag{G.3}$$

$$\begin{aligned} L_{ls}\dot{\imath_{L_{ls}}}(t) = -\frac{N_s}{N_p}R_c i_{L_{lp}}(t) + \frac{N_s}{N_p}R_c i_{L_m}(t) - \left(r_{seq} + \frac{N_s^2}{N_p^2}R_c + R_{ESRo}\right)i_{L_{ls}}(t) \\ + s_2(t)v_{C_o}(t) - R_{ESRo}s_2(t)i_o(t) \end{aligned} \tag{G.4}$$

$$C_o\dot{v_{C_o}}(t) = -s_2(t)i_{L_{ls}}(t) - i_o(t) \tag{G.5}$$

$$i_{in}(t) = -\frac{1}{R_{ESRin}}v_{C_{in}}(t) + s_1(t)i_{L_{lp}}(t) + \frac{1}{R_{ESRin}}V_{PV} \tag{G.6}$$

$$v_o(t) = -R_{ESRo}s_2(t)i_{L_{ls}}(t) + v_{C_o}(t) - R_{ESRo}i_o(t) \tag{G.7}$$

The switching functions at the input and output, $s_1(t)$ and $s_2(t)$ respectively, are well-described in the literature as piecewise constant functions of time, with periods given as functions of the phase shift(s) between bridges. Since the single phase shift method is used in this work, the formulation featuring a fixed period for $s_1(t)$ is employed here, as shown in$(G.8)$.

$$\begin{aligned} s_1(t) &= \begin{cases} 1 & 0 \le t < \frac{T_s}{2} \\ -1 & \frac{T_s}{2} \le t < T \end{cases} \\ s_2(t) &= \begin{cases} 1 & d\frac{T_s}{2} \le t < (1+d)\frac{T_s}{2} \\ -1 & 0 \le t < d\frac{T_s}{2} \vee (1+d)\frac{T_s}{2} \le t < T \end{cases} \end{aligned} \tag{G.8}$$

The FHA for this model is very similar to that provided for simpler models in literature, but as described in the main text, the significant second harmonic content in the output equations indicates that the SHA may be a better starting place, despite the existence of correction methods for inclusion of truncated harmonics. Since higher order approximations have been left to the imagination in the literature, the derivation process and results have been recorded here.

The first task for adding new harmonics would normally be to derive the average expressions at each harmonic for the switching functions; however, since we are adding an even harmonic, no new derivations need to be performed due to the fixed 50% duty ratio. The second harmonic product of the switching frequency, like its DC component, spends equal time above and below the t-axis within a switching period, and so its integrals, both real and imaginary, evaluate to zero.

Next, the convolution terms $\langle xy \rangle$ in the average expressions should be derived. The FHA expressions for harmonic k are not valid within this framework, because more adjacent terms are added per $(G.9)$.

$$\langle xy \rangle_k = \sum_{i=\max_k K}^{k-\max_k K} \langle x \rangle_{k-i} \langle y \rangle_i \qquad (G.9)$$

Here the series has been truncated to contain only terms appearing in the set of harmonics $K = \{-k_{max}, \dots, k_{max}\}$, which in this case is given by $K = \{-2, -1, 0, 1, 2\}$. Its order has also been reversed to yield terms in increasing order of harmonics of x.

For the DC terms, this is given by $(G.10)$, for the first harmonic, by $(G.11)$, and for the second harmonic, by $(G.12)$.

$$\langle xy\rangle_0 = \sum_{i=2}^{-2} \langle x\rangle_{-i}\langle y\rangle_i \tag{G.10}$$

$$\langle xy\rangle_1 = \sum_{i=2}^{-1} \langle x\rangle_{1-i}\langle y\rangle_i \tag{G.11}$$

$$\langle xy\rangle_2 = \sum_{i=2}^{0} \langle x\rangle_{2-i}\langle y\rangle_i \tag{G.12}$$

Recognizing that for complex number ξ, $\langle\xi\rangle_k = \langle\xi\rangle^*_{-k}$, we write the real and imaginary portions of each expression, with subscripts denoting the harmonic $k \in \{0,1,2\}$ and real and imaginary components R and I, respectively, as $(G.13)$ – $(G.17)$. Here we are making the further simplification that the DC and second harmonic average values of the switch functions (taken as x) are zero.

$$\langle xy\rangle_0 = \cancel{\langle x\rangle_0^0}\langle y\rangle_0 + 2\left(\cancel{\langle x\rangle_{2R}^0}\langle y\rangle_{2R} + \langle x\rangle_{1R}\langle y\rangle_{1R} + \langle x\rangle_{1I}\langle y\rangle_{1I} + \cancel{\langle x\rangle_{2I}^0}\langle y\rangle_{2I}\right)$$

$$\rightarrow \langle xy\rangle_0 = 2(\langle x\rangle_{1R}\langle y\rangle_{1R} + \langle x\rangle_{1I}\langle y\rangle_{1I}) \tag{G.13}$$

$$\langle xy\rangle_{1R} = \langle x\rangle_{1R}\langle y\rangle_{2R} + \langle x\rangle_{1I}\langle y\rangle_{2I} + \cancel{\langle x\rangle_0^0}\langle y\rangle_{1R} + \langle x\rangle_{1R}\langle y\rangle_0 + \cancel{\langle x\rangle_{2R}^0}\langle y\rangle_{1R} + \cancel{\langle x\rangle_{2I}^0}\langle y\rangle_{1I}$$

$$\rightarrow \langle xy\rangle_{1R} = \langle x\rangle_{1R}\langle y\rangle_{2R} + \langle x\rangle_{1I}\langle y\rangle_{2I} + \langle x\rangle_{1R}\langle y\rangle_0 \tag{G.14}$$

$$\langle xy\rangle_{1I} = \langle x\rangle_{1R}\langle y\rangle_{2I} - \langle x\rangle_{1I}\langle y\rangle_{2R} + \cancel{\langle x\rangle_0^0}\langle y\rangle_{1I} + \langle x\rangle_{1I}\langle y\rangle_0 - \cancel{\langle x\rangle_{2R}^0}\langle y\rangle_{1I} + \cancel{\langle x\rangle_{2I}^0}\langle y\rangle_{1R}$$

$$\rightarrow \langle xy\rangle_{1I} = \langle x\rangle_{1R}\langle y\rangle_{2I} - \langle x\rangle_{1I}\langle y\rangle_{2R} + \langle x\rangle_{1I}\langle y\rangle_0 \tag{G.15}$$

$$\langle xy\rangle_{2R} = \cancel{\langle x\rangle_0^0}\langle y\rangle_{2R} + \langle x\rangle_{1R}\langle y\rangle_{1R} - \langle x\rangle_{1I}\langle y\rangle_{1I} + \cancel{\langle x\rangle_{2R}^0}\langle y\rangle_0$$

$$\rightarrow \langle xy\rangle_{2R} = \langle x\rangle_{1R}\langle y\rangle_{1R} - \langle x\rangle_{1I}\langle y\rangle_{1I} \tag{G.16}$$

$$\langle xy\rangle_{2I} = \cancel{\langle x\rangle_0^0}\langle y\rangle_{2I} + \langle x\rangle_{1R}\langle y\rangle_{1I} + \langle x\rangle_{1I}\langle y\rangle_{1R} + \cancel{\langle x\rangle_{2I}^0}\langle y\rangle_0$$

$$\rightarrow \langle xy\rangle_{2I} = \langle x\rangle_{1R}\langle y\rangle_{1I} + \langle x\rangle_{1I}\langle y\rangle_{1R} \tag{G.17}$$

This adds ten variables and ten equations to the state space representation as compared with the FHA, and while the explicit output equations are not typically

represented in literature, this adds four more equations to what would normally represent the FHA of the outputs bringing the total to ten.

For convenience, the convolution terms resulting from the application of $(G.13)$ – $(G.17)$ to $(G.1)$ – $(G.7)$ are given here in $(G.18)$ – $(G.42)$. It is assumed that the variation of the input voltage v_{PV} and output current i_o are slow compared with the switching frequency, so their average values above DC are taken as zero, and at DC they are represented by V_{PV} and I_o, respectively.

$$\langle s_1 v_{PV} \rangle_0 = 0 \tag{G.18}$$

$$\langle s_1 v_{PV} \rangle_{1R} = 0 \tag{G.19}$$

$$\langle s_1 v_{PV} \rangle_{1I} = -\frac{2}{\pi} V_{PV} \tag{G.20}$$

$$\langle s_1 v_{PV} \rangle_{2R} = 0 \tag{G.21}$$

$$\langle s_1 v_{PV} \rangle_{2I} = 0 \tag{G.22}$$

$$\langle s_2 v_{C_o} \rangle_0 = -\frac{4\sin(d\pi)}{\pi} \langle v_{C_o} \rangle_{1R} - \frac{4\cos(d\pi)}{\pi} \langle v_{C_o} \rangle_{1I} \tag{G.23}$$

$$\langle s_2 v_{C_o} \rangle_{1R} = -\frac{2\sin(d\pi)}{\pi} \langle v_{C_o} \rangle_{2R} - \frac{2\cos(d\pi)}{\pi} \langle v_{C_o} \rangle_{2I} - \frac{2\sin(d\pi)}{\pi} \langle v_{C_o} \rangle_0 \tag{G.24}$$

$$\langle s_2 v_{C_o} \rangle_{1I} = -\frac{2\sin(d\pi)}{\pi} \langle v_{C_o} \rangle_{2I} + \frac{2\cos(d\pi)}{\pi} \langle v_{C_o} \rangle_{2R} - \frac{2\cos(d\pi)}{\pi} \langle v_{C_o} \rangle_0 \tag{G.25}$$

$$\langle s_2 v_{C_o} \rangle_{2R} = -\frac{2\sin(d\pi)}{\pi} \langle v_{C_o} \rangle_{1R} + \frac{2\cos(d\pi)}{\pi} \langle v_{C_o} \rangle_{1I} \tag{G.26}$$

$$\langle s_2 v_{C_o} \rangle_{2I} = -\frac{2\sin(d\pi)}{\pi} \langle v_{C_o} \rangle_{1I} - \frac{2\cos(d\pi)}{\pi} \langle v_{C_o} \rangle_{1R} \tag{G.27}$$

$$\langle s_2 i_o \rangle_0 = 0 \tag{G.28}$$

$$\langle s_2 i_o \rangle_{1R} = -\frac{2\sin(d\pi)}{\pi} I_o \tag{G.29}$$

$$\langle s_2 i_o \rangle_{1I} = -\frac{2\cos(d\pi)}{\pi} I_o \tag{G.30}$$

$$\langle s_2 i_o \rangle_{2R} = 0 \tag{G.31}$$

$$\langle s_2 i_o \rangle_{2I} = 0 \tag{G.32}$$

$$\langle s_2 i_{L_{ls}} \rangle_0 = -\frac{4\sin(d\pi)}{\pi}\langle i_{L_{ls}} \rangle_{1R} - \frac{4\cos(d\pi)}{\pi}\langle i_{L_{ls}} \rangle_{1I} \tag{G.33}$$

$$\langle s_2 i_{L_{ls}} \rangle_{1R} = -\frac{2\sin(d\pi)}{\pi}\langle i_{L_{ls}} \rangle_{2R} - \frac{2\cos(d\pi)}{\pi}\langle i_{L_{ls}} \rangle_{2I} - \frac{2\sin(d\pi)}{\pi}\langle i_{L_{ls}} \rangle_0 \tag{G.34}$$

$$\langle s_2 i_{L_{ls}} \rangle_{1I} = -\frac{2\sin(d\pi)}{\pi}\langle i_{L_{ls}} \rangle_{2I} + \frac{2\cos(d\pi)}{\pi}\langle i_{L_{ls}} \rangle_{2R} - \frac{2\cos(d\pi)}{\pi}\langle i_{L_{ls}} \rangle_0 \tag{G.35}$$

$$\langle s_2 i_{L_{ls}} \rangle_{2R} = -\frac{2\sin(d\pi)}{\pi}\langle i_{L_{ls}} \rangle_{1R} + \frac{2\cos(d\pi)}{\pi}\langle i_{L_{ls}} \rangle_{1I} \tag{G.36}$$

$$\langle s_2 i_{L_{ls}} \rangle_{2I} = -\frac{2\sin(d\pi)}{\pi}\langle i_{L_{ls}} \rangle_{1I} - \frac{2\cos(d\pi)}{\pi}\langle i_{L_{ls}} \rangle_{1R} \tag{G.37}$$

$$\langle s_1 i_{L_{lp}} \rangle_0 = -\frac{4}{\pi}\langle i_{L_{lp}} \rangle_{1I} \tag{G.38}$$

$$\langle s_1 i_{L_{lp}} \rangle_{1R} = -\frac{2}{\pi}\langle i_{L_{lp}} \rangle_{2I} \tag{G.39}$$

$$\langle s_1 i_{L_{lp}} \rangle_{1I} = \frac{2}{\pi}\langle i_{L_{lp}} \rangle_{2R} - \frac{2}{\pi}\langle i_{L_{lp}} \rangle_0 \tag{G.40}$$

$$\langle s_1 i_{L_{lp}} \rangle_{2R} = \frac{2}{\pi}\langle i_{L_{lp}} \rangle_{1I} \tag{G.41}$$

$$\langle s_1 i_{L_{lp}} \rangle_{2I} = -\frac{2}{\pi}\langle i_{L_{lp}} \rangle_{1R} \tag{G.42}$$

Now the state vectors and output vectors can be defined. These vectors are of the same form at each harmonic, so they can be represented succinctly by using the subscript c, which takes the value of 0, $1R$, $1I$, $2R$, or $2I$ as appropriate. This is shown in $(G.43)$ and $(G.44)$.

$$\boldsymbol{x}_c = \begin{bmatrix} \langle v_{C_{in}} \rangle_c & \langle i_{L_{lp}} \rangle_c & \langle i_{L_m} \rangle_c & \langle i_{L_{ls}} \rangle_c & \langle v_{C_o} \rangle_c \end{bmatrix}^T \tag{G.43}$$

$$\boldsymbol{y}_c = \begin{bmatrix} \langle i_{in} \rangle_c & \langle v_o \rangle_c \end{bmatrix}^T \tag{G.44}$$

The state space matrices A, B, C, and D are obtained by evaluating the differential equations at each harmonic, while the mass matrix for each harmonic, which is the same for all harmonics, is formed by $M_i = [C_{in} \quad L_{lp} \quad L_m \quad L_{ls} \quad C_o]I$, where I is the 5×5 identity matrix.

A straightforward, organized approach to constructing these matrices is to arrange the terms for a given harmonic component in order, first by harmonic component, then by state or input. This allows separation into submatrices relating values for harmonic component c_i to harmonic component c_j, for example, the submatrix A_{01R} gives the first harmonic real terms contributing to the DC average state derivatives.

Equations $(G.45)$ – $(G.51)$ give the general form of the equations, while $(G.52)$ gives the full system using the previous description for brevity.

$$C_{in}\langle \dot{v_{C_{in}}} \rangle_k = -\frac{1}{R_{ESRin}}\langle v_{C_{in}} \rangle_k + \frac{1}{R_{ESRin}}\langle v_{PV} \rangle_k + jk\omega C_{in}\langle v_{C_{in}} \rangle_k \tag{G.45}$$

$$L_{lp}\langle \dot{\imath_{L_{lp}}} \rangle_k = -\left(r_{peq} + R_c\right)\langle i_{L_{lp}} \rangle_k + R_c\langle i_{L_m} \rangle_k - \frac{N_s}{N_p}R_c\langle i_{L_{ls}} \rangle_k + \langle s_1 V_{PV} \rangle_k + jk\omega L_{lp}\langle i_{L_{lp}} \rangle_k \tag{G.46}$$

$$L_m\langle \dot{\imath_{L_m}} \rangle_k = R_c\langle i_{L_{lp}} \rangle_k - R_c\langle i_{L_m} \rangle_k + \frac{N_s}{N_p}R_c\langle i_{L_{ls}} \rangle_k + jk\omega L_m\langle i_{L_m} \rangle_k \tag{G.47}$$

$$L_{ls}\langle \dot{\imath_{L_{ls}}} \rangle_k = -\frac{N_s}{N_p}R_c\langle i_{L_{lp}} \rangle_k + \frac{N_s}{N_p}R_c\langle i_{L_m} \rangle_k - \left(r_{seq} + \frac{N_s^2}{N_p^2}R_c + R_{ESRo}\right)\langle i_{L_{ls}} \rangle_k + \langle s_2 v_{C_o} \rangle_k - R_{ESRo}\langle s_2 i_o \rangle_k + jk\omega L_{ls}\langle i_{L_{ls}} \rangle_k \tag{G.48}$$

$$C_o\langle \dot{v_{C_o}} \rangle_k = -\langle s_2 i_{L_{ls}} \rangle_k - \langle i_o \rangle_k + jk\omega C_o\langle v_{C_o} \rangle_k \tag{G.49}$$

$$\langle i_{in} \rangle_k = -\frac{1}{R_{ESRin}}\langle v_{C_{in}} \rangle_k + \langle s_1 i_{L_{lp}} \rangle_k + \frac{1}{R_{ESRin}}\langle v_{PV} \rangle_k \tag{G.50}$$

$$\langle v_o \rangle_k = -R_{ESRo}\langle s_2 i_{L_{ls}} \rangle_k + \langle v_{C_o} \rangle_k - R_{ESRo}\langle i_o \rangle_k \tag{G.51}$$

$$\left[\frac{\dot{\boldsymbol{x}}}{\boldsymbol{y}}\right] = \left[\frac{M^{-1}A \mid M^{-1}B}{C \mid D}\right]\left[\frac{\boldsymbol{x}}{\boldsymbol{u}}\right]$$

$$\boldsymbol{x} = [\boldsymbol{x}_0^T \quad \boldsymbol{x}_{1R}^T \quad \boldsymbol{x}_{1I}^T \quad \boldsymbol{x}_{2R}^T \quad \boldsymbol{x}_{2I}^T]^T$$

$$\boldsymbol{y} = [\boldsymbol{y}_0^T \quad \boldsymbol{y}_{1R}^T \quad \boldsymbol{y}_{1I}^T \quad \boldsymbol{y}_{2R}^T \quad \boldsymbol{y}_{2I}^T]^T$$

$$\boldsymbol{u} = [V_{PV} \quad i_o]^T$$

$$A = \begin{bmatrix} A_{00} & A_{01R} & A_{01I} & A_{02R} & A_{02I} \\ A_{1R0} & A_{1R1R} & A_{1R1I} & A_{1R2R} & A_{1R2I} \\ A_{1I0} & A_{1I1R} & A_{1I1I} & A_{1I2R} & A_{1I2I} \\ A_{2R0} & A_{2R1R} & A_{2R1I} & A_{2R2R} & A_{2R2I} \\ A_{2I0} & A_{2I1R} & A_{2I1I} & A_{2I2R} & A_{2I2I} \end{bmatrix} \quad B = \begin{bmatrix} B_0 \\ B_{1R} \\ B_{1I} \\ B_{2R} \\ B_{2I} \end{bmatrix} \qquad (G.52)$$

$$C = \begin{bmatrix} C_{00} & C_{01R} & C_{01I} & C_{02R} & C_{02I} \\ C_{1R0} & C_{1R1R} & C_{1R1I} & C_{1R2R} & C_{1R2I} \\ C_{1I0} & C_{1I1R} & C_{1I1I} & C_{1I2R} & C_{1I2I} \\ C_{2R0} & C_{2R1R} & C_{2R1I} & C_{2R2R} & C_{2R2I} \\ C_{2I0} & C_{2I1R} & C_{2I1I} & C_{2I2R} & C_{2I2I} \end{bmatrix} \quad D = \begin{bmatrix} D_0 \\ D_{1R} \\ D_{1I} \\ D_{2R} \\ D_{2I} \end{bmatrix}$$

$$M = \bigoplus_{i=1}^{5} M_i$$

In $(G.45)$ – $(G.51)$, the terms of the form $jk\omega m\langle x\rangle_k$, where $m \in M_i$, are the result of differentiation with respect to time, as described in the literature. As mentioned in the main text, the operator $\oplus$ denotes the n-ary direct sum, which is a block diagonalization operation when applied to matrices.

In this form, the state space model is unterminated, and may be used as the basis for closed-loop control perturbation and linearization. To simulate the model in open loop, a load resistance term must be added to maintain the power output at the desired level. This term appears in the system of equations in the main text and will not be repeated here.

APPENDIX H

ACCESS TO TRANSFORMER DESIGN SCRIPT AND REMOTE-CONTROL SOFTWARE

Programming is a skill with an importance that cannot be understated in today's world, and for engineering tasks, having at least a basic understanding of programming principles and best practices is essential. However, this does not necessitate writing every single tool oneself, as it is often the case that open-source programs exist that perform the desired task.

In this report, two software tools have been described, namely the MATLAB transformer design script 'transformerDesign.m' and remote-control software 'RTModbusControl', but their codebases are impractically large for inclusion in the report itself, even as addenda. Instead, the popular version control, programming collaboration, and code-sharing website GitHub hosts up-to-date versions of each tool, available for inspection and download. The repositories for each tool are open-source, and available through the ASU Power Electronics group's profile at https://github.com/ASU-Power-Electronics.

Open-source software is a two-way street: not only are these files available for inspection and personal use, they can be contributed to by others via the fork and pull request process on GitHub. In this way, we as researchers and programming enthusiasts can work together to make the world a better place, one line of code at a time.